Analysis of Tubular Adhesive Joints in Aluminum and Composite Structures under Crush and Tensile Loads

by

Monish Urapakam Ramakrishnan

A dissertation submitted in partial fulfillment
of the requirements for the degree of
Doctor of Philosophy
(Mechanical Science and Engineering)
in the University of Michigan-Dearborn
2021

Doctoral Committee:

Professor Pankaj K. Mallick, Chair
Associate Professor Jian Hu
Professor HongTae Kang
Associate Professor German Reyes-Villanueva

Monish Urapakam Ramakrishnan

mramakri@umich.edu

ORCID iD: 0000-0002-9984-7679

Dedication

This dissertation is dedicated to my beloved Parents for all their unconditional love, kindness, and encouragement without which this work would not have been possible.

I would also like to dedicate this dissertation to my friends who have become a family away from home.

Acknowledgements

I would like to express sincere gratitude to my advisor Dr. Pankaj Mallick for his unwavering patience, motivation, and support. Dr. Mallick's guidance and insights helped me greatly in pursuing research and in writing this dissertation. I could not have asked for a better mentor for my doctoral studies, Thank you.

I would like to thank my doctoral committee: Dr. HongTae Kang, Dr. German Reyes-Villanueva and Dr. Jian Hu for their valuable time and advice. Their insightful comments and questions pushed me to broaden my research perspectives.

I thank my fellow colleagues Kishore Reddy and Caroline Kella for the fascinating discussions and fun we have had in the lab over the last three years.

I would like to thank the staff at UM-Dearborn Information Technology Services for their prompt technical assistance. Thank you, Rebekah Awood and Dr. Debi Butler, for your administrative support.

Table of Contents

List of Tables

List of Figures

Abstract

As the automotive industry moves toward developing lightweight crashworthy structures, it is expected that a multi-material solution involving steels, aluminum alloys and high-performance composites will become increasingly common in future vehicles. Joining a variety of materials with different physical, mechanical, and thermal characteristics is one of the major challenges for such multi-material designs. Adhesive joining is emerging as one of the key joining methods in multi-material structures, since in general, adhesives are compatible with most materials under consideration for lightweight vehicles.

There are many body, chassis and powertrain components in vehicles that are designed with tubular sections. A few examples of these components are the front rails, underbody frames or sub-frames, instrument panel crossbeams, drive shafts and spaceframe structures. Increasing use of hydroforming and closed-section extrusions will lead to even more use of tubular sections, especially in crush-resistant components, such as front rails and roof rails. Tubular joints are also used in buses and other heavy vehicle constructions. Unlike the seam adhesive joints between thin sheets or panels, there has not been much research and design studies on tubular adhesive joints in which a tube is fitted in another tube of the same material or different materials.

In a crash condition, tubular structures are designed to crush in a controlled manner. In addition to the crush mode, crush energy absorption and peak crush load are the two most critical parameters to consider for improved crashworthiness. If the tubular structure is made of

adhesive joints, it is important that the joint failure does not occur before controlled crushing of the joined tubes. The crush characteristics are affected by joint geometry and material properties. Hence, the key objective of this research is to develop a crush resistant tubular adhesive joint in aluminum-aluminum, composite-composite, and composite-aluminum structures using finite element analysis.

A Design of Experiments approach is used to understand the interactions between different joint parameters and their effects. Since such tubular structures are likely to be subjected to different forms of loading, the dissertation aims to present optimal tubular adhesive lap joint design choices for maximum energy absorption under crush load and joint failure strength under tensile load using finite element analysis.

Chapter 1 Introduction

1.1 Background

Need for better performance, efficiency and economics has shifted the automotive industry from predominantly using steel in vehicle builds to a more multi material approach [1, 2]. Until a few years ago, mass produced automobiles used steel solely for the BIW and body panels. This is shifting toward an increasingly multi-material philosophy, where each part of an automobile uses the material that is best suited for its performance and functionality (Figure 1.1). Different OEMs have adopted different philosophies in their design approach. For example, European auto makers such as Jaguar and Audi have adopted aluminum as the major material for BIW, with composites for some body panels and semi-structural applications [2, 3]. American and Japanese automakers have chosen a more multi-material approach, with, advanced high strength and ultra-high strength steels, aluminum and magnesium being used in the BIW based on the strength or stiffness requirement of its components and low carbon and high strength steels, composites and aluminum for body panels and semi-structural applications.

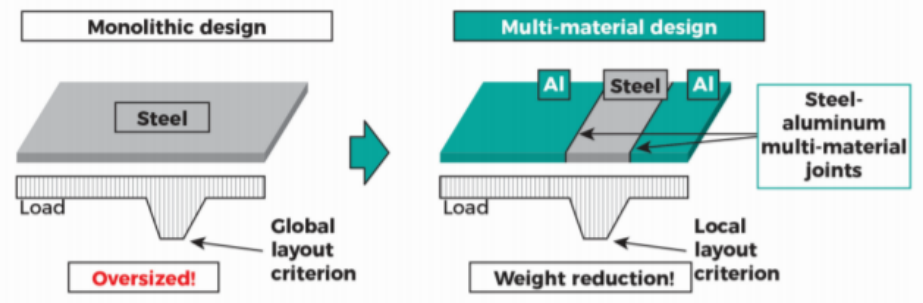

Figure 1.1 Multi-material design approach [4].

This difference in philosophies is due to difference in opinion on efficiency and economics of using aluminum. The primary driving force behind the shift from mild steels was the need for increased weight saving and environmental friendliness. Aluminum was found to be a very good substitute for mild steel with its better strength-to-weight properties. However, the carbon footprint incurred during the production of aluminum from ore is almost ten times higher than steel [5]. This along with new developments in the steel industry, such as advanced high strength steels (AHSS) and ultra-high strength steels (UHSS) which have higher strength-to-weight ratios compared to aluminum, has reduced the drive towards the use of aluminum in body structure components. The use of magnesium has similar issues.

The use of composites has been increasing steadily due to advances in manufacturing technology and reduction in costs [6]. High performance, super cars in the motor sports industry have been successfully using carbon fiber composites for constructing the chassis for a number of years. In the automotive industry, low-cost chopped fiber composites, such as random glass fiber sheet molding compounds, are popular in body panels, fascia, and other semi-structural applications. Even though carbon fiber composites offer the highest potential for weight reduction in body structure components, such as roof rails and B-pillar, their use has seen very little progress in mass-produced cars. This is due to several factors such as high cost of carbon fibers, their availability, manufacturing process control, and difficulty in modelling material behavior.

These issues have pushed automakers to adopt a multi-material approach to automotive design, with material selection for each individual component decided based on strength, stiffness, cost, and weight saving requirements. Figure 1.2 provides an example on the multi material construction of an automobile [2], and Figure 1.3 illustrates the future possibilities of

the changing demographic in automotive materials that includes predominantly mild steels in 2020 vehicles to a more diverse group of materials in 2040 vehicles [7].

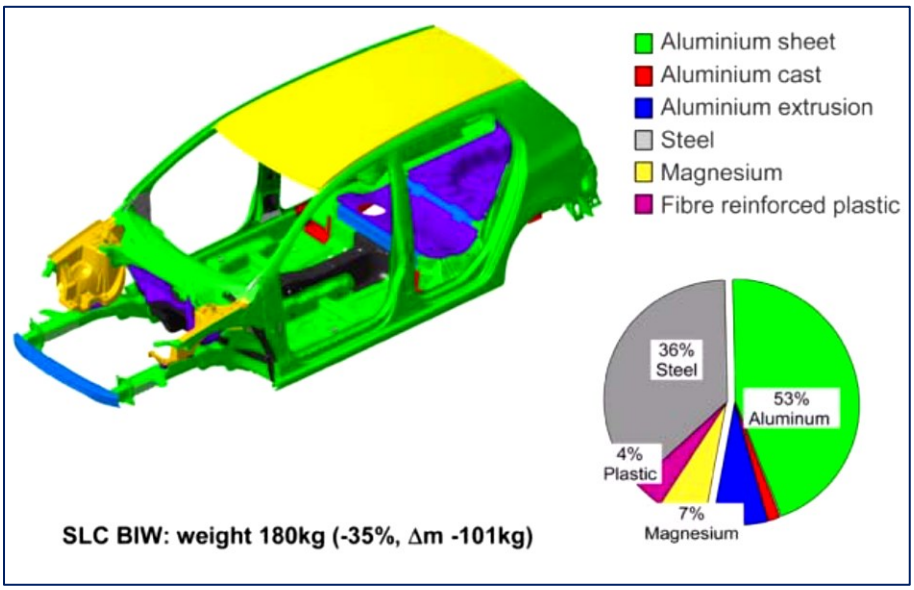

Figure 1.2 Example of multi material construction of an automobile [2].

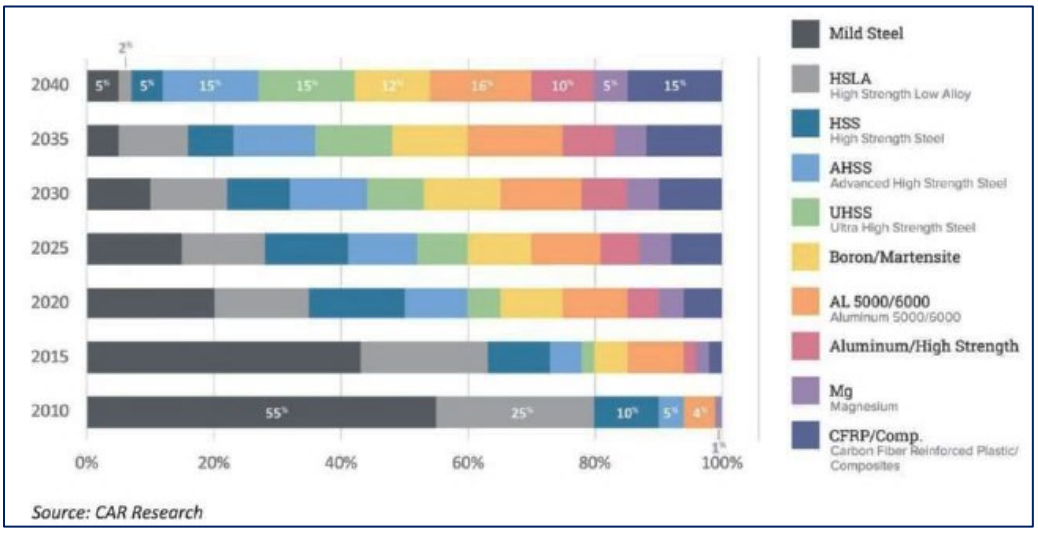

Figure 1.3 Expected demographic of automotive materials from model year 2020 to 2040 [7].

Occupant safety and crashworthiness is an important requirement of automotive design, due to increasingly strict regulatory requirements as well as consumer expectations. Even though the focus has shifted to crash avoidance technology with many such devices being made mandatory from 2022 by the National Highway Transportation Safety Agency (NHTSA), the crashworthiness of a car remains critical to protect the occupants in the event of a crash. And, to maintain high safety standards, the use of different materials in the construction of a car places greater emphasis on the joints, making joint design a critical area of study. Currently, welding is widely used to join components due to the high welding speed, low cost, and easy automation of the process. However, welding can only be used to join similar materials, such as steel with steel or aluminum with aluminum. For joining of dissimilar materials, joining techniques such as adhesive bonding and mechanical fastening methods are used. Figure 1.4 indicates the prospects of various joining processes due to a multi-material design approach [7]. Most notables among them are the growth of adhesive bonding and decreasing use of resistance spot welding (RSW).

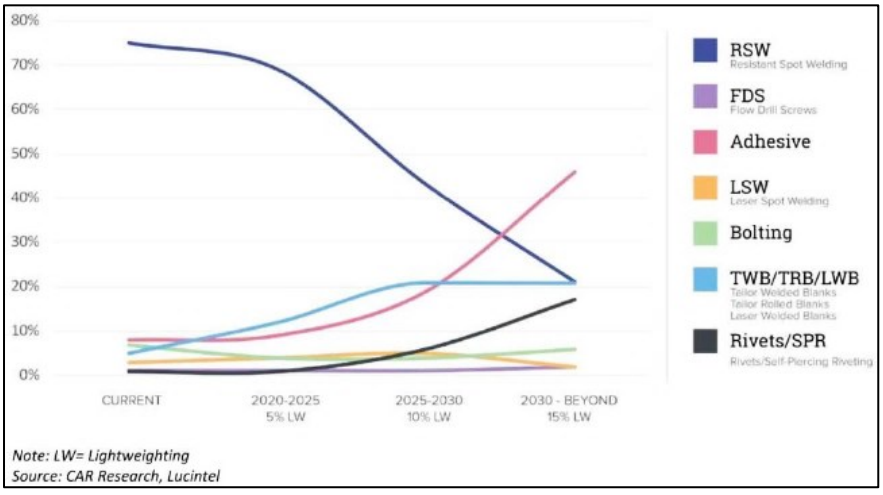

Figure 1.4 Current and future trends in joining processes in the automotive industry [7].

Mechanical joining methods such as self-piercing riveting (SPR) are suitable for joining aluminum alloys; but in the case of composites, processes involved in SPR and bolted joints, such as punching or drilling of holes, may cause delamination and fiber breakout. Also, the clamping load of the fasteners may cause localized damage to the materials under the fastener head and hence, precautions must be taken to ensure that the clamping forces are distributed over a wider area. Other problems such as electrical discontinuity and fastener corrosion also affect mechanical joints in composites.

Unlike mechanical joints, adhesive joints do not need any significant alteration to the components that may damage the material and hence, are suited for joining composite-metal or composite-composite parts [4, 8]. Other advantages of adhesive joining are low cost, ability to join complex shapes, higher shear strength and attenuation of noise and vibration. Disadvantages include the possibility of out-of-plane joint deformation under load, the need for surface treatment before joining to ensure good adhesion with the substrates, poor resistance to heat or cold, etc. The demerits to adhesive joining can be avoided through altering the joint design and proper surface treatment. Hence, adhesive joining has become a popular technique for composite joints.

As the automotive industry moves toward developing lightweight crashworthy structures, it is expected that a multi-material solution involving steels, aluminum alloys and high-performance composites will become increasingly common in future vehicles. Joining a variety of materials with different physical, mechanical, and thermal characteristics is one of the major challenges for such multi-material designs. Adhesive joining is emerging as one of the key joining methods in multi-material structures, since in general, adhesives are compatible with most materials under consideration for lightweight vehicles.

There are many body, chassis and powertrain components in vehicles that are designed with tubular sections. A few examples of these components are the front rails, underbody frames or sub-frames, instrument panel crossbeams, drive shafts and spaceframe structures. Increasing use of hydroforming and closed-section extrusions will lead to even more use of tubular sections, especially in crush-resistant components, such as front rails and roof rails. Tubular structures are also widely used in buses, trains, and other heavy transportation vehicle constructions. Such structures are being paid particular attention in the railroad industry to reduce weight of steel-based carriages. Examples of tubular construction in different applications are shown in Figure 1.5. Such tubular structures in a multi-material design would require the use of adhesive bonding to join different sections.

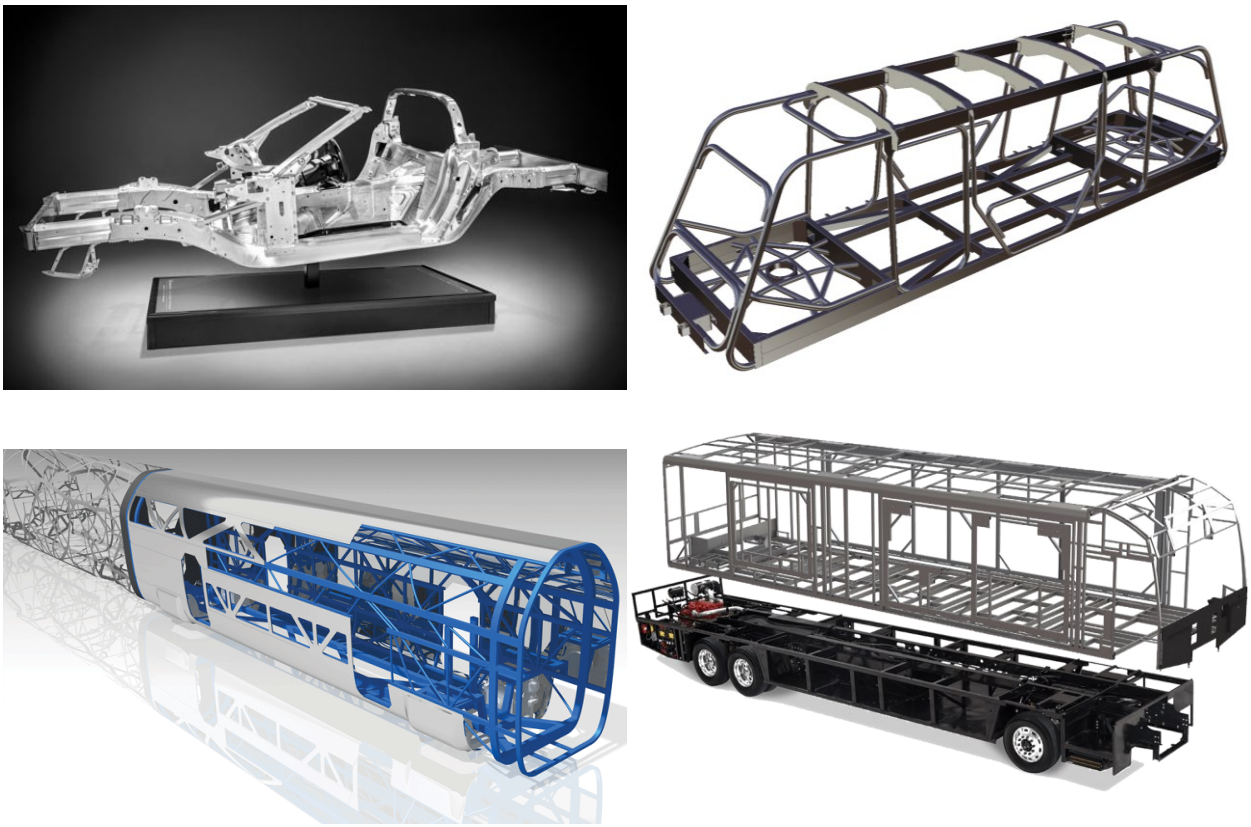

Figure 1.5 Tubular structures in cars, light rail, RVs, and rail coaches (clockwise from top left). (Source: Web)

Tubular joints are not limited to the transportation industries. The oil and gas industry uses long, slender tubes called riser to extract crude oil and natural gas from underground and ocean floor reserves. The use of polymer composite tubes is noticing an increase in acceptance as risers due to several advantages offered by them, such as weight reduction, high strength and stiffness, corrosion resistance, and better thermal insulation. This has been effectively adopted by Saudi Aramco [9] across a significant portion of their oil and gas flow line network. An example of their glass fiber reinforced composite tubes is shown in Figure 1.6. These risers extend thousands of feet from the ocean bed to the floating unit on the ocean surface and are constructed by joining several sections of tubes using adhesive bonds. Typical joining techniques include tubular lap joints, flange joints and socket type joints.

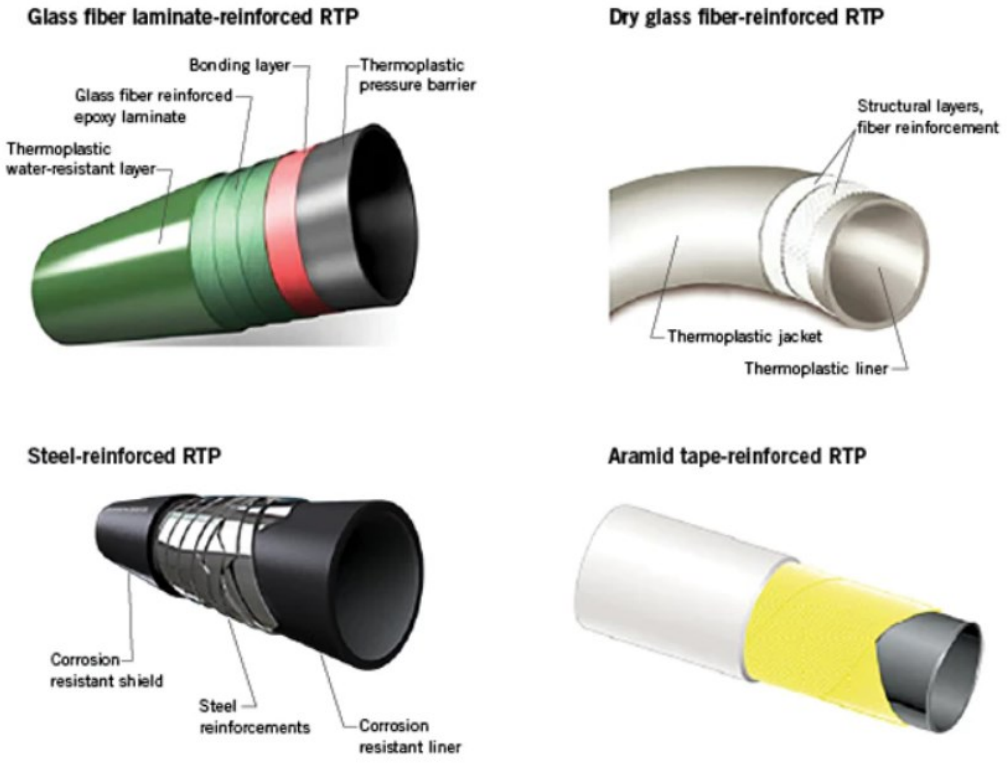

Figure 1.6 Reinforced thermoplastic (RTP) risers offered by Saudi Aramco [9].

Unlike the adhesive seam or lap joints in thin sheets or panels, there has not been much research and design studies on tubular adhesive joints. Recent literature on tubular lap joints is based on loading conditions generally faced in riser joints, such as hydrostatic pressure, internal pressure, bending due to water currents, torsion, tensile loading due to the riser tube's weight, and a combination thereof. These joints are generally bonded using brittle adhesives and the joint including substrates are not designed to yield. Hence, most studies on tubular joints in literature involve linear stress analysis of bonded area and use strength-based failure conditions. The results in these studies suggest that several factors influence joint characteristics such as boundary conditions, tube and joint geometry, and material properties.

Tubular adhesive joints in automotive and aerospace industries are structural joints that are required to not only have high strength and stiffness, but also absorb energy during crash. Hence, there is a need to investigate the characteristics of such joints under different types of loads which would result in different forms of deformation and joint failure. The objective of this study is to develop a numerical model to analyze the characteristics of multi-material structures with tubular single lap joints under different load cases and optimize the joint design for strength and energy absorption. The findings of this study will provide insight on the performance of such joints if used in the design of front-end structure in automotive chassis and help other ground transportation industries such as trains, buses, and trucks in designing structures with light weight composite materials, particularly with joining of multi-material tubular members in the coach structures.

1.2 Objectives

The objective of this dissertation is to analyze the performance of aluminum and composite tubes with single lap adhesive joints under axial crush and tensile loads at quasi-static

and high loading rates using finite element analysis. A parametric study using a design of experiments-based approach is conducted to analyze the influence of geometric and material variables on the crush performance indicators such as energy absorption, peak load and modes of collapse and tensile failure performance, such as peak loads and failure modes. Optimal configurations for Al-Al, Al-composite and composite-composite joints are presented with the objectives of maximizing energy absorption under compressive crush load. Since tubular structures are also subjected to tensile loading, the dissertation also studies the performance of the same tubular lap joints under tensile load for similar joint configurations and present optimal tubular adhesive lap joint design choices for joint failure strength under tensile load using finite element analysis.

1.3 Research Methodology

The dissertation presents a numerical analysis of tubes with single lap adhesive joints subjected to compressive crush loads and tensile loads. Performance of the joints is measured in terms of energy absorption, crush load and modes of deformation under compression and joint strength under tension. The results of analysis are obtained using numerical simulations constructed and processed using LS Dyna, a commercial finite element solver. Due to unavailability of resources to conduct experiments, the necessary material properties are obtained from literature and necessary calibration is done wherever possible.

The structure considered here consists of three major parts, the two circular tubes that are joined using a thin adhesive layer. Varying the joint design and material parameters, such as overlap length, tube dimensions, substrate material properties and adhesive properties is expected to significantly influence the performance of the joint. This hypothesis is based on several stress analysis studies available in literature that show that joint geometry and substrate

materials have a significant influence on the stress distribution in the adhesive layer. Hence, this study considers the influence of the following parameters on joint performance:

- Load conditions considered are quasi-static and high speed compressive and tensile loadings,
- Joint parameters include joint geometry variables such as tube thickness, tube length, bond overlap length, and adhesive thickness.
- Material properties of the tubes and adhesive.

Design of experiments, a statistical approach is used to plan and interpret results obtained from numerical simulations. A full factorial model is used to analyze the effects and interactions of different variables on the tubular joint performance. Optimal joint configurations are determined by optimizing the simulation response criteria. The analysis of data is conducted using Minitab, a commercially available statistics package.

1.4 Chapter Distribution

The dissertation is divided into the following chapters to present the methodology, results, and outcomes:

- Chapter 2: Literature review. This chapter presents a brief review of the existing literature on the crush characteristics of aluminum and composite tubes, a brief discussion on adhesive joints and finally, the current literature on tubes with single lap adhesive joints.
- Chapter 3: Stress analysis of tubular single lap joints. A finite element analysis of the stress distributions across the adhesive overlap of tubular single lap joints is presented in this chapter. The results discussed in this chapter are based on quasi-static compressive loading and linear elastic material conditions for different joint configurations. The

influence of various joint design parameters on the stress distributions in the adhesive layer is considered.

- Chapter 4: Crush analysis of Al-Al tubular single lap joints. Quasi-static and high-speed crush analysis of Al-Al joints is presented in this chapter using explicit finite element simulations. The chapter begins with a description of the modeling technique employed and then presents a parametric study on the influence of load type, joint geometry, and material properties on the crush performance of Al-Al tubular joints. It also presents a study to determine the optimal joint design parameters for both maximum energy absorption and peak load.
- Chapter 5: Quasi-static crush analysis of Al-composite and composite-composite tubular single lap joints. The focus of this chapter is on the crush performance of tubular joints in which either one or both tubes are made of a carbon fiber composite. The results compare influence of tube length, tube material combination and layup of the composite tubes under quasi-static crush.
- Chapter 6: Analysis of Al-Al and Al-composite joints under tension. This chapter presents the tensile performance of tubular joints in which at least one tube is made of aluminum and the other tube is either an aluminum or a carbon fiber composite. It considers the key joint design parameters that influence the failure modes and the peak loads as the tensile load is increased quasi-static and high loading rates.
- Chapter 7: Conclusions. A summary of results and recommendations for future work are presented in this chapter.

Chapter 2 Literature Review

When tubular members joined by adhesive lap joints are subjected to an axial load, the function of the joint is to transmit the load between the tubular members and maintain integrity until the tubes fail, either by plastic collapse in the tubes if the axial load is compressive or by tensile yielding or fracture if the axial load is tensile. Good joint performance requires that the adhesive failure should not occur before the tube failure. Under crash conditions, the tubular sections are expected to deform with progressive folds if they are made of ductile metals or fail with progressive damage development if they are made of composite materials for best crash energy absorption. The deformation and failure characteristics of tubular sections with an adhesive lap joint depend on several factors such as tube and adhesive material properties, joint geometry, type of load, and fabrication issues. Hence, in this chapter, a review of crush characteristics of thin-walled metal and composite tubes, adhesive properties, and current state of research on such joints is presented.

2.1 Crush Characteristics of Thin-Walled Metal Tubes

Thin-walled metal tubes have long been used as energy absorbers due to their high load carrying and energy absorption capabilities. This is particularly true for axially loaded tubular members which are commonly used in automotive crash structures. Under axial crush, thin-walled tubes with properly designed dimensions exhibit load-deformation characteristics resembling the buckling and post-buckling behavior of thin plates rather than columns. Hence, such tubular members offer continued resistance to deformation even after buckling.

The characteristics of thin-walled steel and aluminum tubes subjected to axial crush has been well researched over the years and several publications have investigated the various factors determining modes of deformation and crush load. The primary modes of collapse in crush can be broadly classified as Euler or global buckling, progressive collapse, and mixed collapse. Progressive collapse mode can be further classified based on the nature of progressive collapse under crush such as axisymmetric folding, n-lobe diamond shaped folding, and mixed diamond-axisymmetric type. An illustration of some of these modes of collapse with their load-deflections curves are shown in Figure 2.1. Highest resistance to crush is offered by tubes undergoing regular folding illustrated by a high mean crush load in (a) compared to global buckling case where there is a rapid drop in resistance to axial crush (b).

The different modes of collapse are initiated by elastic local buckling leading to bending collapse or progressive crush of the cross section. In tubes with circular cross section, the basic column buckling theory [10] proposes that elastic buckling is a function of tube geometry and occurs as m half waves in circumferential direction and n half waves in longitudinal direction, where m and n are whole numbers and vary based on tube dimensions and tube material. In this theory, for axisymmetric crush m is zero and in case of diamond mode of failure m has a whole number value. However, experimental observations indicate that such wave forms do not occur or become visible at the same time but occur one after the other.

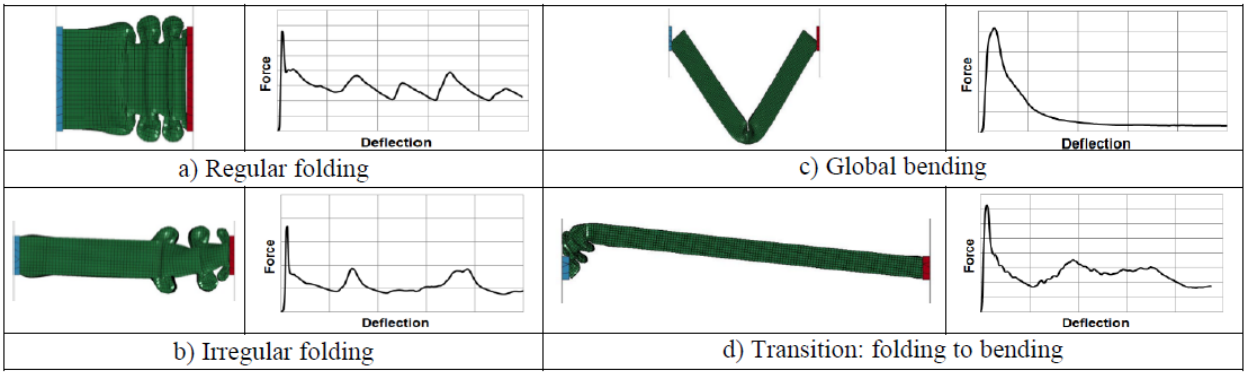

Figure 2.1 Modes of Axial collapse in thin-walled tubes [11].

An alternate analysis of axial collapse was proposed by Allan [10] who considered tube deformation as a pressure vessel problem. The author states that the wall deformation which is a result of Poisson effect causes a tensile or compressive hoop stress. Under stable regime, wall deformation will result in axisymmetric crush and unstable stresses will result in diamond formation. The author proposes that for low t/D values initial imperfections in the tube and effect of friction at the ends could result in instabilities resulting in diamond lobe formation compared to tubes with high t/D values where any imperfections are averaged out over a larger thickness.

A detailed experimental classification of axial collapse in tubes with cylindrical cross sections was published by Andrews et al. [12]. Numerous specimens with different lengths (L), diameters (D) and thicknesses (t) were tested, and the results indicated a grouping of collapse modes based on t/D and L/D ratios. This is represented in Figure 2.2. Slender tubes with high L/D ratios tend to fail by Eulerian buckling which is undesirable because of their low energy absorption. For similar L/D values, the thickness of the tube determines the mode of progressive collapse. There is a transition from mixed mode to axisymmetric crush with increasing t/D ratio. This is in accordance with the theoretical explanation stated previously. Other factors influencing the mode of collapse include material properties, cross-section shape and boundary conditions.

An appropriately designed thin-walled tube subjected to axial crush is characterized by a reasonably constant mean crush force and progressive plastic collapse resulting in high energy absorption capacity. The force displacement curve for such a tube under axial crush is shown in Figure 2.3. The curve is characterized by an initial peak force or crippling force followed by several peaks and valleys representing formation of folds. This initial peak force is desired to be as low as possible to reduce transmitted impulse forces on the occupant or equipment. Crush triggers are used for this purpose. An ideal force displacement curve for an energy absorber with a crush trigger is shown in Figure 2.3.

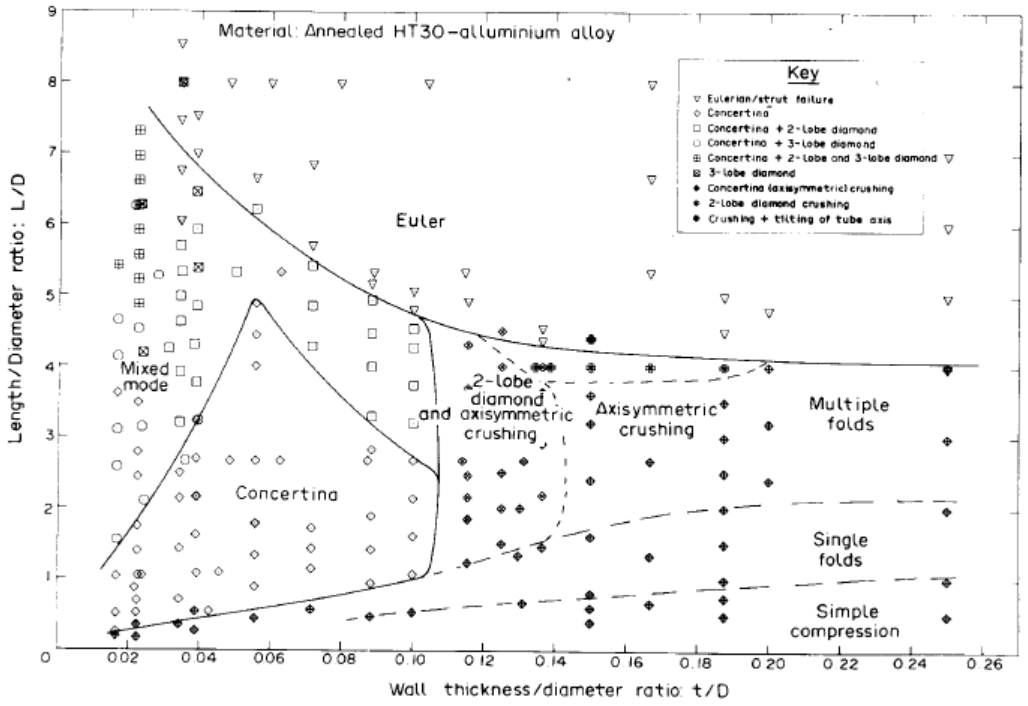

Figure 2.2 Collapse modes of aluminum tubes with circular cross section [12].

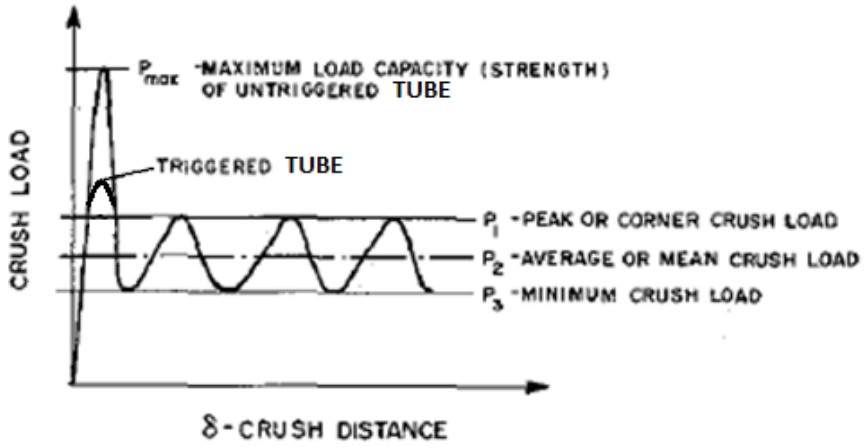

Figure 2.3 Ideal load-displacement curve for an axially collapsing tube.

The energy absorbed during axial progressive collapse of the tube is the area under the force-displacement curve, which can be approximated as the product of mean crush force and crush distance. Many studies have proposed theoretical or empirical models to predict mean crush force. A widely accepted theoretical expression for mean crush force (P_m) was developed by Alexander [13]. The expression was obtained by assuming that the tube is a rigid, perfectly plastic material, and the deformation mode is an axisymmetric progressive collapse. The expression is:

$$P_m = K\sigma_y t^{1.5}\sqrt{D} \qquad \text{Eq. 2.1}$$

where, $K \cong 6.08$, σ_y is the yield strength of the material, t is tube thickness and D is mean diameter. The expression compares well with the experimental results. Another useful empirical expression for mean crush force, given by Equation 2.2, was developed by Guillow et al. [14] using data from quasi-static crush of circular aluminum tubes. Equation (2.2) for the mean crush force works for any deformation type.

$$P_m = 18.075\sigma_y t^2 \left(\frac{D}{t}\right)^{0.32} \qquad \text{Eq. 2.2}$$

As can be seen in Equations 2.1 and 2.2, deformation of tubes and crush force depend on the yield strength of the material. Hence, if the tube is made from a strain rate dependent material, the mean crush force equations need to be modified appropriately [15]. Commonly used model to define rate sensitivity for yield strength is the Cowper-Symonds equation. Incorporating this into Equation 2.1 we get P_m as,

$$P_m = K\sigma_y \left[1 + \left(\frac{\dot{\varepsilon}}{D}\right)^{1/q}\right] t^{1.5}\sqrt{D} \qquad \text{Eq. 2.3}$$

where, D and q are material constants. Also, at very high strain rates circular tubes with high wall thickness exhibit mushrooming at the impacted end.

To compare experimental results of tubes with different geometry and cross sections two dimensionless parameters are commonly used. They are structural effectiveness and solidity ratio [16]. Structural effectiveness, η, (Equation 2.4) is defined as the ratio of mean crush force to the peak crush force, and solidity ratio, ϕ, (Equation 2.5) is defined as the ratio of cross-sectional area (A) to area enclosed by the cross-section (A_c).

$$\eta = \frac{P_m}{A\sigma_y} \qquad \text{Eq. 2.4}$$

$$\phi = \frac{A}{A_c} \qquad \text{Eq. 2.5}$$

Equating these two parameters indicates effectiveness of different cross sections. Equation 2.6 gives the effectiveness expression for a square tube and Equation 2.7 represents the relationship for a circular tube [17]. Comparing the two expressions, we see that structural effectiveness is higher for a circular tube compared to a square one. In fact, experimental results show that circular tubes have the highest structural effectiveness but are rarely used due to manufacturing difficulties such as distortion in shape and axis, and assembly constraints.

$$\eta = 1.3\phi^{2/3}, for\ a\ square\ tube \qquad \text{Eq. 2.6}$$

$$\eta = 2\phi^{0.7}, for\ a\ circular\ tube \qquad \text{Eq. 2.7}$$

2.2 Crush Characteristics of Thin-Walled Composite Tubes

Thin-walled tubes made of fiber reinforced polymer composites have become increasingly popular as energy absorbers especially in the aerospace industry where weight is an important design consideration. Composite tubes with appropriate design show much higher energy absorption per unit mass or specific energy absorption compared to aluminum tubes [18, 19, 20]. Similar to thin-walled metal tubes, the preferred mode of collapse in composite tubes is also a progressive crush. However, unlike elasto-plastic collapse in metal tubes, progressive crush in composites is governed by different principles due to the brittle nature of the constituents. Factors influencing the crush mode are fiber and matrix properties, fiber-matrix interactions, interfacial properties, fiber orientation and layup, fiber volume fraction and geometry of the tube. For certain material and geometry parameters, composite tubes can exhibit unstable crush or catastrophic failure. Tube thickness is a crucial parameter as thin-walled tubes can fail due to global buckling and thick-walled tubes can fail due to circumferential tension. This is a result of much larger load required to initiate crush compared to buckling for thin tubes. Hence, crush initiators such as end chamfers are provided to reduce the load needed to initiate crush at the crush front.

Under axial crush, primary driving forces for crush are transverse shearing, lamina bending and local buckling [18]. A combination of the first two failure modes results in brittle fracture of the lamina in the case of brittle fiber/matrix, and if the material has some ductility, local buckling of the lamina occurs. Energy absorption in composite tubes is governed by the energy dissipated due to fracture and crack growth. Hence, for high energy absorption stable crack growth or progressive local buckling is preferred. In the event of unstable crack growth or

if crack length is less than interlaminar thickness, tubes fail catastrophically. Possible failure modes in composite tubes are illustrated in Figure 2.4.

Transverse shearing mode results in a wedge at the crash front due to fragmentation resulting from interlaminar and longitudinal cracks. Such fracturing and crack growth contributes to the energy absorption in this mode. The crack lengths in this mode are generally smaller than interlaminar thickness resulting in single or multiple lamina bundles. Such bundles support crush force until crack growth causes lamina failure. Lamina bending results in long inter- and intra-laminar cracks. Such cracks are parallel to fiber orientation and do not result in lamina failure but show significant bending deformation. This deformation along with friction at lamina-impactor interface are major sources of energy absorption in this mode. A combination of these two results in brittle fracture type crush mode.

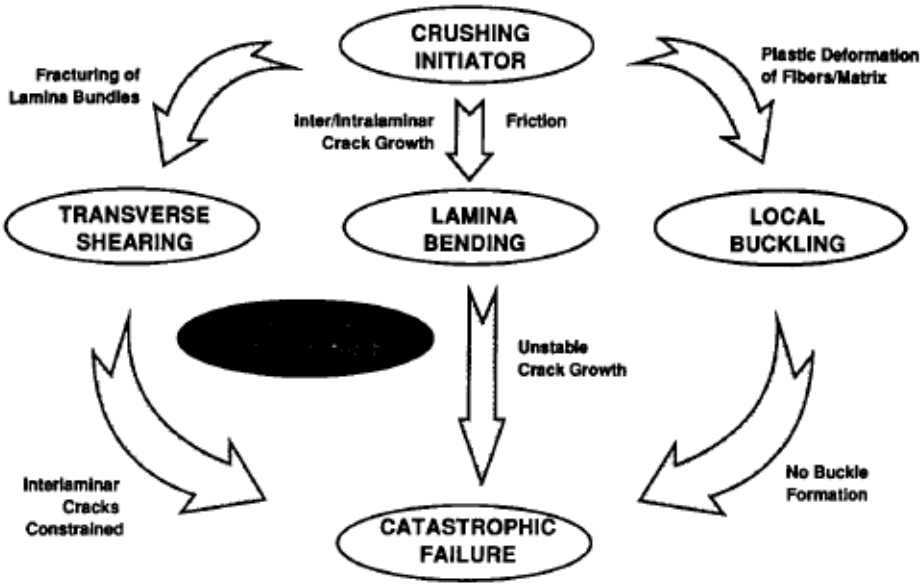

Figure 2.4 Failure modes in composite tubes [18].

Hull [21] presented a unified theory of composite tube crush where progressive crush occurs due to a fragmentation mode or splaying mode. Fragmentation is stated occur when the stress builds up at the crush front is sufficiently high to cause shear failure in the lamina. Both types of failure are initiated at the crush front and final crush mode depends on the laminate configuration and material properties of the fiber and the matrix.

Several studies have investigated the influence of strain rate, crush initiators, fiber/matrix properties and laminate configurations to determine optimal configuration for energy absorption and peak crush force in composite tubes. However, due to a large number of variables involved in determining crush mode, there is no single model that describes the possible outcomes. In general, experimental observations and numerical simulations are used to design composite structures for crush applications. Furthermore, the effect of cross section is also present in composite tubes. Structural effectiveness of composite tubes with circular cross-section are observed to be much higher than tubes with square cross-section.

2.3 Adhesive Properties

Adhesives commonly used in industry are synthetic polymers such as epoxies, urethanes, acrylics, and cyanoacrylates [22]. Epoxy based adhesives are widely used in the automotive and aerospace industries for structural composite or composite-metal joints. They show good shear strength, stiffness, and temperature resistance, but have low impact resistance. This is improved with the addition of elastomeric toughenners. Urethanes have high impact resistance but low strength and temperature resistance, while acrylics exhibit similar properties to epoxies, but have high coefficient of thermal expansion that leads to high thermal residual stresses after curing. Urethanes and acrylics are also widely used in the automotive industry. Adhesive selection is quite important and depends on several factors such as adherend materials, surface preparation

requirements, application method, production time, use environment, strength, and operating costs.

Physical testing to determine joint performance under a variety of loading conditions and with different material combinations is an expensive process; to avoid this, numerical analysis of the problem is performed to analyze and optimize the joint design. A commonly used method to model adhesive bonds in finite element analysis is using the cohesive zone model. This model uses traction separation laws based on fracture energy to determine bond deformation and failure. To predict accurate results, confidence in material properties across different conditions is critical. Apart from the basic material properties of strength and modulus, numerical simulation using a cohesive zone model requires failure displacement and fracture energy (G_{IC}, G_{IIC}) data. For crush simulations, it is also important to consider the effect of strain rate on these parameters.

A large amount of information is available on the general characteristics of adhesives; however, structural adhesives are designed to meet specific joint design requirements with the use of additives that alter their mechanical properties of the adhesive and hence is difficult to predict their properties under different loading and environmental conditions using existing models. This is especially true for the effects of strain rate and bond thickness on the mechanical properties of adhesives. The use of adhesives in structural joints is a recent development; therefore, the research in this area is limited. The following sections review the literature on these topics.

2.3.1 Effect of Strain Rate on Adhesive Properties

Adhesives show high susceptibility to the effect of strain rate. Most studies focus on the tensile strength, modulus, and fracture toughness of adhesives due to their importance in

modeling adhesive joints and predicting failure. However, there is no consensus on a single material model to describe the effect of strain rate on the adhesive properties due to a wide variety of possible formulations and outcomes. Several studies have applied existing models used in polymers, metals, or the Time-Temperature Superposition Principle (TTSP) to describe the variation in properties. This section investigates the existing literature on the effect of strain rate on adhesives and related modeling methods. Since the number of adhesive formulations available in the market are numerous, with different characteristics, the results presented in literature cannot be compared as such. However, they provide a general direction on the important factors affecting the material behavior.

2.3.1.1 Adhesive Strength

Goglio et al. [23] studied the changes in the stress-strain curve and modulus of a two-part epoxy adhesive with increasing strain rate (ranging from $1x10^{-3}$ to $3x10^{3}$ s^{-1}) under tensile and compressive loads. The effect of curing conditions was also studied. The tests were conducted on a servo-hydraulic test machine for low to moderately high strain rates and split Hopkinson pressure bar test apparatus for very high strain rates. The adhesive shows an increase in strength and decrease in failure strain with an increase in strain rate. There is little effect on the elastic modulus with increasing strain rate. The study also explores the application of yield stress sensitivity models used for metals such as Johnson-Cook model and Cowper-Symonds model to adhesive data obtained in the study, without taking into consideration the viscoelastic nature of the material. Figure 2.5 shows the variation in stress-strain behavior with strain rate and Figure 2.6 compares the yield stress sensitivity models with the experimental data under tensile load. The models did not provide a good fit to the experimental data, especially at high strain rates; hence an arbitrary bilinear fit was proposed to describe the experimental results.

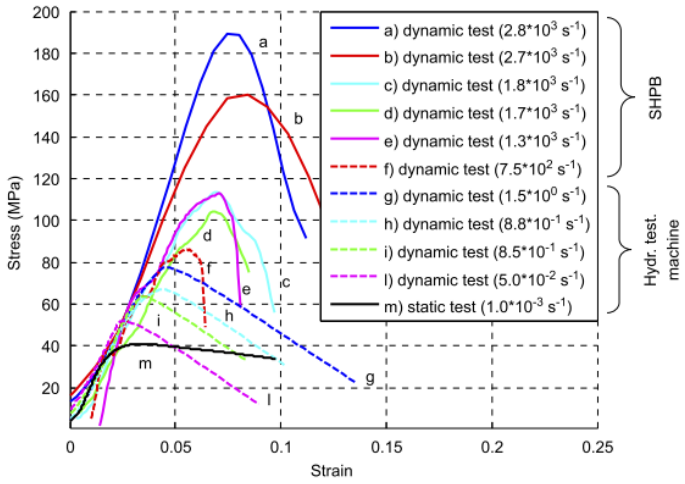

Figure 2.5 Effect of strain rate on the stress-strain behavior of a bulk epoxy adhesive [23].

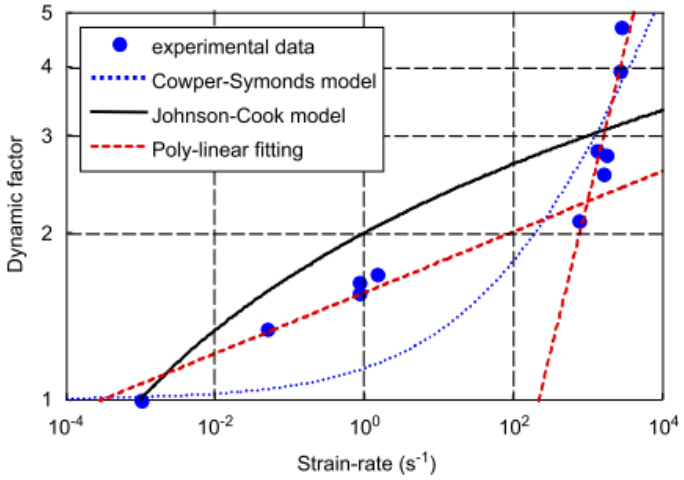

Figure 2.6 Comparison of dynamic factor, representing yield stress sensitivity to strain rate, with Johnson-Cook and Cowper-Symonds models [23].

The study by Chai [24] presents the effect of strain rate (ranging between 10^{-4} and 1 s^{-1}), temperature and adhesive thickness on the properties of structural adhesives under shear load. A napkin ring specimen was used to study the strength and failure strain of an epoxy resin. The

failure strain and strength are observed to decrease with increasing bond thickness at a fixed strain rate; the decrease in strain is explained as due to the probability of more flaws in a thicker bond. The shear strength is seen to increase with increasing strain rate, however, there is no effect on the failure strain (Figure 2.7).

Eyring's model is a commonly used to relate yield stress with strain rate and temperature in polymers. It relates the motion of molecules with strain rate and stress applied to the activation energy required to move the molecules. A mathematical representation of this model is expressed as follows.

$$\frac{\sigma_y}{T} = A[\ln 2C\dot{\varepsilon}_y + (Q/RT)] \quad \text{Eq. 2.8}$$

A modified version of Eyring's theory of molecular activation with constants A_1 and A_2, defined as activation energy and activation volume is used to predict shear strength and ultimate shear strain (Equations 2.9 and 2.10). The experimentally observed behavior is consistent with model predictions.

$$\tau_y = A_1[1 + A_2(T/T_g)\log(\dot{\gamma}/\dot{\gamma}_0)] \quad \text{Eq. 2.9}$$

$$\gamma_F = 3.5(T/T_g)(h_0/h)^c \quad \text{Eq. 2.10}$$

The shear fracture energy model is approximated as the product of shear stress and shear strain obtained from equations 2.9 and 2.10. The fracture energy normalized with height decreases with increasing height and increases with increasing strain rate. This model is verified using an end-notched fracture (ENF) specimen and shows reasonably good fit for lower bond thickness (Figure 2.9). Fracture energy also shows a decrease with increasing bond thickness.

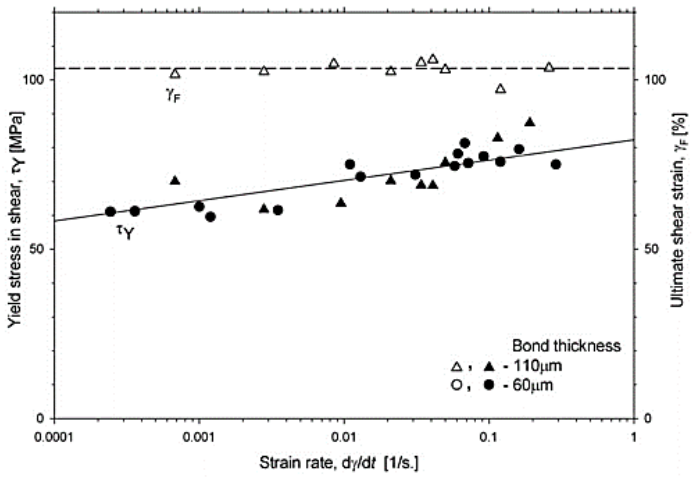

Figure 2.7 Effect of strain rate on yield stress and ultimate strain in shear [24].

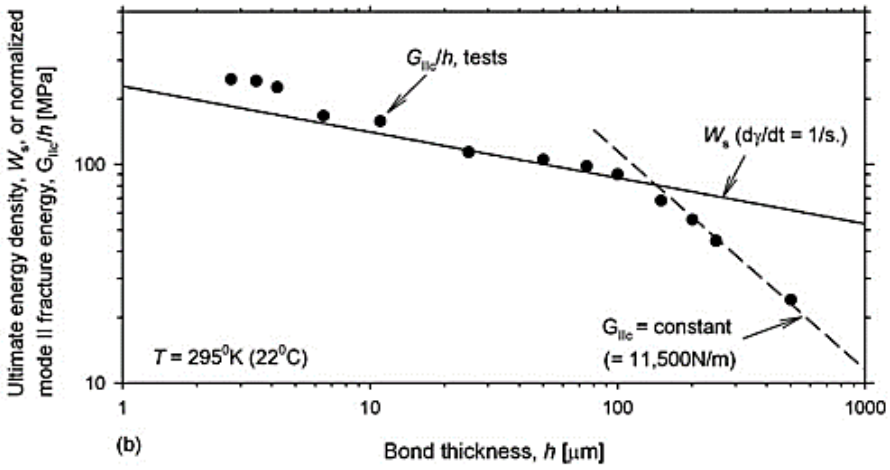

Figure 2.8 Effect of bond thickness on Mode II fracture Energy [24].

The shear strength model presented by Chai [24], has also been applied for tensile load cases by Banea et al [25]. However, this study investigates quasi-static extension rates (0.1, 1 and 10 mm/min) hence no significant variation in properties is seen.

Another extension of this model, with added parameters for α and β relaxation processes is applied to test data of epoxy and acrylic adhesives, in tensile and shear loads at different temperatures and a wide range of strain rates by Read et al [26]. Figure 2.9 plots the model fit with experimental data from tensile tests on epoxy specimens. Young's modulus is seen to increase with strain rate by about 6% per decade increase in strain rate. Tensile and shear strengths also increase with increasing strain rate, which is in line with other studies. Both epoxy and acrylic adhesives behave similarly under the influence of strain rate and temperature, however the magnitude of change is seen to be slightly higher in acrylic. Furthermore, their mechanical behavior in tension is shown to differ significantly from that in shear due to cavitation or crazing under tensile load for both epoxy and acrylic adhesives.

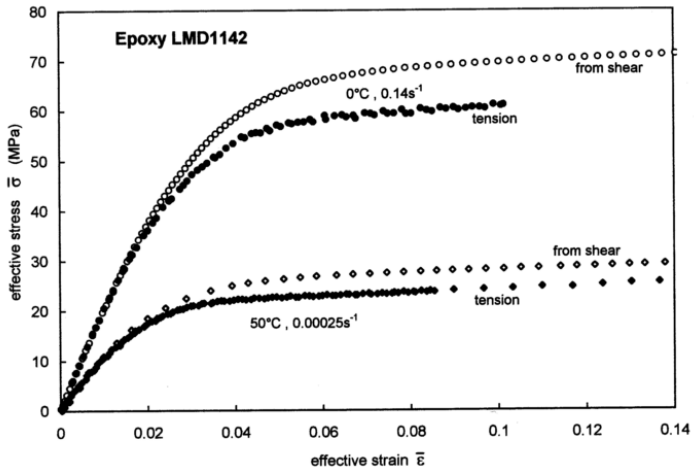

Figure 2.9 Stress-strain curve for an epoxy adhesive in tension and shear [26].

Brinson et al. [27] presents the effect of strain rate on the failure response as well as creep characteristics of structural adhesives. The study uses different Meltbond epoxy adhesives to conduct tensile tests. Tensile tests were done on an Instron testing machine over crosshead velocities of 0.002 to 2 in/min and on a pneumatic testing machine at 20 in/min. These tests showed that modulus of the linear elastic region remains constant with increasing strain rate; however, the elastic limit is seen to vary with the rate. Crazing or stress whitening is observed prior to yielding or fracture depending on the strain rate, but at the same strain value.

The study by Brinson et al. [27] shows that material properties such as yield stress, elastic limit stress and elastic limit strain can be described using Ludwick's equation at different strain rates (Figure 2.10), which is given by,

$$\sigma_{yp} = \sigma'_{yp} + \sigma' \log \frac{\dot{\varepsilon}}{\dot{\varepsilon}'} \qquad \text{Eq. 2.11}$$

where, σ_{yp} and $\dot{\varepsilon}$ are the yield stress and strain rate respectively, and σ', σ'_{yp} and ε' are material constants. The yield stress and elastic limit stress show an increase with increasing strain rate. The stress-strain behavior of the material is described using a modified Bingham's equation (Equation 2.12 given below). The results are plotted in Figure 2.11.

$$\begin{aligned} &\varepsilon = \sigma / E, for \sigma < \theta \\ &\sigma = \theta + ER\tau[1 - e^{-(\varepsilon - \varepsilon_\theta)/R\tau}], for \theta < \sigma < Y \end{aligned} \qquad \text{Eq. 2.12}$$

where, τ is the relaxation time and Θ is the elastic limit stress. It is important to note here that the relaxation time is seen to decrease with increasing strain rate; therefore, appropriate values need to be used in the modified Bingham's equation to determine the stress-strain response. The model provides a good correlation with experimental data in linear elastic region for the low strain rates considered here. This study does not consider the non-linear response of the adhesive and hence cannot predict properties for crash resistant adhesives.

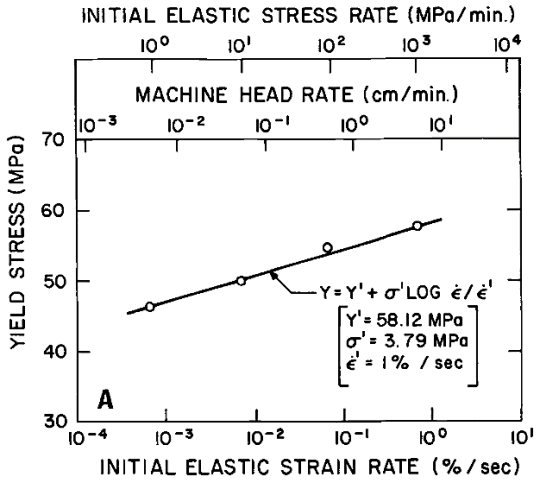

Figure 2.10 Effect of strain rate on yield stress modeled using Ludwick's equation and compared with experimental results [27].

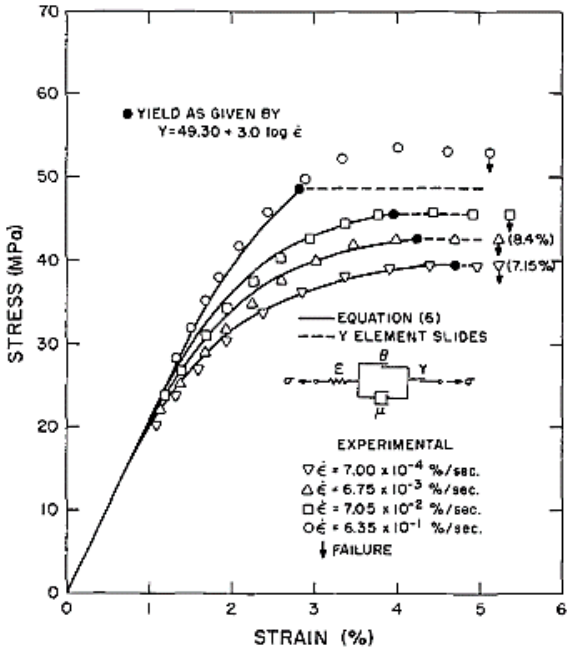

Figure 2.11 Stress-strain curve plotted using modified Bingham's model at different strain rates [27].

A study conducted on the effect of strain rate on an Epon epoxy adhesive by Chen and Zhou [28] considers a wide range of strain rates from 10^{-3} to 10^{4} s^{-1}. An MTS servo-hydraulic test machine was used for quasi-static tests and a split-Hopkinson bar was used for the high strain rate tests. The study showed a significant increase in the yield stress as well as the strength with increasing strain rate up to a certain test speed beyond which no significant change was observed. This saturation limit is attributed to adiabatic heating of the material due to plastic deformation. The softening due to heat generated at low strain rates is not sufficient to overcome the strain hardening of the adhesive resulting in an increase in strength. However, at high strain rates the two-phenomenon balance each other resulting in a saturation point. In the current study, this point is observed to be at 10^{3} s^{-1}. Figure 2.12 shows the variation in compressive strength with strain rate. The trend line for compressive strength is described using a hyperbolic tangent function with an arbitrary reference point.

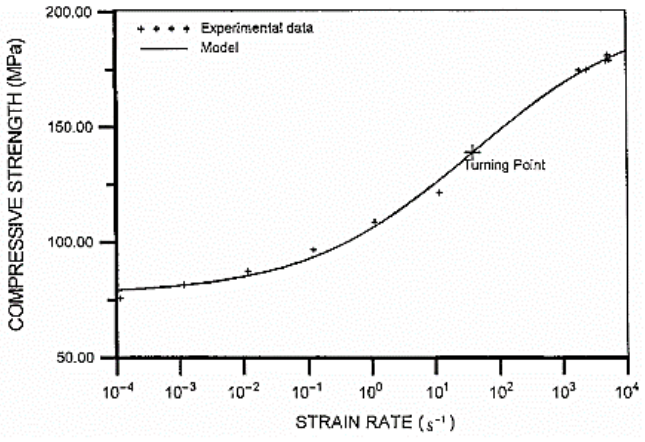

Figure 2.12 Effect of strain rate on compressive strength [28].

The authors also apply a modified Johnson-Cook model (equation 2.13), which is modified based on Eyring's equation to describe the stress-strain response at different strain rates.

$$\sigma = A\varepsilon^{n} e^{[-(\varepsilon/\varepsilon_y)^{m}(n/m)]}[1-(\frac{T-T_r}{T_m-T_r})^{k}] \qquad \text{Eq. 2.13}$$

where, n is a strain-hardening factor, m is a strain rate factor and A is a material constant. The exponential term describes the material softening region while, the term in the square brackets describes the temperature dependence. This model is seen to provide an accurate representation of the stress-strain curve obtained from test data in this study.

2.3.1.2 Fracture Toughness

A study on the rate dependent changes in fracture toughness of an epoxy adhesive was done by Pohlit et al. [29]. This study looks at the Mode I fracture toughness values for bulk adhesive using a compact tension specimen. The tests are conducted on an MTS servo hydraulic test machine with slack adapters to ensure uniform crosshead rate for the duration of the experiment. Crosshead rates of 10^{-6} to 1 m/s are considered. The fracture toughness is seen to decrease linearly with an increasing crosshead rate as shown in Figure 2.13, and failure is seen to be increasingly brittle as the crosshead rate is increased. To predict properties at higher crosshead rates, the time-temperature superposition principle (TTSP) is used. The predicted values up to 10^{10} m/s are plotted in Figure 2.14.

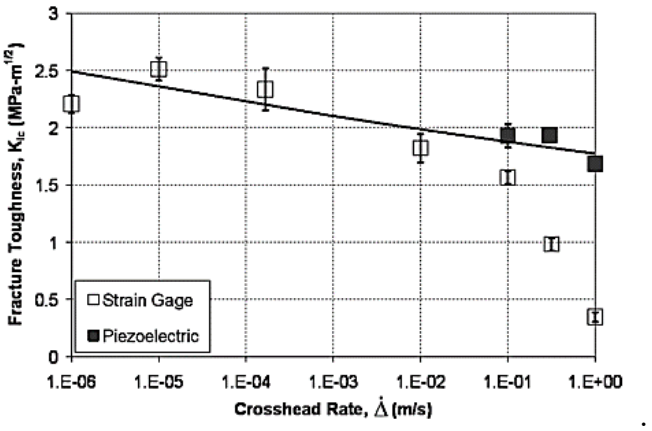

Figure 2.13 Effect of loading velocity on fracture toughness [29].

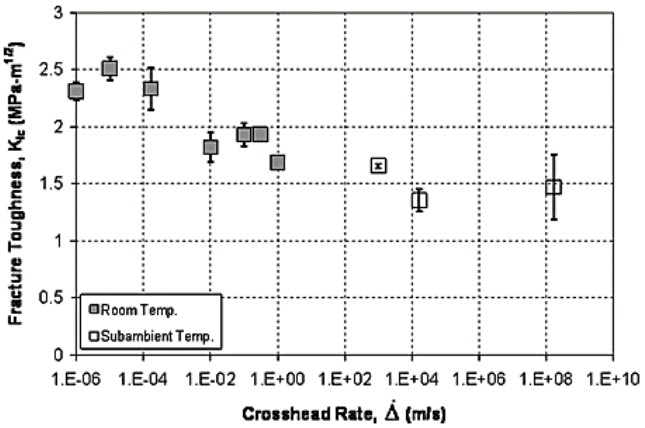

Figure 2.14 Fracture toughness values obtained using TTSP at high strain rates [29].

Automotive crash applications require data at high strain rates, and to obtain this, the Pohlit et al. [29] used the time-temperature superposition principle (TTSP), which works on the basis that linear viscoelastic polymers show a strong correlation between time and temperature [30]. At high temperatures, molecular motion is more rapid compared to low temperatures. Therefore, the response of time dependent properties at high temperatures for a short duration is equivalent to that at low temperatures for a longer duration. This principle is used to determine a master curve that can be used to predict time dependent properties over a longer duration, if the

nature of relationship between the property and time remains the same over the temperature range considered. The same principle is also used by Lim and Mizumachi [31] over a much wider set of experimental data to obtain the master curve for strength and fracture energy at 20^{o}C. The temperature range in their experiments is -80 to 80^{o}C and the testing speed is from 0.5 mm/min to 500 mm/min. Their results indicate an initial increase in strength and fracture energy with strain rate for a polyurethane adhesive. After reaching maximums at around a rate corresponding to the glass transition temperature of the adhesive, both show a decreasing trend.

Kinloch and Shaw [32] used compact tension (CT) specimens to determine Mode I fracture energy of a bulk adhesive and compared it with the fracture toughness obtained by using double cantilever beam (DCB) specimens in which the same adhesive is used to bond two steel substrates. The adhesive is a rubber toughened epoxy, and the tests are conducted on an Instron testing machine at four different displacement rates ranging from 10^{-6} to 10^{-3} m/s. To understand the differences in fracture toughness values between the two methods, effect of adhesive thickness, bond width and temperature are studied.

The adhesive fracture energy of the joints (determined in DCB tests) is found to be a strong function of the adhesive thickness. It increases initially with increasing adhesive thickness, attains a peak value, and then decreases. The peak fracture energy and the thickness at which it is attained depend on the strain rate, temperature, and bond width. The adhesive thickness for maximum fracture energy is seen to decrease with increasing strain rate and is nearly constant with different specimen widths, though increasing specimen width results in higher fracture toughness. Another important observation in this study is that the fracture energy of the bulk adhesive determined using a compact tension specimen is nearly 50% lower compared to the adhesive fracture energy of the joint (Figure 2.15).

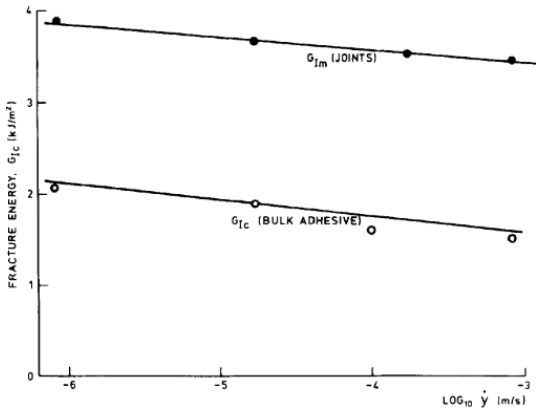

Figure 2.15 Comparison of fracture energies in bulk adhesive and adhesive joints at different strain rates [32].

This difference in the fracture energy values in the rubber-toughened epoxy can be qualitatively explained in terms of the constraints imposed by the substrates for the development of the plastic deformation zone ahead of the crack tip. The size of the plastic deformation zone has been observed to be higher in the presence of high modulus constraints on the adhesive resulting in an increase in the G_{IC} values. Fracture toughness is maximum when adhesive thickness is equal to the size of the plastic deformation zone. A lower thickness results in over-constrained adhesive layer leading to lower toughness, and with a higher thickness the degree of constrain reduces the plastic deformation zone to have the same size as in bulk adhesive, i.e., G_{IC} value of joint decreases till it reaches the bulk G_{IC} value.

Carlberger et al. [33] used the J-integral approach to determine fracture energy for DCB and ENF tests to compare results in shear and peel. This study also investigates the influence of temperature and strain rate on strength and fracture energy of an epoxy adhesive. A temperature range of -40 to 80 ^{o}C and strain rates of 10^{-3} to 1 s^{-1} are considered. There is no significant change in the fracture energy for the temperatures considered here, though the ultimate strength decreases with increase in temperature. Fracture energy is observed to increase with increasing strain rate in peel, but the opposite is observed for shear (Figure 2.16).

In Carlberger et al.'s study, the properties of the adhesive are observed to be more rate dependent compared to previous studies. This is attributed to the use of thicker adhesive layers, which may result in greater rate dependent plasticity. Also, the strain rate is noted to be ramping up during the loading of DCB specimens instead of having a constant value.

Angelidi et al. [34] studied the effect of strain rate on the physical properties of acrylic adhesives. The paper explores strain recovery, ductility, and Poisson's ratio under tensile and compressive loads. Tensile testing is done using dog bone specimens and compressive testing is done using brick shaped specimens. Poisson's ratio is seen to become steady after yield point and increases marginally with increasing strain rate in tension. The stress-strain data obtained from these experiments is also used to analyze the effect of strain rate on yield strength, ultimate strength, and failure strain. The results show a similar increase in strength and decrease in failure strain under tensile load with a logarithmic trend.

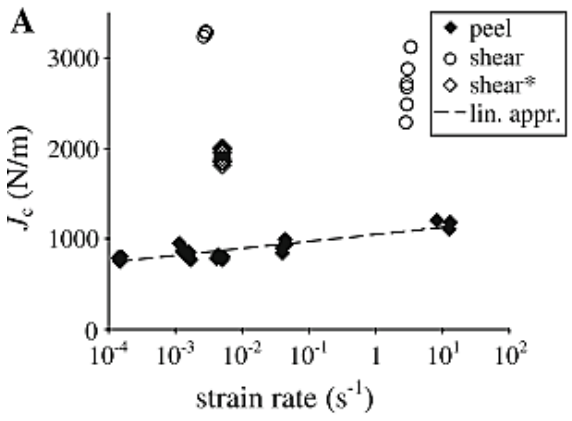

Figure 2.16 Effect of strain rate on fracture energy under peel and shear load [33].

Most of the above studies have developed specimens and test fixtures to obtain the required data as there is no standard test methodology to determine several material properties. The American Society for Testing and Materials (ASTM) is responsible for determining standard test practices to determine material properties, and the D14 subcommittee is responsible for setting standards for adhesive joint testing. The current standard for determining Mode I fracture toughness is given by ASTM D3433-99. There is no such standard for Mode II fracture toughness. Tensile and shear properties can be determined by using ASTM standards for polymers.

To summarize, adhesive properties are sensitive to strain rate, substrate material and bond thickness. Strength and modulus of epoxy adhesive show a positive correlation with strain rate, while fracture energy decreases with increasing strain rate. Properties also show a decrease with increasing bond thickness up to a critical thickness determined by the plasticity of the adhesive.

2.4 Adhesive Joints

A joint of two or more components made by using a bonding agent or adhesive that binds them together is referred to as an adhesive joint. A layer of adhesive is spread uniformly between the surfaces required to be joined and cured over a period of time, and if necessary, at elevated temperatures to accelerate the process. Adhesive joints can be broadly classified into lap shear, peel and butt joints based on the joint configuration and the type of load applied on them. Joint strength is usually poorer under peel and tensile loads compared to shear; therefore, design of structural adhesive joints is done such that load acting on the joint is principally in shear. Lap joints are the most used adhesive joints due to their superior properties and easy construction. Figure 2.17 shows a few different types of lap joints [35]. In single lap joints, the tensile or compressive load applied on the adherends creates a bending moment due to load line

eccentricity. The adhesive layer in a single lap joint not only experiences a shear stress, but also a normal (peel) stress due to the bending effect, both of which show a non-uniform distribution with their maximum values occurring at the overlap ends. The bending effect can be reduced either by using thicker adherends or by using a double lap joint. The use of a strap also helps reduce the bending moment. Scarf and step joints exhibit higher strength, however the complexity in manufacturing such joints make them less practical [36].

The strength of an adhesive joint is influenced by the bond joint geometry and the cohesive forces between the substrate and the adhesive. Several studies have considered the effects of joint geometry parameters such as overlap length, adhesive thickness, adherend thickness, spew, fillets etc. in determining the stress distributions across the joint and hence its strength. The presence of a fillet or chamfer at the leading edges of the joint are seen to reduce normal and shear stresses at the edges [37]. This is likely due to the absence of stress concentrations. The strength and energy absorption characteristics of the joint are found to be dependent on the nature of adhesive (brittle or ductile) and the thickness of the bond. Increasing adhesive thickness makes the bond prone to a greater number of flaws resulting in a decrease in strength.

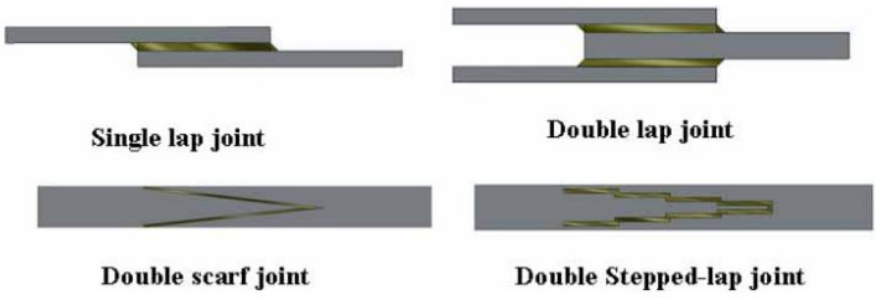

Figure 2.17 Different forms of adhesive joints [35].

The optimum thickness of the adhesive depends on the nature of the adhesive and function of the joint. The load bearing capacity of an adhesive lap joint increases with increasing bonded area, however, the study by da Silva et.al. [38] shows that increase in strength is possible only to a certain value beyond which there is no benefit. In fact, increasing bond length could potentially decrease strength due to the inclusion of a greater number of voids and thermal residual stresses during curing. Optimal bond length can be predicted using the following two equations [38] which describe the maximum load carried by the adhesive (F_a) (Equation 2.14) and the substrate (F_s) (Equation 2.15).

$$F_a = \tau_y w l \qquad \text{Eq. 2.14}$$

$$F_s = \frac{\sigma_{ys} w t_s}{1 + 3k} \qquad \text{Eq. 2.15}$$

where, k is a bending moment factor which depends on overlap length and load applied. For $l/t_s > 20$, k tends to be 0. τ_y and σ_{ys} are the yield strength of the adhesive and adherend substrate respectively and w, l and t_s are geometry parameters width, overlap length and substrate thickness, respectively.

The study of adhesion phenomenon is equally important, however, there is no unifying theory to explain all the factors affecting bond strength as it is a multidisciplinary field of study. Adsorption theory [39] is a widely accepted model, which explains that the cohesive forces are set up due to intermolecular interactions between the adhesive and adherend such as van der Waals forces, hydrogen bonds, covalent bonds etc., and hence, the bond strength depends on the surface free energy of the adhesive and adherends, and quality of the interface to ensure complete wetting of the substrate surface by the adhesive [39] [40].

2.4.1 Effect of Strain Rate on Adhesive Joints

The effect of strain rate on bulk adhesive has been explained in detail in a previous section. However, when designing adhesive joints, this knowledge alone is insufficient as changes in strain rate has a significant effect on the behavior of substrate materials as well as the interaction between the adhesive and the substrates. Several studies have considered the aspect of impact behavior of different types of adhesive joints, but there are few which compare the strength and failure response at various strain rates.

A study on the mechanical behavior of Betamate epoxy-DP steel double lap shear joints at different loading rates (1, 100 and 500 mm/min) and temperatures by Deb et al. [41] shows significant influence on the failure strength at both room temperature and high temperature (82^{o}C). Room temperature experiments show no change in failure load with different loading rates but show a higher failure strain compared to the tests at higher temperatures, which could be due to yielding in the substrate. Increase in the extension rate results in an increase in the failure load, though no significant difference in failure strain is observed. Since the extension is measured across the ends of the specimen and not the joint section, it is difficult to judge the effect of loading rate on the failure strain, especially since yielding is observed in the substrate in the non-overlap area. Joint failure in all cases is observed to be a cohesive failure. The study also investigates the application of failure models provided by ABAQUS in predicting the stress-strain response. At room temperature or below, von Mises yield criterion shows good correlation with the test data; however, at high temperature, Raghava/EDP failure criterion is suggested to be more appropriate as it includes hydrostatic stress.

Zhang et. al. [42] considered the effect of strain rate up to 100 s^{-1} on single lap joints with steel and aluminum substrates and crash resistant adhesive using a servo-hydraulic test machine.

The substrates used in this study show the effect of having a rate sensitive adherend versus an insensitive one. The aluminum used for the joint has no significant rate sensitivity. Figure 2.18 shows the load displacement curves for the joint at different strain rates, where (a) is for a steel-steel joint and (b) is for an aluminum-aluminum joint. The two plots show that while there is an increase in yield strength with increasing rate in the steel joint, there is no such change observed for the aluminum joint. This is attributed to the rate sensitivity of steel's yield point. The quasi-static curve in both cases shows similar characteristics, with adhesive failure prior to substrate yielding due to low adhesive strength at that strain rate. In the steel joint, there is no obvious yielding of the adherend and the increase in strength could be due to increase in adhesive strength with strain rate. But the aluminum joint shows clear yielding in the substrate characterized by the perfectly plastic portion of the curve followed by adhesive failure. Therefore, the adhesive joint strength could be said to be limited by the yield point of substrate material. Also, the fracture is observed to be of mixed nature, with both interfacial and cohesive failure at all strain rates in this study.

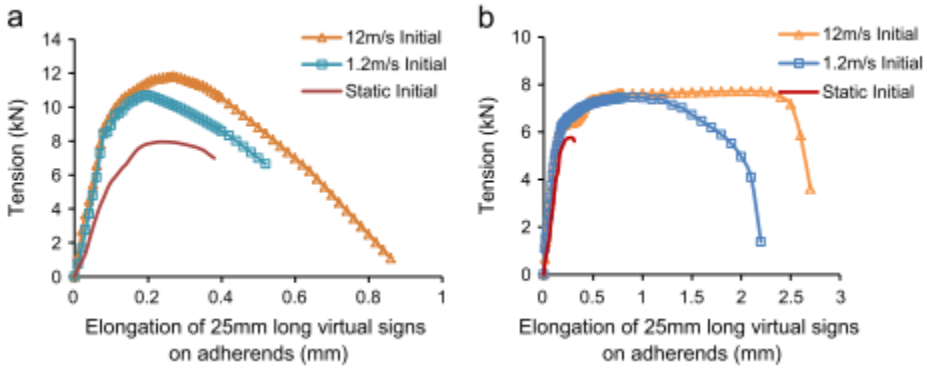

Figure 2.18 Effect of strain rate on load-deflection curves in (a) Aluminum and (b) Steel [42].

The increase in bond strength is also observed by Srivastava [43] in a study considering the effect of strain rate on Ti-Al alloy-C/C SiC composite adhesive joint. The effect of spew fillets is seen to be beneficial to the bond strength and increase in bond length is observed to lead to a decrease in strength upon reaching a certain limiting value due to the moment induced under load in single lap joints.

2.5 Tubular Joints

Adhesive bonding is a popular method to join composite-composite or composite-metal tubular or box sections. These joints are usually single lap joints with the two sections bonded across an overlap region. Several other forms of adhesive tubular joints have been studied such as a sleeve or a coupler joint analogous to the strap joints for flat plates and co-curing in the case of composite-composite joints [44]. These joints have found applications in the chemical and energy industries where they are used in the piping structures. However, the simplicity of single lap tubular joints has made it a popular method to join multi-material tubular or box sections in the aerospace and automotive industries. Such joints may experience axial and torsional loads depending on their application. Several studies have investigated the normal and shear stress distribution across the bond length using numerical methods under axial loads. These studies consider only an axial tensile load on the adherend. A review of various adhesive stress models in axially loaded tubular joints was published by Dragoni and Goglio [45]. Their article compares the models with finite element results of a particular joint configuration under quasi-static tensile load. The results indicate that Lubkin and Reissner model closely follows the FEA data, but the other models are not able to predict the peel stress in the adhesive.

Lubkin and Reissner [46] published one of the earliest works on the stress distribution across the adhesive in a circular tube joint under tensile load, and presented design data for

different cases of adhesives, adherends and geometries using an analytical approach like the models used for flat lap joints. This study assumes that the adhesive is a thin-flexible layer whereby the stresses are constant through thickness, and the adhesive is only subjected to normal (peel) and shear stresses. To reduce computations, the adhesive is approximated by a set of infinitesimal springs, and materials are linear elastic. Results of this approach indicate high peel and shear stress concentration at the overlap ends, and nearly uniform shear and peel stress distributions in much of the overlap length. The magnitude of stress concentration is seen to vary based on the adhesive thickness, tube thickness and tube diameter.

Figure 2.19 shows normalized stress distribution across bond length for two design cases with $\beta = 100$ (flexible adhesive) and $\beta = 4$ (stiff adhesive). β is the elasto-thickness parameter given by, $\beta = \eta E/E_a t$, where t and η are the adhesive thickness and tube thickness, respectively and E_a and E are their tensile modulus values. Stress concentrations are observed at the adhesive bond edges in both cases, which is more pronounced in flexible adhesives.

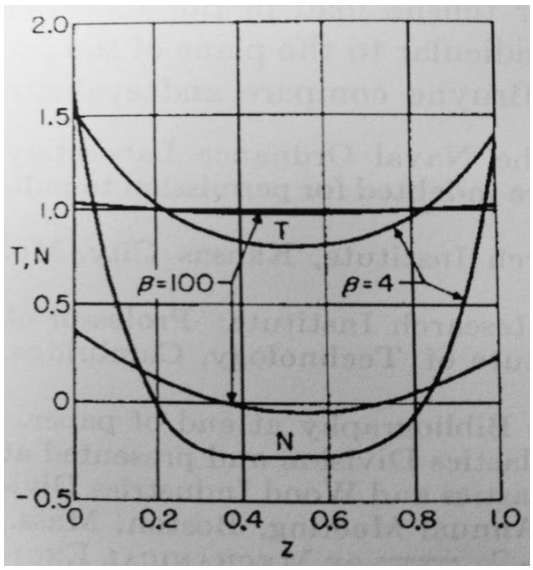

Figure 2.19 Normalized shear (T) and normal (N) stress distributions across the bond length in a tubular adhesive joint [46].

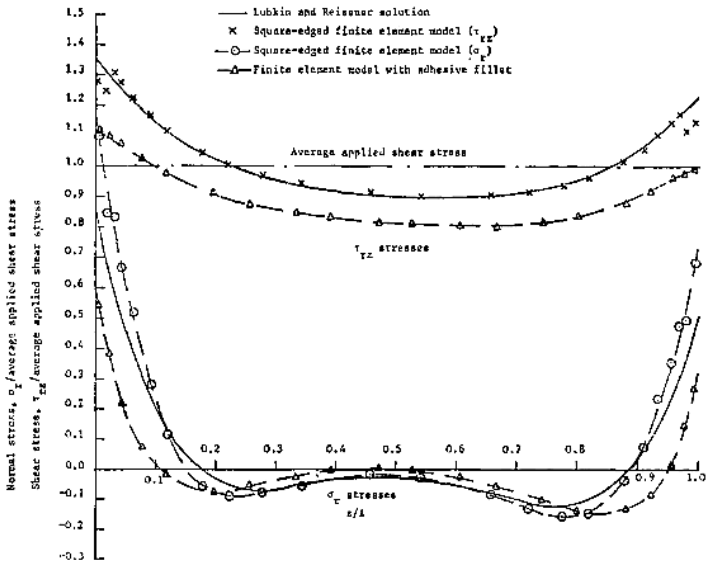

Figure 2.20 Comparison of Lubkin and Reissner's solution with finite element results of Adams and Peppiatt [47].

A finite element simulation and verification of the above study is presented by Adams and Peppiatt [47]. Quasi-static tensile and torsional loads are applied on the joint. There is no information regarding the model apart from mesh geometry, but it can be assumed that the materials are modeled as linear elastic. The results show that theoretical model of Lubkin and Reissner is quite accurate for the specific design cases presented in the study. The paper also verifies the model for another two cases again from Lubkin and Reissner's design data. Figure 2.20 shows a comparison of results for one such design case.

Adams and Peppiatt [47] also explore the effects of fillets and scarf joints on the stress distribution in the adhesive. The use of fillets shows a significant improvement in the design; however, the use of scarf joints shows negligible improvement in design and is not worth the cost as fillets are a cheaper and easier solution.

Another numerical model presented by Nakano et al. [48] uses axisymmetric elasticity theory to establish the equilibrium equations for stress and strain in the joint. The study compares

the effect of adherend modulus on the stress distribution at the adhesive-adherend interface, adhesive thickness and overlap length using a numerical method presented in the study. The results indicate that a decrease in overlap length causes an increase in peel stress concentration at the joint ends more so at the loaded end of the joint and, with decrease in adhesive thickness von Mises equivalent stress is lower across the overlap but show higher stress concentration values. In terms of adherend modulus, a stiffer inner tube leads to lower stresses at the inner tube and adhesive interface, but a stiffer tube leads to a higher stress at the outer tube and adhesive interface. The study also presents limited experimental work to determine the joint strength with different substrates. It is reported that failure occurs at the inner interface if both substrates are of the same material. Additionally, test results have shown that a joint with a stiffer inner tube has the highest strength (Table 2.1).

Shi and Cheng [49] published a model for tubular adhesive joints with an approximate closed form solution based on minimum complimentary energy. The solution here is much more complex due to the large number of variables and boundary conditions considered. The nature of shear stress distribution is similar to the results published by Lubkin and Reissner [46], but the peel stress distribution is seen to be different. Peel stress distribution across the overlap varies almost linearly from a positive value at the leading edge to a negative value at the trailing edge, which is quite different when compared to previous studies (Figure 2.21). The authors conclude by mentioning that the results are akin to other flat single lap joint theories, however, they fail to compare their results with other tubular joint theories which is more appropriate. The effects of adhesive thickness and overlap are also analyzed numerically. Decrease in adhesive thickness is seen to decrease shear stress while the normal stress does not change much and increase in overlap length causes the stress concentration to move towards the joint ends.

Table 2.1 Effect of tube material on joint strength under tensile load [48].

Inner Shaft	Outer Shaft	Tensile Strength (kN)	Standard Deviation (kN)
Steel	Steel	24.0	0.79
Al alloy	Al alloy	22.2	1.35
Steel	Al alloy	25.2	1.53
Al alloy	Steel	12.9	2.36

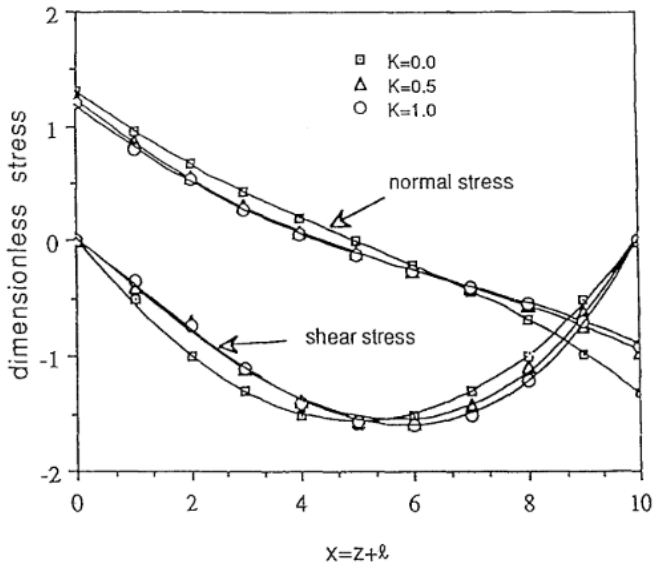

Figure 2.21 Stress distribution across bond length according to model proposed by Shi and Cheng [49].

The mathematical models provide a method to arrive at the stress distributions in the adhesive through a complex numerical solution, but do not provide a failure criterion which is more relevant in joint design. Kim et al. [50] proposed a failure criterion based on the adhesive properties and adhesive stresses under load in CFRP-Steel tubular joints. The study consists of three parts, first is the effect of adhesive thickness and fiber angle on the load carrying capacity of the bond, second, a two-parameter exponential equation to define the stress-strain curve of adhesive in tension and shear, and finally a failure model for the adhesive in a tubular adhesive joint.

The load bearing capacity is observed to decrease with an increase in adhesive thickness. This decrease is observed to be marginal at a stacking angle of 15°, but quite significant at 30° and 45°. The authors attribute the decrease to higher residual thermal stresses in thicker adhesive layers, leading to premature failure. There is no further explanation on the effect of stacking angle on the joint strength as the 15° angle seems to indicate a very low dependence of thickness on load carrying capacity, while the decrease at higher stacking angles could be attributed primarily to the decrease in adherend strength. Non-linear adhesive behavior is described as shown in Equation 2.16.

$$\sigma = \sigma_m (1 - e^{-(E/\sigma_m)\varepsilon}) \qquad \text{Eq. 2.16}$$

Where, σ is the tensile stress in the adhesive, σ_m is ultimate tensile strength of the adhesive, E is the Young's modulus of the adhesive and ε is the tensile strain in the adhesive.

A finite element model is used to calculate the 3D stresses in the adhesive layer. The model considers residual thermal stress, calculated by considering the differences in coefficient of thermal expansion between adhesive and adherend, and by modeling the adhesive layer using equation 2.16. The tensile load data used in FEA is obtained from the experimental results. The stresses in adhesive elements at the interface are used to calculate a failure index given by Equation 2.17.

$$k = \sqrt{\left(\left(\frac{\sigma_{rr}}{S_T}\right)^2 + \left(\frac{\sigma_{\theta\theta}}{S_T}\right)^2 + \left(\frac{\sigma_{zz}}{S_T}\right)^2 + \left(\frac{\tau_{rz}}{S_S}\right)^2 + \left(\frac{\tau_{r\theta}}{S_S}\right)^2 + \left(\frac{\tau_{z\theta}}{S_S}\right)^2\right)} \qquad \text{Eq. 2.17}$$

where, S_T and S_S are the tensile and shear strength of the adhesive, and the rest of the terms are the calculated stresses in polar coordinates. To predict joint failure, a model based on Equation 2.18 is proposed. The fracture criterion or k_f is defined as follows,

$$k_F = \alpha(0.1 - \frac{t}{L})^{\beta}\sqrt{1-(1-k_i)^2} \qquad \text{Eq. 2.18}$$

Here, α and β are arbitrary constants based on the stacking angle of the composite tube and k_i is an initial failure index calculated using equation 3 with only residual thermal stresses in 3D. Failure occurs when failure index (2.17) is equal to the fracture index (2.18). Hence, this model requires joint geometry and curing cycle details to predict joint failure. The experimental data from a brittle adhesive are applied here to verify the model (Figure 2.22) for various joint thicknesses and show reasonable accuracy.

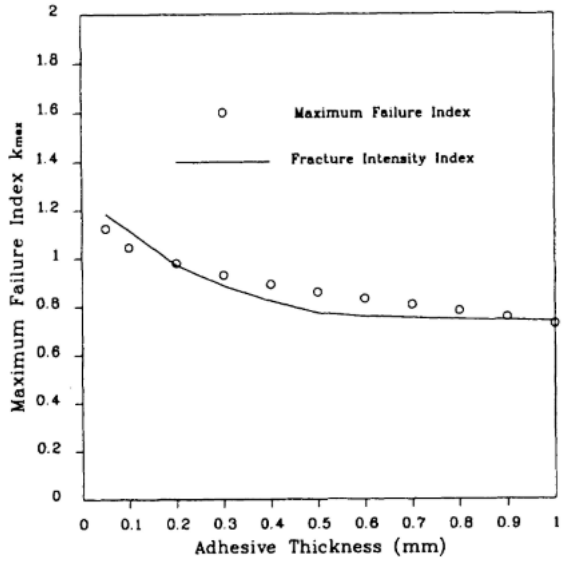

Figure 2.22 Joint failure index variation with adhesive thickness [50].

Fracture mechanics of tubular adhesive joints is explored by Reedy and Guess [51]. Linear elastic and elastic plastic approaches are used to study the joint failure mechanics. Limited experimental work is also done to compare the strength of the composite to Aluminum joint under quasi-static, fatigue tensile and compressive loads. Experimental results indicate that compressive strength is about half of the tensile strength of the joint, and failure is abrupt under quasi-static as well as fatigue conditions. Cohesive adhesive failure is seen to initiate at the edge of adhesive aluminum interface in tensile tests. And tapering of the inner aluminum adherend is seen to improve compressive strength and decrease tensile strength, leading to similar failure load values in both tension and compression.

ABAQUS finite element software is used to determine the fracture energy and stress intensity factors of the adhesive in this joint configuration. Two approaches are adopted, an elastic-plastic material approach with no crack in the adhesive and linear elastic approach with a crack in the adhesive. The crack tip yield zone dimension is obtained from the elastic-plastic model and no further work is shown. While the element displacements are used to calculate the stress intensity factors, and energy release rate is obtained using ABAQUS codes in the linear-elastic model. The model is used to compare the parameters for different substrate combinations, but there is insufficient data to draw accurate conclusions since data from tensile cases are compared to compressive cases to draw conclusions on the effect of substrate material. The authors observe that linear-elastic approach is not applicable in this case to determine joint failure as the yield zone is bigger than adhesive thickness at a lower load level.

An extension of this study by Guess et.al. [52] shows that the difference in tensile and compressive strength is negated with use of a taper in an aluminum-plain weave composite joint, but the taper has no effect if the composite adherend is changed to a triaxial reinforced

composite. And, according to finite element analysis, peel stress concentration at joint ends is observed to cause failure initiation.

Another approach to numerical investigation of inter-locked tubular joints done by Sonia Braeik et. al. [53] uses cohesive zone model to define the adhesive and composite is modeled using volume elements. Damage in the joint is observed to cause delamination, matrix crack and fiber matrix debonding. The damage data from FE is comparable to the test observations.

An extensive study on optimizing the parameters influencing joint performance under tensile load was published by Labbé and Drouet [54]. The study uses a linear elastic approach to model the materials with a strength-based failure criterion for the adhesive. While the results of this study provide a good direction on the ideal joint parameters, the use of linear elastic models makes the end results less accurate since most structural adhesives are toughened and have some degree of non-linearity in their stress-strain response. Barbosa et. al. [55] [56] have investigated the same using cohesive zone model, but the scope of their study was limited to different brittle adhesives and influence of overlap length.

Most studies on such joints and joint parameters are based on the stress distributions in the adhesive layer when modeled as a linear elastic material which may not be an effective representation of structural joint behavior. Hence, there is a need for further investigation on the influence of joint parameters as well as optimization of the joint considering non-linearity in adhesive behavior and material failure.

Chapter 3 Analysis of Adhesive Stresses in Tubular Lap Joints

The existing analytical and finite element models on the stress distributions in the adhesive layer of tubular single lap joints are based on tensile and torsional loads on the tubes. They not only provide insight into the stress distributions in the joints under a tensile or a torsional load, but also provide important information on joint design under quasi-static and linear elastic conditions. However, the existing findings may not be sufficient for the design for crush performance of tubular joints since the loading condition in crush condition is typically compressive in nature. For this reason, stress distributions in the adhesive layer in tubular joints under an axial compressive load and the effects of different joint parameters on them are studied in this chapter.

3.1 Joint Design and Model Parameters

Review of existing literature on lap joints and tubular joints under tensile loads show that the important parameters in joint design are joint geometry including overlap length (L), bond thickness (t), tube diameters, inner tube thickness (t_i), outer tube thickness (t_o), tube end design and tube overlap design, tube material and the characteristics of the adhesive itself. Figure 3.1 illustrates the joint with important parameters for a joint under compressive load. Stress analysis of the adhesive overlap under compressive load is performed using Altair Hyperworks' Optistruct (v2017.1.0.10) solver.

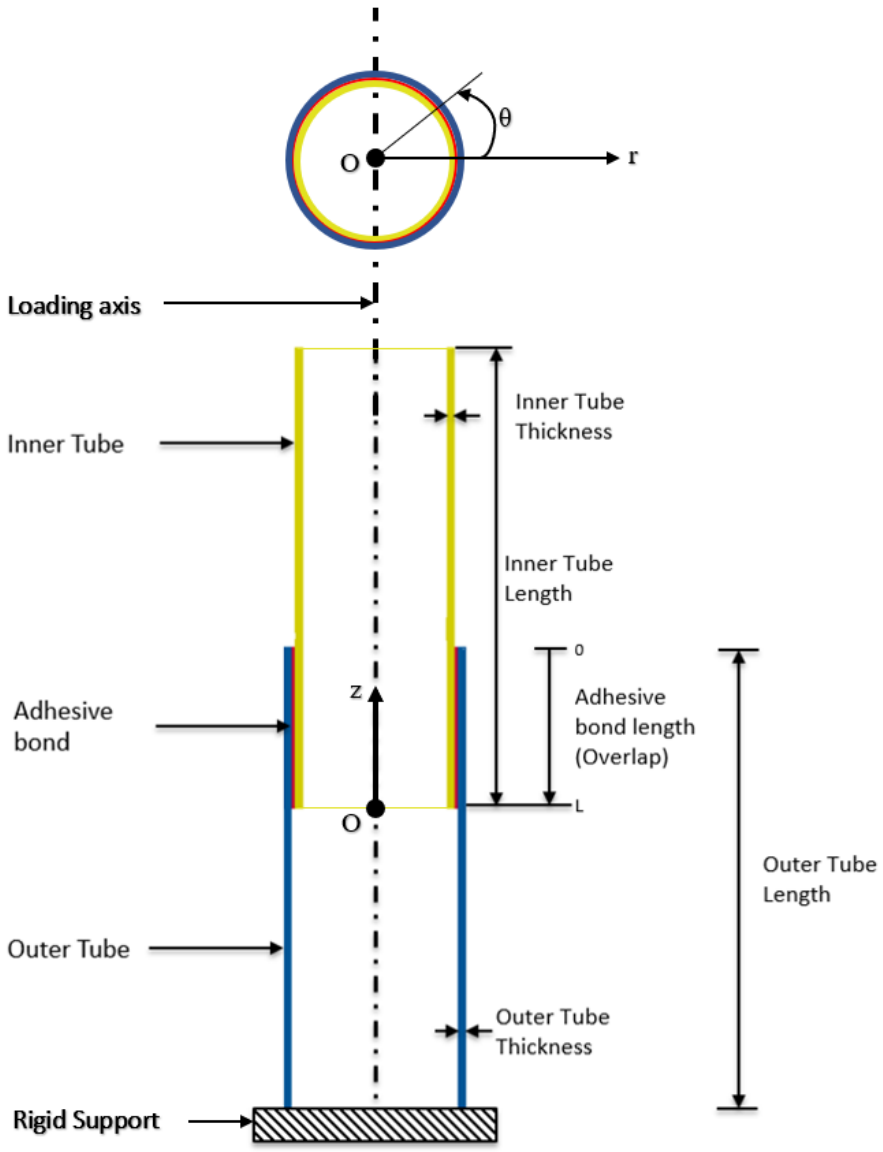

Figure 3.1 Illustration of tubular joint under compressive loading with important joint parameters.

Table 3.1 Geometry of joint.

Parameter	Value
Inner tube length (Li)	40 mm
Outer tube length (Lo)	40 mm
Inner tube thickness (ti)	1 mm
Outer tube thickness (to)	1 mm
Inner tube outer diameter (di)	9.8 mm
Outer tube outer diameter (do)	11 mm
Adhesive thickness (t)	0.2 mm
Mean adhesive diameter	10 mm
Overlap length (l)	10 mm

The geometric parameters for a reference model of the joint are listed in Table 3.1. For easy interpretation of stress data, a cylindrical coordinate system is used as shown in Figure 3.1. Adhesive overlap is measured from zero at the leading edge to l0 mm at the trailing edge. The material of both substrate tube and adhesive are defined as linear elastic. In the reference model, both tubes are made of steel with a modulus of 200 GPa and they are bonded with an adhesive having a modulus of 3.5 GPa. Variations of the joint parameters and material properties are considered in the Section 3.2.

The finite element model of a joint under compressive load is shown in Figure 3.2. It is constructed of 8-noded 3-D brick elements. The tubes are meshed with brick elements of varying height, ranging from 0.167 mm in the bonded region to 1 mm at top end of the inner tube and bottom end of the outer tube; thickness varies similarly from 0.167 mm at the joint to 1 mm at the tube ends and width of the elements is appropriately adjusted for 64 elements around the tube and adhesive circumferences. The adhesive layer is meshed with 0.1 mm thick and 0.167 mm high brick elements.

The axial compressive load is applied to the top end of the inner tube via a point force. The point force acts on a floating node which is connected to all the top end nodes of the inner tube with 1D rigid elements as shown in Figure 3.2. The joint is constrained by providing a rigid boundary condition to the bottom end nodes of the outer tube preventing all movements of the bottom end of the joint.

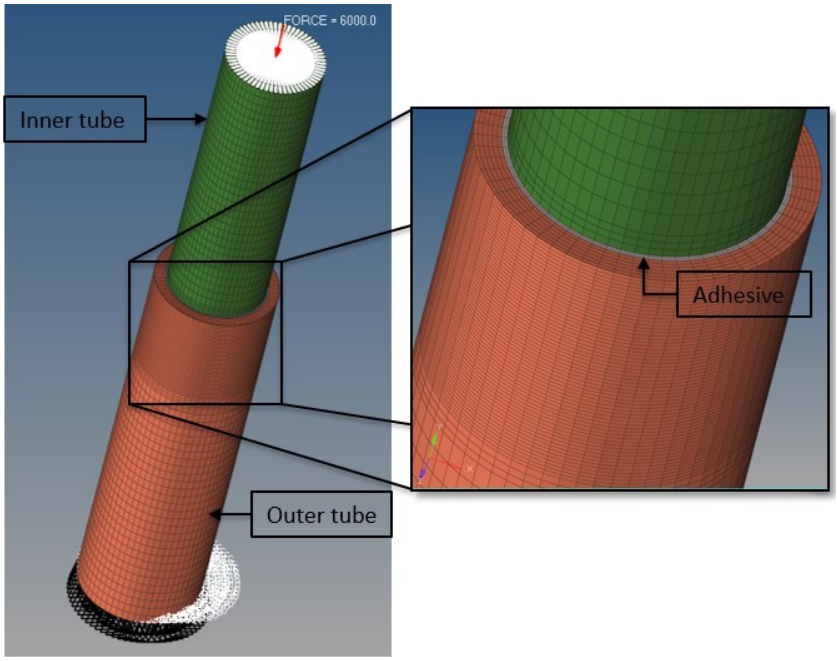

Figure 3.2 Tubular adhesive joint model in OPTISTRUCT under compressive load.

Before conducting the finite element analysis with a compressive load, an initial simulation was conducted with an axial tensile load of 6000 N to verify the resulting stress distributions with the analytical results of Lubkin and Reissner [43] described in Chapter 2. Figure 3.3 plots the normalized distributions of shear (τ_{rz}) and radial normal (σ_{rr}) stresses at the inside and outside interfaces for a joint with a mean diameter of 10 mm, adhesive thickness of 0.2 mm and overlap length of 10 mm, the same adhesive layer dimensions as was used by Lubkin and Reissner [46]. The normalized stresses are calculated by dividing the actual stress values with the average shear stress in the adhesive layer. The results show shear concentrations near the two edges of the joint. The radial normal stress distribution shows significant stress concentration at the edges of the bond but is close to zero across the middle of the bond. Results also show a difference in stress magnitudes between the inside and outside interface of the bond. The normal stress is tensile on the leading edge, but compressive at the trailing edge for the

outside interface and tensile at both edges for the inside interface. The tensile normal stress can be characterized as peel stress, which can contribute to the initiation of failure of the adhesive layer when the tubular joint is subjected to an axial tensile load. Also, comparing the finite element results with those shown in Lubkin and Reissner's study (Figure 3.4), a good correlation can be observed.

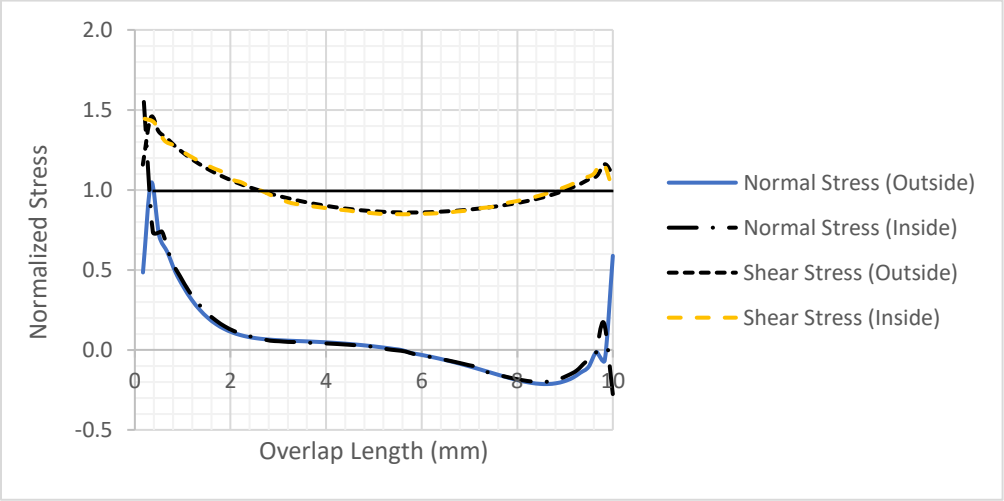

Figure 3.3 Normalized stress distributions in the tubular adhesive joint along the overlap length (for the joint dimensions listed in Table 3.1). The loading is tensile.

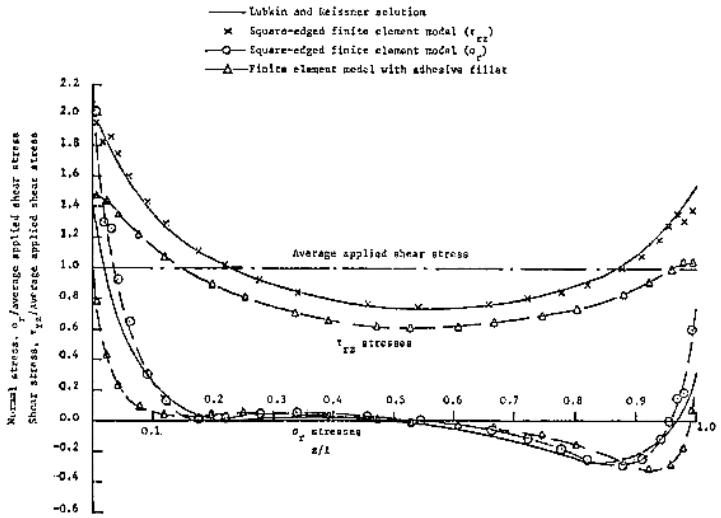

Figure 3.4 Normalized stress distributions in the tubular adhesive joint along the overlap length according to Lubkin and Reissner's results [46]. The joint dimensions are the same as in Figure 3.3.

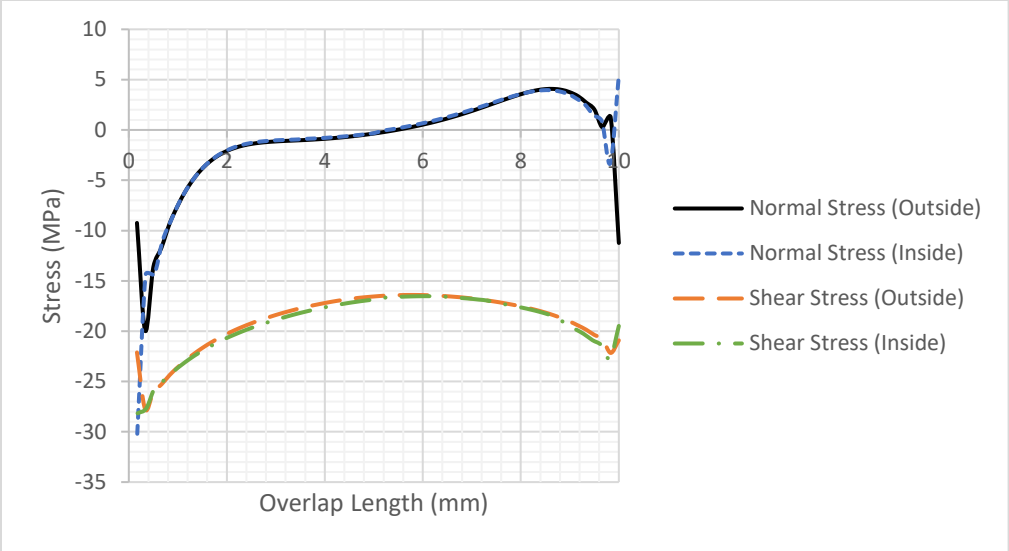

Figure 3.5 Stress distribution across joint overlap under a compressive load of 6000 N. The joint dimensions are the same as in Figure 3.3.

Since the primary objective of this dissertation is to understand the crush characteristics of single lap tubular joints under compressive loading, the finite element stress analysis from here on is performed under a compressive load. The same model is used to study the stress distributions under an axial compressive load of 6000 N, which is the same as the tensile load applied before.

Figure 3.5 plots the shear and normal stress distributions across the overlap length under an axial compressive load of 6000 N. The black solid line in Figure 3.5 represents the average shear stress acting on the adhesive, which is equal to 1.91 MPa. It is observed that the change of the applied load from tension to compression does not affect the magnitude of the normal and shear stresses, but their directions have changed. This is as expected since the material is considered linear elastic with the same modulus under both tensile and compressive loads. When compared with the results under a tensile load, the positive normal stress at the leading edge has become negative under a compressive load, or the normal stress concentration zone at the

leading edge has become compressive. At the trailing edge, the normal stress is now positive or tensile on the inside interface, but negative or compressive on the outside interface, which is the opposite of the normal stresses at the trailing edge under tensile loading. The shear stress also changes its direction under the compressive load, and as with the tensile load, shows higher values at the ends of the joint. These stress concentration areas near the ends of the overlap are expected to play a major role in crack initiation and propagation in the adhesive layer. Also, as with the tensile load, there are differences in the magnitudes of the normal stresses between the inside and outside interfaces of the adhesive. The inside interface shows higher magnitudes of normal stress at both edges compared to the outside interface. This makes the study of the inside interface more crucial for failure studies, and hence, moving forward the study will mostly describe the stresses at the inside interface obtained from elements in contact with inner tube.

3.2 Effect of Joint Parameters on Stress Distributions

For efficient design of adhesive joints in multi-material tubular constructions, it is important to consider the effects of various joint design parameters on the stress distributions and maximum stresses in the adhesive layer. In the following subsections, the effects of joint design parameters, such as tube materials, adhesive modulus and joint geometry on the shear and normal stresses in the adhesive layer are investigated. The axial compressive load applied on the joint is 6000 N.

3.2.1 Effect of Tube Materials

The study below considers the effect of joining two aluminum tubes (Al-Al), an inner steel tube with an outer aluminum tube (Steel-Al), and an inner aluminum tube with an outer steel tube (Al-Steel). The joint geometry parameters are the same as in Table 3.1. The modulus of aluminum is 70.3 GPa, which is approximately one-third the modulus of steel, and therefore,

for equal cross-sectional area, the axial stiffness of aluminum tubes is one-third that of steel tubes. Figures 3.6 compares the shear and normal stress distributions for different tube material combinations with the stress distributions for a steel-steel joint.

The studies with different tube materials show a much greater variation in the shear stress distributions (Figure 3.6 (b)) than in the normal stress distributions (Figure 3.6(a)). In an aluminum-aluminum joint, the shear stress shows much lower values across the length of the joint, despite having almost equal shear stresses as in a steel-steel joint at the edges. Looking at the steel-Al and Al-steel joints, it is observed that the stiffness difference of the two tubes affects the shear stress distributions significantly. A softer aluminum tube on the inside and a stiffer steel tube on the outside in the Al-Steel combination causes the highest shear stress at the trailing edge and low shear stress at the leading edge. The lowest shear stress occurs at the trailing edge with Steel-Al combination in which the steel is the inner tube and aluminum is the outer tube; however, at the leading edge, the shear stress is the highest in the Steel-Al combination among all considered here.

In Figure 3.6 (b), it can be seen that there is little effect of the tube material combination on the normal stress distribution in the middle length of the overlap; however, normal stress concentrations near the edges are significantly influenced by the tube material combination. The case of steel inner tube bonded to aluminum outer tube in Steel-Al combination is of particular interest. The softer outer tube has resulted in a positive shift of stress concentration magnitudes resulting in a high tensile normal stress at the trailing edge of the overlap. On the other hand, the highest compressive normal stress distribution at the leading edge and the lowest tensile stress concentration at the trailing edge occur with aluminum inner and steel outer tube in Al-Steel combination.

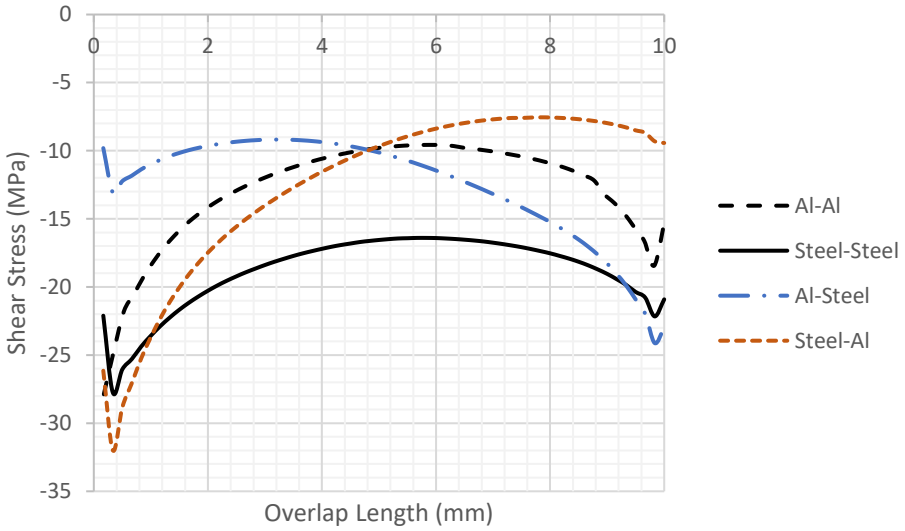

(a)

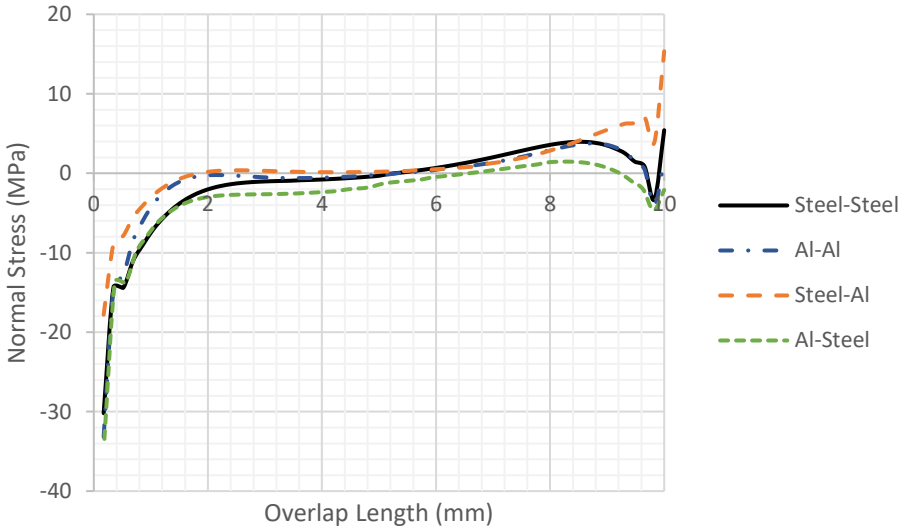

(b)

Figure 3.6 Comparison of adhesive stresses in joints with different tube material combinations. (a) and (b) compare shear and normal stresses on the inner surface of the adhesive layer.

3.2.2 Effect of Adhesive Modulus

Another important factor to consider in adhesive joints is the modulus of the adhesive. Several studies on tubular lap joints under tensile loading have presented results on the effect of adhesive modulus showing an increase in stress concentrations with increase in adhesive modulus. To determine the effect of adhesive modulus for tubular joints under compressive loading, three different adhesive modulus values, namely 2, 3.5 and 5 GPa, are considered in steel-steel joints with the same joint geometry as in Table 3.1. The 2 GPa adhesive is referred to as the softer adhesive and 5 GPa adhesive is called the stiffer adhesive. Figure 3.7 (a) plots the normal stress distribution in tubular joints with adhesives having the different modulus and Figure 3.7 (b) plots shear stress distribution. Changing the adhesive modulus is seen to mainly affect the stresses at the leading edge of the overlap. Lowering the adhesive modulus allows higher strains to be developed in the adhesive layer at a given stress level, resulting in a greater difference in the deformation between inner and outer tubes. This difference results in both higher compressive stresses and higher shear stresses, particularly at the leading overlap edge.

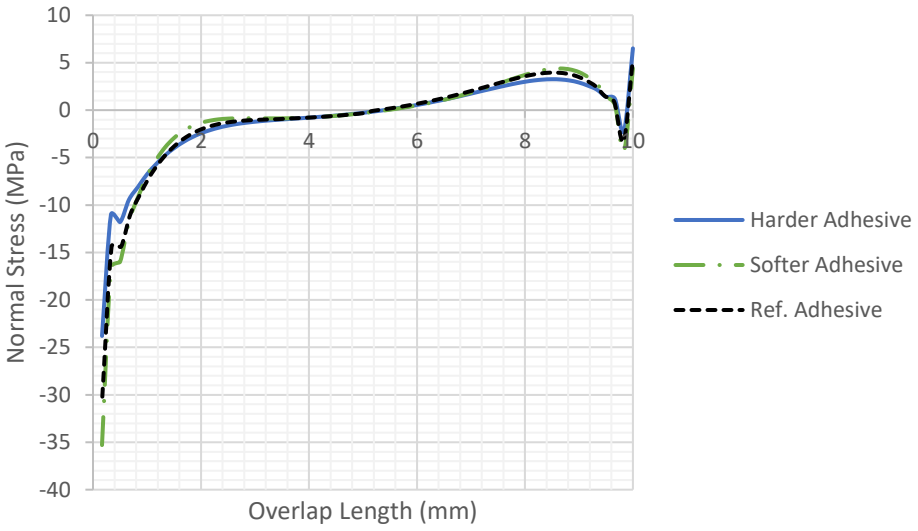

(a)

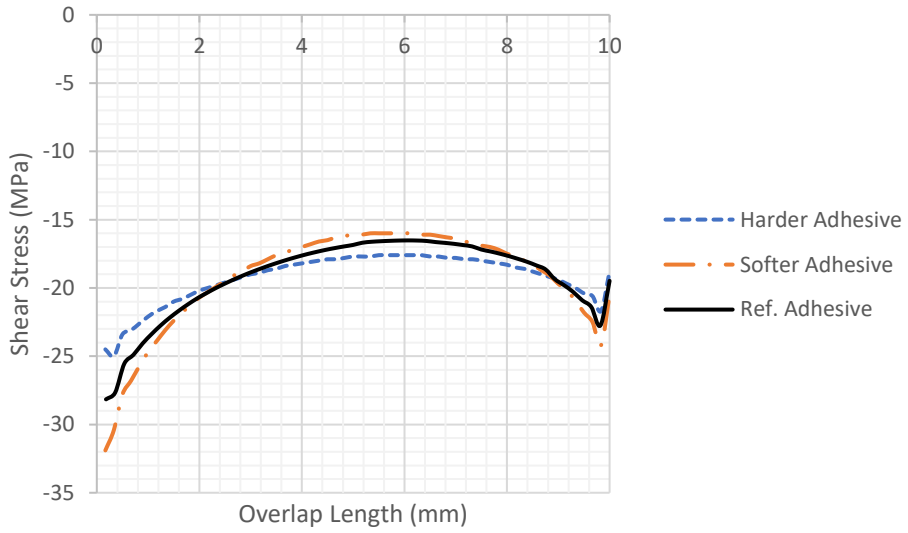

(b)

Figure 3.7 Plot showing the effect of adhesive modulus on the normal stress (a) and shear stress (b) distribution across bond length in steel-steel tubular joints. The joint geometry is given in Table 3.1.

3.2.3 Effect of Tube Thickness

The effect of changing tube thickness is seen to be analogous to changing the modulus of the tube material, since both affect the axial stiffness of the tubular joint. For this study, the thicker outer or inner tube has a tube thickness of 1 mm, while the other tube has a thickness of 0.5 mm. Thus, the three tube thickness combinations are thicker inner tube with 1 mm inner tube/0.5 mm outer tube, thinner inner tube with 0.5 mm inner tube/1 mm outer tube and the reference tube with 1 mm inner tube/1 mm outer tube. The tubes are made of steel and other joint parameters are the same as in Table 3.1.

The stress distributions for different tube thickness combinations are plotted in Figure 3.8 The tube thickness combinations considered have little effect on the normal stress distributions but have considerable effect on the shear stress distributions. Thicker inner tube produces the highest shear stress concentration at the loading edge and the lowest shear stress concentration at the trailing edge. The opposite is true with the thicker inner tube.

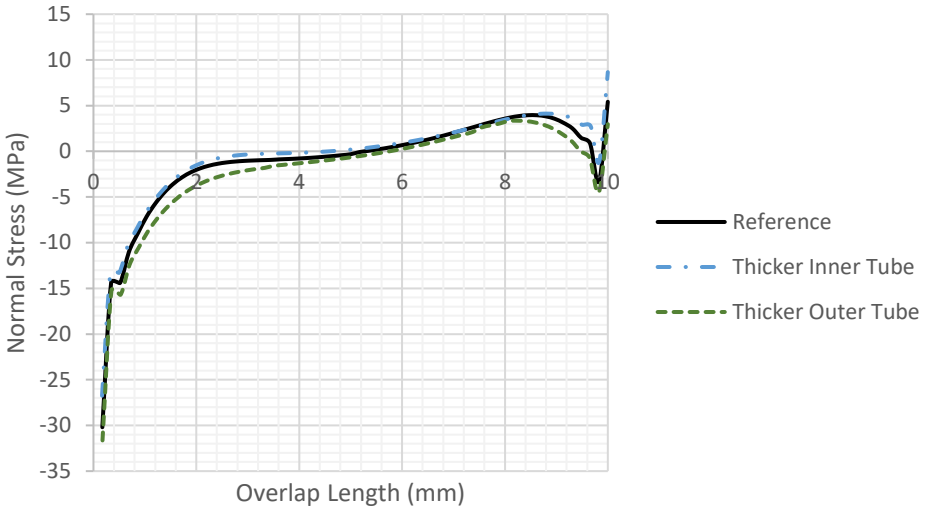

(a)

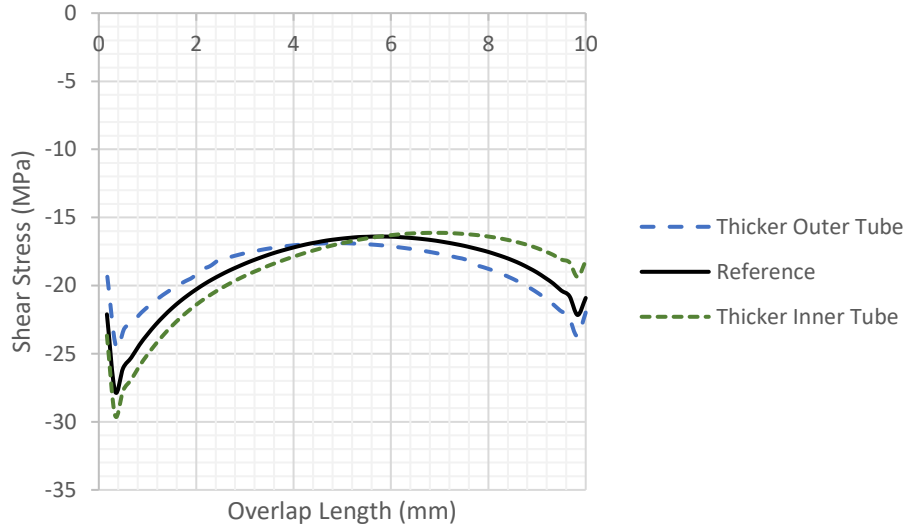

(b)

Figure 3.8 Plots showing the effect of tube thickness combinations on the normal stress (a) and shear stress (b) distributions across bond length. The other joint geometry parameters are given in Table 3.1

3.2.4 Effect of Adhesive Thickness

Adhesive thickness is another important design parameter in adhesive joints affecting the joint strength as well as the energy absorbed by the joint. Hence, it is important to study the effect of adhesive thickness on the stress distribution along the length and thickness of the

adhesive layer. Three different adhesive thicknesses, 0.2 mm, 0.5 mm, and 1 mm, are considered here, and the overlap length is maintained at 25 mm. In this study, the outer tube has an outside diameter of 25.4 mm, both inner and outer tube thicknesses are 1.25 mm, and each tube length is 75 mm. To consider different adhesive thicknesses, the inside diameters of the inner tube are 10, 9.7 and 9.2 mm for 0.2, 0.5- and 1-mm adhesive thickness, respectively. In the finite element models, the 0.5 mm and 1 mm adhesive layers are modeled with 5 through thickness brick elements and the 0.2 mm adhesive layer with 2 through thickness elements.

Figure 3.9 (a) plots the normal stress and Figure 3.9 (b) plots the shear stress versus overlap length for the three adhesive layer thicknesses considered. At the trailing edge of the adhesive layer in Figure 3.9(a), 0.2 mm thickness shows compressive stress concentration compared to 0.5- and 1-mm thicknesses that show tensile stress concentration. It can be observed in Figure 3.9 (b), that shear stress concentrations at both adhesive edges increase with decreasing adhesive thickness and the shear stress distribution becomes more uniform with increasing adhesive thickness.

Figure 3.10 plots the variation of normal stress across the adhesive thickness. As noted in Section 3.1, there is a significant difference in normal stresses between inside and outside interfaces at the overlap edges. The difference in normal stresses between the two interfaces is seen to increase with adhesive thickness as shown in Figure 3.10. Top end and bottom end in this figure refer to the leading edge and trailing edge of the adhesive overlap, respectively. The nature of normal stress changes from compressive to tensile at the inside interface of the trailing edge with increase in adhesive thickness, while at the outside interface the magnitude of normal stress is similar. At the leading edge, the normal stress is compressive, but the difference in magnitude between the interfaces increases greatly with increase in adhesive thickness.

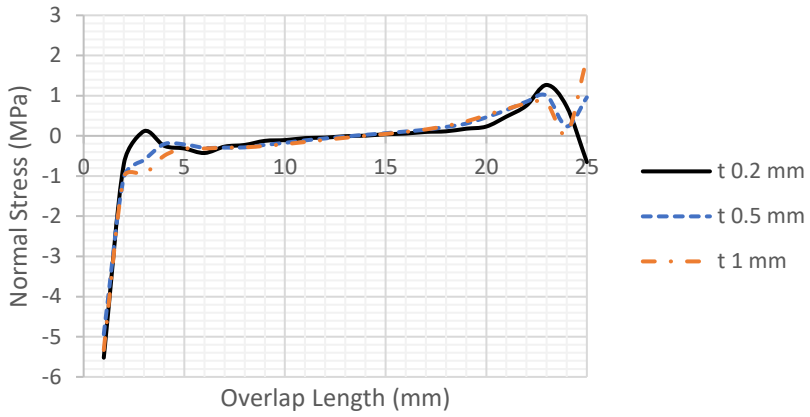

(a)

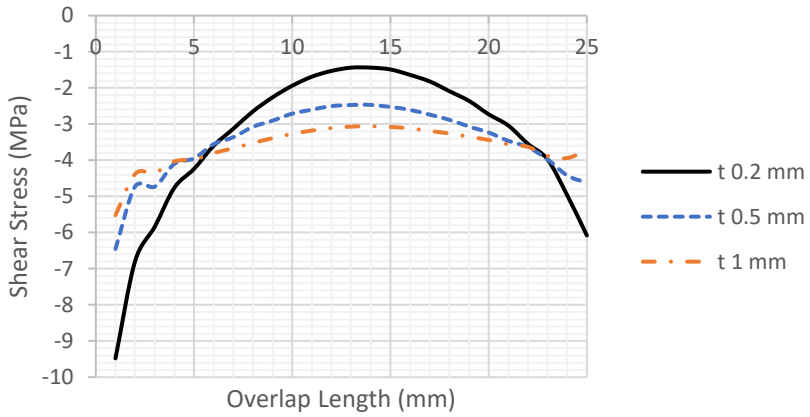

(b)

Figure 3.9 Plot showing the effect of adhesive thickness on the normal (a) and shear (b) stress distribution across bond length.

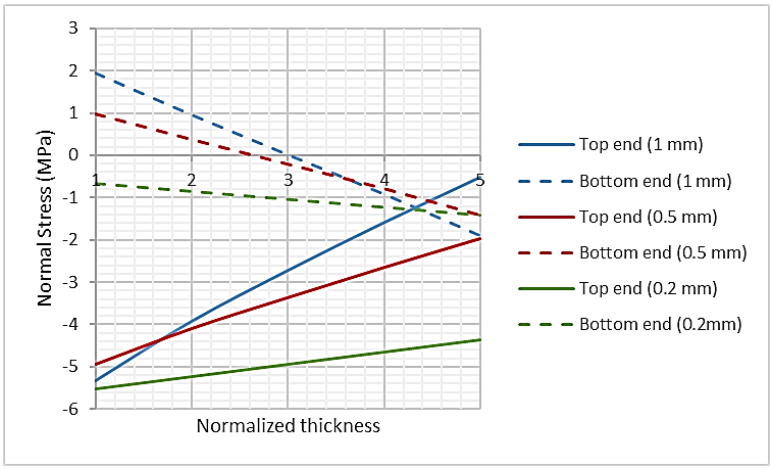

Figure 3.10 Plot showing the effect of adhesive thickness on the normal stress distribution across adhesive thickness. (1: inside interface, 5: outside interface, Top end: leading edge, bottom end: trailing edge)

3.2.5 Effect of Tube Length

Tube length plays a major role in determining crush characteristics of tubular structures. Hence, different tube lengths were considered for stress analysis. However, under linear elastic conditions, changes in tube length or changes in the ratio of inner tube to outer tube lengths do not show any influence on the stress distributions across the adhesive overlap.

3.2.6 Effect of Overlap Length

To join a given set of tubes the overlap length is a critical parameter in determining joint strength. Increasing bond length directly increases the bonded region, reduces the average shear stress, and hence allows for greater load carrying capacity. Apart from the basic understanding of higher overlap length leads to lower stress, it is important to understand the changes in stress distributions with overlap length. For this, two cases are considered: 10 mm and 25 mm overlaps. The tubular joint is made of steel tubes. Both tubes have a length of 75 mm and thickness of 1.25 mm. The outer tube has an outside diameter of 25.4 mm, and the adhesive thickness is 0.2 mm. The normal and shear stress distributions for the two cases are plotted in Figures 3.11 (a) and (b), respectively. To better compare the stress distributions, normalized stress values are also shown in Figure 3.11.

The normal stress plot indicates compressive stress concentrations at both edges of the overlap are higher for the 10 mm overlap and more uniform stress distribution for the 25 mm overlap. Also, the normal stress is zero for much of the mid-length of the 25 mm overlap. The shear stress concentrations at both edges of the overlap are much higher for the 10 mm overlap, but the shear stress distribution is more uniform for the 10 mm overlap. However, since the average shear stress is 2.5 times lower for the 25 mm overlap, the normalized shear stress values are higher for the 25 mm overlap compared to the 10 mm overlap.

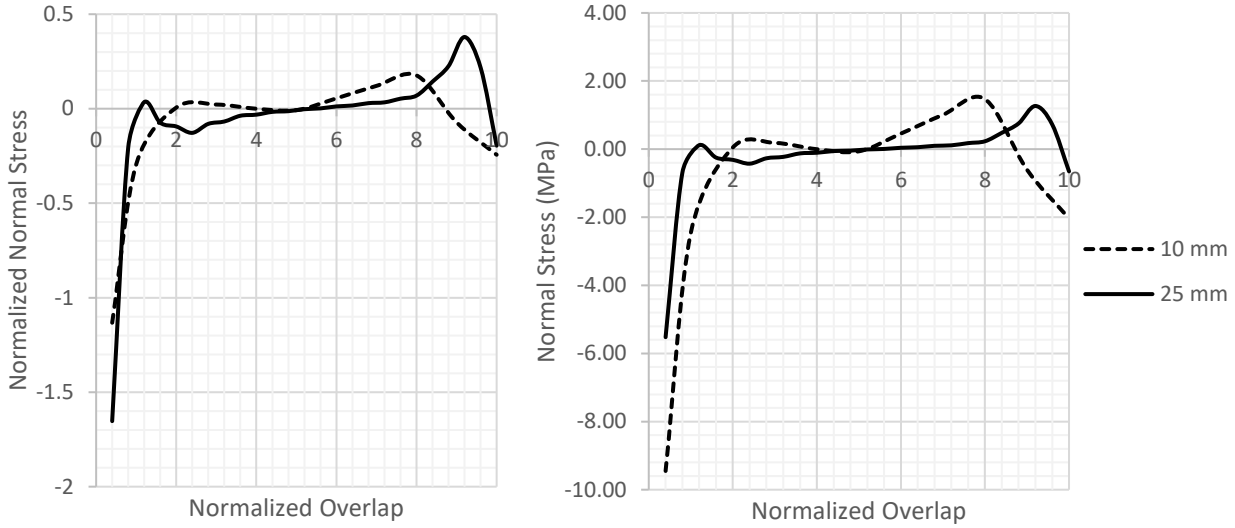

(a)

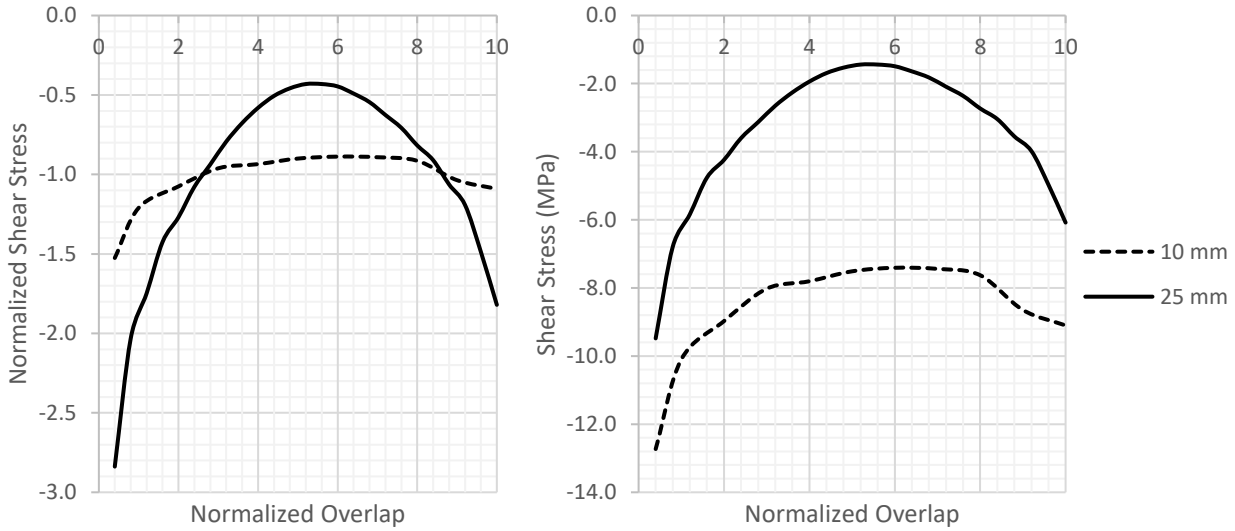

(b)

Figure 3.11 Plot showing the effect of overlap length on the normal (a) and shear (b) stress distributions across the overlap length.

3.2.7 Effect of Adhesive Spew

Finally, the end geometry of the adhesive joint also plays an important role in affecting the stresses in the adhesive layer. Changes made to the tube such as chamfered tube ends at the joint or scarfing and the presence of adhesive spew at the overlap ends help reduce stress concentrations in the adhesive layer. Triangular adhesive spews as shown in Figure 3.12 are considered here. Figure 3.13 (a) plots the normal stress for a joint with a 0.5 mm adhesive spew in a 0.2 mm thick adhesive joint. The introduction of a small spew marginally reduces the normal stresses at the joint edges while the stresses across rest of the adhesive length remains the same. The same is observed for shear stress values (Figure 3.13 (b)).

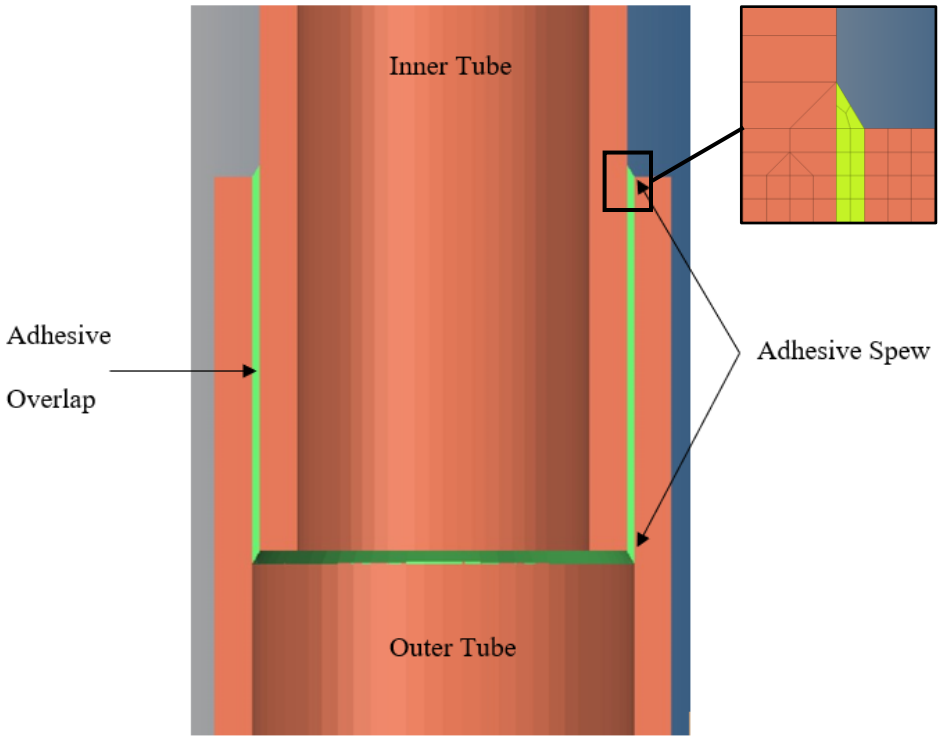

Figure 3.12 Tubular single lap joint with spew

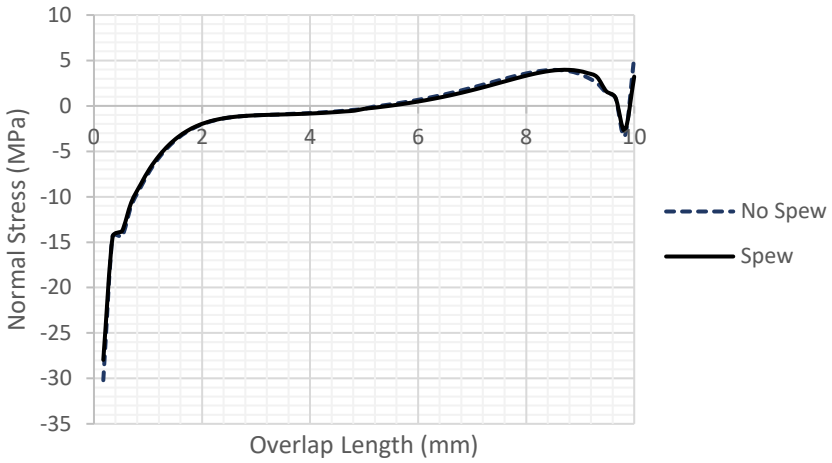

(a)

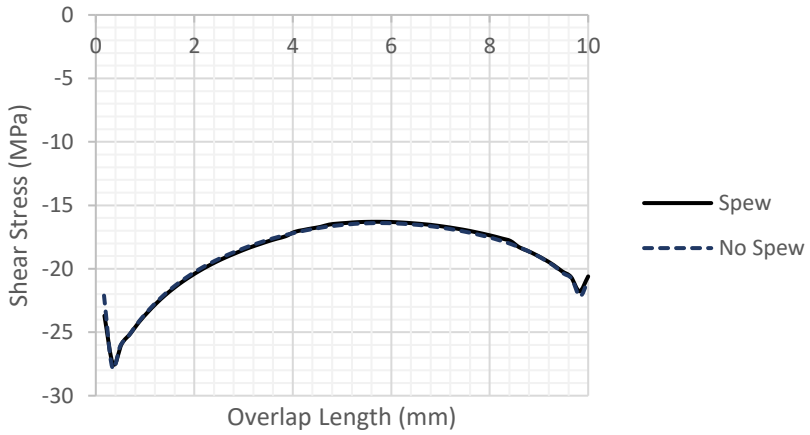

(b)

Figure 3.13 Plot showing the effect of small triangular adhesive spews shown in Figure 3.12 on the normal (a) and shear (b) stress distributions across bond length. The other joint parameters are given in Table 3.1.

3.3 Conclusions

A linear elastic finite element analysis of the bonded region was conducted to gain insight into the stress distributions in the adhesive layer in tubular joints subjected to an axial compressive load. Adhesive overlap exhibits regions of shear stress concentrations at the overlap ends and relatively low shear stress across the bond length. Unlike tensile loading on the joint, compressive loading creates high compressive radial normal stresses at the leading overlap

edge. Depending on adhesive thickness, the normal stress at the trailing edge is either compressive or tensile. Stress values are higher at the leading edge compared to trailing edge. Critical joint design parameters are found to be tube material modulus, tube thickness, adhesive thickness and overlap length.

Chapter 4 Crush Performance of Aluminum-Aluminum Tubular Lap Joints

The existing analytical and numerical stress analysis models provide insight into the stress distributions in tubular lap joints under quasi-static, linear elastic conditions; however, this information is not sufficient to design such joints for structural applications. Studies on stress analysis do not provide insight into the crush and failure characteristics of the joint under axial loads. Hence, an explicit finite element analysis of tubular single lap joints using LS-Dyna was performed to determine failure modes, peak loads and energy absorption characteristics under compressive and tensile loads. This chapter presents the methodology used and the results of the finite element analysis of the crush characteristics of aluminum-aluminum tubular joints under compressive loads.

The single lap tubular adhesive joint considered in this research has a circular cross-section with three parts - an inner tube, an outer tube and an adhesive layer joining them over a small overlap. The geometric and material properties of each part have an influence on the deformation response and failure characteristics of the tubular joint under axial loads. The following sections of this chapter will explore the influence of these parameters and use Design of Experiments (DOE), a statistical analysis approach, to determine their degrees of influence on the joint performance under compressive loads.

4.1 Joint Configuration

The single lap tubular joint comprises of two co-axial tubes joined together across an overlap region using an adhesive as shown in Figure 4.1. For the purposes of this analysis under

compressive load, the joint is supported by a plug at the stationary bottom end of the outer tube and an axial compressive load is applied at the top of the inner tube by means of another plug moving at a constant velocity. The bottom plug is constrained across all degrees of freedom and the top plug is constrained in all but the y-direction displacement. Schematic drawings of the bottom and top plugs are given in Figures 4.2 (a) and (b).

As shown in Figure 4.1, the joint consists of three parts: top tube, bottom tube, and an adhesive overlap. The bottom tube is the outer tube and is larger in diameter than the top tube or inner tube. Each of the three parts have several geometric parameters to be considered for the crush-resistant design of the joint. Previous studies [10, 12] have shown that crush characteristics of round tubes are affected by the slenderness ratio which is the ratio of tube length to mean diameter. Typically, tubes with high slenderness ratio fail by global buckling with low energy absorption, which is an undesirable failure mode in crash conditions. A more sustained local buckling with fold formation occurs with tubes with low slenderness ratio. Tube thickness also plays a significant role in the type of deformation that may occur in tubes under compressive loads. Stress analysis of single lap tubular joints in literature [46, 47] shows that both tube thickness and diameter have significant influence on the stress distributions across the overlap length. In addition, the adhesive thickness and overlap length also influence the stress distributions in the adhesive. This was also verified using quasi-static stress analysis presented in Chapter 3.

In the crush analysis conducted in this chapter, the mean diameter of the joint, defined as the average of the inside diameter of the outer tube and the outside diameter of the inner tube, is kept constant at 26.46 mm. Two different adhesive thicknesses are considered and other parameters, such as outer and inner tube lengths, outer and inner tube diameters, and adhesive

overlap length (Figure 4.1) are varied. A list of these parameters along with their range of values is given in Table 4.1. The set of joint configurations used in the finite element simulations are listed in Table 4.2.

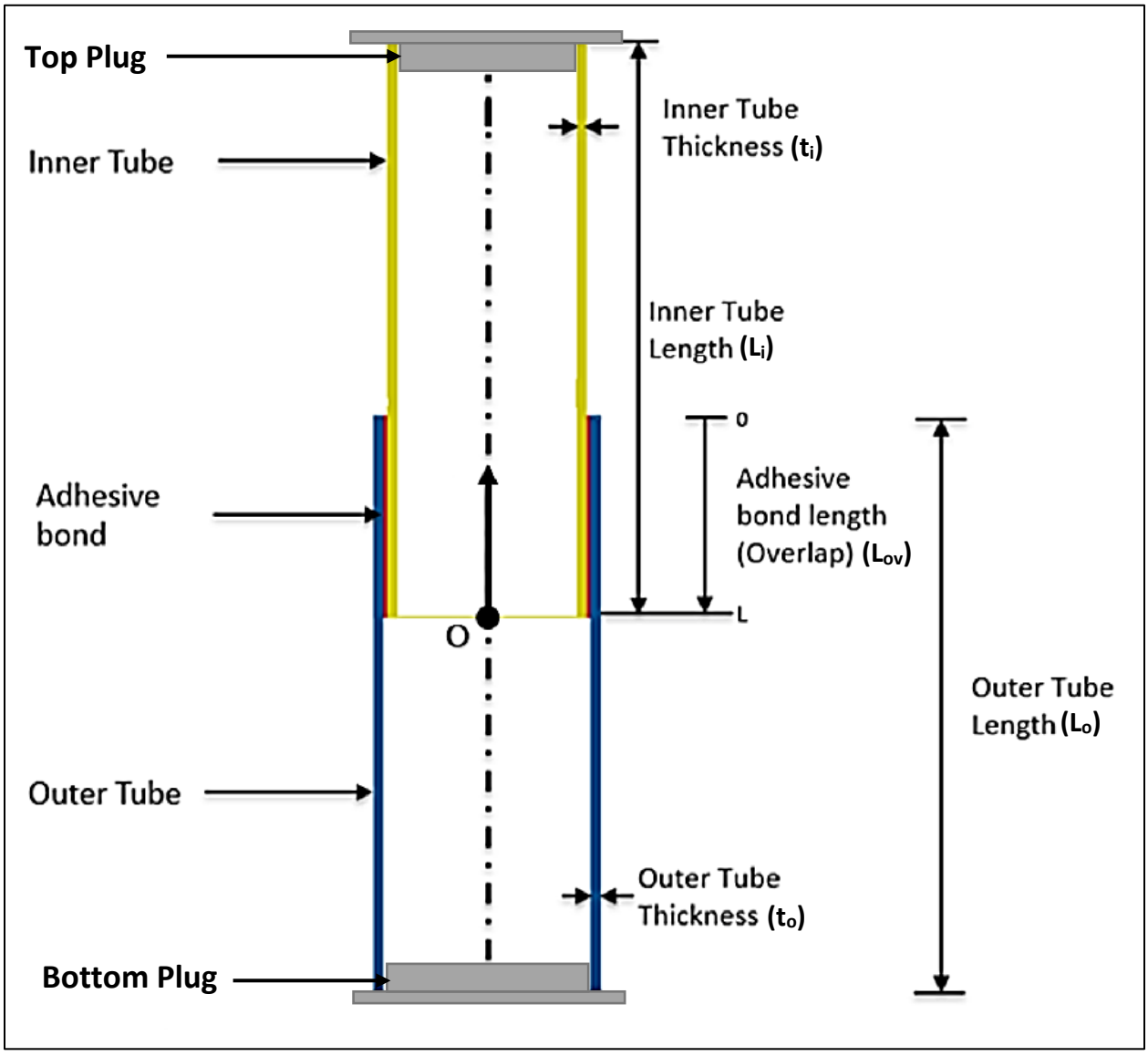

Figure 4.1 Joint configuration with end plugs.

Table 4.1 Geometric parameters of single lap tubular joints considered in the study (All dimensions are in mm)

Parameter	Symbol	Values
Joint length	$L = L_i + L_o - L_{ov}$	125, 137.5, 150, 162.5, 175
Inner tube length	L_i	75, 87.5, 95, 97.5, 100, 105
Outer tube length	L_o	75, 87.5, 95, 97.5, 100, 105
Overlap length	L_{ov}	15, 20, 25, 35
Mean joint diameter	d_m	26.46
Inner tube thickness	t_i	0.8, 1.2, 1.6
Outer tube thickness	t_o	0.8, 1.2, 1.6
Adhesive thickness	t_a	1.06, 1.5

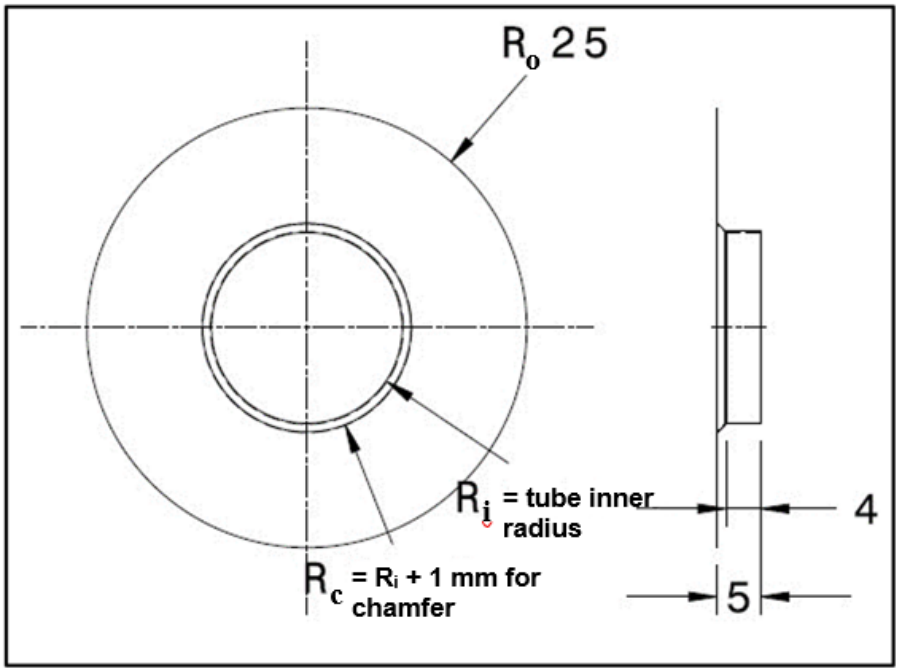

Figure 4.2 Plug schematic drawing with dimensions in mm.

Table 4.2 List of Joint configurations

L/dm	Li/Lo	ti/to	ti	Li	L	Overlap
6.6	1	1	1.6	95	175	15
6.6	1	1	1.2	95	175	15
6.6	0.95	1	1.6	95	175	20
6.6	0.95	1	1.2	95	175	20
6.6	1	0.75	1.2	97.5	175	20
6.6	1	1	1.6	97.5	175	20
6.6	1	1	1.2	97.5	175	20
6.6	1	1.33	1.6	97.5	175	20
6.6	1.05	1	1.6	100	175	20
6.6	1.05	1	1.2	100	175	20
4.7	1	1	1.6	75	125	25
4.7	1	1	1.2	75	125	25
4.7	1	1	0.8	75	125	25
5.19	0.86	1	1.6	75	137.5	25
5.19	1.17	1	1.6	87.5	137.5	25
5.7	0.75	1	1.6	100	150	25
5.7	0.75	1	1.2	100	150	25
5.7	0.75	1	0.8	100	150	25
5.7	1	1	1.6	87.5	150	25
5.7	1	1	1.2	87.5	150	25
5.7	1	1	0.8	87.5	150	25
5.7	1.33	1	1.6	75	150	25
5.7	1.33	1	1.2	75	150	25
5.7	1.33	1	0.8	75	150	25
6.14	0.875	1	1.6	87.5	162.5	25
6.14	1.14	1	1.6	100	162.5	25
6.6	1	0.75	1.2	100	175	25
6.6	1	1	2	100	175	25
6.6	1	1	1.6	100	175	25
6.6	1	1	1.2	100	175	25
6.6	1	1	0.8	100	175	25
6.6	1	1.33	1.6	100	175	25
6.6	0.95	1	1.6	100	175	30
6.6	0.95	1	1.2	100	175	30
6.6	1	0.75	1.2	102.5	175	30
6.6	1	1	1.6	102.5	175	30
6.6	1	1	1.2	102.5	175	30
6.6	1	1.33	1.6	102.5	175	30
6.6	1.05	1	1.6	105	175	30
6.6	1.05	1	1.2	105	175	30
6.6	0.91	1	1.6	100	175	35
6.6	0.91	1	1.2	100	175	35
6.6	1	0.75	1.2	105	175	35
6.6	1	1	1.6	105	175	35
6.6	1	1	1.2	105	175	35
6.6	1	1.33	1.6	105	175	35
6.6	1.1	1	1.6	110	175	35
6.6	1.1	1	1.2	110	175	35

4.2 Material Properties

The material properties of both tubes as well as the adhesive greatly influence stress distributions across the overlap as described in the previous chapter. This in turn will affect crush characteristics of the joint. Hence, both tube and adhesive material properties are important variables to be considered for joint design. The required material properties for the adhesive and the tubes are obtained from literature [57 - 59].

The tube material in the aluminum-aluminum joints is a 6061-T4 aluminum alloy, which is an Al-Mg-Si alloy and is widely used in the automotive industry. The T4 designation for the aluminum alloy indicates that it is naturally aged. Its properties are listed in Table 4.3.

An assortment of adhesives is available in the market with properties tailored for different applications. Some adhesives are designed to have high strength and stiffness, while some are optimized for energy absorption at the cost of strength and stiffness. To better understand the influence of adhesive properties on joint crush characteristics, three different epoxy adhesives are considered: Betamate 1496, Araldite 2015 and Araldite AV138. The quasi-static properties for these adhesives are listed in Table 4.4. Strength, modulus, and fracture toughness of an adhesive are important parameters to be considered in crush-resistant design. Fracture toughness is critical since it indicates the resistance to crack propagation in the adhesive, and therefore, the amount of energy absorbed by the adhesive prior to its failure. The three adhesives selected in this study exhibit distinct characteristics that will help understand the influence of adhesive characteristics on the crush performance of the joint.

Betamate 1496 is a one-component epoxy adhesive, optimized for crash resistant multi-material joints. It shows the highest fracture toughness among the adhesives considered along with moderate strength properties. Both Araldite adhesives are two-component epoxy adhesives.

Araldite AV138 is a brittle adhesive with high strength and stiffness, but low fracture toughness. Araldite 2015 has properties that are intermediate between the other two adhesives.

Table 4.3 Aluminum 6061 -T4 [57].

Density (g/cc)	2.69
Modulus (GPa)	70.3
Yield Strength (MPa)	252
% Elongation to Failure	19
Power Law Parameters	
k (MPa)	400
n	0.069
Rate Effect Parameters	
C	6500
p	4

Table 4.4 Adhesive Properties [58, 59]

	Betamate 1496	**Araldite 2015**	**Araldite AV138**
Density (g/cc)	1.6	1.6	1.6
Modulus (E) (GPa)	1.6	1.85	4.89
Poisson's ratio (ν)	0.42	0.33	0.35
G_{IC} (N/mm) (1)	4.46	0.43	0.2
G_{IIC} (N/mm) (2)	25.1	4.7	0.38
Tensile strength (MPa)	30	21.63	39.45
Shear strength (MPa)	24	17.9	30.2
Strength strain rate factor at 1000 s^{-1}	2.5	-	-
Fracture energy strain rate factor at 1000 s^{-1}	2.75	-	-

(1) G_{IC} is Mode I fracture toughness and (2) G_{IIC} is Mode II fracture toughness.

4.3 Finite Element Model Parameters

The finite element analysis of the single lap tubular adhesive joint is conducted using LS-DYNA (Version R9.0.1), a non-linear finite element software commonly used in the automotive industry for vehicle crash analysis. The joint with finite element meshes are shown in Figure 4.3. The tubes are meshed using 2.5 mm 4-noded quadrilateral shell elements and the adhesive is meshed using a single layer of 2.5 mm, 8-noded solid elements across the adhesive thickness. The shell elements are modeled using the default Belytschko-Tsay element formulations with five through-thickness integration points. To reduce hourglass energy under large deformations, hourglass control is opted for adhesive elements. The control type is Flanagan-Belytschko viscous form with exact volume integration for solid elements and hourglass quotient of 0.1.

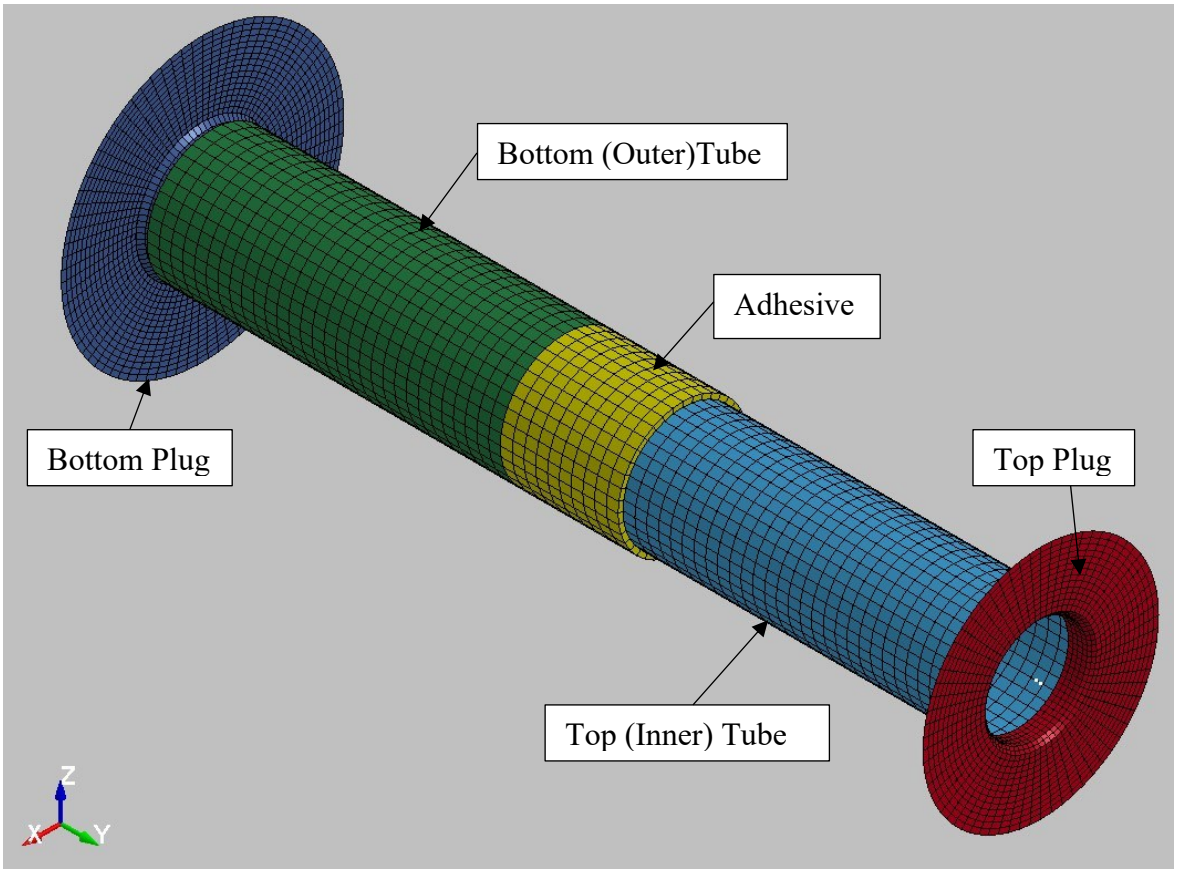

Figure 4.3 Finite element meshing of the tubes, adhesive and the plugs

Boundary conditions for the joint are provided at the top and bottom plugs. The degrees of freedom and constant velocity condition are defined using PRESCRIBED MOTION RIGID card for the top plug. The plug moves at a constant velocity of 1 mm/s to simulate a quasi-static loading condition. The bottom plug is constrained in all degrees of freedom.

Contact conditions are defined using AUTOMATIC_SINGLE_SIRFACE and AUTOMATIC_SURACE_TO_SURAFECE conditions. Surface to surface contact definitions are provided between the tubes and the plugs. Single surface contact definition is provided to inner and outer tube elements to avoid penetration between the tubes or self-penetration under large deformations. Contact static friction is defined as 0.2 and dynamic friction as 0.1.

Simulation data are recorded for 40 s at 0.02 s intervals. Also, mass scaling of the entire system by 1000 times was done to reduce the run time.

4.3.1 Aluminum Material Model

The material for the aluminum tubes is modeled using MAT_18 Power Law Plasticity material model. This model defines the elastoplastic behavior of the material using an isotropic hardening rule. The yield stress is defined using the power law equation as shown in Equation 4.1 [60].

$$\sigma_y = k\varepsilon^n = k(\varepsilon_{yp} + \varepsilon^p)^n \quad \text{Eq. 4.1}$$

where, ε_{yp} is yield strain, ε^p is the plastic strain, and k and n are power law parameters listed in Table 4.2. Rate effects are disregarded for this part of the study.

4.3.2 Adhesive Material Model

LS Dyna offers several material models based on continuum mechanics and cohesive zone model to simulate adhesive behavior. Continuum mechanics models such as MAT_SAMP-1 (MAT_187) and MAT_GURSON (MAT_120) are suggested for detailed representation of the

adhesive and require input of several parameters that need to be calibrated with experimental results for accurate representation [61]. The extensive experimental work required to build the material card using this approach is not feasible for the scope of this dissertation.

Cohesive zone model (CZM) is a fracture mechanics model used to describe crack formation. The separation of surfaces is described using traction-separation laws. This model has been adapted to simulate behavior of delamination in composites and adhesive bonding. LS-Dyna offers several CZM based material models [62]. Cohesive element-based models such as MAT_ARUP_ADHESIVE (MAT_169) show good correlation with experimental data for structural adhesives at quasi-static as well as high strain rates. Hence, they have been widely used in literature to simulate adhesive behavior under different loading conditions. In this study MAT_ARUP_ADHESIVE is used to model the adhesive due to ease of use and availability of material parameters for several adhesives.

The thickness of the adhesive is a critical factor in determining stiffness and failure of adhesive elements. The model assumes that solid adhesive elements are tied to shell elements representing mid-plane of the substrate sheet. Hence, the adhesive elements are assumed to be larger than the actual thickness of the adhesive bond layer. However, this results in erroneous results with respect to bond stiffness and strength, requiring further calibration of a bond thickness parameter (BTHK) and scaling of the adhesive modulus. Another option to model the joint is by offsetting the shell elements. In this case, the shell elements represent the inner surface for the inner tube and outer surface for the outer tube. This results in element thickness being equal to bond thickness. Simulation of models using the previously described two approaches showed completely different results. With substrate shell elements representing mid-plane, a 35 mm overlap bond showed complete failure with tube thickness as low as 0.8 mm, while a model

with shell elements representing outer/inner layers did not exhibit complete adhesive failure. Due to lack of corresponding experimental results, the tubes are modeled with shell elements representing inner surface and outer surface. The through-thickness direction flag (THKDIR) is set to 1 which takes the direction as between adhesive element nodes 1-2-3-4 and 5-6-7-8.

The ARUP adhesive material model is described using two traction separation laws in tension and shear as shown in Figure 4.4. The tension traction separation law is generally represented using a bilinear stress-displacement diagram with an area is equal to G_{Ic}. The shear traction separation law is represented using a bilinear or trilinear stress-displacement diagram with an area equal to G_{IIc}. For viscoplastic adhesives such as Betamate 1496, a trilinear diagram is suggested, while for brittle adhesives a bilinear diagram is suggested. The shear plateau parameter (SHRP) in the trilinear diagram is taken to be 0.77 for Betamate 1496 [58] and zero for the brittle adhesives AV138 and Araldite 2015. It should be noted that SHRP can have a significant influence on the crush characteristics of the joint. A sensitivity study conducted here showed a value of 0.75 resulted in progressive inner and outer tube crush, while a value of 0.9 resulted in no adhesive failure and global buckling. The strength and fracture energy properties of the adhesives are as listed in Table 4.4.

The yield condition for the adhesive material is defined using a power law combination of tension and shear parameters (Equation 4.2). The power terms PWRT and PWRS are set as two [58]. Figure 4.5 represents the yield surface. The strain rate effects of material strength and fracture toughness are modeled using a log-linear approach.

$$\left(\frac{\sigma}{\sigma_{max}}\right)^{PWRT} + \left(\frac{\tau}{\tau_{max}}\right)^{PWRS} = 1 \; at \; yield \qquad \text{Eq. 4.2}$$

where, σ_{max} (TENMAX) is the tensile strength and τ_{max} (SHRMAX) is the shear strength of the adhesive. The slope of yield surface at $\sigma = 0$ is zero.

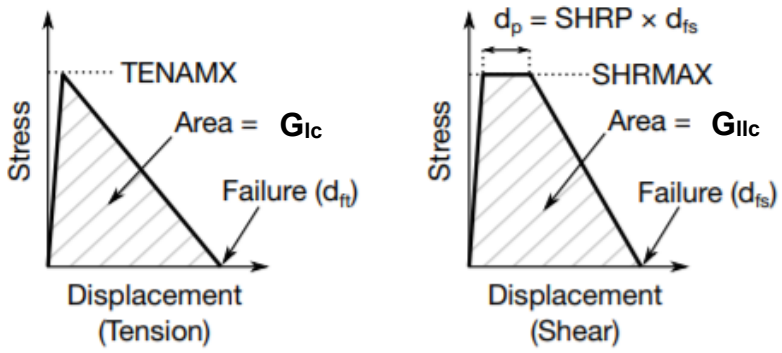

Figure 4.4 Traction-separation laws in tension (left) and shear (right).

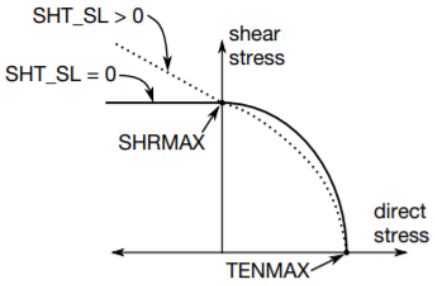

Figure 4.5 Yield surface for ARUP adhesive model.

4.4 Finite Element Simulation Results

Crush characteristics of single lap tubular joints are analyzed by considering the tube deformation, nature of the force-time plot, peak load and energy absorbed in the tubes and the adhesive. An ideal joint would exhibit progressive accordion fold type failure in one or both tubes along with no or minimal adhesive failure. A weak bond that fails prior to any significant folding deformation of the tubes is not acceptable as it results in low energy absorption in crash. The adhesive bond failure is largely affected by overlap length, adhesive thickness, and adhesive properties, while the nature of crush in the tubes is also affected by the tube geometry. Hence, crush simulation of single lap tubular adhesive joints is conducted with different joint configurations as described in Section 4.1.

A reference model is first built and analyzed using two 100 mm long aluminum tubes bonded with Betamate 1496 adhesive. The lap joint has an overlap length of 25 mm. The outside diameter of the inner tube is 25.4 mm, and the outside diameter of the outer tube is 30.72 mm. Both tubes are 1.6 mm thick. The adhesive thickness is 1.06 mm. The crush behavior of the reference model is shown with a sequence of images in Figure 4.6. The numbers below the figure represent the points on the force-time plot at which the images are captured. The resultant force-time plot is shown in Figure 4.7. The reference model exhibits minor tube crush of both the inner and outer tubes followed by global buckling of the inner tube which tilts the joint to the right. The inner tube deforms first (2), which is then followed by the deformation of the outer tube (3). The tubes continue to show increasing crush prior to global buckling of the inner tube (4), leading to the joint failure. The tube crush is characterized by several peaks and valleys on the force-time plot before reaching (4), and when the buckling sets in, a steady decrease in load carried by the joint.

The yellow elements in Figure 4.6(a) represent the adhesive bond before any failure initiation in the adhesive layer. Adhesive failure is first observed at the leading edge of the overlap in Figure 4.6(c) where several yellow elements are deleted. The failure region initially grows along the circumference and then toward the center of the overlap length. The region of initial adhesive failure also coincides with initial buckling of the inner tube near the leading edge of the bond. The buckled region deforms further to result in global buckling of the joint accompanied by increasing amount of adhesive failure. Figure 4.8 illustrates this in two images taken at 10s and 30s. The circled areas in Figure 4.8 show the localized deformation of the inner tube at 10s.

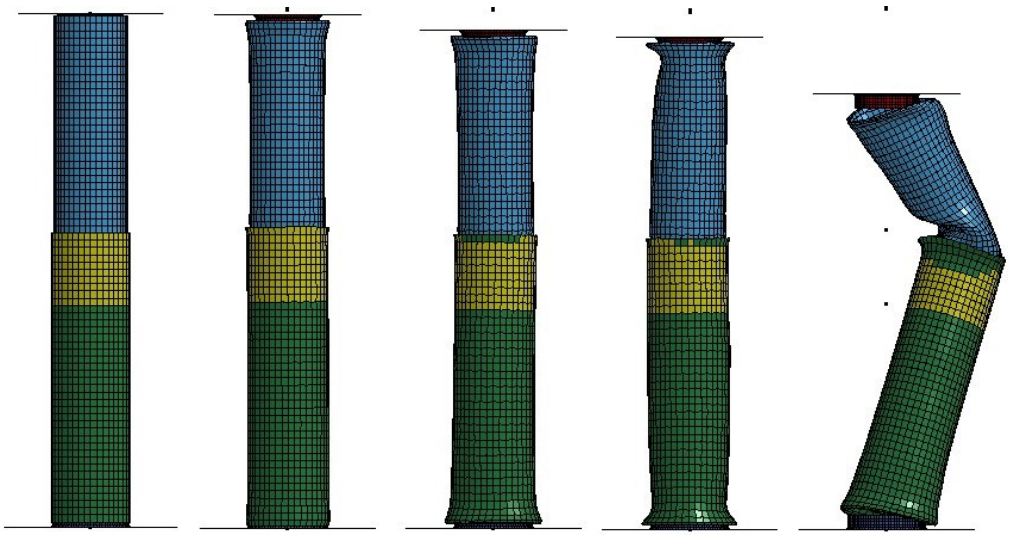

Figure 4.6 Sequence of reference model crush.

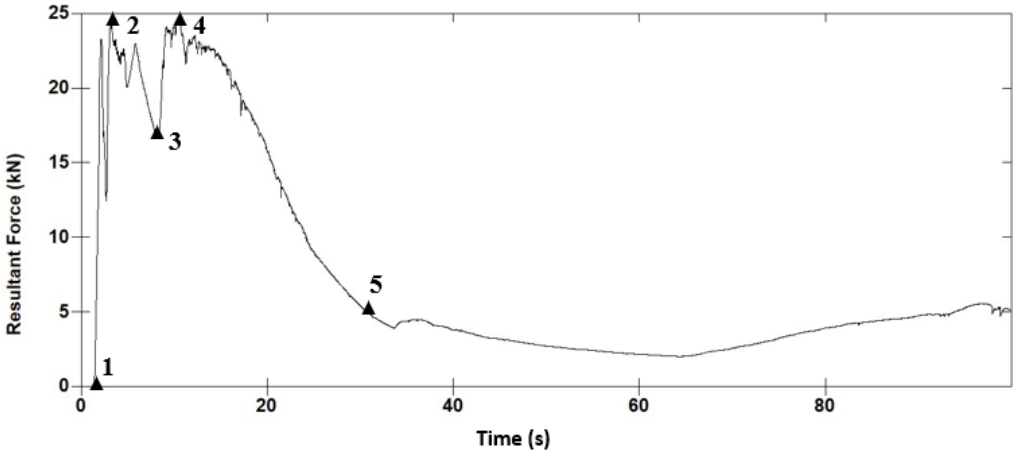

Figure 4.7 Force-time plot for reference model.

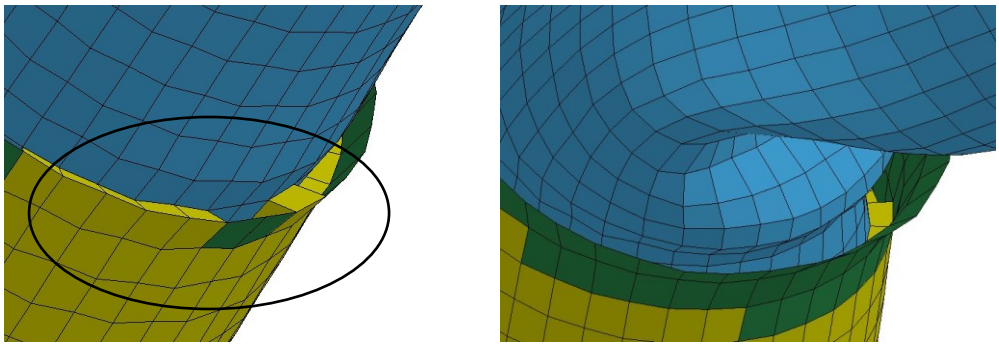
Figure 4.8 Deformation of the inner tube and adhesive failure zone at 10 s (Left) and 30 s (Right).

The maximum resultant force under crush for the tubular joint is not observed at the first peak of the force-time plot. In this case, the resultant force at the first peak is 22.9 kN which occurs as the top end of inner tube starts to deform and the maximum resultant force is 23.4 kN which occurs as the lower end of the outer tube starts to deform. The total energy absorbed by the joint is 498 J and the energy absorbed by the adhesive is 19.3 J over a deformation of 40 mm. Thus, the energy absorbed by the adhesive only 3.9% of the total energy absorbed.

Global buckling of the specimen is not an ideal form of failure for tube crush, since in general, it produces low energy absorption and a sudden large load drop after global buckling is not desirable. Hence, a preliminary study was conducted based on the reference model by varying several joint geometry parameters and the adhesive material to understand their influence on crush characteristics of the joint. The adhesive materials are crash resistant epoxy (Betamate 1496), toughened epoxy (Araldite 2015), and brittle epoxy (Araldite AV138). Geometric parameters considered are adhesive thickness (t_a), overlap length, ratio of inner and outer tube thicknesses (t_i/t_o), and ratio of inner and outer tube lengths (Li/Lo). The results of the simulations using these factors are listed in Table 4.5 and are discussed below. Failure modes of the joints fall broadly into four categories, namely, global buckling, tube wrinkling and folding, adhesive failure, or combinations thereof. This in turn results in differences in force-time characteristics, peak load, energy absorbed by the joints as well as by the adhesive.

Table 4.5 Crush characteristics for different joint configurations.

L/d_m	L_i/L_o	t_i/t_o	t_i (mm)	L_i (mm)	L (mm)	Overlap (mm)	P_{max} (kN)	Total Energy Absorbed @40 s (J)	Adhesive Failure	Adhesive Energy Absorbed @40 s (J)	Comments
6.6	1.05	1	1.6	105	175	30	23 (28.1)	783	10 mm failure in the middle of overlap (2.5 mm from leading edge)	25.7	Global buckling with IT wrinkling, folding
6.6	1.05	1	1.2	105	175	30	16.7 (18.7)	446	No failure	18	IT wrinkling, folding
Li = 1.05 Lo = 105 mm, ti = to, overlap = 30 mm: Lower ti, inner tube wrinkling, lower peak force, lower energy absorption											
6.6	1	1	1.6	102.5	175	30	23.0 (27.4)	783	7.5 mm failure in the middle of overlap (2.5 mm from leading edge)	24.7	Global Buckling
6.6	1	0.75	1.2	102.5	175	30	17.2 (21.8)	508	2.5 mm circumferential failure at leading edge	17.2	IT wrinkling, folding
6.6	1	1	1.2	102.5	175	30	16.8 (18.0)	512	No failure	15.5	OT wrinkling, folding
6.6	1	1.33	1.6	102.5	175	30	19.4 (24.8)	509	10 mm crack from trailing edge, 5 mm circumferential failure	21.4	OT wrinkling, folding
Li = Lo =102.5 mm, overlap = 30 mm: Compare 1 and 2: Lower ti, inner tube wrinkling, lower peak force, and lower energy absorption. Compare 1 and 3: Lower ti, outer tube wrinkling, lower peak force, and lower energy absorption Compare 2 and 3: ti less than to, inner tube wrinkling; ti equal to or higher than to, outer tube wrinkling											
6.6	0.95	1	1.6	100	175	30	23.4 (24.9)	718	2.5-5 mm adhesive failure in the middle of overlap (2.5 mm from leading edge)	20.3	Global buckling with OT wrinkling, folding

6.6	0.95	1	1.2	100	175	30	17.0 (18.2)	454	2.5 mm circumferential failure at leading edge	16.2	IT wrinkling, folding
Li = 0.95 Lo = 1oo mm, ti = to, overlap = 30 mm: Lower ti, Inner tube wrinkling, lower peak force, lower energy absorption											
6.6	1	1	2.0	100	175	25	29.1 (29.9)	715	15 mm crack from leading edge, 5 mm circumferential failure	8	Global Buckling
6.6	1	1	1.6	100	175	25	22.9 (23.4)	498	15 mm crack from leading edge, 5 mm circumferential failure	17.9	Global Buckling
6.6	1	1	1.2	100	175	25	16.7 (17.6)	471	5 mm crack from leading edge, 2.5 mm circumferential failure	16.6	IT wrinkling, folding
6.6	1	1	0.8	100	175	25	10.8	243	2.5 mm crack from leading edge, single location	7.7	IT wrinkling, folding
Li = Lo, ti = to, overlap = 25 mm: Global buckling at ti = 2 and 1.6 mm, Inner tube wrinkling at ti = 1.2 and 0.8 mm; Lower ti, lower peak force, lower energy absorption											
6.6	1	0.75	1.2	100	175	25	16.6 (21.1)	305	10 mm crack from leading edge, 2.5 mm circumferential failure	14.3	Global Buckling
6.6	1	1.33	1.6	100	175	25	19.2 (23.2)	600	10- and 5-mm cracks on opposite sides	21.1	Global buckling with OT wrinkling, folding
Li = Lo, ti = 0.75 and 1.33 to, overlap = 25 mm: Global buckling; higher ti, higher peak force and higher energy absorption											
6.6	1.05	1	1.6	100	175	20	23.8	461	10- and 17.5-mm cracks on opposite sides	5.0	Global Buckling

6.6	1.05	1	1.2	100	175	20	17.1	232	7.5- and 5-mm cracks, 2.5 circumferential failure	14.8	Global Buckling with no second peak
6.6	1	1	1.6	97.5	175	20	23.3	310	12.5- and 5-mm cracks on opposite sides	7.7	Global Buckling with no second peak
6.6	1	1	1.2	97.5	175	20	16.5	218	7.5- and 5-mm cracks, 2.5 circumferential failure	13.3	Global Buckling with no second peak
6.6	0.95	1	1.6	95	175	20	22.7	329	12.5- and 10-mm cracks on opposite sides	8.6	Global Buckling with no second peak
6.6	0.95	1	1.2	95	175	20	17.2	242	7.5- and 5-mm cracks, 2.5 circumferential failure	15.4	Global Buckling with no second peak
6.6	1	0.75	1.2	97.5	175	20	17.4 (17.7)	222	7.5- and 5-mm cracks, 2.5 circumferential failure	14.8	Global Buckling
6.6	1	1.33	1.6	97.5	175	20	19.4 (19.7)	353	Complete failure	15.1	Global buckling
Li = Lo = 175 mm, ti = 0.75, 1 and 1.33 to, overlap = 20 mm: ti = 1.2 and 1.6 mm, all Global buckling											
6.6	1	1	1.6	95	175	15	23.4	405	Complete failure	13.9	Global Buckling
6.6	1	1	1.2	95	175	15	16.3	195	two 2.5 mm cracks on opposite sides	1.9	Global Buckling
Li = Lo, ti = to, overlap = 15 mm: ti = 1.2 and 1.6 mm, global buckling; lower ti, lower peak force and energy absorption											

6.14	0.875	1	1.6	87.5	162.5	25	23.5 (27.0)	633	15 mm crack from leading edge, 7.5 mm circumferential failure	18.2	Global Buckling
6.14	1.14	1	1.6	100	162.5	25	23.1 (24.7)	572	17.5 mm crack from leading edge, 12.5 mm circumferential failure	23.4	Global Buckling
5.7	1	1	1.6	87.5	150	25	23.1 (25.9)	589	15 mm crack from leading edge, 7.5 mm circumferential failure	19.4	Global Buckling
5.7	1	1	1.2	87.5	150	25	17.7 (18.5)	496	5 mm crack from leading edge, 2.5 mm circumferential failure	18.5	IT wrinkling, folding
5.7	1	1	0.8	87.5	150	25	11.0	251	5 mm crack from leading edge, 2.5 mm circumferential failure	18.3	IT wrinkling, folding
5.7	1.33	1	1.6	75	150	25	22.6 (24.0)	693	7.5 mm crack from leading edge, 2.5 mm circumferential failure	16.3	Global Buckling
5.7	0.75	1	1.6	100	150	25	22.9 (29.5)	569	10 mm crack from leading edge, 5 mm circumferential failure	17.6	Global Buckling
5.7	1.33	1	1.2	75	150	25	16.9 (19.3)	458	12.5 mm crack from leading edge, 2.5 mm circumferential failure	17.6	Global Buckling with IT folding
5.7	0.75	1	1.2	100	150	25	16.9 (19.01)	368	12.5 mm crack from leading edge, 2.5 mm circumferential failure	12.9	Global Buckling with some IT folding
5.7	1.33	1	0.8	75	150	25	10.4 (11.1)	263	5 mm crack from leading edge, 2.5 mm circumferential failure	16.7	IT wrinkling, folding

5.7	0.75	1	0.8	100	150	25	11.5	240	5 mm crack from leading edge, single location	14.8	IT wrinkling, folding
5.19	0.86	1	1.6	75	137.5	25	23.6 (27.7)	752	7.5 mm crack from leading edge, 2.5 mm circumferential failure	16.6	Global Buckling
5.19	1.17	1	1.6	87.5	137.5	25	22.4 (27.7)	770	10 mm crack from leading edge, 2.5 mm circumferential failure	19.4	Global Buckling
ti = to = 1.6 mm, overlap = 25 mm: Li = 0.86 and 1.17 Lo, global buckling, no changes in peak forces and energy absorptions											
4.7	1	1	1.6	75	125	25	23.3 (28.1)	748	7.5 mm circumferential failure	23.0	Global Buckling
4.7	1	1	1.2	75	125	25	17.0 (20.5)	489	10 mm crack from leading edge, 5 mm circumferential failure	22.1	IT wrinkling, folding
4.7	1	1	0.8	75	125	25	10.8 (11.8)	274	5 mm crack from leading edge, 2.5 mm circumferential failure	16.0	IT wrinkling, folding
Li = Lo, ti = to, overlap = 25 mm: to = 1.6 mm, global buckling; ti = 1.2 and 0.8 mm, inner tube wrinkling; lower ti, lower peak force and lower energy absorption											

4.4.1 Effect of Adhesive Material Properties

To understand the effect of different types of adhesives on the joint behavior, three adhesives are chosen for comparison, namely, a crash optimized adhesive (Betamate 1496), a toughened epoxy adhesive (Araldite 2015) and a brittle adhesive (Araldite AV138). The joint with overlap length of 25 mm and tube lengths of 100 mm is subjected to compressive load as described previously. Figure 4.9 plots force-time curve for the three adhesive joints. The results show that all three adhesives have the same initial peak load, indicating a similar crush initiation and progression at the initial crush front. But as the impactor moves downward, the brittle AV 138 adhesive is the first to fail followed by Araldite 2015. Both adhesives fail suddenly with little deformation in the tubes. Figure 4.10 illustrates the failure of the joint with Araldite 2015 adhesive. Once the adhesive completely fails, the inner tube starts sliding inside the outer tube with only resistance to its downward displacement arising from friction. The force increases in a stick-slip manner, but there is very little plastic deformation taking place in the tubes. In contrast, as can be observed in Figure 4.9, the joint with Betamate 1496 adhesive exhibits global buckling and only partial adhesive failure. A much slower crack progression in the adhesive in this case allows for greater tube deformation to take place.

The same set of adhesive properties are also applied to a joint with 35 mm overlap and 105 mm tubes. The tube lengths are increased to keep the free length constant. Results of these simulations are plotted in Figure 4.11. The increase in overlap lengths seems to have little impact on joints with Araldite 2015 and AV138 in terms of the failure mode. Both adhesives show complete adhesive failure followed by load increase in a stick-slip manner. The Betamate adhesive shows a combination of wrinkling and buckling as explained in the previous section.

Betamate 1496 and Araldite AV138 have similar tensile and shear strengths, however AV138 being a brittle adhesive shows poor fracture properties. This results in poor performance in crush applications compared to a toughened epoxy adhesive as illustrated here. Hence, further studies will only include Betamate adhesive.

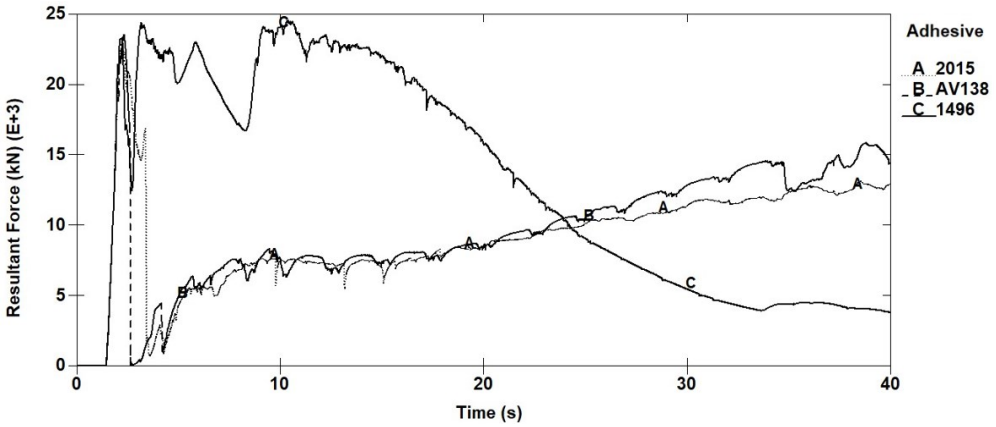

Figure 4.9 Force-time plot comparison of three types of adhesives for joint with 25 mm overlap: (A) Araldite 2015, (B) Araldite AV138 and (C) Betamate 1496

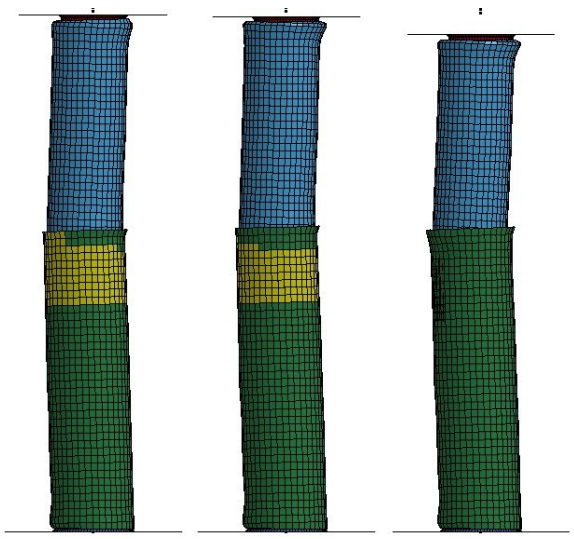

Figure 4.10 Deformation of specimen with Araldite 2015, 25 mm overlap at 2.9, 3.42 and 9s (left to right).

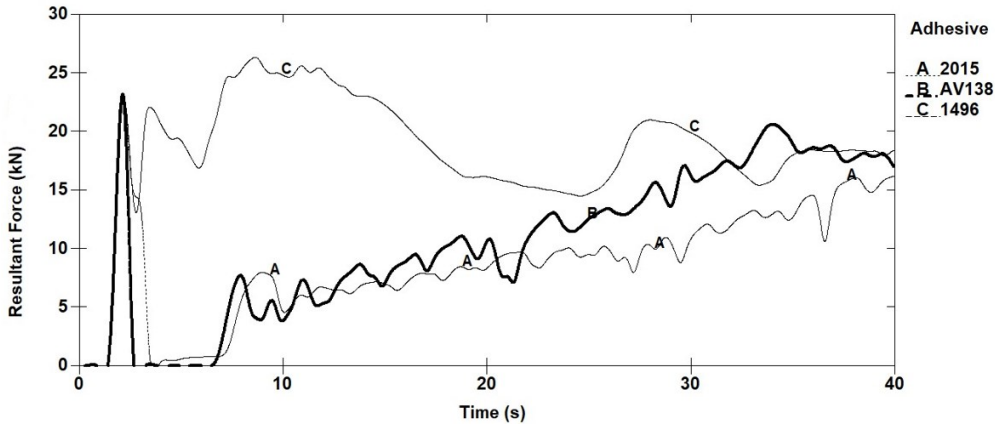

Figure 4.11 Force-time plot comparison of three types of adhesives for joint with 35 mm overlap: (A) Araldite 2015, (B) Araldite AV138 and (C) Betamate 1496

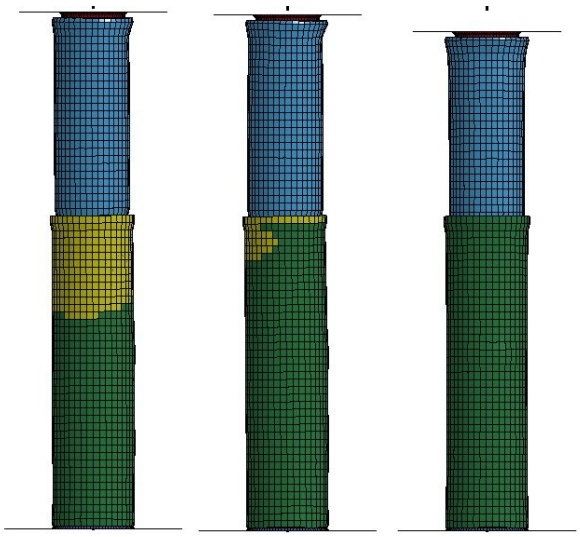

Figure 4.12 Deformation of specimen with Araldite 2015, 35 mm overlap at 2.8, 3.28 and 9s (left to right).

4.4.2 Effect of Overlap Length

In design of single lap joints joining two flat plates, increasing overlap length shows a corresponding increase in the joint strength. In single lap tubular joints, the objective of the adhesive is not only to transfer load between the tubes and provide good load carrying capacity but also to ensure progressive crush in the tubes for high energy absorption. To study this, a

range of overlap lengths, 10, 12.5, 15, 20 and 25 mm, was considered with a total joint length of 175 mm, equal tube lengths and equal tube thicknesses. The simulations had a termination time of 0.5s and a deformation speed of 100 mm/s to reduce runtime, thus producing the top plug displacement up to 50 mm. Strain rate effects are not considered in this part of the study. Total energy and peak load are recorded. Figures 4.13 and 4.14 illustrate the results and show that an increase in overlap length results in greater peak load as well as higher energy absorption. At overlap lengths below 15 mm, the adhesive fails prior to any significant plastic deformation in the tubes, whereas at overlap lengths greater than 15 mm, significant tube deformation occurs prior to adhesive yield or failure and a plateau in peak load appears to have reached.

Overlap lengths of 10 and 12.5 mm showed complete adhesive failure prior to any tube deformation. At overlap lengths of 15 and 20 mm, tube deformation is followed by complete adhesive failure and partial adhesive failure with further increase in overlap up to 25 mm. None of the simulations with 1.2 mm tube thickness show complete adhesive failure, while all simulations with 2.4 mm tube thickness show complete adhesive failure. Most of the simulations that show some degrees of deformation result in global buckling with little wrinkling/folding type deformation in the tubes at lower overlap lengths. Overlap of 25 mm show some wrinkling and folding in both tubes prior to buckling.

Further studies on joint crush characteristics will exclude overlap of 10 and 12.5 mm due to their poor performance. Also, since with different overlap lengths, the tube length also varies, the relationship between tube length, joint length and overlap length is also further explored in this section.

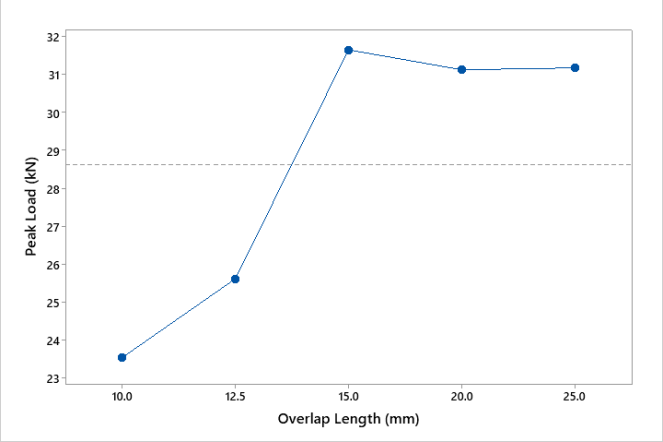

Figure 4.13 Variation of peak load with overlap length. (L = 175 mm, d_m = 26.46 mm)

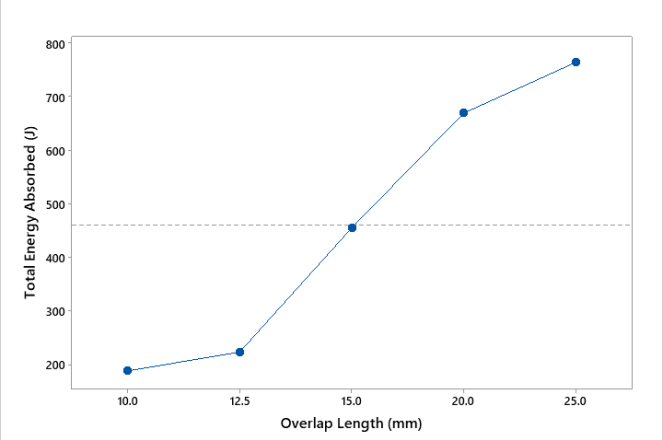

Figure 4.14 Variation of total energy absorbed versus overlap length. (L = 175 mm, d_m = 26.46 mm)

Results listed in Table 4.5 indicate that the modes of tube deformation depend on the adhesive overlap length. The 15 mm overlap joint, smallest considered in this set of studies shows complete bond failure for 1.6 mm thick tubes and global buckling for 1.2 mm thick tubes. For 20- and 25-mm overlap lengths, the mode of deformation is global buckling. Some joints with lower tube thickness show progressive crush at these overlap lengths. At higher overlap lengths of 30- and 35-mm, the deformation mode is either progressive folding or folding with some buckling in one of the tubes.

An example of joint deformation with progressive crush is shown in Figure 4.15. The figure illustrates crush of a specimen with 35 mm overlap, equal tube lengths of 105 mm and equal tube thicknesses of 1.6 mm. The sequence of images shows increasing amount of adhesive failure accompanied by inner tube folding followed by some wrinkling of the outer tube, and finally buckling of the joint. Compared to the 25 mm overlap discussed previously, both simulations indicate some adhesive failure starting at the leading edge of the overlap. In both cases, there is no adhesive failure at the trailing edge of overlap.

Figure 4.16 compares the force-time curves of 25 mm and 35 mm overlap joints. The 35 mm overlap joint shows several peaks and valleys owing to the folding of the inner tube up to 60 s where there is an increase in resultant force due to the folding of the inner tube reaching the top end of the outer tube, resulting in additional resistance to the downward movement of the top plug and flaring of the top end of the outer tube. This peak in force-time plot is followed by a steady decrease in load due to buckling of the outer tube.

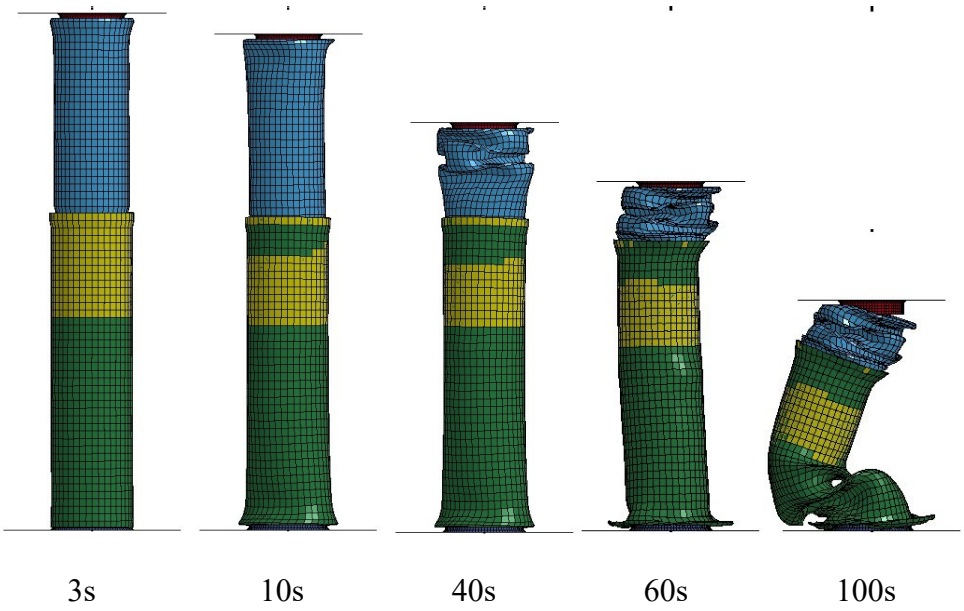

Figure 4.15 Deformation of specimen with Betamate 1496 with 35 mm overlap. (Tube thickness =1.6 mm)

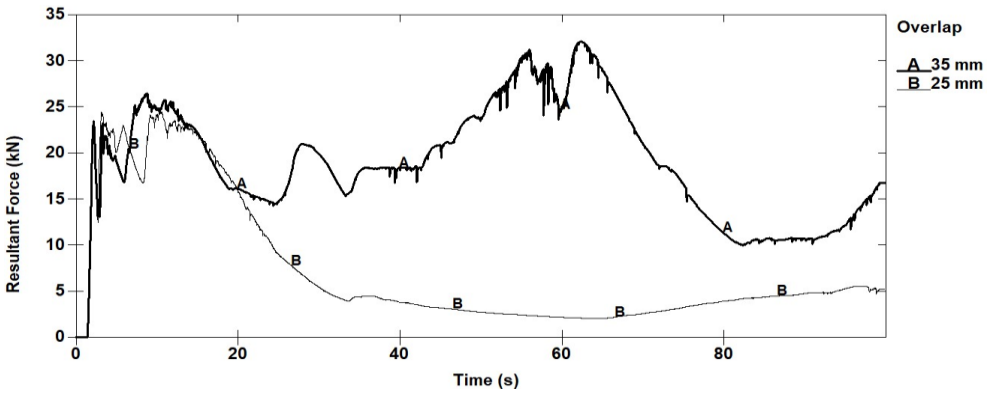

Figure 4.16 Force time plot comparing joints with (A) 25- and (B) 35-mm overlaps.

The crush mode has a direct impact on the peak load and energy absorption as stated earlier. For smaller overlap lengths, the joint fails due to bond failure or undergoes global buckling without any significant deformation in the tubes. With larger overlap, there is some tube wrinkling at both tube-plug interfaces even in cases with global buckling type failure. This results in a higher second peak load which is absent in smaller overlap joints as shown in Figure 4.17. The range in data shown is due to different tube thicknesses and joint lengths.

Any change in overlap length also corresponds to a change in the unbonded or free length of the tubes. Figure 4.18 plots the crush results against joint aspect ratio (JAR), which is defined as the ratio of the length of the joint and the bond overlap length. The dashed curve indicates results for joints with 175 mm joint length, but different overlap lengths resulting in different JAR values, and the solid curve indicates results for joints with 25 mm overlap length, but different joint lengths. In general, crush parameters improve with decreasing free length. From a design perspective, the specimen length is most likely to be the controlling parameter and the data shown in these curves indicates that a higher overlap length improves crush performance.

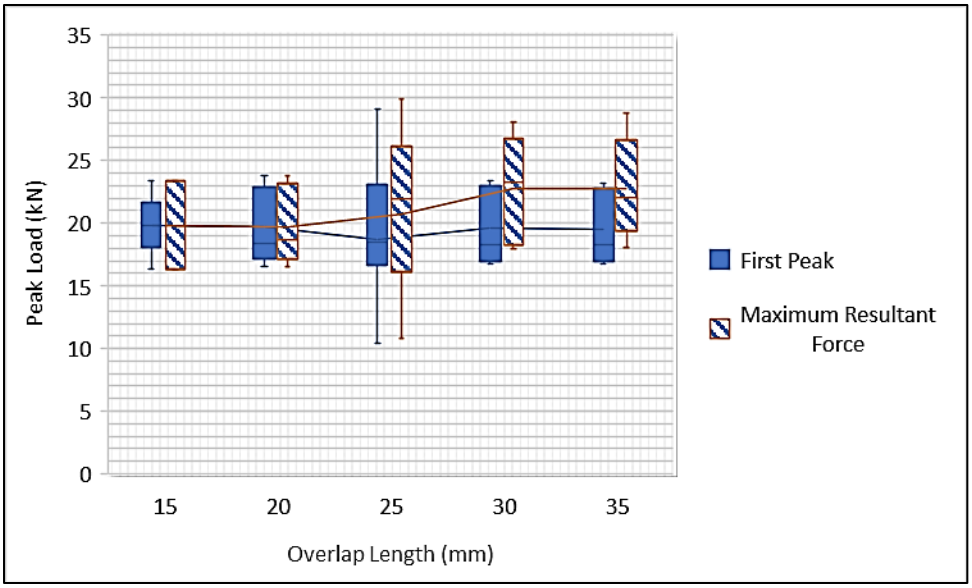

Figure 4.17 Variation in resultant force at first peak and maximum resultant force (up to 40s) for different overlap lengths.

The joint aspect ratio has a significant influence on crush performance of the joint. At higher JAR values where the overlap length is smaller compared to the joint length, its effect is relatively small. But, at smaller values of JAR, the joint performance improves with decreasing JAR. This is true with fixed overlap length or fixed joint length. As seen in Figure 4.16, a 35 mm overlap joint with JAR of 5 continues to carry load beyond the 40 mm crush considered here compared to 25 mm joint with JAR of 7 which buckles. Hence, to achieve high crush performance, not only should the overlap length be such that adhesive failure does not occur, but also joint aspect ratio should be low so that tube deformation is by folding rather than by global buckling. Additionally, tube thickness and ratio of tube lengths also play a major role in crush.

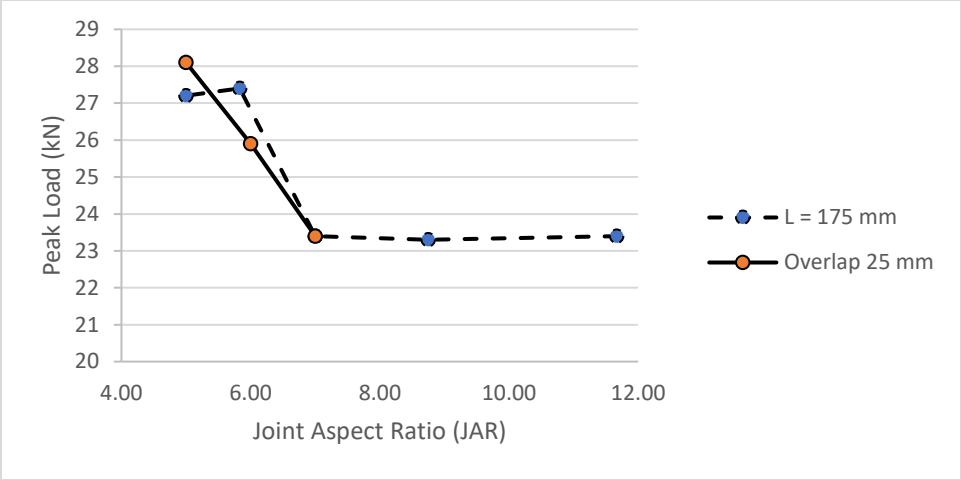

(a)

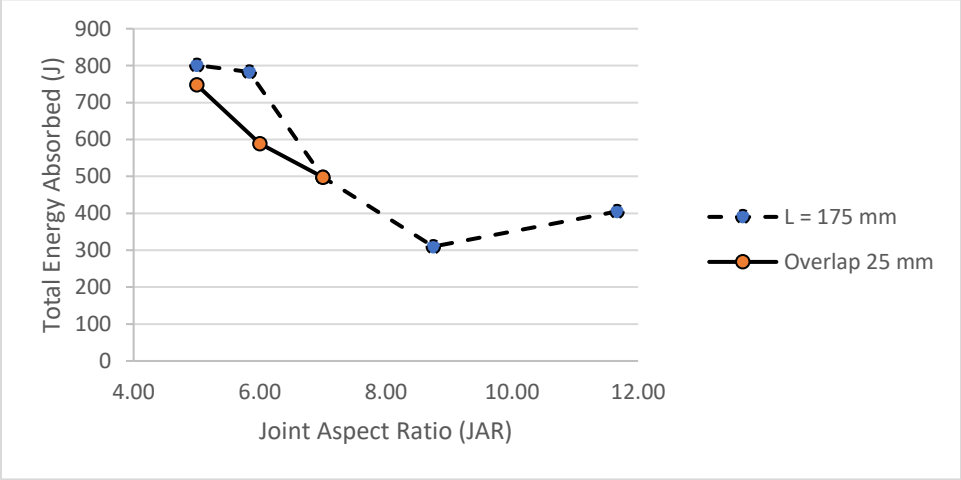

(b)

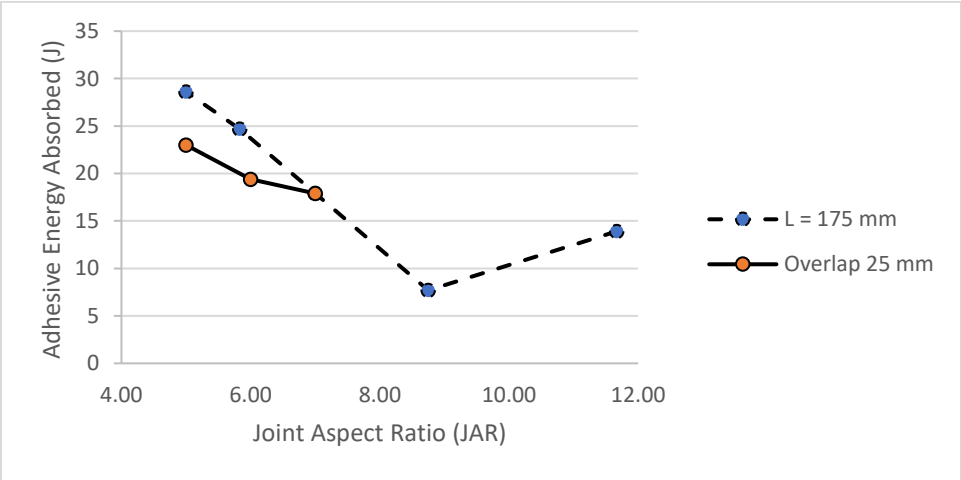

(c)

Figure 4.18 Crush performance results as a function of joint aspect ratio for 40 mm crush deformation. For L=175 mm curve, overlap length varies from 15 – 35 mm and for overlap length 25 mm curve L = 125, 150 and 175 mm.

4.4.3 Effect of Tube Thickness

To consider the effect of tube thickness on the crush performance of tubular joints, a study is first conducted with inner and outer tubes of equal thickness. The tube thickness is varied from 1.2 to 2.4 mm. A comparison of force-displacement plots for different tube thicknesses and 25 mm overlap is shown in Figure 4.19. With increasing tube thickness, the force required for the aluminum tubes to yield and plastically deform increases and the adhesive fails prior to yielding of the aluminum tubes, resulting in very low energy absorption. Alternatively, when the adhesive does not fail first, higher thickness tubular joints show global buckling compared to lower thickness tubes that show a greater degree of folding under crush. For these tube thicknesses, the energy absorption is high, but the peak load is low. The results of this study are plotted in Figures 4.20 (a) and (b), in which an increasing trend in peak load and a decreasing trend in energy absorption with increasing thickness can be observed.

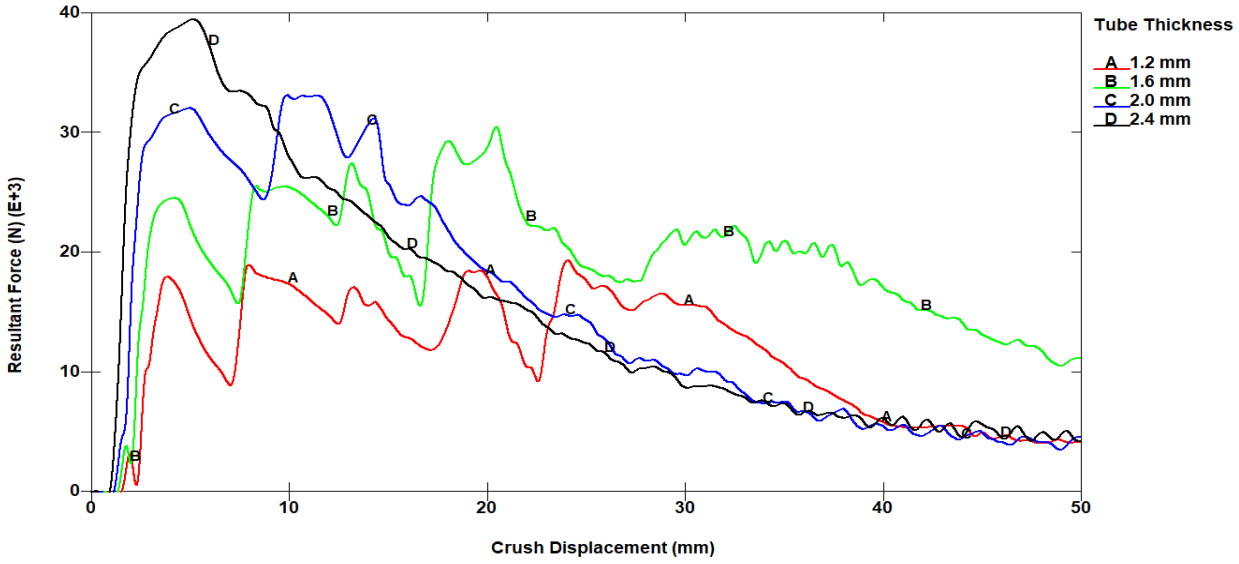

Figure 4.19 Force-displacement plot for two joints with 25 mm overlap, same tube length and diameter. Inner and outer tubes are of same thickness.

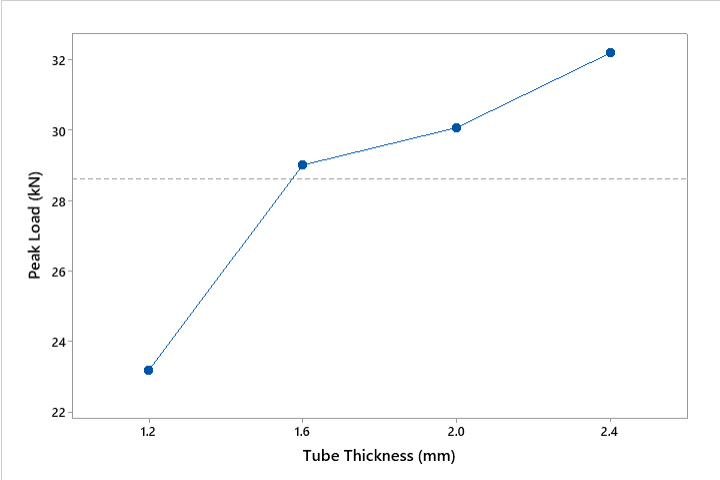

(a)

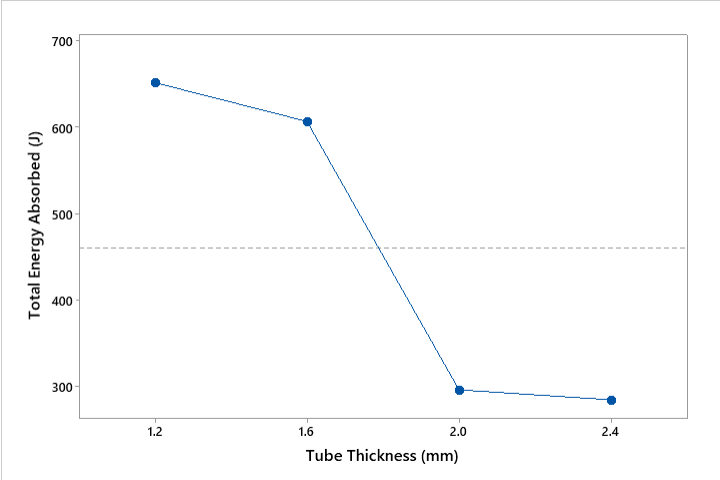

(b)

Figure 4.20 Variation of peak load (a) and total energy absorbed (b) with tube thickness. (L = 175 mm, d_m = 26.46 mm)

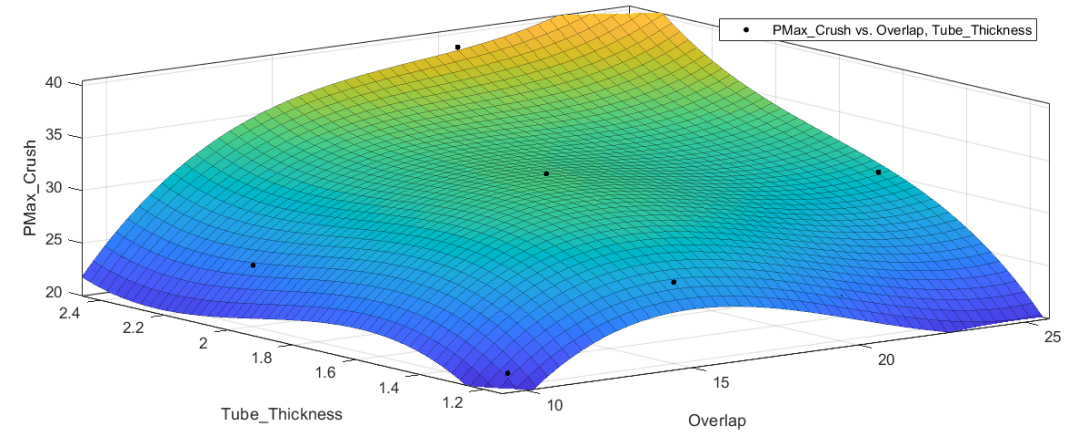

(a)

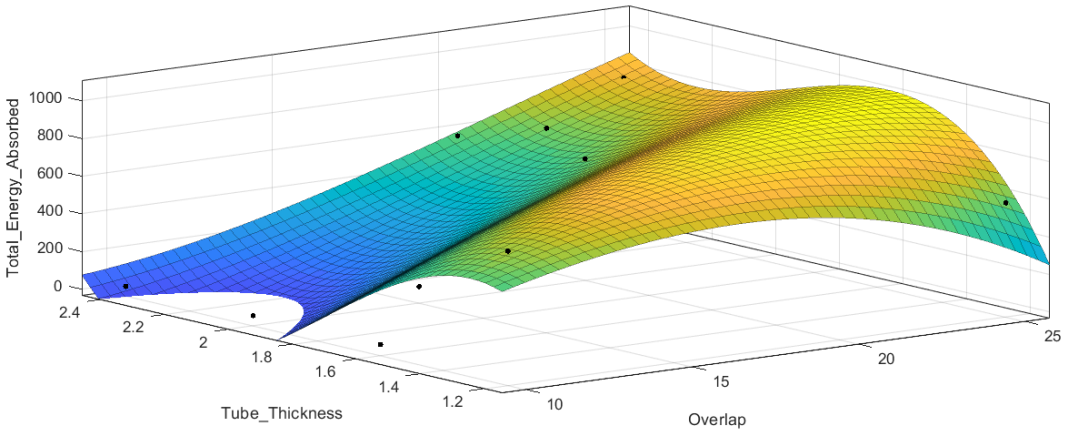

(b)

Figure 4.21 Response surface for peak load (Pmax_Crush) (kN) and total energy absorbed (J) during crush for different tube thickness and overlap lengths in mm.

Tube thickness and overlap length have a significant influence on crush performance. To predict performance under compressive load for the different joint configurations, a polynomial response surface is fit to the data. Responses of peak load and energy absorption are plotted for different overlap length and tube thickness values. Figure 4.21 (a) and (b) show the response surfaces for the peak load and total energy absorbed by the joint under crush, respectively. Empirical equations describing the response surfaces are given in Equations 4.3 and 4.4.

$$PMax\_Crush = -185.3 + 14.37x + 221.2y - 0.7605x^2 - 0.782xy - 118.8y^2 + 0.01227x^3 - 0.02x^2y + 0.275xy^2 + 20.31y^3 \quad \text{Eq. 4.3}$$

$$Total\_Energy\_Absorbed = -6478 - 70.07x + 13790y - 4.802x^2 + 225.4xy - 9462y^2 - 0.0891x^3 + 4.311x^2y - 91.25xy^2 + 2022y^3 \quad \text{Eq. 4.4}$$

where x is overlap length and y is tube thickness. Both variables are in mm. PMax is the peak crush load and TotE is the total energy absorbed by the joint under crush loading. The empirical equations have a R-sq value of 0.936 and 0.81 respectively.

Among the four tube thicknesses considered so far, 1.6 mm produces high energy absorption as well as a relatively high peak load. Therefore, it is selected as the reference thickness in the next study in which the joints consist of tubes of different thicknesses. The next study on effect of tube thickness considers the inner and outer tube thickness combinations of 1.2-1.6, 1.6-1.6 and 1.6-1.2; correspondingly, the thickness ratios (ti/to) are 0.75, 1 and 1.33. Results of varying combinations of thickness is shown in Figure 4.22. For comparison, 1.2-1.2 mm thickness combination with thickness ratio of 1 is also included. Joints with unequal thickness and joint with lower thickness is seen to exhibit some form of folding type deformations. The load-time curves indicate that the inner tube thickness plays a greater role in load carrying capacity of the joint as both joint configurations with 1.6 mm inner tube thickness show similar first peak. However, once folding initiates in the inner tube, the load carried by the joint is similar to the other joint configurations while the joint with both 1.6 mm tubes undergo buckling and a gradual decrease in load vs time.

Figure 4.23 illustrates deformation modes of the different tubular joint configurations. The reference joint with 1.6 mm tubes shows global buckling. Reducing thickness of inner tube shows no major change in crush mode. But reducing outer tube thickness keeping inner tube at 1.6 mm results in wrinkling and folding in outer tube along with global buckling. When both tubes have lower thickness of 1.2 mm, both inner and outer tubes show folding along with global buckling.

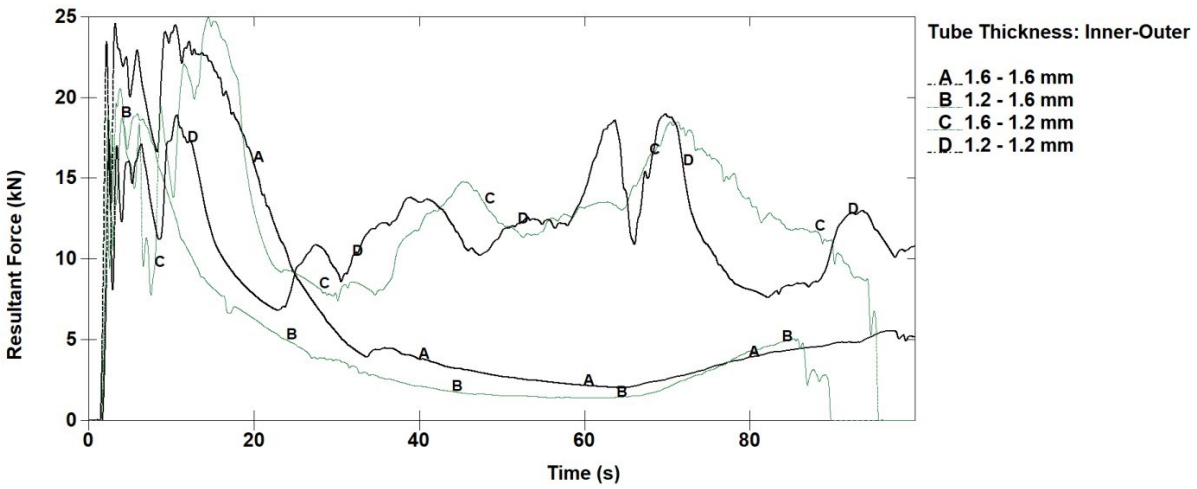

Figure 4.22 Comparison of force-time plots for joints with different tube thicknesses.

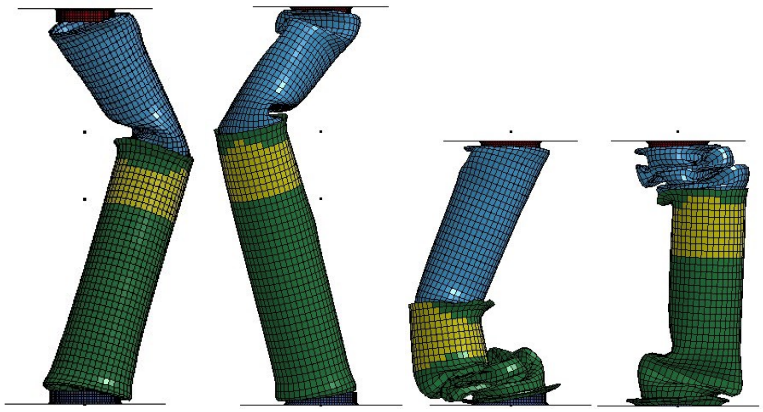

(a) 1.6-1.6 (b) 1.2-1.6 (c)1.6-1.2 (d) 1.2-1.2

Figure 4.23 Deformation of joints with different tube thickness combinations. (Top tube thickness – bottom tube thickness in mm)

Figure 4.24 plots total energy absorbed, adhesive energy absorbed and peak load versus tube thickness ratios. The overlap length and the tube lengths are 25 mm and 175 mm, respectively. And, for thickness ratio 1, the tube thickness is 1.6 mm. From the force data at the first peak, we can see the influence of inner tube thickness. Higher inner tube thickness results in higher first peak force. This corresponds with results in Figure 4.24 (a). Both figures 4.24 (b) and 4.24 (c) show that total energy absorbed by specimen and energy absorbed by adhesive are greatly affected by tube thickness and thickness ratio.

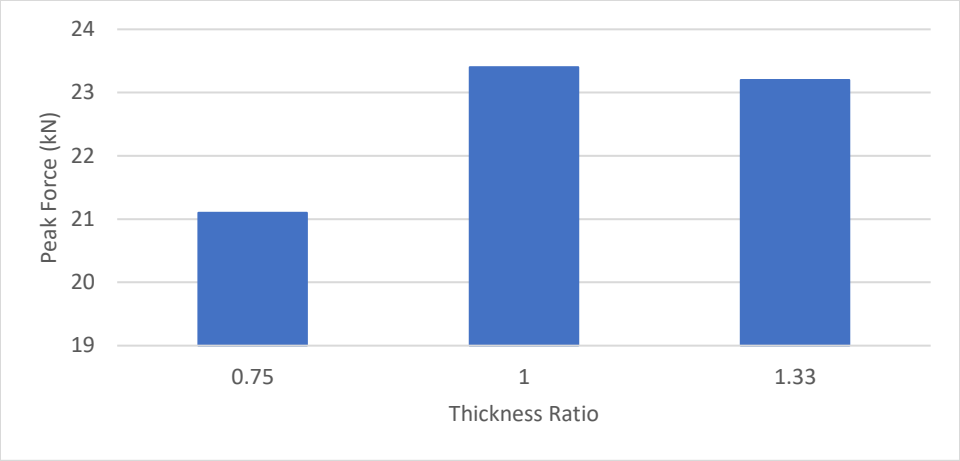

(a)

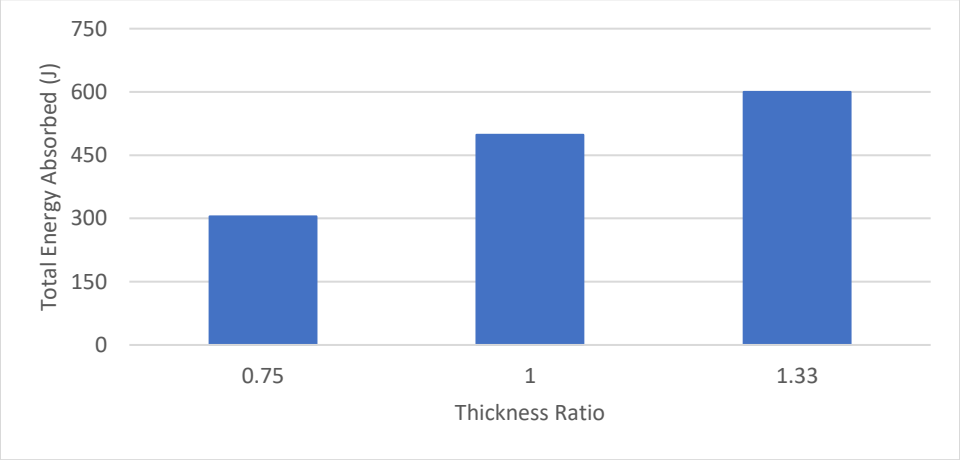

(b)

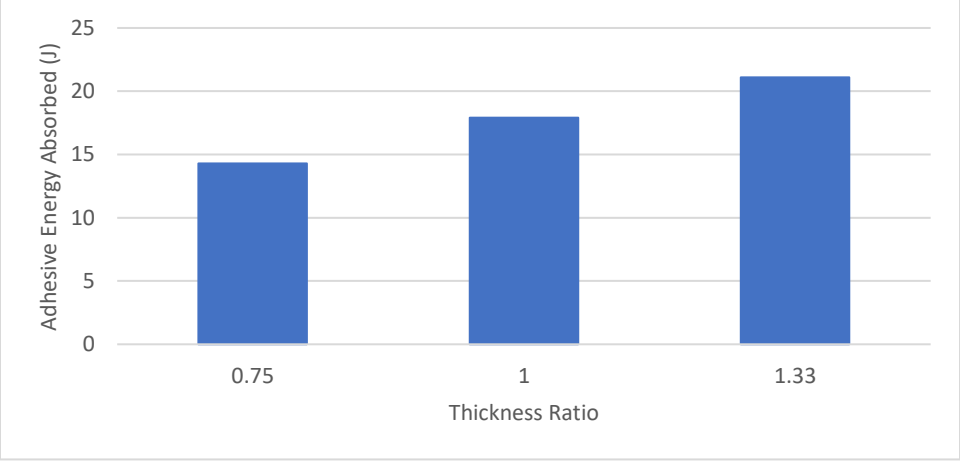

(c)

Figure 4.24 (a) Peak load, (b) Total energy absorbed by the joint and (c) Energy absorbed by adhesive for different tube thicknesses ratios (ti / to). Tube thickness ratios of 0.75, 1 and 1.33 correspond to inner and outer tube thickness combinations of 1.2-1.6, 1.6-1.6 and 1.6-1.2 mm.

4.4.4 Effect of Tube Length

The third geometric variable considered is the tube length. Any change in tube length affects the free length of the specimen and also the overall length of the specimen. While linear elastic analysis of adhesive stresses presented in Chapter 2 shows no influence of tube length on the adhesive stress distributions, it is one of the factors that control the deformation behavior of thin-walled tubes under compressive load.

Three joint lengths 125, 150 and 175 mm were considered with 25 mm adhesive overlap. The joints showed global buckling as the final failure mode, however with decreasing length, there is greater wrinkling and folding deformation in tubes prior to buckling.

The tube length parameter is presented as a ratio of inner tube length to outer tube length (L_i/L_o). For the same overlap length of 25 mm, equal tube thickness of 1.6 mm and joint length of 150 mm three different length ratios are considered: 0.75, 1 and 1.33 corresponding to inner tube-outer tube lengths of 75-100, 87.5-87.5, and 100-75 mm. Figure 4.25 plots crush characteristics versus ratio of inner tube length to outer tube length. All joints showed global buckling with partial adhesive failure. However, for the same joint length, joint with L_i/L_o =1 showed the highest peak load during crush while joint with length ratio 1.33 showed the highest energy absorption.

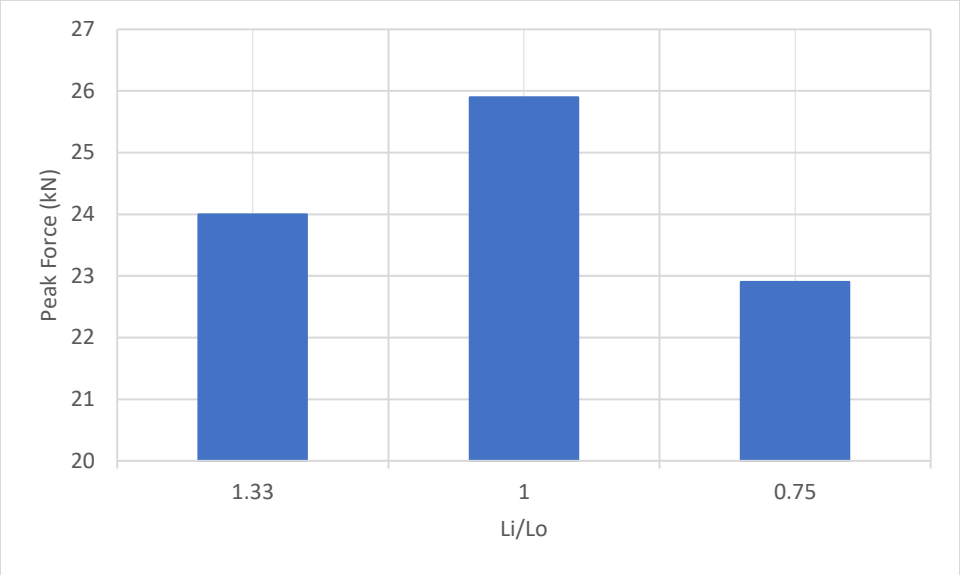

(a)

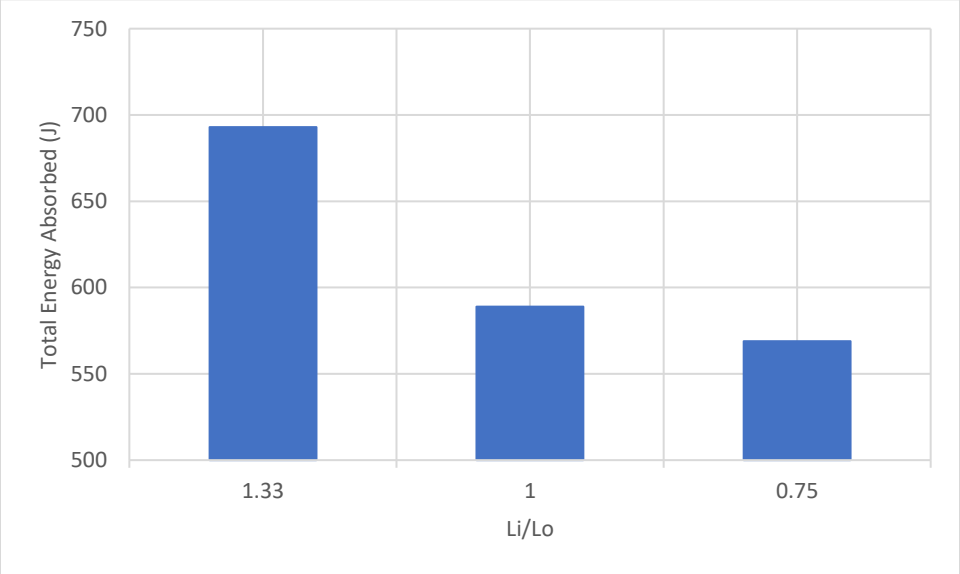

(b)

Figure 4.25 Crush characteristics, (a) Peak Force and (b) Total energy absorbed up to crush displacement of 40 mm for 150 mm specimens with 25 mm overlap length and equal tube thickness of 1.6 mm

The above discussion on finite element analysis results mostly focused on one variable at a time but results in Table 4.5 which include multi-parameter specimens show that considering more than one parameter at a time changes the nature of joint crush. For better understanding of

the influence of these parameters, a Design of Experiments (DOE) approach is used to determine the main effects and interactions between them.

4.5 Design of Experiments: Analysis of the Effects of Joint Design Variables

Discussed in the previous sections are the important geometric variables that influence crush characteristics of tubular lap joints in aluminum. However, analyzing the effects of geometric variables one factor at a time is inefficient and may not provide conclusive results. Hence, a Design of Experiments (DOE) approach is used in this section in which the effects of two or more variables and interactions between them are considered.

Design of Experiments (DOE) [63], a branch of applied statistics, is a powerful tool used for data collection and analysis of experimental results. DOE provides a methodology for planning, analyzing, and interpreting controlled experiments to evaluate independent factors affecting an outcome or a set of outcomes. Multi-factor analysis of variance is conducted in DOE to identify important interactions and rank main effects by manipulating multiple variables at a time. Further, results of the analysis of variance provides insight into the optimization of experimental variables.

The DOE approach to experimental design is implemented using Minitab 18 statistical software. The software tool provides for different DOE designs such as fractional factorial, full factorial, and Taguchi methods. As discussed in previous sections, results in Table 4.4 indicate varied response to different tube length and thickness ratio. Hence, a fractional factorial design which accepts only two levels for each variable cannot be implemented to accurately represent the data. While both Taguchi methods and full factorial design provide for multi-level multi-factorial analysis, full factorial design is implemented in this study due to ease of its application.

4.5.1 Effect of Joint and Tube Geometry

An experiment is designed to understand the effect of bond overlap lengths, tube thickness ratios, and tube length ratios for a given reference configuration of 175 mm long joint bonded with Betamate 1496 adhesive. The outer diameter of top tube is 25.4 mm and outer diameter of bottom tube is 30.84 mm. The adhesive thickness is 1.06 mm. A full factorial implementation of this experiment with two 3-level factors and one 2-level factor requires 18 experiments as listed in Table 4.5. The details of tube length, tube thickness and overlap length for each simulation is listed in Table 4.6. The Minitab 18 software provides Pareto, main effects, and interaction plots to analyze the responses, which in this study are the peak load and the energy absorption. The results are recorded up to 100 mm displacement of top plug. The range of data is increased to record more details of tube deformation. In addition, energy absorbed by the adhesive is also analyzed in these simulations.

Table 4.6 Variables and Levels for full-factorial simulation design.

Variables	Levels		
Overlap (mm)	25	35	
Tube Length Ratio (Li/Lo)	0.75	1	1.33
Tube Thickness Ratio (ti/to)	0.75	1	1.33

Table 4.7 Values of tube length, tube thickness and overlap length for different joint configurations.

Li	Lo	Li/Lo	ti	to	ti/to	Overlap (mm)
85	115	0.75	1.2	1.6	0.75	25
90	120	0.75	1.2	1.6	0.75	35
85	115	0.75	1.6	1.6	1	25
90	120	0.75	1.6	1.6	1	35
85	115	0.75	1.6	1.2	1.33	25
90	120	0.75	1.6	1.2	1.33	35
100	100	1	1.2	1.6	0.75	25
105	105	1	1.2	1.6	0.75	35
100	100	1	1.6	1.6	1	25
105	105	1	1.6	1.6	1	35
100	100	1	1.6	1.2	1.33	25
105	105	1	1.6	1.2	1.33	35
85	115	1.33	1.2	1.6	0.75	25
90	120	1.33	1.2	1.6	0.75	35
85	115	1.33	1.6	1.6	1	25
90	120	1.33	1.6	1.6	1	35
85	115	1.33	1.6	1.2	1.33	25
90	120	1.33	1.6	1.2	1.33	35

Pareto charts obtained from analyzing the full factorial data provides a preliminary view of important factors or combination of factors. The standardized effects of different factors are plotted. Figure 4.26 shows the effects Pareto for (a) peak load (PMax), (b) total energy absorbed (TotE) and (c) energy absorbed by the adhesive (AdhE). The dotted line is a reference value which denotes significance level for the analysis and is one minus confidence level. A comparison of standardized effects with reference line helps indicate variables with significant influence on outcome. The plots indicate overlap length as the main factor in influencing all three joint behaviors. Pareto chart for peak load in Figure 4.26 (a) also indicates significant influence of the interaction between tube thickness ratio and length ratio, and the factor of tube length ratio itself. The tube thickness ratio and length ratio do not much influence on either joint or adhesive energy absorptions.

For a detailed understanding of the nature of interactions between different factors we look at the main effects and interaction plots. Figures 4.27 – 4.29 illustrate the main effects and interaction plots for peak load, total energy absorbed, and adhesive energy absorbed, respectively. Since at each level multiple results are available, the mean value is plotted. Examining the plots there is no significant interaction between variables for energy absorbed by joint or adhesive, but for peak load there is significant interaction between tube length ratio and thickness ratio. Joint configuration of thinner top tube and shorter top tube has the worst peak load, but joint with thinner top tube and longer top tube has the best peak load. This is due to change in mode of deformation from buckling with longer outer tubes to folding/wrinkling with shorter outer tubes. The modes of deformation for different joint configurations are illustrated in Figure 4.30. Joints with equal tube thickness tend to buckle while ones with unequal thickness show some degree of folding in tubes. Also, joints with longer overlap length show less buckling type deformation.

Examining the results, to maximize peak load the best joint configuration is with tube length ratio of 1.33, thickness ratio of 1 and overlap of 35 mm. Highest energy absorbed by the structure is with a configuration of length ratio 1.33, thickness ratio 0.75 and overlap length 35 mm. To maximize both outcomes, response optimizer tool is used to provide a statistical analysis of the data. The tool indicates a joint configuration with Li/Lo = 1.33, ti/to = 0.75 and overlap length 35 mm as the best configuration for maximum peak load and energy absorption.

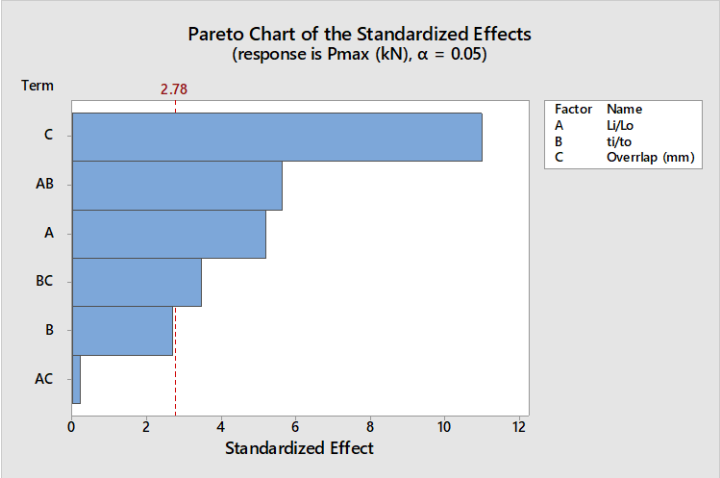

(a)Peak Force

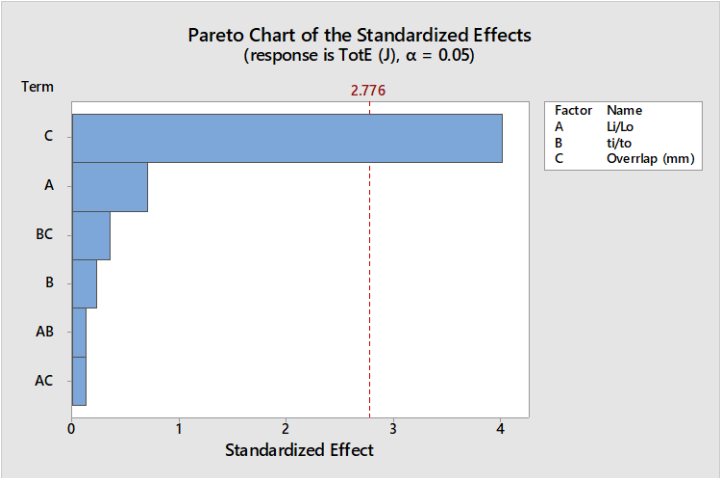

(b)Total Energy Absorbed

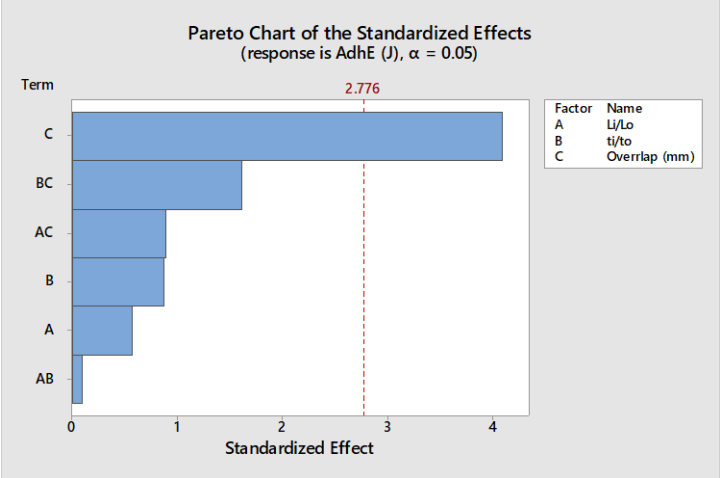

(c)Adhesive Energy absorbed.

Figure 4.26 Pareto plots of tube geometry and overlap study simulation results for (a)peak load, (b) total energy absorbed and (c) adhesive energy absorbed.

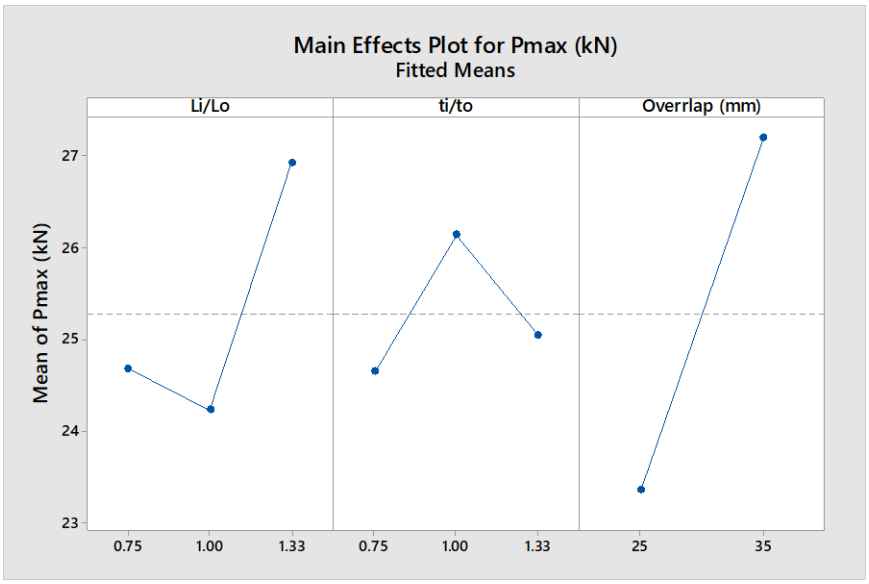

(a)

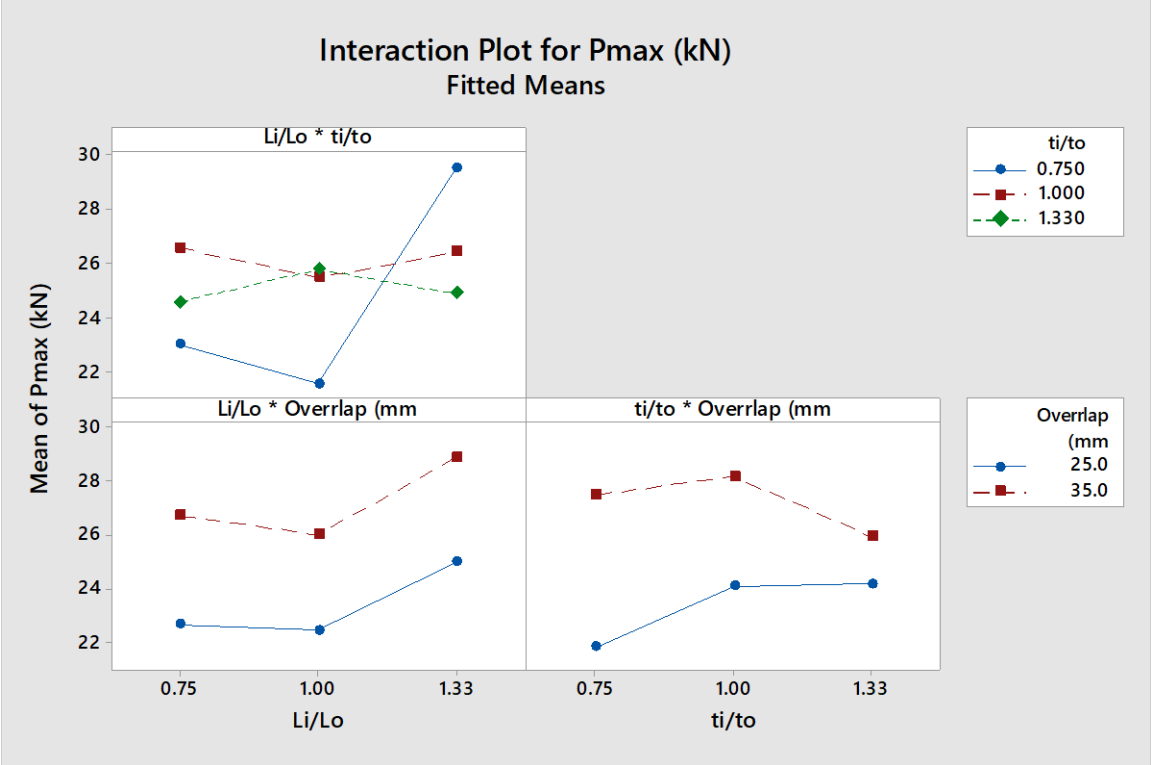

(b)

Figure 4.27 (a) Main effects and (b) interaction plots for peak load (PMax).

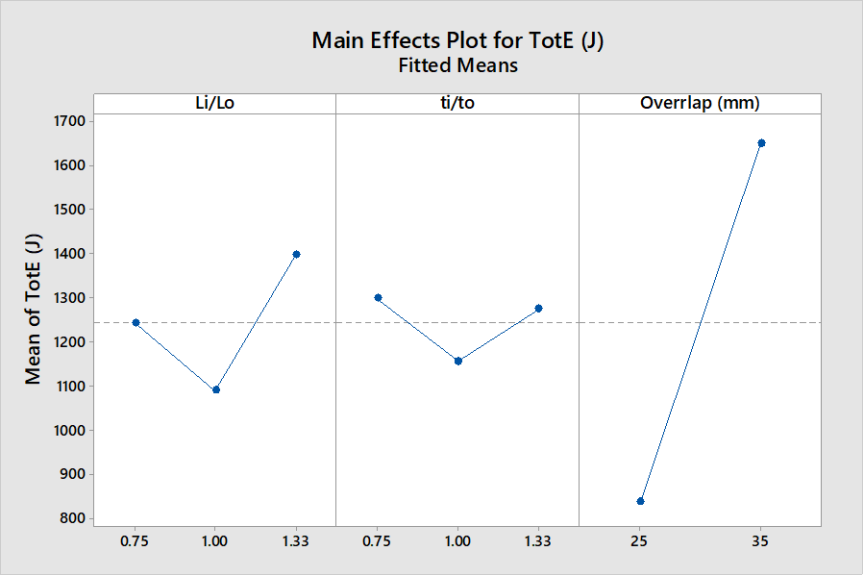

(a)

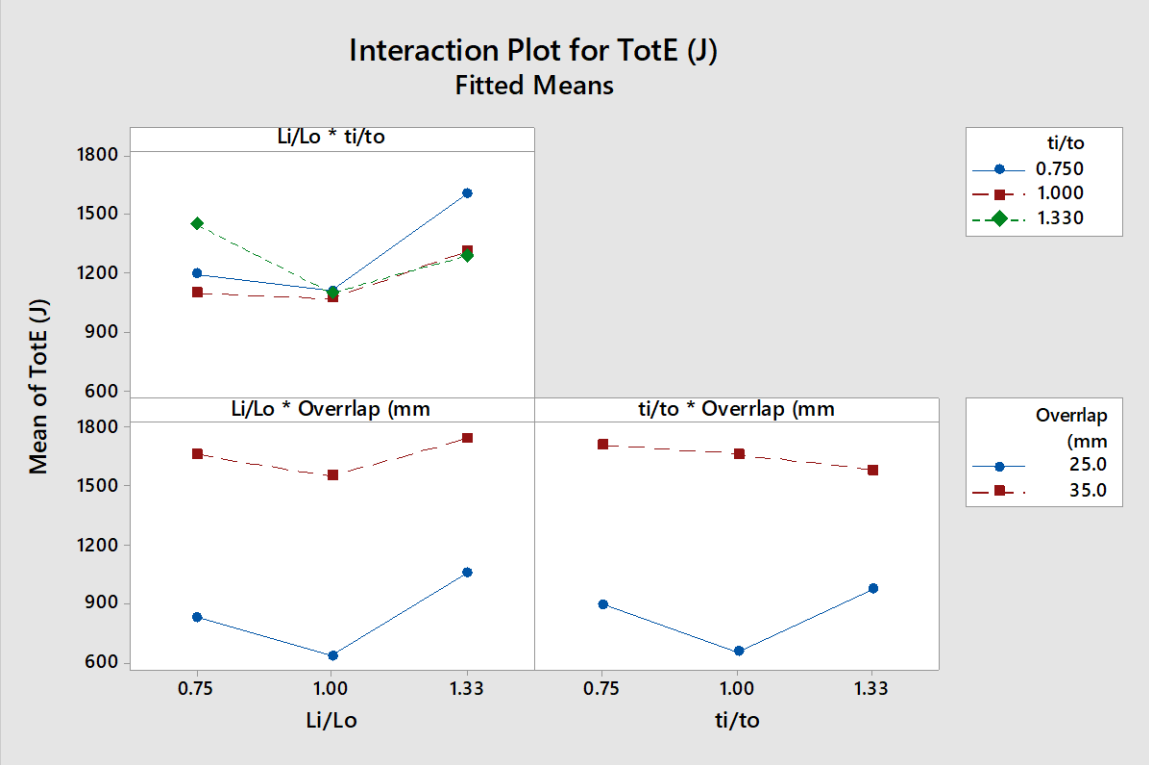

(b)

Figure 4.28 (a) Main effects and (b) interaction plots for total energy absorbed by structure.

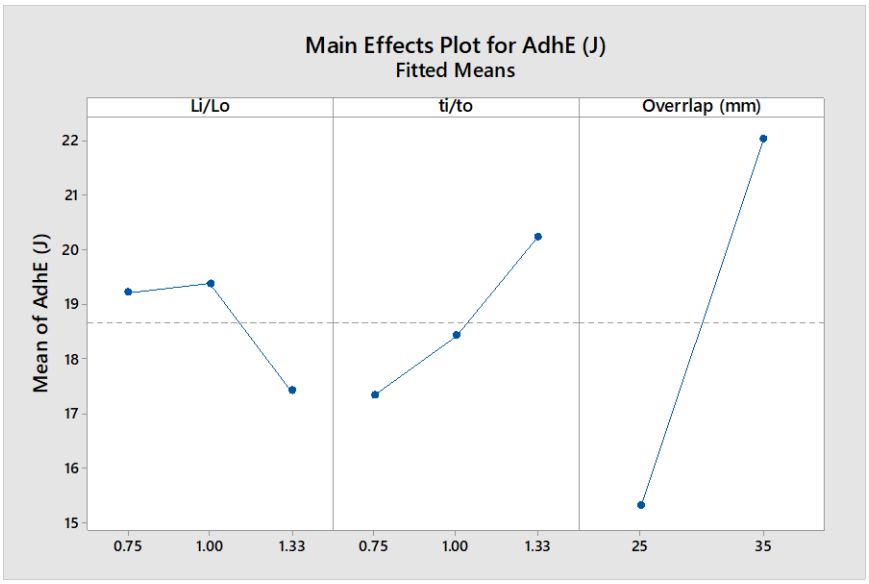

(a)

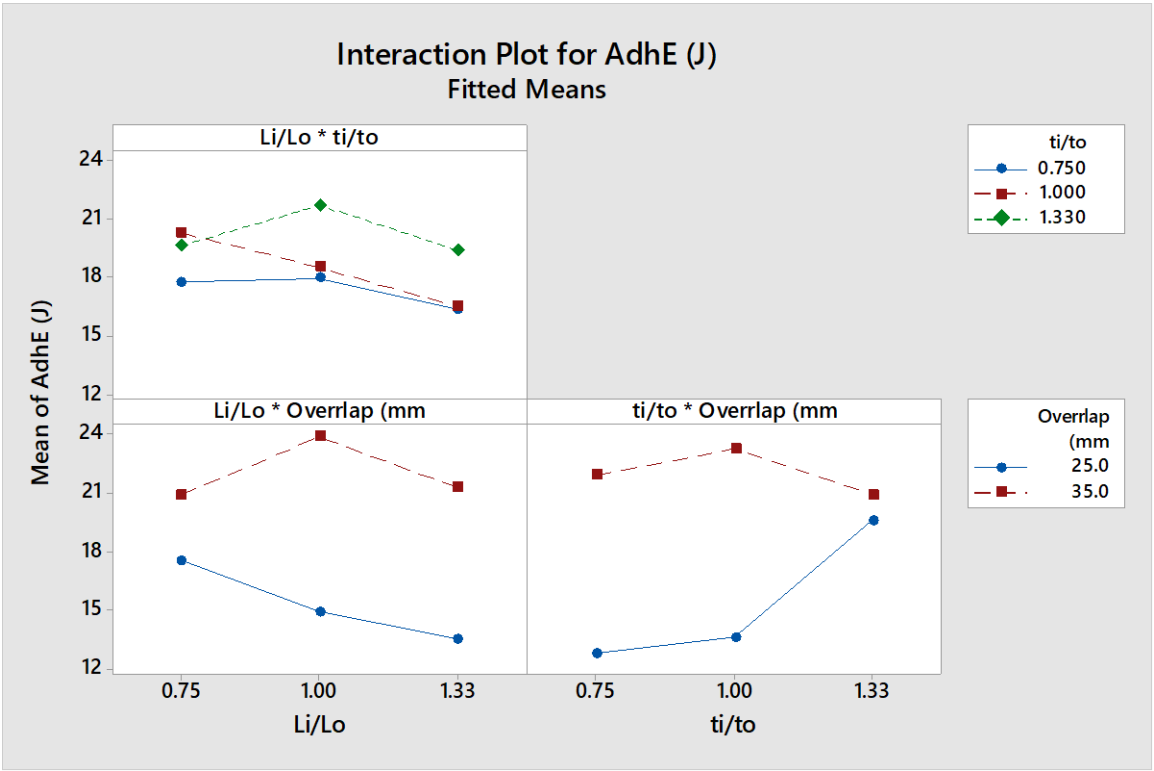

(b)

Figure 4.29 (a) Main effects and (b) interaction plots for energy absorbed by adhesive.

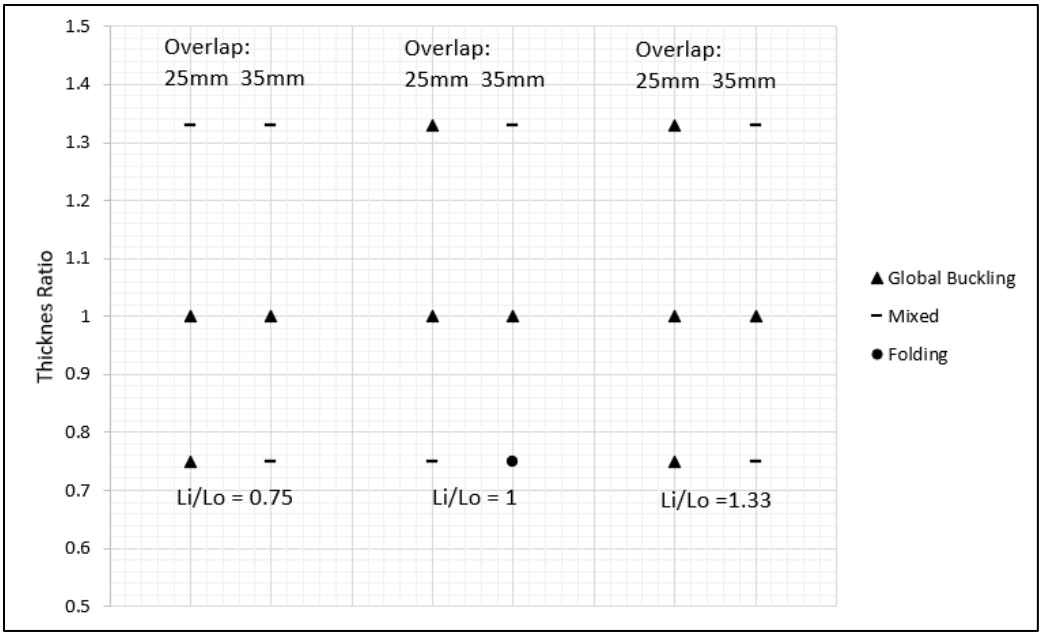

Figure 4.30 Deformation modes for different tube length and thickness ratios, L_i/L_o and t_i/t_o, having 175 mm joint length and 26.46 mm mean diameter. Mixed mode is folding followed by global buckling.

Figures 4.31 and 4.32 plot the response surfaces for the peak load and total energy absorbed by joints with 25 mm and 35 mm overlap. The response surfaces are plotted to show the effects of tube thickness ratio and tube length ratio on these two crush characteristics. Equations for the response surfaces are given below along with goodness of fit values.

$$PMax\_25Ov = -4.867 - 7.401x + 54.48y + 14.44x^2 - 18.19xy - 15.28y^2 \quad \text{Eq. 4.5}$$

Goodness of fit: R-square: 0.6667

$$TotE\_25Ov = 2409 - 2189x - 1969y + 3565x^2 - 4710xy + 3335y^2 \quad \text{Eq. 4.6}$$

Goodness of fit: R-square: 0.8733

$$PMax\_35Ov = 8.744 - 17.28x + 51.85y + 19.8x^2 - 19.65xy - 16.5y^2 \quad \text{Eq. 4.7}$$

Goodness of fit: R-square: 0.6593

$$TotE\_35Ov = 4815 - 4882x - 1344y + 1753x^2 + 1339xy - 119y^2 \quad \text{Eq. 4.8}$$

Goodness of fit: R-square: 0.6287

where, x represents thickness ratio and y is the length ratio.

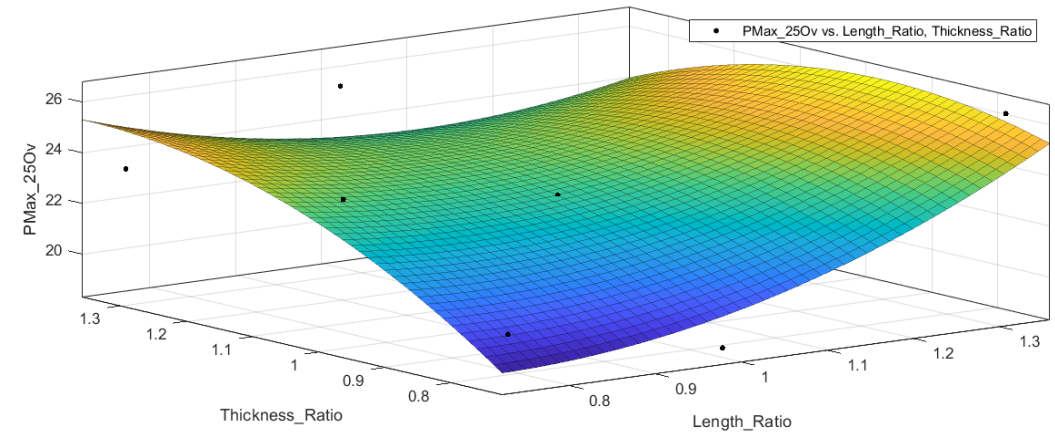

(a)

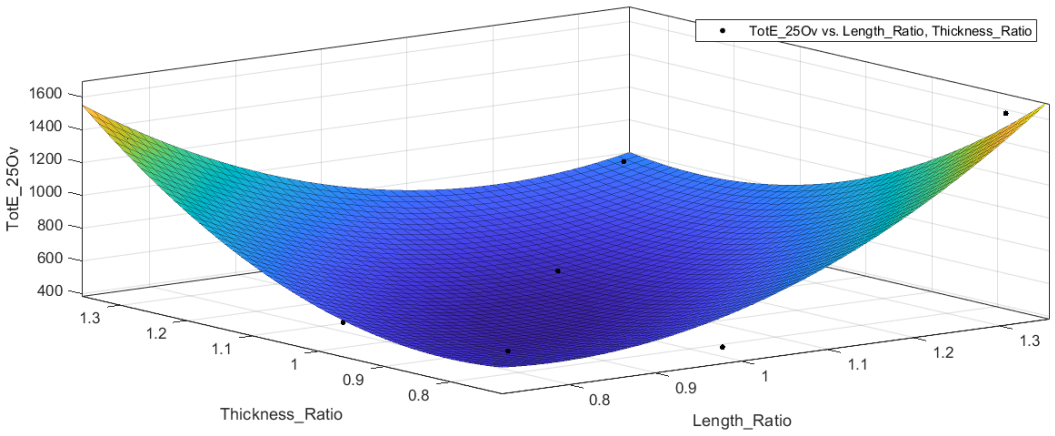

(b)

Figure 4.31 Response surface for (a) peak load (kN) and (b) total energy absorbed by joints (J) for different tube thickness and length ratios in joints with 25 mm overlap.

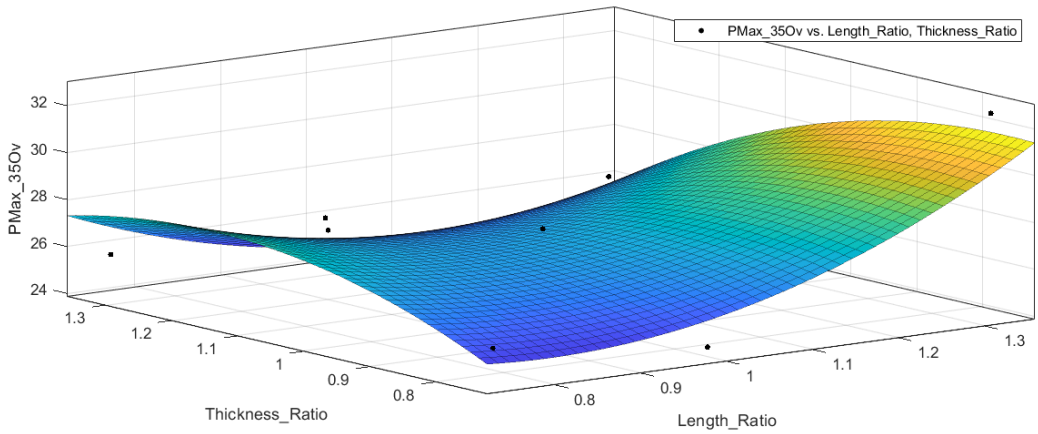

(a)

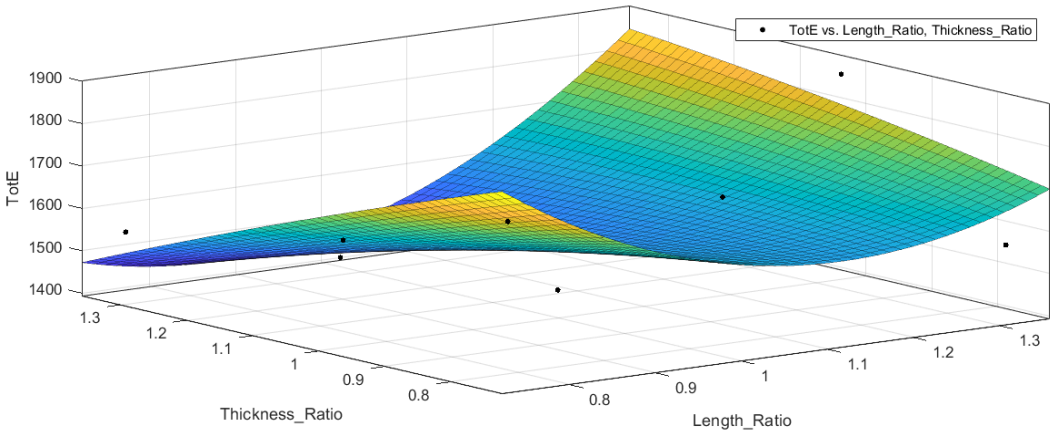

(b)

Figure 4.32 Response surface for (a) peak load (kN) and (b) total energy absorbed by joints (J) for different tube thickness and length ratios in joints with 35 mm overlap.

Adhesive thickness is an important parameter to be considered for the design of any bonded joint which is not included in the previous DOE. To understand the influence of adhesive thickness on the crush performance of the tubular structure, additional simulations are conducted with a higher adhesive thickness of 1.5 mm in addition to the reference 1.06 mm thickness. The adhesive thickness is now considered an additional variable in the DOE analysis of the joint geometry with two levels of 1.06 mm and 1.5 mm. With the inclusion of adhesive thickness, the full-factorial design requires an additional 18 simulations. This helps to check for interaction between bond thickness and tube thickness ratio, length ratio and overlap length.

Pareto charts for peak load, total energy absorbed, and adhesive energy absorbed are illustrated in Figure 4.33. These charts also indicate standard effects of up to third order interactions between the variables. The Pareto charts show that both overlap length and adhesive thickness are the leading factors affecting crush response. Peak load is affected by several variables as indicated by the reference line such as adhesive thickness, overlap length and interaction between thickness ratio and adhesive thickness. Main effects and interaction plots for peak load are shown in Figure 4.34. Higher overlap length results in higher peak load while higher adhesive thickness reduces peak load. The interaction plot for adhesive thickness and thickness ratio shows that with higher adhesive thickness, a thickness ratio of 1.33. i.e., a higher inner tube thickness greatly reduces peak force during crush. For energy absorbed by the tubular structure, the Pareto plot indicates overlap length followed by adhesive thickness as critical factors. Higher overlap length shows higher total energy absorption, while higher adhesive thickness reduces total energy absorption. This is reflected in main effects and interaction plots for total energy absorption in Figure 4.35.

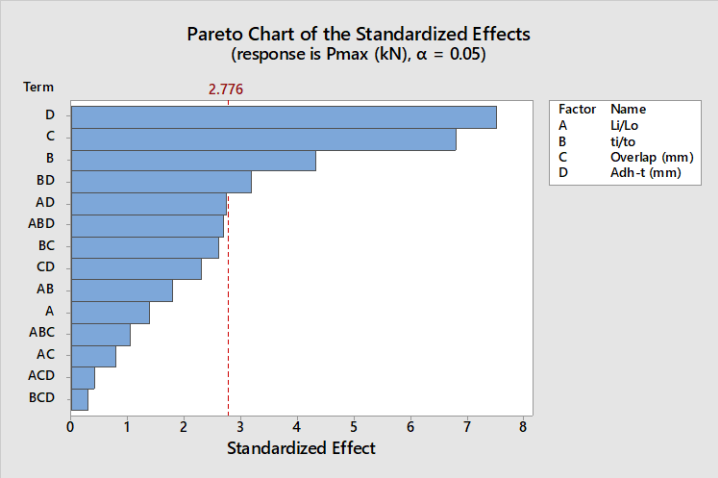

(a) peak load

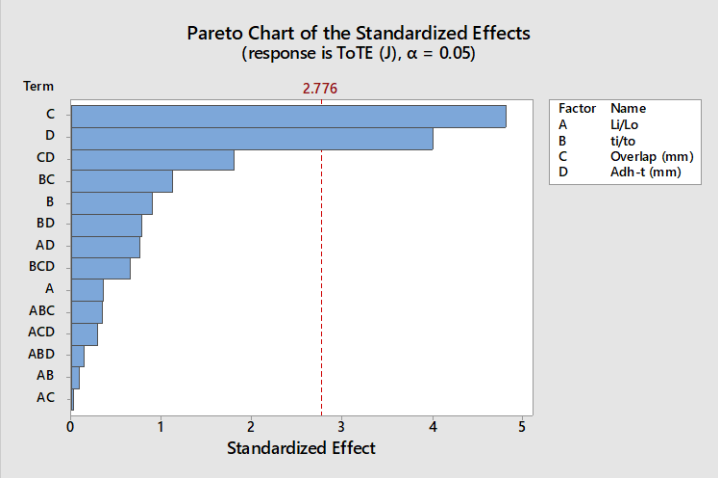

(b) total energy absorbed

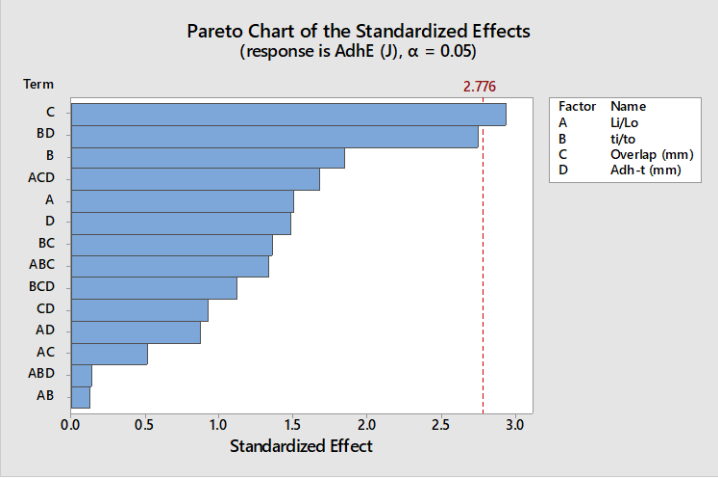

(c) adhesive energy absorbed

Figure 4.33 Pareto plots of tube geometry and overlap study simulation results for (a) peak load, (b) total energy absorbed and (c) adhesive energy absorbed.

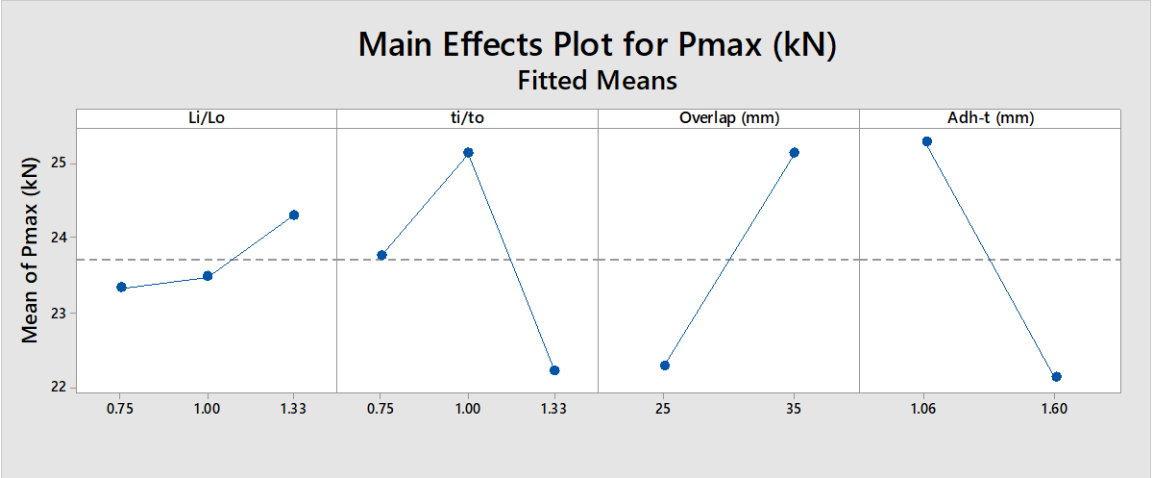

(a)

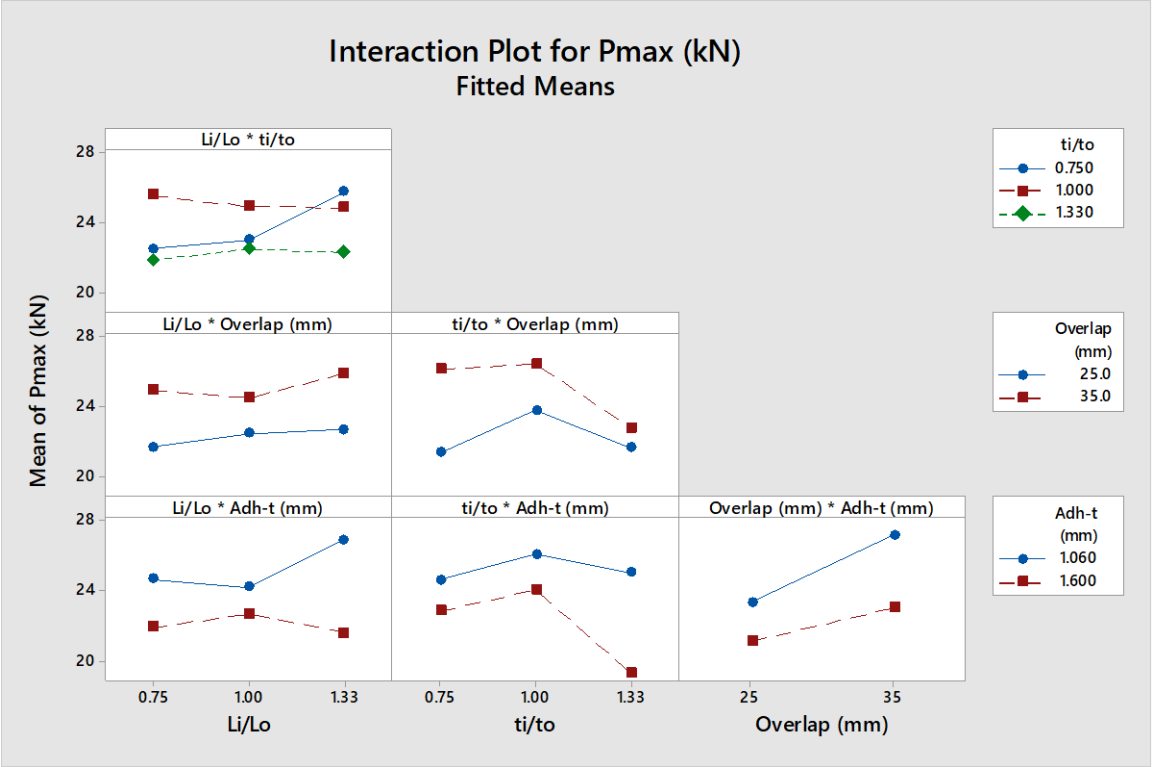

(b)

Figure 4.34 (a) Main effects and (b) interaction plots for peak load during crush.

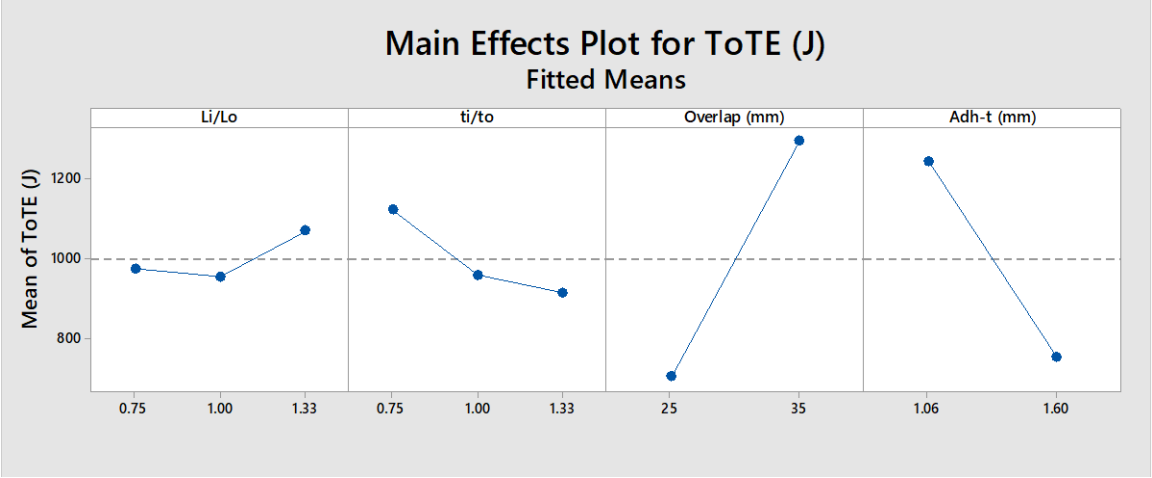

(a)

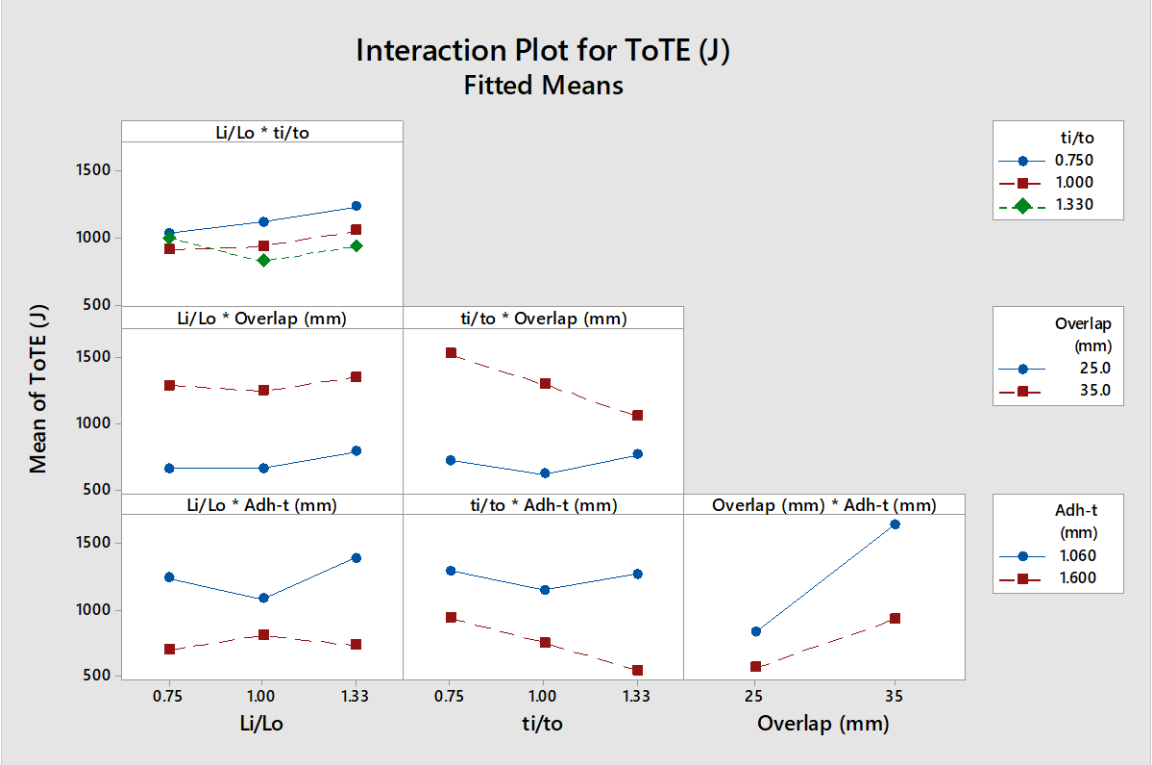

(b)

Figure 4.35 (a) Main effects and (b) interaction plots for total energy absorbed by structure.

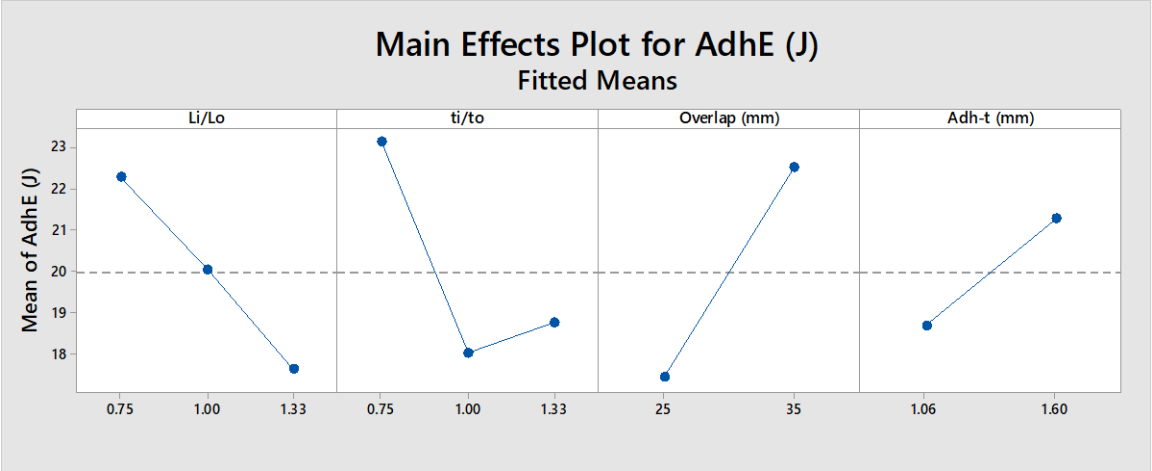

(a)

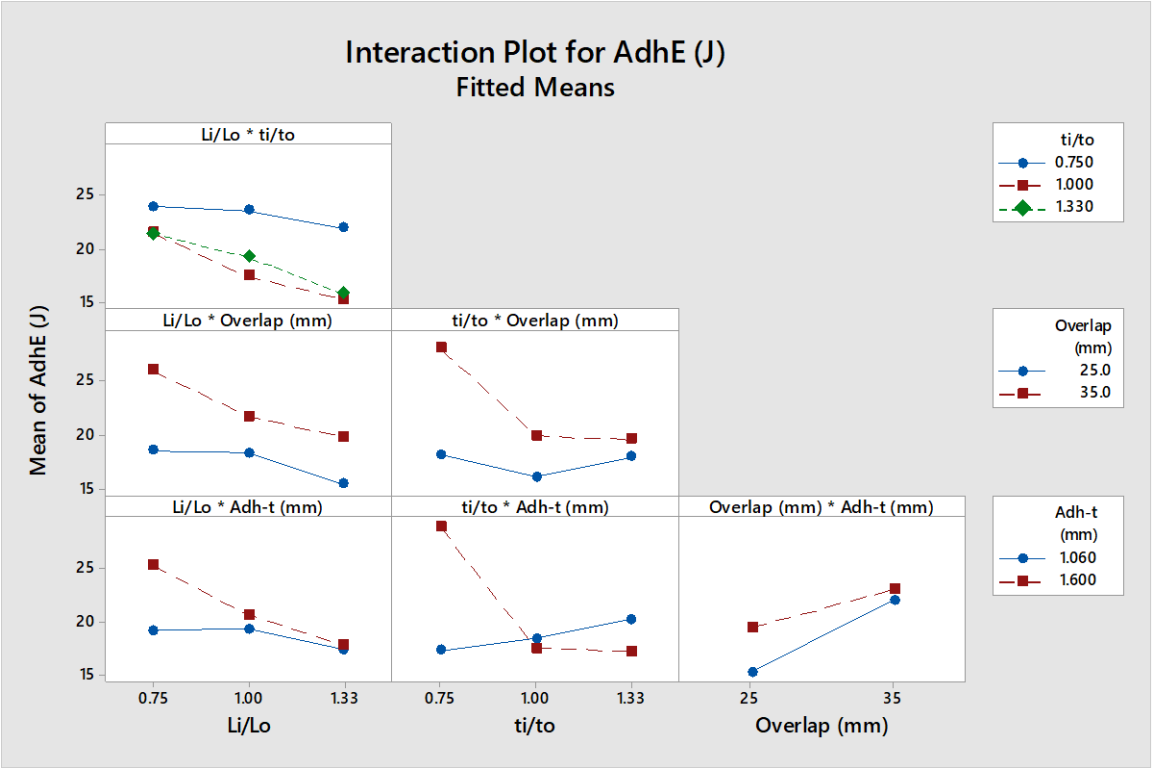

(b)

Figure 4.36 (a) Main effects and (b) interaction plots for energy absorbed by the adhesive.

No significant interaction between adhesive thickness and other variables are observed. In terms of adhesive energy absorption, Pareto plot indicates overlap length as the most significant. While other variables do show an influence, the effects are lower compared to the reference value. The main effects and interaction plots for energy absorption in adhesive are shown in Figure 4.36.

In general, the higher adhesive thickness of 1.5 mm results in reduced crush performance across the board. Interaction between adhesive thickness and other geometry variables do not result in any significant influence on the crush response of the structure. Optimal joint design is as previously discussed with an adhesive thickness of 1.06 mm.

4.5.2 Effect of High-Speed Crush

Studies presented in the previous sections were obtained at a load application rate of 1 mm/s, which can be considered a quasi-static condition. Under crash test conditions, the load application rate is in the range of 1 to 3 m/s. The tubular lap joints considered in this chapter comprises of AA 6061-T4 aluminum tubes and Betamate 1496 adhesive, and both materials show strain rate sensitivity that can affect the crush characteristics of the tubular joints. To understand the effect of strain rate, the downward speed of the top plug is increased to 1 m/s and the results are compared with those at 1 mm/s. The adhesive overlap lengths are 25 and 35 mm at which adhesive failure did not precede the tube deformation in quasi-static simulations. The joint length and mean diameter are 175 mm and 26.46 mm, respectively. The bottom tube length and thickness are selected such that both the tube length ratios (L_i/L_o) as well as tube thickness ratios (t_i/t_o) are 0.75, 1 and 1.33.

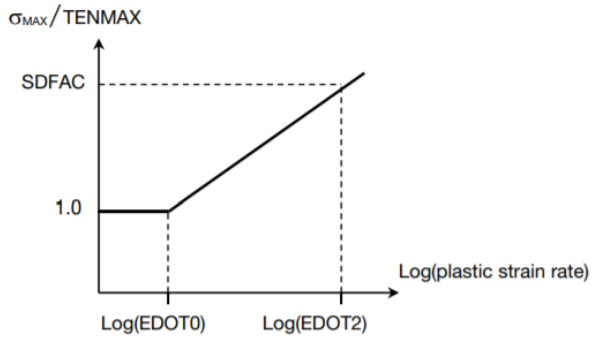

Figure 4.37 Strain rate effect model for adhesive in MAT_ARUP_ADHESIVE [60].

The strain-rate sensitivity of AA 6061-T4 is represented by the following Cowper-Symonds Equation.

$$\sigma_y = 1 + \left(\frac{\dot{\varepsilon}}{C}\right)^{1/p} \quad \text{Eq. 4.9}$$

where, σ_y is yield strength and $\dot{\varepsilon}$ is strain rate. C and p are material constants defined in Table 4.3.

For Betamate 1496, the strain-rate sensitivity is represented by a log-linear curve illustrated in Figure 4.37. EDOT0 represents quasi-static strain rate and EDOT2 represents impact strain rate. The strain rate values are defined as 10^{-4} s^{-1} and 10^{3} s^{-1}, respectively [58]. SDFAC is a scale factor for strength and is given to be 2.5. A similar curve is used for fracture energy and the scale factor is defined as 2.75.

Figures 4.38 and 4.39 illustrate the difference in crush performance at 1 mm/s and 1 m/s. In Figure 4.36, the force-displacement curves are for joints with 100 mm tube lengths, 1.6 mm tube thicknesses and 25 mm overlap length. In Figure 4.39, the force-displacement curves are for joints with 0.75 length ratio, 1.33 thickness ratio and 35 mm overlap length. In both figures it can be observed that the peak load is much higher at 1 m/s than at 1/mm/s, which is due to higher yield strength of the tube material and the adhesive at higher strain rates.

The results of the analysis are represented by the total energy absorbed and peak load diagrams shown in Figures 4.40 and 4.41 respectively. The diagrams compare results at quasi-static and high-speed crush. In none these cases, adhesive failure has occurred, and the joint failure is due to tube folding, buckling or a combination of the two. Increase in crush speed shows an increase in energy absorption across most joint configurations and increase in peak load in all the joints. The results show joint configurations with 25 mm overlap length does not present significant variation in performance. But for 35 mm overlap, changes in length ratio or thickness ratio affect crush performance. Joints with 35 mm overlap and thickness ratio of 1.33 show comparatively poorer performance, particularly with tube length ratio of 0.75. A combination of shorter and thicker inner tube results in buckling prior to any significant folding in either the inner or the outer tube. The highest peak load is when both thickness and length ratios are 0.75, and the highest energy absorption is when the length ratio is 1.33, the thickness ratio is 1 and the overlap length is 25 mm.

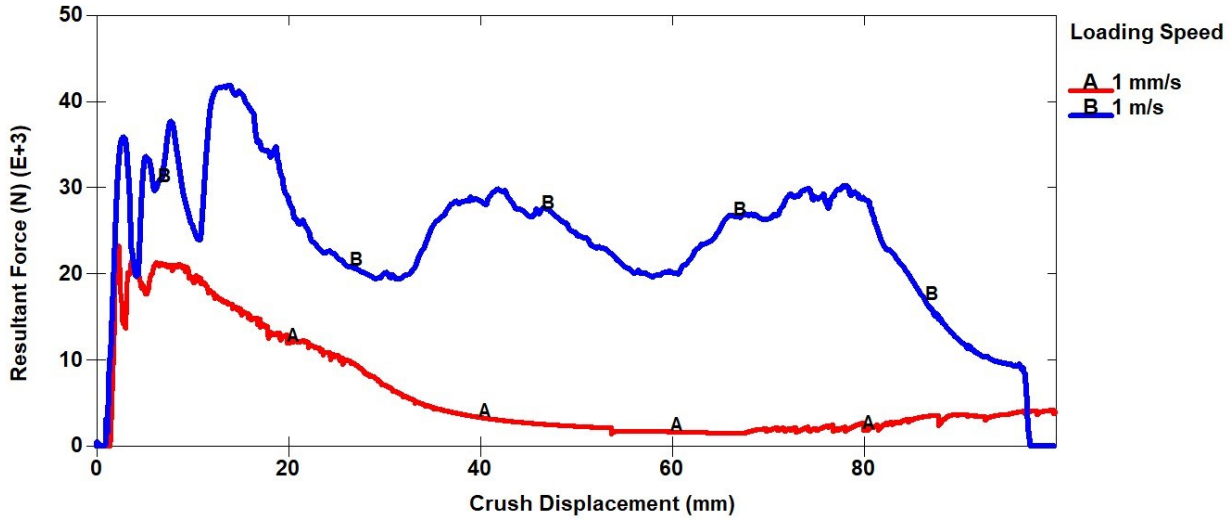

Figure 4.38 Comparison of force-displacement plots at 1 mm/s and 1 m/s for joints with 25 mm overlap and equal tube thickness of 1.6 mm and lengths of 100 mm.

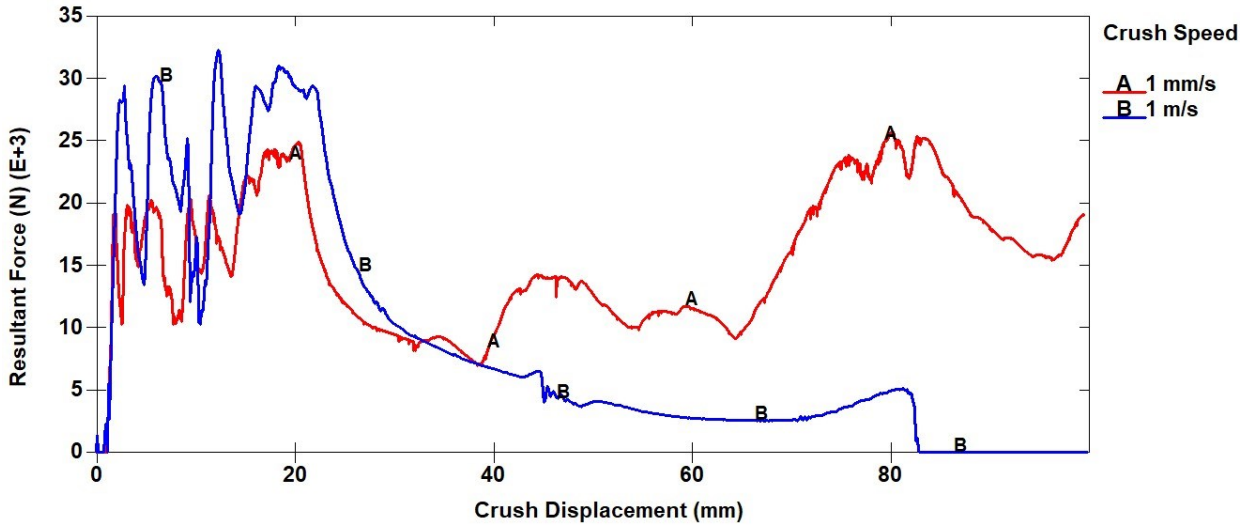

Figure 4.39 Comparison of force-displacement plots at different crush speeds at 1 mm/s and 1 m/s for joints with $L_i/L_o = 0.75$, $t_i/t_o = 1.33$, and 35-mm overlap.

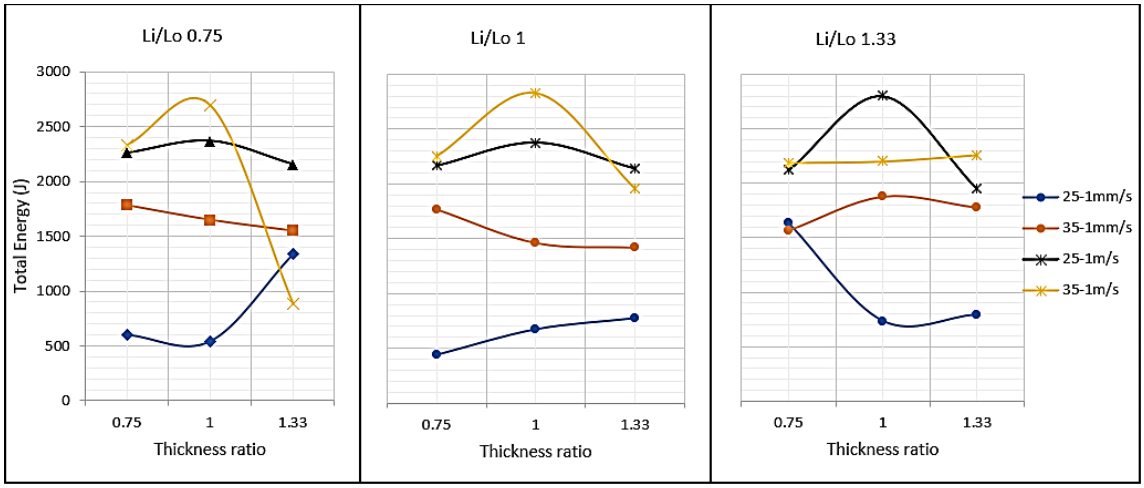

Figure 4.40 Total energy absorbed by tubular joint at different speeds and for different configurations.

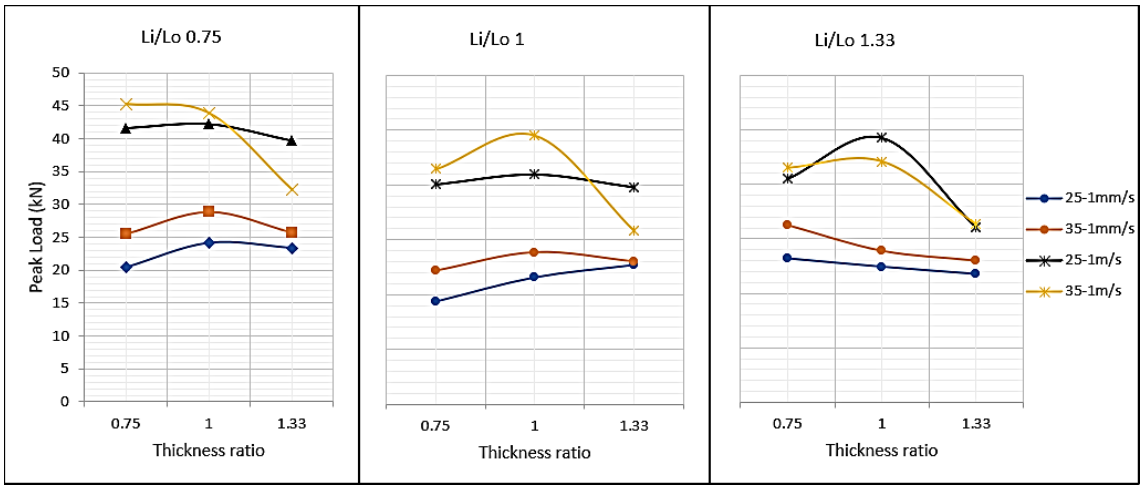

Figure 4.41 Peak load during crush for tubular joint at different speeds and for different configurations.

A set of crush simulations are run at 1 m/s based on DOE-defined full factorial set of 18 simulations. Variables considered are tube thickness ratio, length ratio and overlap length. The levels for each variable and dimensions are as listed in Tables 4.6 and 4.7 respectively. The results of the simulations are illustrated by the Pareto plots in Figure 4.42 and main effects plots in Figure 4.43. At quasi-static speeds, overlap length was the most crucial factor as discussed previously. However, at 1 m/s impact speeds the Pareto plots indicate tube thickness ratio as the most important variable determining the peak load. The same is true for energy absorption, however the effects are not as significant as indicated by the bar plots shorter than the reference line in Figure 4.41 (b). Other geometric variables do not have a significant influence on crush performance.

A closer look at the main effects plot details the influence of tube thickness ratio on crush characteristics. The tubular section shows a drastic decrease in performance with thinner bottom tube. This occurs due to a greater possibility of bottom tube buckling prior to any wrinkling or folding type deformation. Best results are obtained when both tubes are of equal thickness.

Changes in tube length ratio and overlap length do not show much change in crush characteristics.

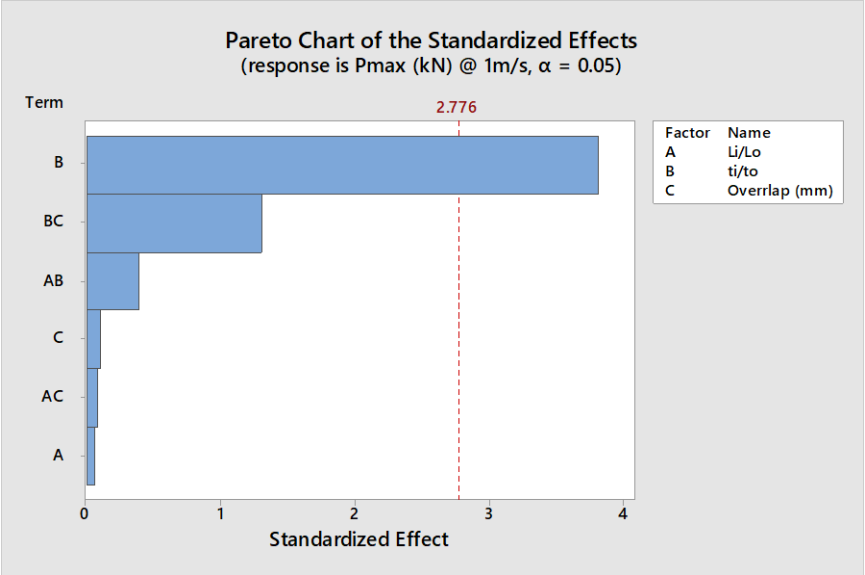

(a)

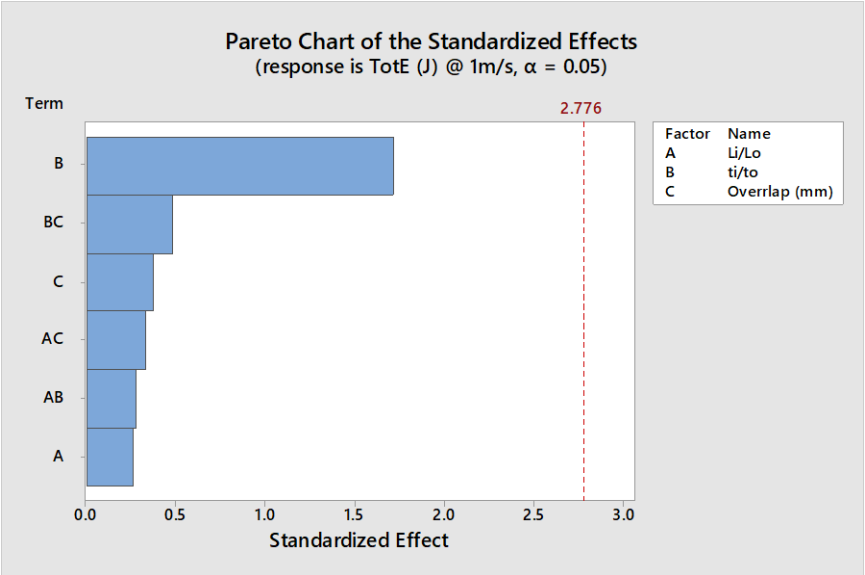

(b)

Figure 4.42 Pareto plots for (a) total energy absorption and (b) peak load at 1 m/s.

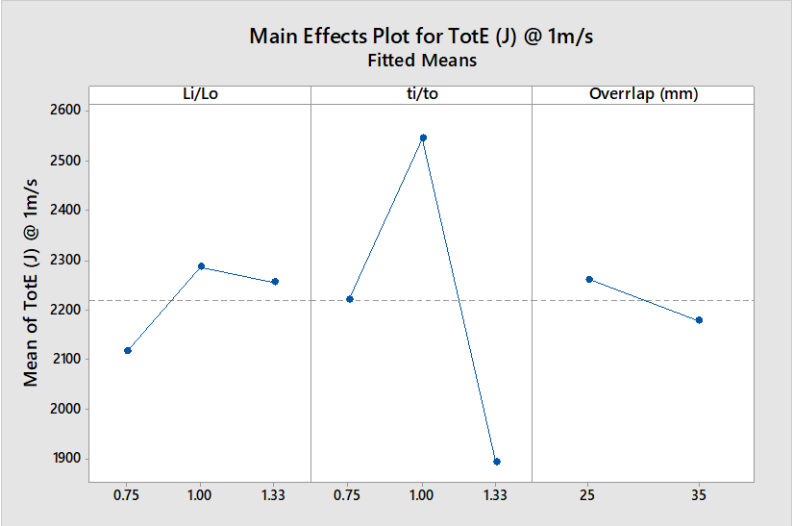

(a)

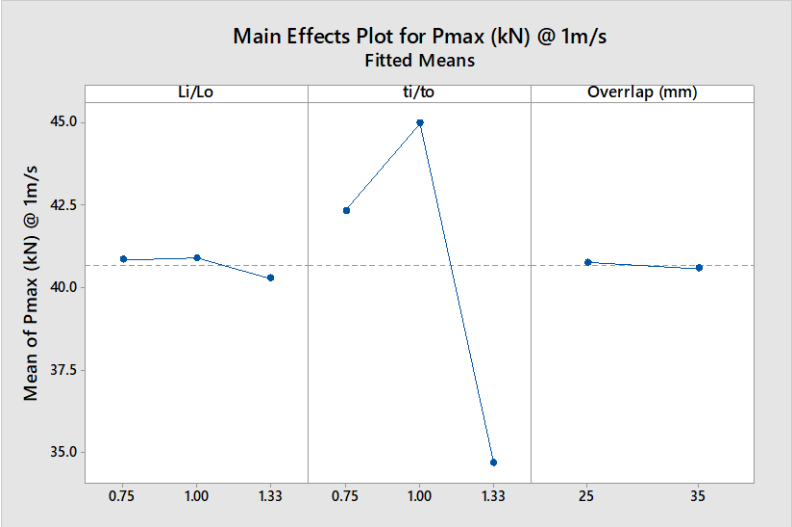

(b)

Figure 4.43 Main effects plot for (a) total energy absorption and (b) peak load at 1 m/s.

4.5.3 Optimum Joint Configurations

Table 4.8 summarizes the joint configurations that produce the maximum peak loads and total energy absorptions in single lap tubular adhesive joints between two aluminum tubes. It shows that the joint parameters for the maximum peak loads and energy absorption at high loading rates, such as 1 m/s, and at quasi-static loading rates, such as 1 mm/s are not all the

same. The optimal configurations are obtained by maximizing or minimizing predicted response for the stored model. A 2-sided 95% confidence interval is used to obtain the predicted response for optimal designs. In general, the statistical analysis presents 35 mm overlap as the most suitable for crush performance. At impact speeds, for maximum energy absorption and peak load, joints with equal tube length and thickness are suggested. However, when designing for crash front structures, the requirement is to maximize energy absorption while minimizing crush initiation load. For such a design condition, the tube geometry should have longer and thicker inner tube, and an overlap of 25 mm. If a condition of maximizing peak load at quasi-static speeds is desired, an increase in overlap to 35 mm is suggested.

Table 4.8 Optimal design parameters for different response requirements at 1 mm/s and 1 m/s.

Tot E (J) @ 1 mm/s	**P_{max} (kN) @ 1 mm/s**	**Tot E (J) @ 1 m/s**	**P_{max} (kN) @ 1 m/s**	**Li/Lo**	**ti/to**	**Overlap (mm)**
max	-	-	-	1.33	0.75	35
-	max	-	-	1.33	1	35
max	max	-	-	1.33	0.75	35
-	-	max	-	1	1	35
-	-	-	max	1	1	35
-	-	max	max	1	1	35
-	max	-	max	1.33	0.75	35
max	-	max	-	1	1	35
max	max	max	max	1.33	1	35
-	-	max	min	1.33	1.33	25
max	min	-	-	1	0.75	35

4.6 Conclusions

Non-linear finite element simulation of tubular lap joints under compressive load is studied in this chapter to determine the crush characteristics of adhesively bonded single lap joints between two aluminum tube. Tube geometry, joint geometry, and material properties are observed to influence the crush characteristics of such joints Important geometry variables are identified as tube length ratio, tube thickness ratio and overlap length. A study of different adhesives provided insight on the influence of brittle or ductile adhesives on crush characteristics.

Crush characteristics of Al-Al joints at quasi-static loading rates analyzed using a Design of Experiments approach delineate that overlap length is the most important design parameter, followed by tube thickness ratio and length ratio. At a high loading rate of 1 m/s, tube thickness ratio is the main influencer for crush performance followed by overlap length.

Chapter 5 Crush Characteristics of Aluminum-Composite and Composite-Composite Tubular Lap Joints

Crush characteristics of thin-walled aluminum tubes and composite tubes have been studied in the past in terms of their load carrying capacity and energy absorption capabilities. For ideal crush characteristics, thin-walled metal tubes are expected to collapse or fold in a progressive manner, while composite tubes to show progressive failure at the crush front. Studies have shown that crush characteristics of such tubular sections are influenced by geometric parameters such as length, diameter, and thickness. As the use of aluminum alloys and fiber-reinforced composites increases in multi-material designs of automotive, aerospace, and other structures, it is important to study the crush characteristics of composite-aluminum and composite-composite tubular joints. This chapter considers such as a study in which aluminum-composite and composite-composite tubes are joined by an adhesive in a single-lap configuration. The joined tubes are subjected to a quasi-static compressive load. Influence of joint and tube geometry parameters, such as bond overlap length, tube dimensions and crush initiator on the crush mode and crush parameters, such as peak load and energy absorption, of aluminum-composite and composite-composite tubes are determined using finite element analysis.

5.1 Design of Tubular Single Lap Joint

The single lap tubular joint comprises of two tubes of circular cross section bonded across an overlap using a thin layer of adhesive as discussed in Chapter 4. Figure 5.1 illustrates a tubular single lap joint considered in this study. Critical parameters influencing crush performance are tube material, tube geometry and joint geometry. Table 5.1 lists the geometric parameters considered in this study.

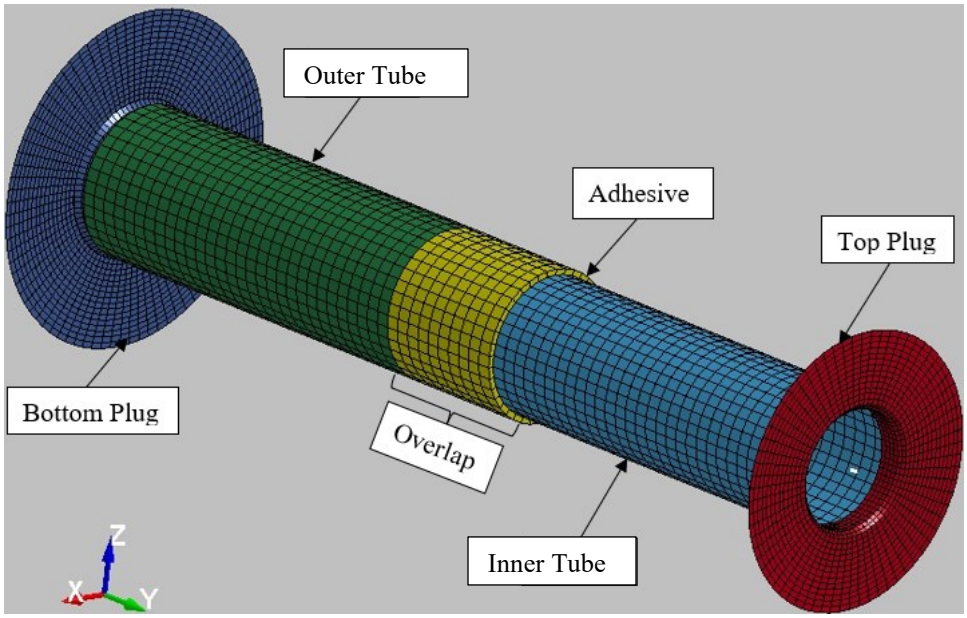

Figure 5.1 Tubular section with single lap joint.

Table 5.1 Geometric parameters of the tubular joint.

Parameter	Values
Joint length (L)	175 mm
Aluminum tube thickness	1.2 and 1.6 mm
Composite tube thickness	2.16 mm
Top tube outer diameter (di)	25.4 mm
Bottom tube outer diameter (do)	31.84 mm
Adhesive thickness (t)	1.06 mm
Overlap length (l)	10, 12.5, 15, 20 and 25 mm

The tubular joint is supported on a rigid plug at the bottom end of the outer tube and a compressive load is applied by the downward motion of a rigid plug fitted at the top end of the inner tube. The bottom plug is fixed in all directions and the top plug is constrained to move only in the axial direction at a constant velocity of 100 mm/s to create a compressive load on the tubular joint. Both plugs have a 45^{o} corner chamfer to act as a crush trigger.

5.2 Materials

The tube materials are Al 6061-T4 aluminum alloy and a T700 carbon fiber/epoxy composite (CFRP). Two different composite tube layups are considered to determine their influence on the joint crush performance. These layups are $[0/90]_{8s}$, a symmetric cross-plied laminate, and $[0/\pm45/90]_{4s}$, a symmetric quasi-isotropic laminate, each containing 16 laminae. For the $[0/90]_{8s}$ tube, two different lamina thicknesses, namely 0.135 mm and 0.16 mm, are considered, resulting in tube thicknesses of 2.16 mm and 2.56 mm, respectively. For the $[0/\pm45/90]_{4s}$ tube, the lamina thickness is 0.135 mm, which results in a tube thickness of 2.16 mm. The adhesive joining the inner and outer tubes is Betamate 1496, which is a crash-optimized epoxy resin. Material properties for the aluminum, adhesive and composite are listed in Tables 5.2, 5.3 and 5.4, respectively.

Table 5.2 Aluminum 6061 -T4 [57]

Density (g/cc)	Modulus (GPa)	K (MPa)	n	Yield Strength (MPa)
2.69	70.3	400	0.069	252

Table 5.3 Betamate 1496 adhesive [58]

Density (g/cc)	Modulus (GPa)	ν	G_{IC} (N/mm)	G_{IIC} (N/mm)	Tensile Strength (MPa)	Shear Strength (MPa)
1.6	1.6	0.42	4.46	16.7	30	24

Table 5.4 T700/2510 carbon fiber epoxy unidirectional composite. [64, 65]

Property	LS-Dyna Designation	Value
Density	RO	1.52 g/cc
Modulus in 1-direction (E_{11})	EA	127 GPa
Modulus in 2-direction (E_{22})	EB	8.41 GPa
Shear Modulus (G_{12})	GAB	4.21 GPa
Major Poisson's ratio (ν_{12})	-	0.309
Minor Poisson's ratio (ν_{21})	PRBA	0.02049
Tensile strength in 1-direction (S_{t1})	XT	2.2 GPa
Tensile strength in 2-direction (S_{t2})	YT	48.9 MPa
Compressive strength in 1-direction (S_{c1})	XC	1.47 GPa
Compressive strength in 2-direction (S_{c2})	YC	199 MPa
Shear Strength (S_{12})	SC	154 MPa
Fiber tensile failure strain	DFAILT	0.0174
Fiber compressive failure strain	DFAILC	-0.0116
Matrix failure strain	DFAILM	0.024
Maximum shear strain	DFAILS	0.03
Effective Failure Strain	EFS	0.55

5.3 Finite Element Model

Numerical analysis of crush performance in this study of Al-composite and composite-composite joints is conducted using LS Dyna R9.0.1, a commercial finite element software. The tubes are meshed using 4-noded quadrilateral shell elements. The meshing of Al tubes and rigid end plugs are as described in Chapter 4. The composite tubes are meshed with 2.5 mm 4-noded quad shell elements. The elements used in the composite tubes are created using PART_COMPOSITE option of shell elements, which represents each lamina as an integration point. The composite tube shell elements are defined using Belytschko-Tsay formulation with 16 integration points, one for each lamina according to the layup described in the previous section. Boundary conditions for the two plugs are as defined in Chapter 4. The top plug moves at a rate of 100 mm/s. Rate effect is not considered in this chapter.

Contact condition is found to be critical in modeling of composite-Al joints due to oscillations in the Al tube under progressive composite tube crush. Oscillations in Al tube is

observed under progressive crush of composite tube in an aluminum-composite tubular joint. Under crush of composite tube, layers of elements at the plug-tube interface are deleted progressively because of material failure. Once elements get deleted a gap is created between tube and plug. This gap unloads the joint following which Al tube shows a spring-back type movement until composite tube once again meets the plug.

Contact between tube and plug is defined using AUTOMATIC_NODES_TO_SURFACE definition where the tube nodes are considered as slave and the plug elements are the master. Static and dynamic friction values of 0.5 are assumed to reduce slippage between the tube ends and the plugs, and thereby reduce oscillations. Other contact definitions with user defined load-penetration curve are considered due to better performance under pure composite crush. However, such contact definitions show instability in the presence of any aluminum deformation. Hence, to maintain uniformity across all simulations, nodes-to-surface definition is used. AUTOMATIC_SINGLE_SURFACE contact definition is provided to the tubes to prevent interpenetration of tube elements and penetration between tubes post adhesive failure.

The material model for aluminum tubes is power law plasticity and for adhesive is cohesive zone model as defined in Chapter 4. The material model used for the composite tubes are described below.

5.3.1 CFRP Composite Material Model

LS Dyna offers several material models to model fiber reinforced composites. MAT_54 Enhanced Composite Damage [60] is one such model which has been widely used in literature and verified to be capable of reasonably accurate prediction of composite behavior [66, 67, 68]. The model is a simple brittle model with a crash front algorithm and strength reduction parameters upon lamina failure. The model uses a Chang-Chang failure criteria to predict lamina

failure. The model also requires a fewer number of input parameters making it more user friendly. The Chang-Chang failure criteria predicts lamina failure when one of the following criteria are met: tensile fiber failure, compressive fiber failure, tensile matrix failure or compressive matric failure. The equations for Chang-Chang failure criteria are given below in Equations 5.1-5.4 [60].

Tensile fiber failure mode:

$$\sigma_{11} > 0 \Rightarrow e_f^2 = \left(\frac{\sigma_{11}}{S_{t1}}\right)^2 + \beta\left(\frac{\sigma_{12}}{S_{12}}\right) - 1, \begin{matrix} e_{f\geq 0}^2 \Rightarrow failed \\ e_{f<0}^2 \Rightarrow elastic \end{matrix} \quad \text{Eq. 5.1}$$

$$\mathrm{E}_{11} = \mathrm{E}_{22} = \mathrm{G}_{12} = \vartheta_{21} = \vartheta_{12} = 0$$

Compressive fiber failure mode:

$$\sigma_{11} < 0 \Rightarrow e_c^2 = \left(\frac{\sigma_{11}}{S_{c1}}\right)^2 - 1, \begin{matrix} e_{c\geq 0}^2 \Rightarrow failed \\ e_{c<0}^2 \Rightarrow elastic \end{matrix} \quad \text{Eq. 5.2}$$

$$\mathrm{E}_{11} = \vartheta_{21} = \vartheta_{12} = 0$$

Tensile matrix failure mode:

$$\sigma_{22} > 0 \Rightarrow e_m^2 = \left(\frac{\sigma_{22}}{S_{t2}}\right)^2 + \left(\frac{\sigma_{12}}{S_{12}}\right) - 1, \begin{matrix} e_{m\geq 0}^2 \Rightarrow failed \\ e_{m<0}^2 \Rightarrow elastic \end{matrix} \quad \text{Eq. 5.3}$$

$$\mathrm{E}_{22} = \vartheta_{21} = 0 \Rightarrow \mathrm{G}_{12} = 0$$

Compressive matrix failure mode:

$$\sigma_{22} < 0 \Rightarrow e_d^2 = \left(\frac{\sigma_{22}}{2S_{c2}}\right)^2 + \left[\left(\frac{S_{c2}}{2S_{12}}\right)^2 - 1\right]\frac{\sigma_{22}}{S_{c2}} + \left(\frac{\sigma_{12}}{S_{12}}\right)^2 - 1, \begin{matrix} e_{d\geq 0}^2 \Rightarrow failed \\ e_{d<0}^2 \Rightarrow elastic \end{matrix} \quad \text{Eq. 5.4}$$

$$\mathrm{E}_{22} = \vartheta_{21} = \vartheta_{12} = 0 \Rightarrow \mathrm{G}_{12} = 0$$

An orthotropic elastic stress-strain failure relation is used until failure in each lamina occurs following one of the above four modes. A plane stress condition is assumed for stress calculations. For this study, lamina properties are reduced to zero and the material is set to fail when all laminae fail.

Several simulation parameters are required to validate the simulation results for accurate representation. These parameters control element deletion due to distortion, strength degradation under different conditions, and failure strains. The required parameters are obtained from Deleo and Feraboli's study on crush of carbon fiber composites [66]. The enhanced composite damage model provides a crash front algorithm to ensure progressive crush and suppresses global buckling. The crush front softening factor is defined as 0.083 in this study. This factor reduces the strength of the composite elements at the plug-tube interface by the given value to ensure progressive failure of the material under compressive load. Another important parameter is TFAIL which determines element deletion due to distortion by monitoring the time step size. This factor is given a value of 0.5 which results in material failure when time step size reduces by 50%. Other parameters are given default values, as shown in Table 5.5.

Table 5.5 LS-Dyna model parameters for composite material.

Parameter	**Description**	**Value**
SOFT	Softening reduction factor	0.083
TFAIL	Time step size criteria for element deletion	0.5
ALPHA	Shear stress parameter for the nonlinear term	0.3
YCFAC	Reduction factor for compressive fiber strength after matrix compressive failure	2.0
PEL	Percentage of layers which must fail until crash front is initiated	100
BETA	Weighting factor for shear term in tensile fiber mode	0.5

5.3.2 Tube Mesh Configuration

Progressive crush of composite tubes in finite element simulations is presented as sequential deletion of elements at the crush front as the top plug moves. A small gap forms between the plug and the next layer of elements each time the material at the crush front fails, resulting in sequence of zero loads on the load-displacement plots. To prevent this issue, a couple of options has been explored, such as modifying the contact definition or modifying the mesh arrangement. Nodes to surface contact is chosen for reasons described previously. As for the mesh arrangement, a regular mesh shown in Figure 5.2 (a) and an irregular mesh arrangement shown in Figure 5.2 (b) are compared for single composite tubes with $[0/90]_{8s}$ and $[0/\pm45/90]_{4s}$ layups. The arrangement of irregular mesh is such that all elements at the leading end of the tube do not meet the plug at the same time. This ensures a staggered deletion of elements at the crush front and avoids the formation of a gap between the tube and the plug. To do this, the mesh comprises of quadrilateral and triangular shell elements arranged at an angle to the loading axis. Similar mesh arrangements were explored in [66] for impact of corrugated sheets with $[0/90]_{8s}$ laminates and showed some success. The brown elements at the bottom represents crush triggers with half the material thickness.

Figure 5.3 compares the force-displacement curves for the two mesh types. A SAE 60 Hz low pass filter is used to present data. The plots indicate slightly lower peak load for the irregular mesh type. Both regular and irregular mesh result in a peak and valley type progressive crush after the initial peak, but for the regular mesh the difference in magnitude between peak and valley loads is much higher. This difference is due to time taken by the top plug to resume contact with the tube once a layer of composite elements is deleted at crush front. The constant mean crush force in irregular mesh simulation appears to be approximately equal to that for a

regular mesh. However, when comparing the plots for a quasi-isotropic $[0/\pm45/90]_{4s}$ layup, the peak force, and the mean crush force after the first peak are much lower than expected for the irregular mesh simulation and do not show the expected load-displacement characteristics as is seen with the regular mesh type. Hence, for uniformity across all simulations, the regular mesh type is used henceforth.

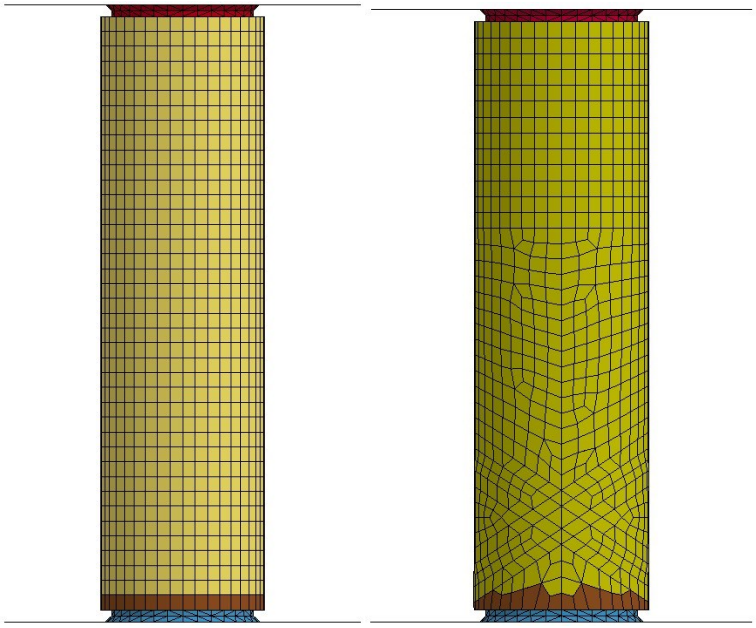

Figure 5.2 (a) Regular and (b) Irregular mesh types.

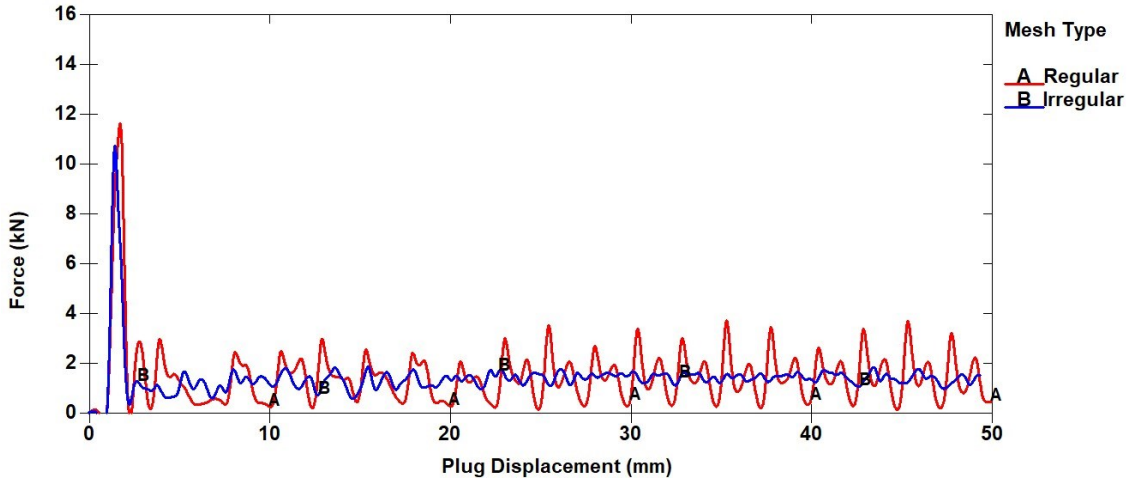

Figure 5.3 Comparison of force-displacement plots for the regular and irregular mesh types for $[0/90]_{8s}$ tubes.

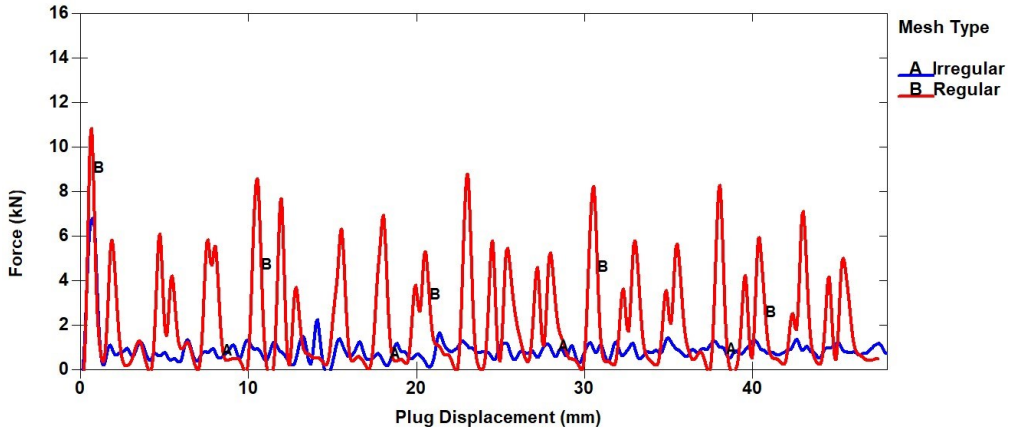

Figure 5.4 Comparison of force-displacement plots for the regular and irregular mesh types for $[0/\pm45/90]_{4s}$ tubes.

5.4 Results of Finite Element Analysis

5.4.1 Aluminum-Composite Tubular Joints without Crush Triggers

The important characteristics defining crush performance of a tubular lap joint are failure or deformation mode, nature of force-displacement diagram, peak load, and energy absorption. Ideally, the tubular sections in a joint should exhibit progressive collapse with little or no adhesive failure. As discussed in the previous chapter, the adhesive overlap length is a critical criterion in determining the joint strength and mode of deformation. A short overlap may lead to complete adhesive failure prior to any significant tube deformation while a long overlap may result in an unnecessary increase in weight and cost. To determine the effect of overlap length in Al-composite joints, a study is conducted with four different overlap lengths, namely 10, 12.5, 15 and 20 mm. All joints have a length of 175 mm and a mean diameter of 26.46 mm. In this study, the composite tube has a $[0/90]_{8s}$ layup and is 2.16 mm thick and does not have a crush trigger. The aluminum tube is either 1.2 mm or 1.6 mm thick. Results from the simulation study are compiled in Table 5.6. The highlighted rows indicate configurations with the highest energy absorption for each overlap length.

Table 5.6 Results of Al - $[0/90]_{8S}$ CFRP composite tubular joint crush with no composite tube crush trigger.

Overlap (mm)	Inner Tube	Outer Tube	Peak Load (kN)	Mean Load (kN)	Total Energy (J)	Adhesive Failure	Tube Deformation Mode
10	2.16 mm Composite	1.2 mm Al	21.7	0.7	33.7	Yes	None / Sliding
	2.16 mm Composite	1.6 mm Al	23.1	0.6	27.1	Yes	None / Sliding
	1.2 mm Al	2.16 mm Composite	23.9	14.1	679	No	Al Folding
	1.6 mm Al	2.16 mm Composite	21.6	1.3	61.5	Yes	None / Sliding
12.5	2.16 mm Composite	1.2 mm Al	28.1	3	147	Yes	Al Folding / Sliding
	2.16 mm Composite	1.6 mm Al	26.8	0.8	40.7	Yes	None / Sliding
	1.2 mm Al	2.16 mm Composite	23.2	13.2	636.4	No	Al Folding
	1.6 mm Al	2.16 mm Composite	26.6	2.7	129.4	Yes	CFRP Crush + Sliding
15	2.16 mm Composite	1.2 mm Al	29.8	13.4	645.2	No	Al Folding
	2.16 mm Composite	1.6 mm Al	30.3	3.4	164.9	No	Al folding + CFRP Offset Crush
	1.2 mm Al	2.16 mm Composite	25.1	12.8	618.3	No	Al Folding
	1.6 mm Al	2.16 mm Composite	32.8	11.9	573.4	No	Al folding + CFRP Crush
20	2.16 mm Composite	1.2 mm Al	30.1	13.8	667.6	No	Al Folding
	2.16 mm Composite	1.6 mm Al	29.7	1.8	86	No	CFRP offset crush
	1.2 mm Al	2.16 mm Composite	20.8	7.8	376.5	Yes	Al Buckling / Sliding + Offset Crush
	1.6 mm Al	2.16 mm Composite	20.6	1.3	62.2	No	CFRP Crush

Notes: (1) Adhesive thickness = 1.06 mm, (2) T: Top Tube, B: Bottom Tube, (3) Load is applied at the top plug and the bottom plug is fixed. Total energy absorbed is measured for a crush distance of 50 mm.

Simulation results show a varied deformation and crush response to the compressive load. Joints with 10- and 12.5-mm overlaps show complete adhesive failure except for cases with 1.2 mm thick Al top tube for which the primary deformation mode is progressive folding of the aluminum tube. Increasing the overlap length to 15 mm increases the peak load. Joints with 15- and 20-mm overlap show little difference in peak load. Highest energy absorption is observed in

cases with no adhesive failure and progressive collapse or folding in the Al tubes. Cases with mostly composite tube crush show poor performance.

Looking at the cases with adhesive failure, we can observe two modes of failure. One where the adhesive fails suddenly prior to any deformation in the aluminum tubes and the other case where the adhesive fails progressively accompanied by aluminum tube deformation. The deformed Al tube resists the sliding of the inner composite tube in a stick-slip fashion, and thereby the joint continues to carry the load after adhesive failure. Hence, a few simulation results show higher energy absorption values despite adhesive failure such as 2.16 mm thick inner composite tube - 1.2 mm thick Al outer tube joint with 12.5 mm overlap and 1.6 mm thick inner Al tube – 2.16 mm thick outer composite tube joint with 12.5 mm overlap.

When there is no adhesive failure, different deformation modes are observed in the tubular joints. They can be broadly classified as (1) axisymmetric or diamond lobe folding of the Al tube, (2) progressive failure of the composite tube at the crush front or composite crush, (3) composite tube offset crush, and (4) a combination of two or more of these deformation modes. The composite tube offset crush occurs when there is simultaneous or sequential deformation of the Al tube and crush of the composite tube. A non-uniform folding deformation of the Al tube or a non-uniform crushing failure of the composite tube at the crush front results in a shift in the tube axis and hence the tubes are offset from the loading axis.

Figures 5.5-5.8 plot the force-displacement diagrams and illustrate representative failure or deformation modes observed in different cases when there is no adhesive failure. Figure 5.5 illustrates the load-displacement diagram for a joint exhibiting progressive crush of the composite tube. Crush of $[0/90]_{8S}$ composite tube is characterized by a relatively high initial peak load at crush initiation, followed by much lower progressive crush load. Figure 5.6 shows a joint

where composite tube crush is offset from the loading axis. This is caused by non-uniform deformation of Al outer tube. Energy absorption in cases with offset crush is much lower as indicated by much lower progressive crush load after the initial peak. Figures 5.7 and 5.8 illustrate partial or complete deformation of the Al tube by folding. Figure 5.7 shows peaks and valleys corresponding to the Al tube folding over a displacement of 25 mm followed by a sharp drop in crush load indicating crush initiation in the composite tube. Figure 5.8 illustrates a case where the Al tube shows folding with no failure in the composite tube over a crush distance of 50 mm.

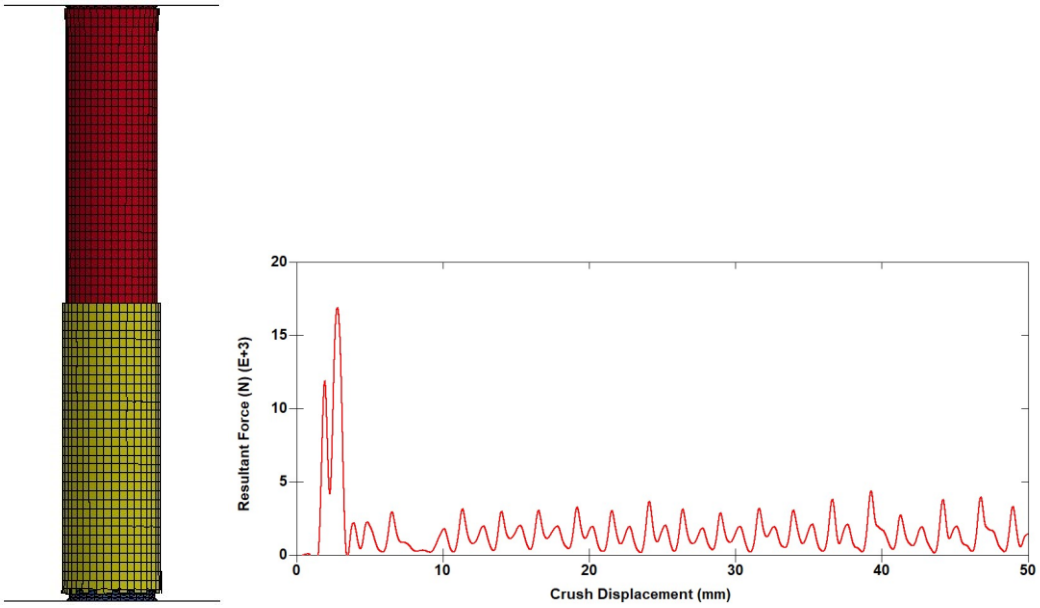

Figure 5.5 Composite tube (bottom) crush with little or no Al tube (top) deformation. (t_i - 1.6 mm Al / t_o - 2.16 mm $[0/90]_{8s}$ CFRP composite joint, overlap length = 20 mm)

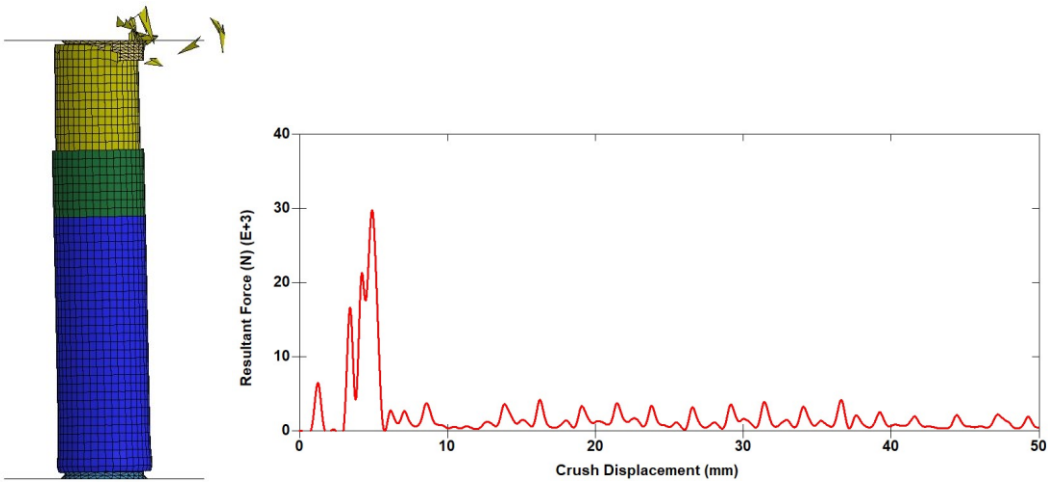

Figure 5.6 Offset crush in composite tube (top) with little Aluminum tube (bottom) deformation. (t_i - 2.16 mm $[0/90]_{8s}$ CFRP composite / t_o - 1.6 mm Al joint, overlap length = 20 mm)

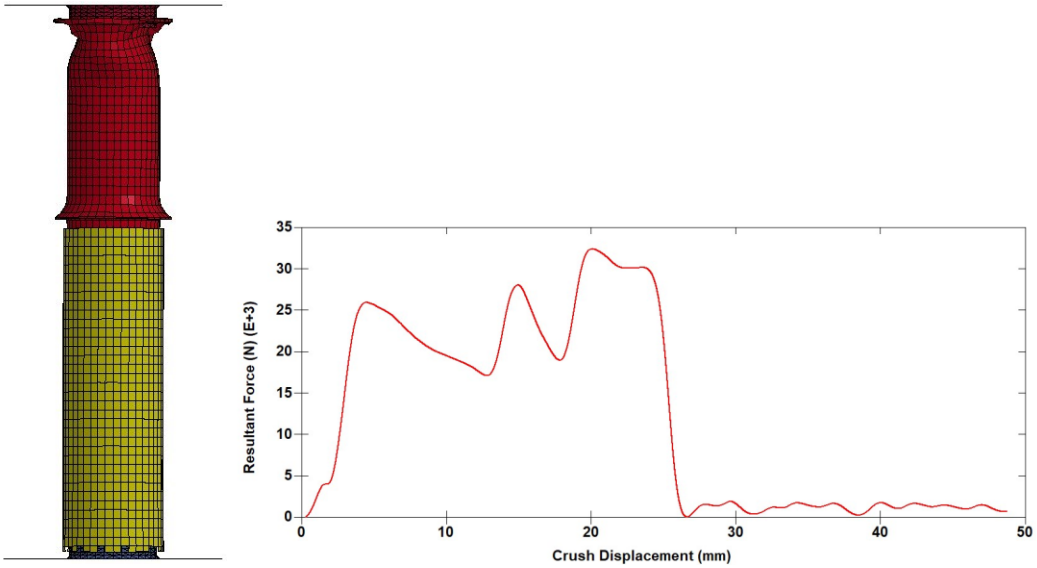

Figure 5.7 Al tube (top) folding along with composite tube (bottom) crush. (t_i - 1.6 mm Al / t_o - 2.16 mm $[0/90]_{8s}$ CFRP composite joint, overlap length = 15 mm)

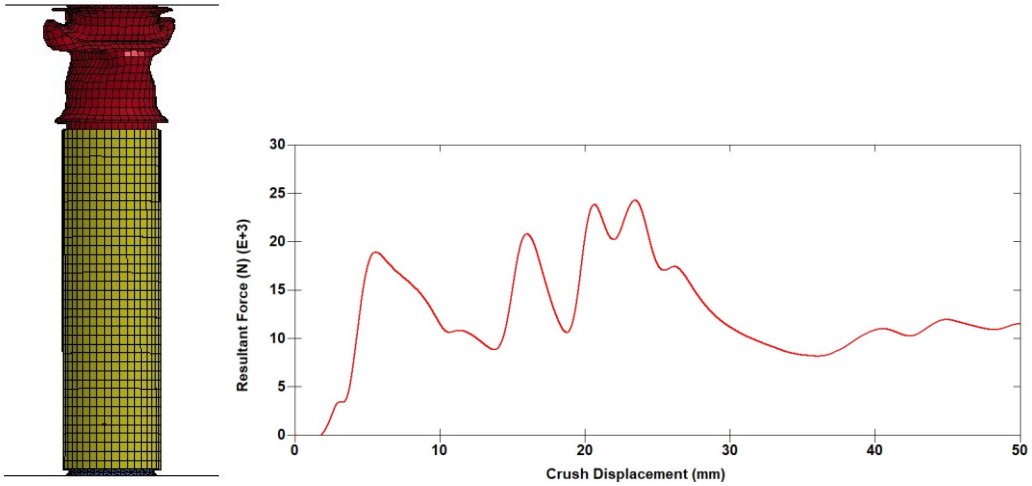

Figure 5.8 Al tube (top) folding with little or no composite (bottom) tube crush. (t_i - 1.2 mm Al / t_o - 2.16 mm $[0/90]_{8s}$ CFRP composite joint, overlap length = 20 mm)

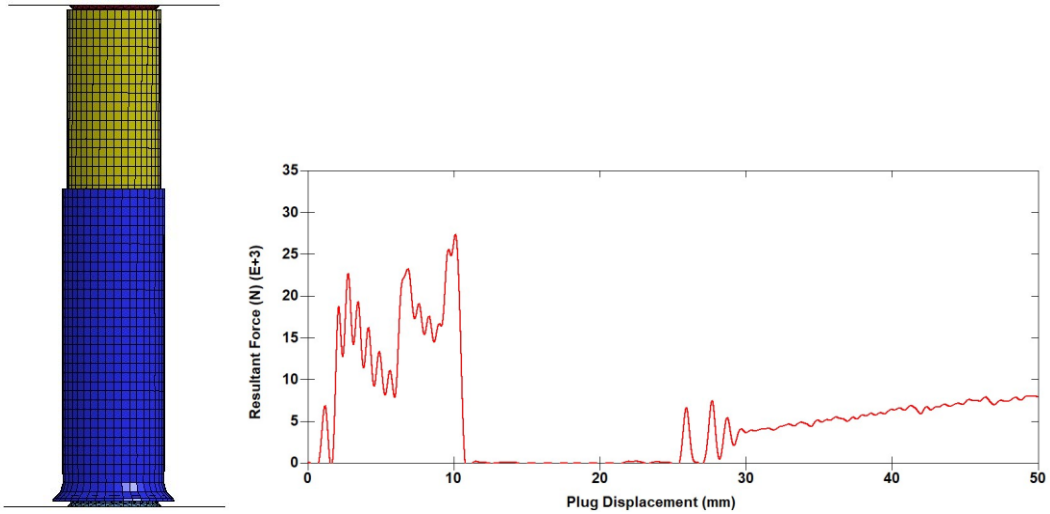

Figure 5.9 Adhesive failure followed by composite tube (top) sliding in deformed Al tube (bottom). (t_i - 2.16 mm $[0/90]_{8s}$ CFRP composite / t_o - 1.2 mm Al joint, overlap length = 12.5 mm)

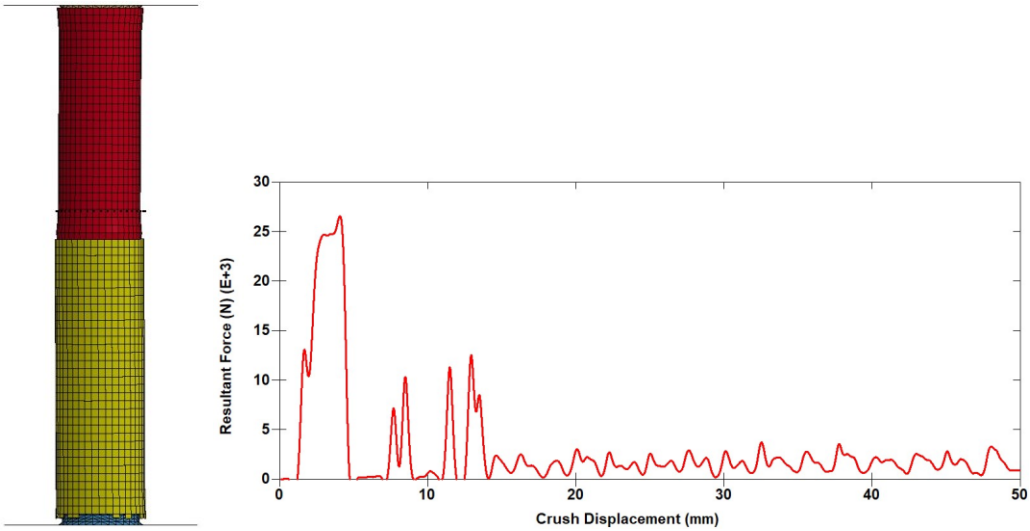

Figure 5.10 Composite tube (outer) crush post adhesive failure due to load transfer by deformed Al tube (inner). (t_i - 1.6 mm Al / t_o - 2.16 mm $[0/90]_{8s}$ CFRP composite joint, overlap length = 12.5 mm)

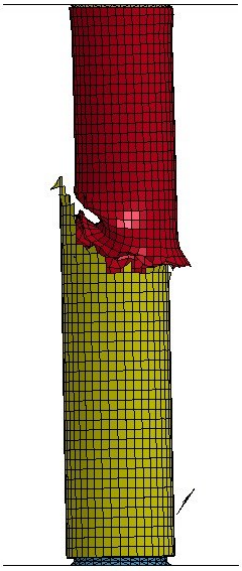

Figure 5.11 Sliding crush of composite tube (bottom) due to load applied by deformed Al tube (top). (t_i - 1.2 mm Al / t_o - 2.16 mm $[0/90]_{8s}$ CFRP composite joint, overlap length = 20 mm)

Figures 5.9 and 5.10 illustrate cases where the tubular joint continues to carry the load post-adhesive failure. Deformation illustrated in Figure 5.9 represents stick-slip phenomenon due to sliding of the deformed Al tube in the composite outer tube post adhesive failure. Figure 5.10

represents a case where the 1.6 mm thick Al inner tube has deformed to an extent where sliding is no longer possible. This deformed Al tube then transfers load to composite tube which then undergoes progressive crush. But with 1.2 mm thick Al inner tube, 20 mm overlap due to buckling in Al tube after initial deformation, joint failed by composite offset crush as shown in Figure 5.11.

5.4.2 Aluminum-Composite Tubular Joints with Crush Triggers

Crush triggers are commonly used to ensure progressive crush. In the following study, two crush triggers are considered; one being a corner chamfer of the plug and the other is a thickness reduction in the leading elements of the composite tube representing a chamfer at the top end of the composite tube. The tube chamfer is used together with the plug corner chamfer. The same set of simulations as in the previous section are run with crush triggers and the results are compiled in Table 5.7. Joint configurations with the highest energy absorption for each overlap length are highlighted in the table.

Comparing the results of joint configurations with no composite tube crush trigger in Table 5.5 and with 2.5 mm composite tube crush trigger in Table5.6, we can clearly observe its influence on crush characteristics of the joint. There is a significant reduction in crush initiation loads. In most cases, the composite tube crush initiates prior to any significant deformation in the Al tubes. Also, none of these simulations except in the case of 10 mm overlap joint with 1.6 mm thick Al show adhesive failure due to low peak loads. In general, since tube deformation is dominated by composite tube crush, crush energy absorption is much lower. Higher energy absorptions are observed in cases with composite tubes on the top and 1.2 mm thick Al tube in the bottom. Higher peak loads are observed in cases with composite tubes in the bottom due to larger tube diameter.

Table 5.7 Results of Al- $[0/90]_{8S}$ CFRP composite tubular joint crush with composite tube crush trigger.

Overlap (mm)	CFRP Tube Thickness (mm)	Al Tube Thickness (mm)	Tube Failure Mode	Adhesive Failure	Peak Load (kN)	Mean Load (kN)	Energy Absorption (J)
10	2.14 (B)	1.2 (T)	Al fold + CFRP Crush	No	14.1	1.3	61.8
	2.14 (B)	1.6 (T)	CFRP Crush	No	16.3	1.2	59.6
	2.14 (T)	1.2 (B)	CFRP Offset Crush	No	20.4	1.4	68.7
	2.14 (T)	1.6 (B)	CFRP Offset Crush	Yes	20.5	1.4	65.7
12.5	2.14 (B)	1.2 (T)	CFRP Crush	No	15.1	1.6	75.7
	2.14 (B)	1.6 (T)	CFRP Crush	No	16.9	1.3	63.9
	2.14 (T)	1.2 (B)	CFRP Offset Crush	No	21.4	1.8	85.6
	2.14 (T)	1.6 (B)	CFRP Offset Crush	No	21.5	1.4	65.2
15	2.14 (B)	1.2 (T)	CFRP Crush	No	12.1	1.3	62.3
	2.14 (B)	1.6 (T)	CFRP Crush	No	14.1	1.3	63.4
	2.14 (T)	1.2 (B)	CFRP offset crush	No	18.2	1.6	78.9
	2.14 (T)	1.6 (B)	CFRP Offset Crush	No	20.6	1.3	64.1
20	2.14 (B)	1.2 (T)	CFRP Crush	No	11.8	1.2	57.5
	2.14 (B)	1.6 (T)	CFRP Crush	No	12.7	1.3	63.4
	2.14 (T)	1.2 (B)	CFRP Offset crush	No	18.4	1.4	67.6
	2.14 (T)	1.6 (B)	CFRP offset crush	No	20.6	1.3	61.5

Notes: (1) Adhesive thickness = 1.06 mm, (2) T: Top Tube, B: Bottom Tube, (3) Load is applied at the top plug and the bottom plug is fixed. Total energy absorbed is measured for a crush distance of 50 mm.

5.4.3 Effect Composite Tube Layup in Al-Composite and Composite-Composite Joints

The typical crush characteristics of a $[0/90]_{8s}$ CFRP composite tube is a relatively high initial peak followed by low mean crush load. This is illustrated in the load-displacement diagrams for single $[0/90]_{8s}$ tubes shown in Figure 5.3. A result of such behavior is low energy absorption under composite crush. These characteristics can be improved by changing the layup to a quasi-isotropic laminate. An example of a commonly used quasi-isotropic laminate is $[0/\pm45/90]_{4s}$. Such a laminate exhibits a more uniform crush characteristics as shown in Figure 5.4 for a single $[0/\pm45/90]_{4s}$ tube. Single tube crush results show a peak load of 10.8 kN for this

laminate compared to 11.6 kN for cross-plied laminate. The first force peak is slightly lower for this laminate due to lower fiber fraction in the loading direction. For the quasi-isotropic laminate, the mean crush force is higher, hence more energy is absorbed under crush. Energy absorbed by this laminate is 93.5 J compared to 40.8 J for cross-plied laminate. Because of this, the influence of changing the composite tube from a cross-plied to a quasi-isotropic laminate is studied with different overlap lengths and compared with results of the Al-composite and composite-composite tubular joints with cross-plied laminate.

Crush simulation results of Al-composite joint with $[0/\pm45/90]_{4s}$ quasi-isotropic composite tubes are listed in Table 5.8. As can be observed in this table, compared to the tubular joints with $[0/90]_{8s}$ cross-plied composite tube, for smaller bond lengths where the peak load is determined by adhesive failure, the results are similar for both laminates. At higher overlap lengths when there is no adhesive failure, tubular sections with quasi-isotropic composite inner tube show lower peak load as well as energy absorption. This is due to lower strength of the composite inner tube with $[0/\pm45/90]_{4s}$ laminate, resulting in crush prior to significant Al tube deformation. The peak loads shown in Table 5.8 for composite inner tube with $[0/\pm45/90]_{4s}$ laminate are lower than corresponding results with cross-plied laminate. With composite outer tube, both laminate types show similar peak loads during crush. Energy absorption of tubular section with quasi-isotropic laminates is higher in cases with only composite tube crush. Examples of such sections are 1.6 mm thick Al inner tube-composite outer tube joints with overlap 15 mm or greater. Joint configuration with the best energy absorption is with 1.2 mm thick Al top tube, except for 15 mm overlap where the joint with 1.6 mm thick Al top tube has a better performance, since it shows non-uniform folding of Al tube followed by composite tube offset crush.

Table 5.8 Results of Al- $[0/\pm45/90]_{4s}$ CFRP composite tubular joint crush with no crush triggers.

Overlap Length (mm)	Inner Tube	Outer Tube	Adhesive Failure	Deformation Mode	Peak Load (kN)	Total Energy (J)
10	Quasi-isotropic 2.16 mm	Al 1.2 mm	Yes	None / Sliding	22.1	85.8
	Quasi-isotropic 2.16 mm	Al 1.6 mm	Yes	None / Sliding	23.7	25.8
	Al 1.6 mm	Quasi-isotropic 2.16 mm	Yes	None / Sliding	21.7	27.2
	Al 1.2 mm	Quasi-isotropic 2.16 mm	No	Al Folding	22.7	642.1
12.5	Quasi-isotropic 2.16 mm	Al 1.2 mm	Yes	Al Folding	26.7	146
	Quasi-isotropic 2.16 mm	Al 1.6 mm	Yes	None / Sliding	26.7	38.4
	Al 1.6 mm	Quasi-isotropic 2.16 mm	Yes	Sliding Crush	26.7	59.7
	Al 1.2 mm	Quasi-isotropic 2.16 mm	No	Al Folding	23.3	634.2
15	Quasi-isotropic 2.16 mm	Al 1.2 mm	No	Al folding + CFRP Crush	24.7	178.6
	Quasi-isotropic 2.16 mm	Al 1.6 mm	No	CFRP Offset Crush	19.4	88
	Al 1.6 mm	Quasi-isotropic 2.16 mm	No	Al folding + CFRP Offset Crush	33	425.3
	Al 1.2 mm	Quasi-isotropic 2.16 mm	No	Al folding + CFRP Crush	25.1	383.8
20	Quasi-isotropic 2.16 mm	Al 1.2 mm	No	Al Folding + CFRP Offset Crush	24.6	202.6
	Quasi-isotropic 2.16 mm	Al 1.6 mm	No	CFRP offset rush	21.5	84.6
	Al 1.6 mm	Quasi-isotropic 2.16 mm	No	Al Buckling + CFRP Crush	33.4	467.7
	Al 1.2 mm	Quasi-isotropic 2.16 mm	Yes	Al Buckling	20.2	515.9

Notes: (1) Adhesive thickness = 1.06 mm, (2) Load is applied at the top plug and the bottom plug is fixed. Total energy absorbed is measured for a crush distance of 50 mm.

Table 5.9 lists the crush simulation results of composite-composite joints with the two different layups, quasi-isotropic and cross-plied. Tube length and mean diameter are 175 mm and 26.46 mm, respectively. When adhesive failure occurs before either the inner or outer tube starts to crush the cross-plied layup has a marginally better performance due to higher crush initiation loads. But when the adhesive is not critical, performance of the quasi-isotropic tube joint is significantly better. However, both energy absorption and peak load are much lower when compared to joints with Al tubes.

Table 5.9 Results of CFRP-CFRP composite tubular joint crush with no crush triggers.

Overlap Length (mm)	Inner Tube	Outer Tube	Adhesive Failure	Deformation Mode	Peak Load (kN)	Total Energy (J)
10	Quasi-isotropic	Quasi-isotropic	Yes	Sliding Offset Crush	22.1	23.3
	Cross-plied	Cross-plied	Yes	Sliding Offset Crush	27	33
12.5	Quasi-isotropic	Quasi-isotropic	Yes	None / Sliding	27.8	31.2
	Cross-plied	Cross-plied	Yes	Sliding Offset Crush	27.2	41.7
15	Quasi-isotropic	Quasi-isotropic	No	Sliding Offset Crush	21.9	105.5
	Cross-plied	Cross-plied	Yes	Sliding Offset Crush	32.3	42.7
20	Quasi-isotropic	Quasi-isotropic	No	CFRP Crush	26.8	92.9
	Cross-plied	Cross-plied	No	CFRP Crush	27.5	75.5

Notes: (1) Adhesive thickness = 1.06 mm, (2) Load is applied at the top plug and the bottom plug is fixed. Total energy absorbed is measured for a crush distance of 50 mm.

5.5 Conclusions

Finite element analysis of composite-composite and composite-Al tubular lap joints was successfully implemented, and influence of material and geometry parameters was examined. Crush failure mode should exhibit significant plastic deformation of aluminum tube to maximize performance indices such as energy absorption and peak load. Joints which show composite crush prior to any aluminum tube deformation produces lower crush performance. As an extension, composite – composite joints exhibit high peak loads but have poor energy absorption characteristics.

Joint strength is limited by the overlap length and crush initiation load, hence as overlap length increases, the strength reaches a plateau when it equals crush initiation load. A minimum bond length is required to ensure load transfer between the tubes prior to failure. This minimum length is a function of tube material and thickness.

To maximize crush performance, peak load and energy absorption of the tubular section, crush mode should include significant amount of aluminum tube folding. Composite crush initiation before aluminum tube folding produces lower crush performance of the tubular section.

Crush initiator in the form of reduced thickness chamfer on the loading end of the composite cross-plied inner tubes greatly reduces the composite failure initiation load; hence tubular joints with such crush initiators do not show much adhesive failure even for smaller overlaps and exhibit poor crush performance due to a lack of deformation in aluminum tubes.

The influence of quasi-isotropic laminate in composite and aluminum joints is analyzed. Composite tube laminate layup is an important factor when joint does not fail due to adhesive failure. Al-composite joints with this laminate perform better when composite crush is the major

mode of deformation. In composite-composite joints, the use of quasi-isotropic laminate is observed to improve energy absorption when crush is not limited by adhesive failure first.

Chapter 6 Strength and Failure Characteristics of Tubular Adhesive Lap Joints under Tensile Load

In Chapters 4 and 5, crush behavior of tubular adhesive lap joints under compressive loads was explored. Tube and joint parameters such as geometry and material properties were shown to greatly influence the crush performance. However, tubular joints in structural applications may not only experience crush loading, but also other forms of loading such as tension, bending and torsion. Changes in loading mode will significantly influence stresses in the adhesive overlap as well as deformation and failure in the joined tubes. In this chapter, the tensile performance of aluminum-aluminum and composite-aluminum tubular adhesive lap joints is studied using finite element analysis. The strength and failure characteristics of the tubular joints are analyzed under tension for different tube and joint geometries such as tube and adhesive thickness and overlap length. The joint performance is also studied at quasi-static and high loading rates since both tube and adhesive material are rate sensitive to varying degrees.

6.1 Tubular Adhesive Lap Joint

The configuration of the tubular adhesive lap joint in tension is similar to that described in Chapter 4. Figure 6.1 illustrates a tubular lap joint under a tensile load. Two aluminum tubes of circular cross section and equal length are bonded together using a thin layer of adhesive across an overlap length. In a few cases, a combination of an aluminum external tube and a carbon fiber/epoxy composite internal tube is also considered. The tensile load and constraints are directly applied to the inner and outer tubes. Table 6.1 lists joint and tube parameters

considered for the Al-Al tubular joints. The outer and inner tube thicknesses are equal, and the tube lengths are varied based on the overlap length to ensure that the total joint length is 175 mm.

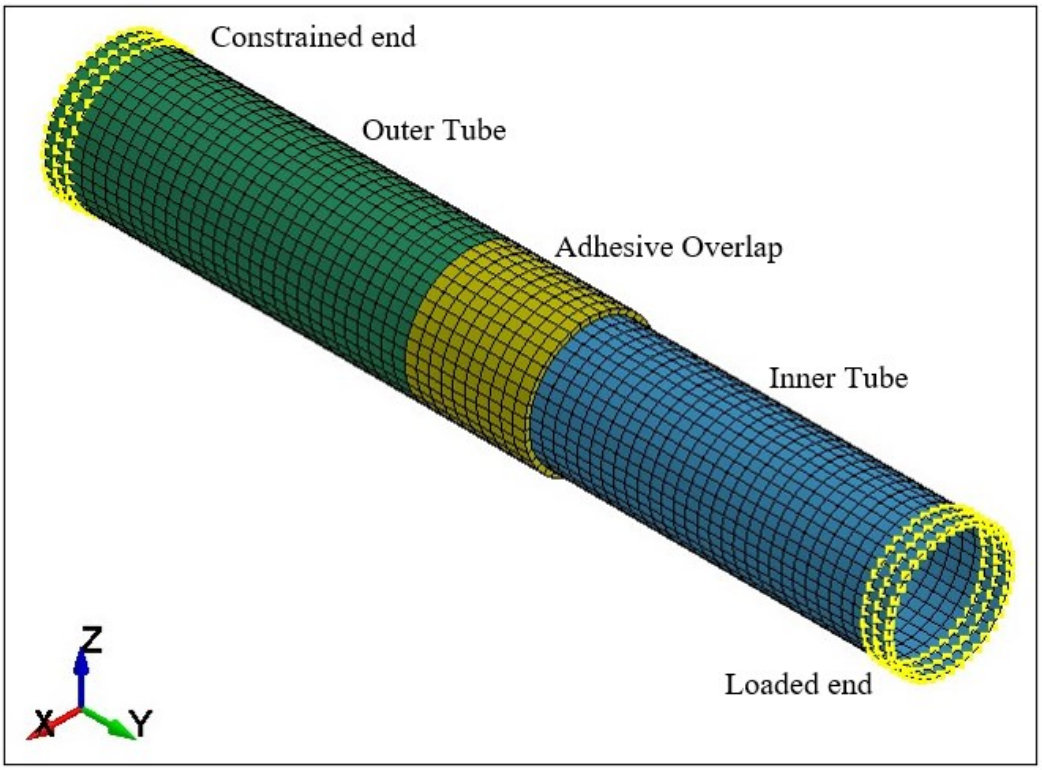

Figure 6.1 Configuration of tubular adhesive lap joint under tensile load.

Table 6.1 Geometric parameters of the Al-Al tubular joints considered for tensile loading

Parameter	Value
Joint length	175 mm
Aluminum tube thickness	1.2, 1.6, 2.0 and 2.4 mm
Inner tube outer diameter (di)	25.4 mm
Adhesive thickness (t)	0.5, 1.06, 1.5, and 2.0 mm
Overlap length (l)	10, 12.5, 15, 20 and 25 mm

6.2 Materials

The tube materials considered in this study are a 6061-T4 aluminum alloy for the aluminum tubes and a $[0/90]_{8s}$ T700 carbon fiber epoxy for the composite tubes. The adhesive is either Betamate 1496, a crash optimized adhesive or AV 138, a brittle adhesive. The properties of the aluminum, the composite and the two adhesives are listed in Table 6.2, 6.3 and 6.4 respectively.

Table 6.2 Aluminum 6061 -T4 [57]

Density (g/cc)	Modulus (GPa)	K (MPa)	n	Yield Strength (MPa)	Strain to Failure (%)
2.69	70.3	400	0.069	252	19

Table 6.3 T700/2510 carbon fiber epoxy unidirectional tape [64, 65]

Property	Value
Density	1.52 g/cc
Modulus in 1-direction (E_{11})	127 GPa
Modulus in 2-direction (E_{22})	8.41 GPa
Shear Modulus (G_{12})	4.21 GPa
Major Poisson's ratio (ν_{12})	0.309
Minor Poisson's ratio (ν_{21})	0.02049
Tensile strength in 1-direction (S_{t1})	2.2 GPa
Tensile strength in 2-direction (S_{t2})	48.9 MPa
Compressive strength in 1-direction (S_{c1})	1.47 GPa
Compressive strength in 2-direction (S_{c2})	199 MPa
Shear Strength (S_{12})	154 MPa
Fiber tensile failure strain	0.0174
Fiber compressive failure strain	-0.0116
Matrix failure strain	0.024
Maximum shear strain	0.03
Effective Failure Strain	0.55

Table 6.4 Adhesive Properties [58, 59]

	Betamate 1496	**Araldite AV138**
Density (g/cc)	1.6	1.6
Modulus (E) (GPa)	1.6	4.89
Poisson's ratio (ν)	0.42	0.35
G_{IC} (N/mm) (1)	4.46	0.2
G_{IIC} (N/mm) (2)	25.1	0.38
Tensile strength (MPa)	30	39.45
Shear strength (MPa)	24	30.2
Strength strain rate factor at 1000 s^{-1}	2.5	-
Fracture energy strain rate factor at 1000 s^{-1}	2.75	-

(1) G_{IC} is Mode I fracture toughness and (2) G_{IIC} is Mode II fracture toughness.

6.3 Finite Element Model

Tensile performance of the tubular lap joint is analyzed using a commercial finite element software: LS Dyna R9.0.1. The joint is modeled by representing tubes with 4-noded quadrilateral shell elements and the adhesive layer with 8-noded solid brick elements. A single layer of solid elements represents the bond between tubes. The size of both elements are approximately 2.5 mm and thickness of the solid adhesive elements varies based on the bond thickness. The element formulation and details are as described in Chapter 4.

Boundary conditions for the joint are defined using nodal definitions. A set of nodes at the bottom end of the outer tube shown in Figure 6.1 are fixed in all directions and rotations using SPC_SET option. The fixed nodes constrain the tube movement at the bottom. The nodes at the top end of the tube are displaced in the positive Y-direction with a nodal velocity of 1 mm/s for the quasi-static condition and 1 m/s for the high-speed loading condition The loading condition is provided using PRESCRIBED_MOTION_SET option. Rate effects are considered at the higher velocity of 1 m/s. The resultant load is calculated by summing up the nodal forces

at the constrained end. An AUTOMATIC_ SINGLE_SURFACE contact definition is provided for the tubes to prevent any penetration errors between the tubes or within a tube.

The aluminum used for the tubes is modeled using power law plasticity and the adhesive is modeled using cohesive zone model. For the composite tube, the Chang-Chang failure model is used. Material models and rate effects are as described in Chapter 4. Additionally, a strain-based failure criterion is provided to model aluminum failure in tension. The aluminum tubes are set to fail when the plastic strain in the material exceeds 19%.

6.4 Results

The performance of the tubular lap joints under tensile load was determined by analyzing the peak load or strength of the joint. Under tensile load, two possible failure outcomes are tube failure and adhesive failure. Ideally, both tube failure and adhesive failure should occur simultaneously. If the bond shows no failure and either one or both tubes fail first, then the joint is stronger than necessary. On the other hand, if the bond fails prior to failure in the tubes, then the full potential of the joint is not reached. Overlap length, bond thickness, tube thicknesses, tube diameters and material properties are the parameters that determine the failure mode and therefore the strength of the joint. Additionally, since the materials are strain rate sensitive, loading rate is also a factor determining the joint performance.

To understand the failure modes in single lap tubular joints in tension, it is important to consider the stress distributions in the adhesive layer. When a tubular adhesive lap joint is subjected to a tensile load, the adhesive layer experiences a shear stress and a radial normal stress (peel stress) across the bond length with regions of shear and normal stress concentrations close to the two edges of the overlap. This is illustrated in Figure 6.2 in which shear and normal stress distributions in the adhesive layer in a single lap tubular joint between two aluminum tubes

under a tensile load are shown. The inner tube has an outer diameter of 9.8 mm and both tubes have a length of 40 mm and thickness of 1 mm. The bond length is 10 mm, and bond thickness is 0.2 mm. The results are obtained using OPTISTRUCT solver as described in Chapter 3. A tensile load of 4000 N is applied to the tubular sections. The normalized stress values shown in the figure are obtained by dividing element shear and normal stresses with the average shear stress in the adhesive layer. The stress distributions indicate regions of high shear and normal stresses at the ends of the joint. The leading edge of the joint (at x = 0) has the highest stresses. Normal stress is close to zero across the middle of the bonded region but increases rapidly at the leading edge to its highest value. The magnitude of shear stress is 1.5 times the average shear stress at the leading edge but reduces to about half the average shear stress at the mid-length of the bond. Several previous studies [46, 47] have shown that magnitude and distribution of adhesive stresses are affected by tube and joint parameters.

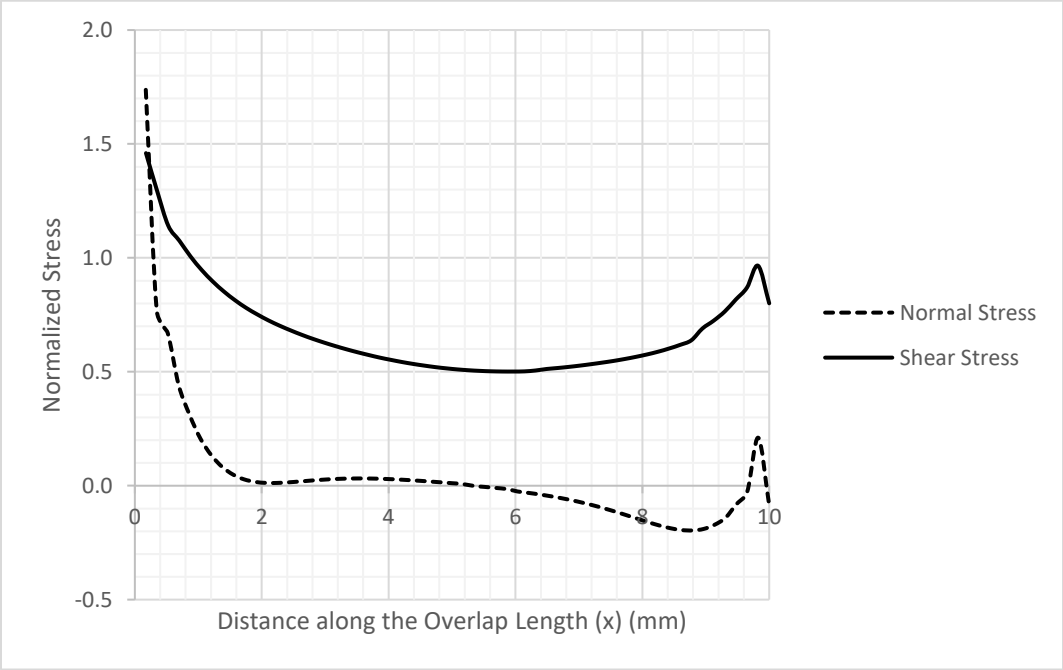

Figure 6.2 Normalized stress distributions across overlap length in an Al-Al tubular joint under tensile load.

The influence of material and joint parameters was further explored under compressive load in Chapter 3. The same is true for tensile load under linear elastic conditions. Tube thickness, overlap length, bond thickness and material properties are seen to significantly influence the magnitude of stresses across the overlap.

6.4.1 Failure Modes of Al-Al Tubular Joints

While understanding stress distribution in the adhesive is important, for design of structural joints it is critical to analyze joint failure and tube deformation characteristics as well. Under tensile loading, two distinct forms of failure are observed in Al-Al tubular joints, one being the tensile failure of the inner Al tube and the other being the failure in the adhesive between the tubes. Since the inner and outer tube thicknesses are the same and the inner tube has a smaller cross-sectional area, it carries a higher axial tensile stress compared to the outer tube. Hence, when tube failure occurs first, it is the inner tube that fails before the outer tube and the failure process includes yielding, plastic deformation, and ultimately fracture of the inner tube.

The two failure modes observed in Al-Al tubular joints with Betamate 1496 adhesive are described below.

6.4.1.1 Tube Failure Mode

Figures 6.3 - 6.6 illustrate the progression of deformation and failure for tube failure mode, variation in the tensile force on the tubular joint, axial stress in the inner Al tube, and stresses in an adhesive element at the leading end of the adhesive layer, each as a function of loading end displacement. The stress curves in Figure 6.5 and Figure 6.6 are plotted with respect to the displacement of tube nodes at the loading end. The numbered sequence of images in Figure 6.4 are correlated with the indicated points on both force, aluminum stress and adhesive stress curves. Initial elastic deformation of tube and adhesive is accompanied by increase in load

with displacement up to 1 mm approximately, when the inner Al tube begins to yield as the combined stress in this tube, plotted in Figure 6.5, reaches 250 MPa, the yield strength of the tube material. Inner tube yielding occurs across one row of elements close to the adhesive overlap. This is reflected in a decrease in applied load as well as stresses in the adhesive. The significant drop in adhesive stresses could be due to a change in strain gradient between the inner and outer tubes post yielding in the inner tube. Further increase in loading results in continued plastic deformation of the inner tube with no major increase in load, which is also accompanied by increasing stresses in the adhesive layer. Decrease in load carried by the joint after 2 mm of displacement reflects necking in the inner Al tube and adhesive failure occurring at the leading edge of the overlap up to 2.9 mm approximately. This is followed by tube failure at 3.1 mm displacement.

In this case, the progression of deformation and failure can be summarized as follows: (1) aluminum tube yielding, (2) initiation of necking in inner tube, (3) beginning of adhesive failure at its leading end, (4) initiation of inner tube failure and (5) inner tube fracture.

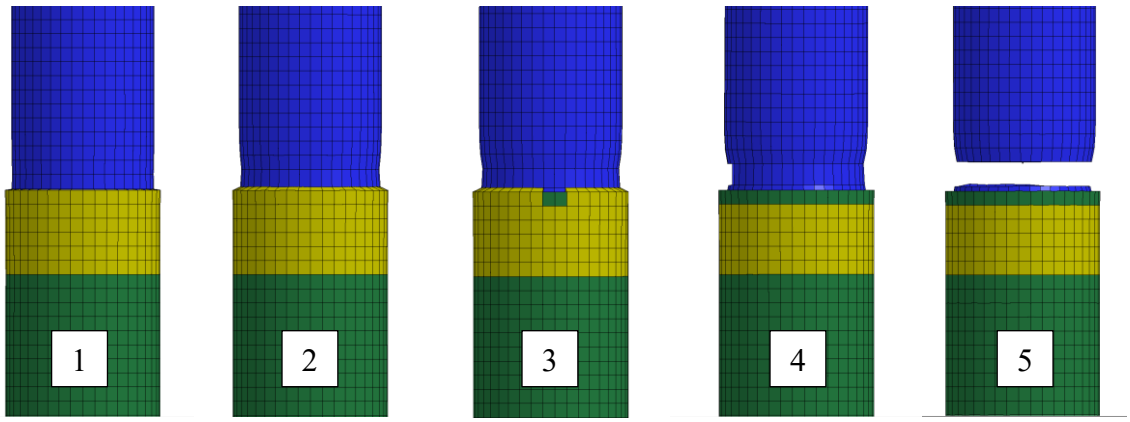

Figure 6.3 Sequence of images illustrating the inner tube failure process under tensile load:(1) tubular joint before load application, (2) inner Al tube is beginning to yield, (3) initiation of adhesive failure, (4) necking in the inner Al tube, and (5) tube fracture. (Tube thickness = 1.6 mm, adhesive thickness = 1.06 mm, overlap length = 15 mm)

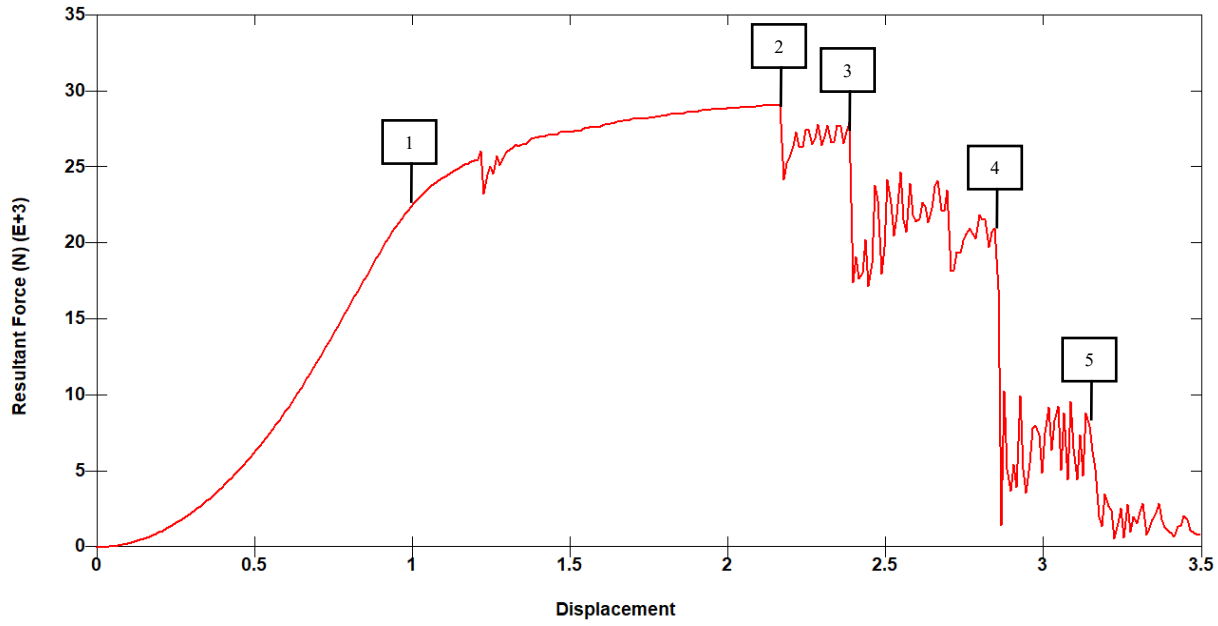

Figure 6.4 Force-displacement curve when the inner Al tube starts to fail before adhesive failure under tensile load.

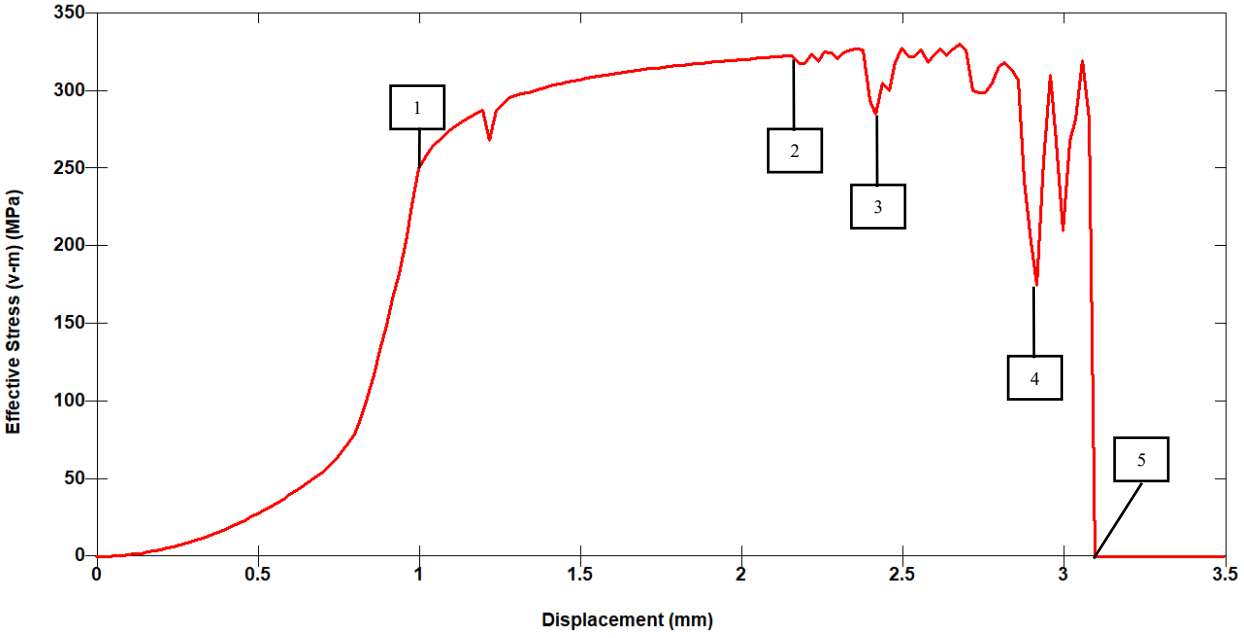

Figure 6.5 Variation in effective stress in an element in the failure region of the inner Al tube versus displacement in the case of tube failure.

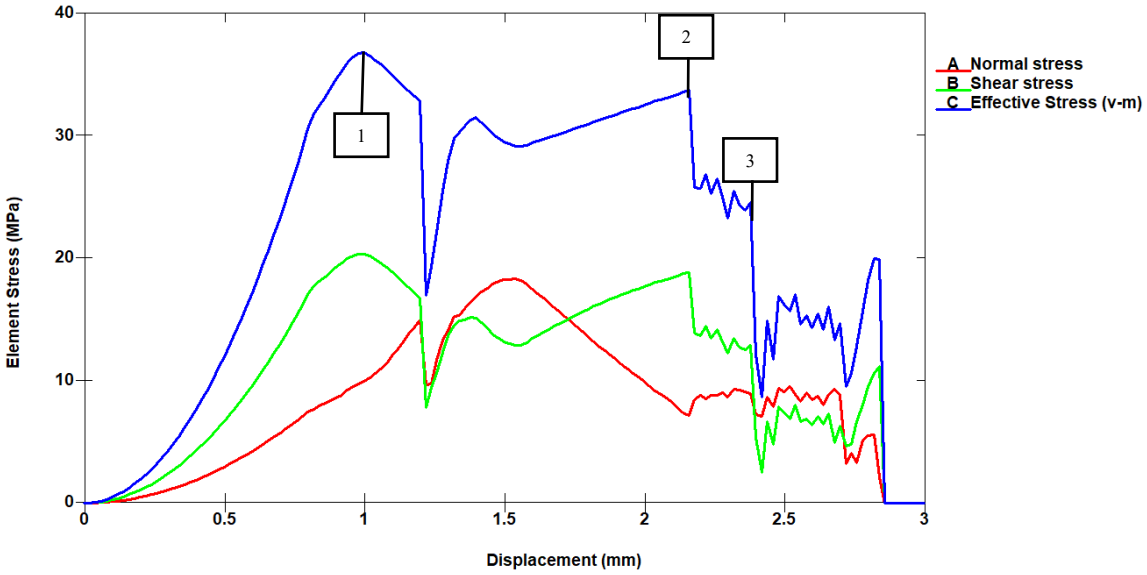

Figure 6.6 Variations of adhesive stresses in an element at the leading edge of the bond versus displacement in the case of tube failure.

6.4.1.2 Adhesive Failure Mode

The second failure mode is the adhesive failure, which is illustrated in Figures 6.7 – 6.10. Figure 6.7 shows the progression of tube deformation and failure in adhesive overlap. Figures 6.8, 6.9 and 6.10 plot the force-displacement, inner tube stress-displacement and adhesive stress-displacement curves, respectively. The adhesive stress plots in Figure 6.9 are for an element at the leading edge of the adhesive overlap, where the highest shear and normal stresses are present. Figure 6.7 shows that the tensile force on the joint increases steadily until the displacement reaches 0.9 mm approximately where it reaches the peak value (1) and then stays at a near constant value until the adhesive failure occurs (2). The tube stress-displacement plot shows a similar curve, but the magnitude of the equivalent stress in the tube remains lower than yield strength of the tube material. The adhesive stress plots in Figure 6.8 indicate that at 0.9 mm displacement (1), the adhesive at the leading edge has reached the yield strength of the adhesive

and is beginning to fail by yielding. Failure in the adhesive layer progresses from its leading edge to the trailing edge until it completely fails (2) at a tube displacement of 1.56 mm.

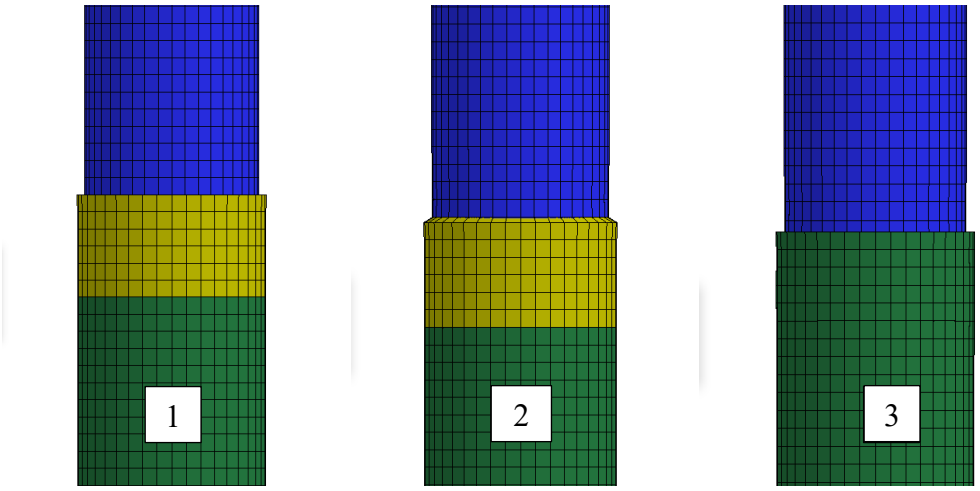

Figure 6.7 Sequence of images illustrating adhesive failure process under tensile load. (1) tubular joint before load application, (2) initiation of adhesive failure, and (3) adhesive failure. (Tube thickness = 2.4 mm, adhesive thickness = 1.06 mm, overlap length = 15 mm)

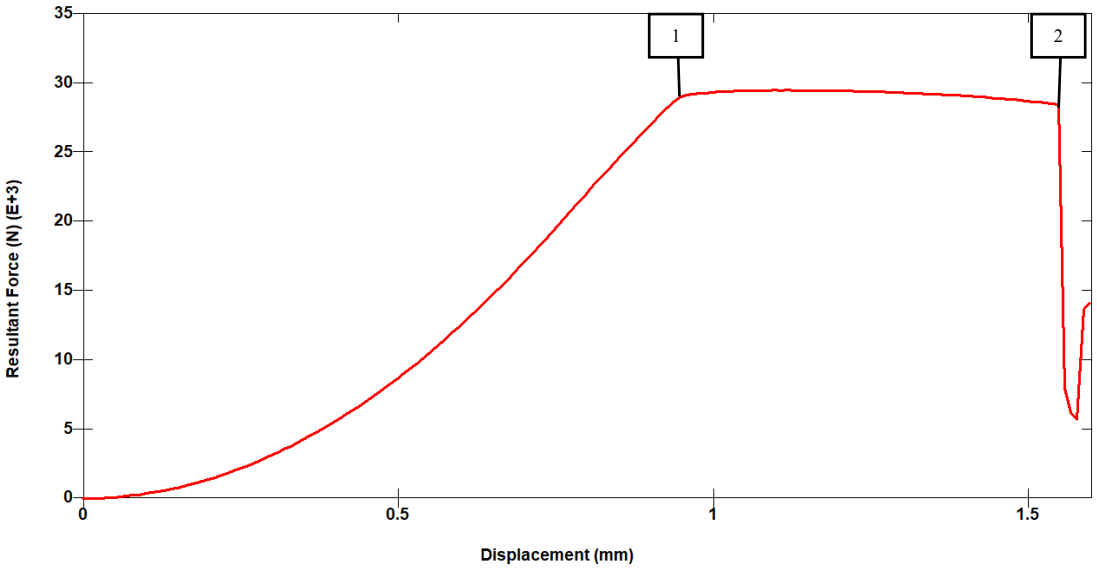

Figure 6.8 Force-displacement curve when adhesive bond fails under tensile load

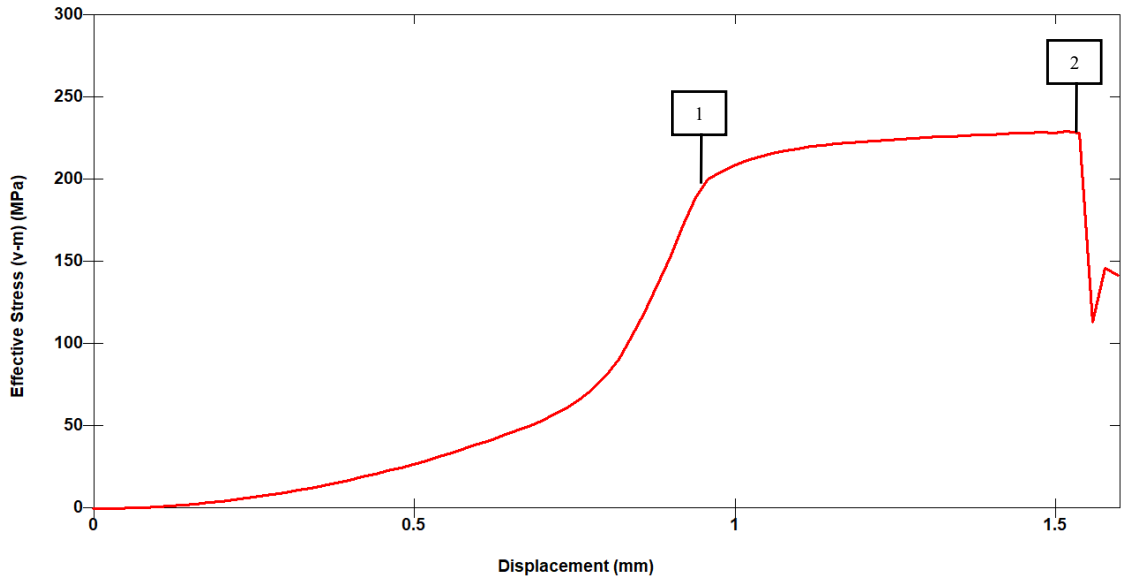

Figure 6.9 Variation in von Mises stress of an element at failure region of the aluminum tube versus displacement of loading end in the case of adhesive failure.

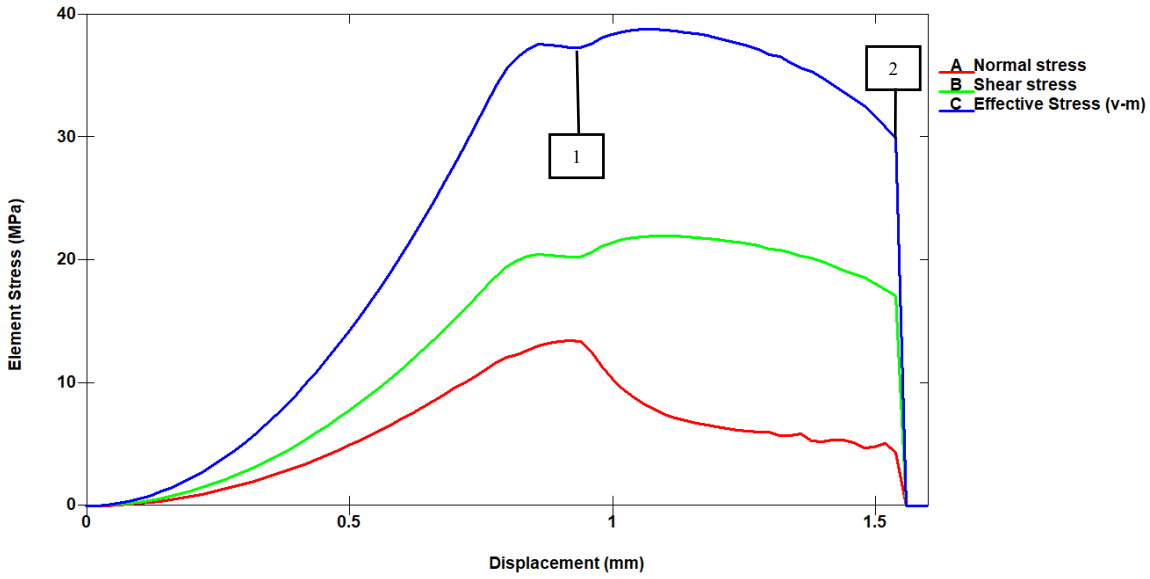

Figure 6.10 Variation in adhesive stresses in an element at the leading edge of the bond versus displacement of loading end in the case of adhesive failure.

A sudden failure of adhesive bond with no significant deformation of aluminum tubes or failure in tubular section without significant deformation or failure initiation in the adhesive are not ideal. Both these cases indicate a higher than necessary thickness of tubes or bond length respectively, depending on design strength requirement. To maximize joint efficiency under tensile load, stresses in either adhesive overlap or tubular section should be close to yielding prior to failure in one of the failure modes. This is affected by material properties and joint geometry. The following section explores influence of overlap length and tube thickness on joint strength.

6.4.2 Effects of Overlap Length, Tube Thickness and Adhesive Thickness

To understand the effects of overlap length and tube thickness on the peak load on Al-Al tubular joints, four different overlap lengths are considered: 10, 15, 20 and 25 mm and for each overlap length, four different tube thicknesses are used: 1.2, 1.6, 2.0 and 2.4 mm. Four different adhesive thicknesses are also considered, namely 0.5, 1.06, 1.5 and 2.0 mm. Results for 10 mm overlap length showed adhesive failure for all four tube thicknesses with 0.5, 1.06, 1.5- and 2.0-mm bond thicknesses. The results of the simulations with overlap lengths 15, 20 and 25 mm are summarized in Table 6.5 and are discussed below.

The results of varying overlap length are shown in Figure 6.11 (a), which plots peak load vs. overlap length for various tube thicknesses. Figure 6.11 (b) plots peak load vs. tube thickness for different overlap lengths. The circled data points in Figures 6.11 (a) and (b) represent configurations with bond failure. At 10 mm overlap length, all tubular joints showed bond failure; at 15 mm overlap length, tubular joints with 2.0- and 2.4-mm tube thickness showed bond failure, and at 20 mm overlap length, the only tubular joint that showed bond failure was with 2.4 mm thick tubes. The rest of the configurations showed tube failure in the inner tube.

Table 6.5 Results of tensile loading of Al-Al tubular joints with different tube thicknesses, bond thicknesses and overlap lengths. (Adhesive: Betamate 1496)

Overlap (mm)	Tube Thickness (mm)	Bond Thickness = 0.5 mm			Bond Thickness = 1.06 mm			Bond Thickness = 1.5 mm			Bond Thickness = 2 mm		
		Pmax (kN)		E (J)	Pmax (kN)		E (J)	Pmax (kN)		E (J)	Pmax (kN)		E (J)
15	1.2	23.4	T	37	23.6	T	37	23.8	T	46	23.9	T	38
	1.6	29.2	T	60	29.1	T	54	28.2	T	61	29.5	T	52
	2.0	29.5	A	28	30	A	31	28.8	A	24	30.8	A	33
	2.4	29.5	A	24	29.5	A	25	29.9	A	26	31.1	A	27
20	1.2	23.6	T	44	24.2	T	46	23.7	T	49	23.9	T	46
	1.6	29.3	T	66	28.7	T	53	29.1	T	65	29.4	T	61
	2.0	34.4	T	75	33.6	T	68	34.5	T	91	34.8	T	81
	2.4	39.5	A	65	39.5	A	68	39.8	A	120	39.8	T	96
25	1.2	23.4	T	36	23.5	T	37	23.6	T	42	23.9	T	37
	1.6	28.9	T	48	29.6	T	51	29.1	T	57	29.3	T	49
	2.0	34.2	T	60	33.7	T	59	34.3	T	69	34.4	T	62
	2.4	39.4	T	71	39.5	T	72	39.6	T	80	39.5	T	84

Note: A = Adhesive Failure, T = Tube Failure

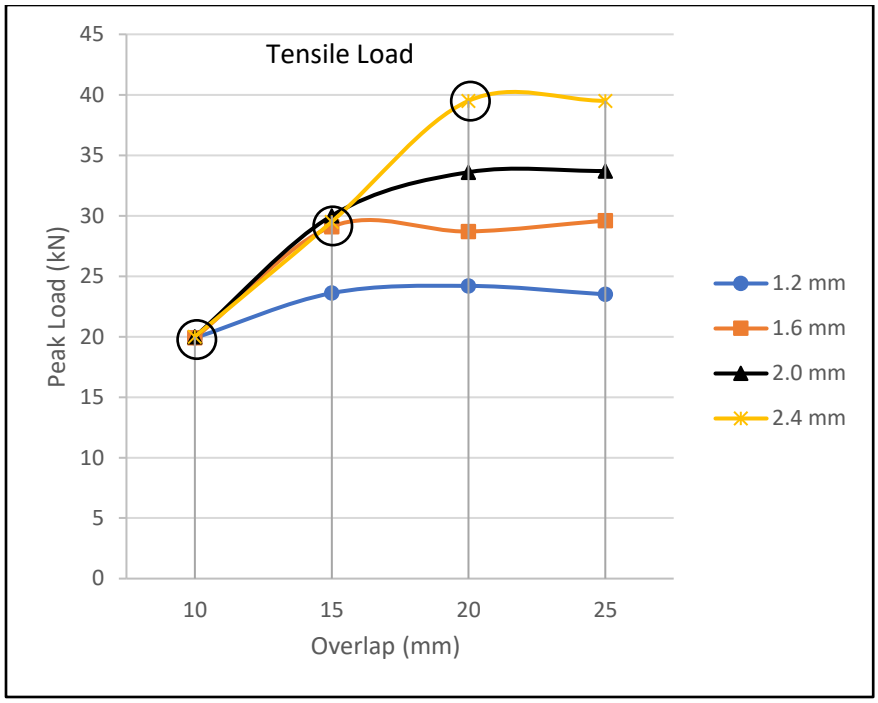

(a)

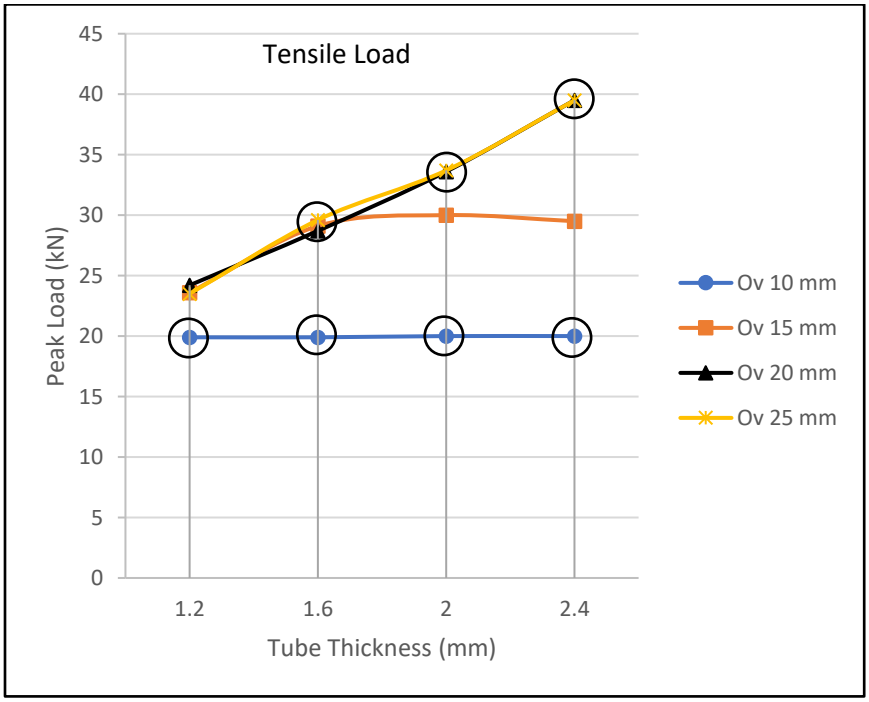

(b)

Figure 6.11 Effect of overlap length (a) and tube thickness (b) on peak load of the joints. (Adhesive thickness 1.06 mm)

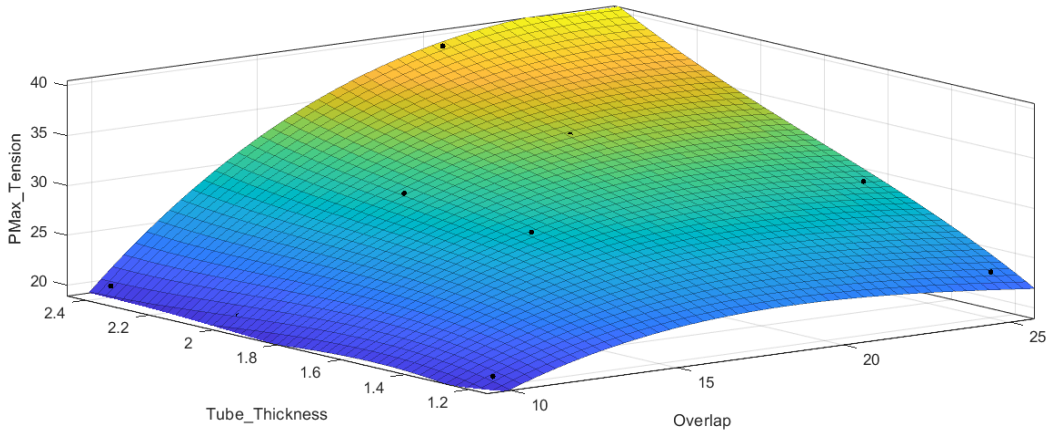

Figure 6.12 Response surface for effect of overlap length and tube thickness on peak load under tension.

Figures 6.11 (a) and 6.11 (b) show that the peak load on the tubular joint increases with overlap length and tube thickness. In two cases which show adhesive failure increase in overlap length or tube thickness did not result in an increase in tensile strength. They are joint configurations of 1.6 mm tubes with 15 mm overlap and 2.4 mm tubes with 20 mm overlap. In the first case, despite tube failure, increasing tube thickness did not result in any change to the strength. Hence, it is evident that tube and bond strength is maximized in this configuration. In the second case, with 2.4 mm thick tubes joint fails at approximately the same load with 20- and 25-mm overlap lengths albeit due to joint failure and tube failure respectively. Both these configurations indicate ideal combination of tube thickness and overlap length. Considering 1.2 mm tubes and 2.0 tubes, results show tubular strengths are between overlap levels of 10-15 mm and 15-20 mm respectively. Hence, they show further increase in strength with increase in overlap and then plateau.

Figure 6.12 plots a response surface for peak load under tension with different tube thicknesses and overlap lengths. The empirical expression (Equation 6.1) shown below is used to fit the response data.

$$PMax\_Tesnion = -19.91 + 1.391x + 42.92y - 0.1015x^2 + 1.759xy - 30.94y^2 + 0.001899x^3 - 0.04372x^2y + 0.1956xy^2 + 4.753y^3 \quad \text{Eq. 6.1}$$

Where, x is overlap length and y is tube thickness in mm. The response, peak load under tension is in kN. The R-square value for the equation is 0.9784 which represents a reasonably good fit for the data.

Among the different configurations of tube thickness and overlap length 1.6 mm tubes with 15 mm overlap and 2.4 mm tubes with 20 mm overlap are the most efficient. Design choice among the two can be made based on strength requirement.

6.4.3 Effect of Adhesive Properties

A crash optimized adhesive, Betamate 1496 and a brittle adhesive AV 138 were considered for aluminum-aluminum tubular lap joints with a bond thickness of 1.06 mm. As mentioned in Chapter 4, the two adhesives have similar behavior under mode I deformation. But under mode II loading, Betamate 1496 shows an elastic-plastic behavior with a much lower shear strength compared to AV 138 which shows a linear behavior up to failure. The modulus of the brittle adhesive is also much higher. The results of different joint configurations with two adhesives are listed in Table 6.6. Most of the joints with brittle AV 138 adhesive show bond failure under tensile load. Another feature of the results is the low energy absorption values due to brittle nature of the adhesive. Figure 6.13 illustrates load-displacement curve for a joint with brittle adhesive. The curve shows an approximately linear load-displacement curve followed by a sudden drop in load due to adhesive failure. The star marker at approximately 0.8 mm displacement indicates point at which adhesive failure began.

Stresses in the adhesive also show a similar behavior as shown in Figure 6.14. The figure plots normal and shear stress in an element at the leading end versus displacement. Both shear and normal stresses show an almost linear increase in magnitude prior to failure. The star marker

on the shear curve indicates point of damage initiation in the adhesive. Unlike a crash optimized adhesive like Betamate which shows significant shear plateau after yielding, the brittle adhesive fails quickly after damage initiation as seen here.

Table 6.6 Results of tensile loading of Al-Al tubular joints with Betamate 1496 and AV 138 adhesives (Adhesive thickness = 1.06 mm).

Overlap (mm)	Tube Thickness (mm)	Betamate 1496			AV 138		
		Pmax (kN)	Failure Mode	E (J)	Pmax (kN)	Failure Mode	E (J)
10	1.2	19.9	A	23.1	18.5	A	7.1
	1.6	19.9	A	18.4	20.6	A	5.2
	2	20	A	16.2	20.9	A	3.9
	2.4	20	A	15.4	20.7	A	3.2
15	1.2	23.6	T	37.1	22.9	A	30.9
	1.6	29.1	T	54.1	22.5	A	6.6
	2	30	A	31.1	26.5	A	7.2
	2.4	29.5	A	24.8	26.1	A	5.3
20	1.2	24.2	T	46.3	23.9	A	35.9
	1.6	28.7	T	52.9	21.7	A	5.8
	2	33.6	T	68.2	26.4	A	6.9
	2.4	39.5	A	67.9	37.3	A	29.7
25	1.2	23.5	T	37.3	22.9	T	34.9
	1.6	29.6	T	51.0	21.4	A	5.3
	2	33.7	T	59.0	26.4	A	6.8
	2.4	39.5	T	71.9	38.7	T	29.8

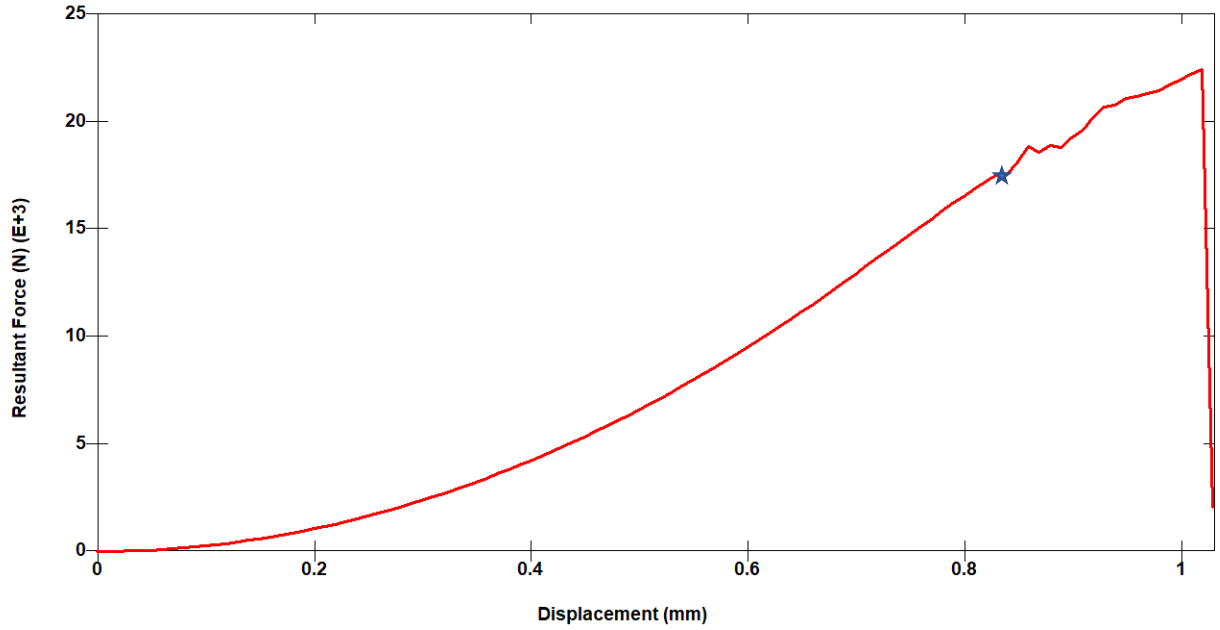

Figure 6.13 Force Displacement curve when tube fails under tensile load with AV 138 adhesive bond. Al tube thickness 1.6 mm and overlap length 15 mm.

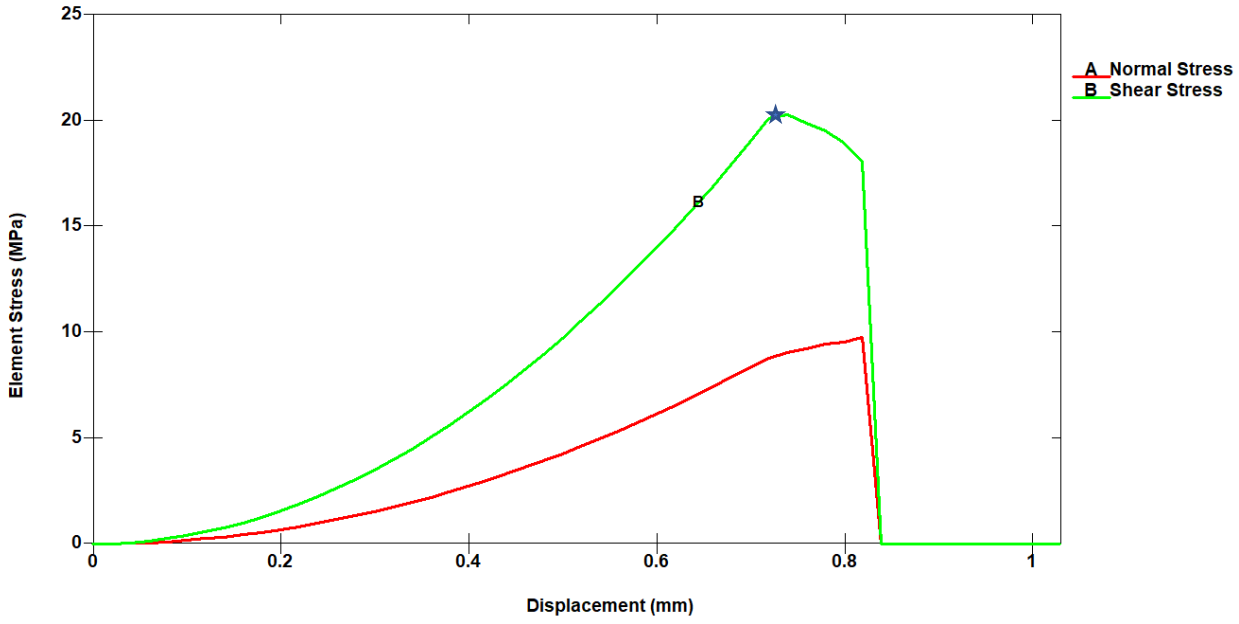

Figure 6.14 Variation in stress of an element at leading edge of the bond versus displacement of loading end in the case of adhesive failure with AV 138 adhesive bond. Al tube thickness 1.6 mm and overlap length 15 mm.

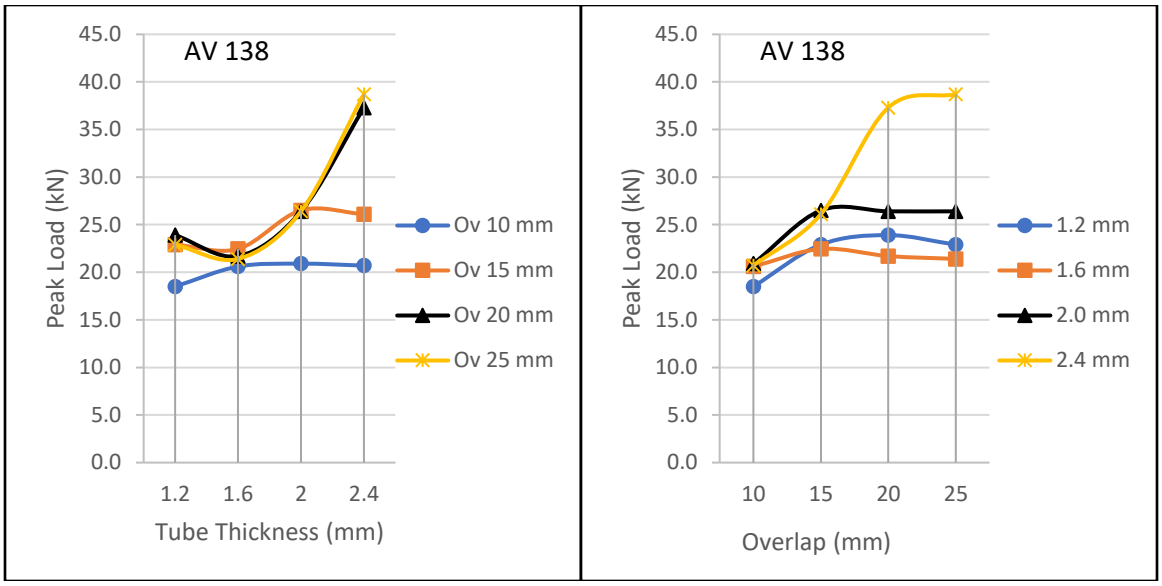

(a) (b)

Figure 6.15 Effect of (a) tube thickness and (b) overlap length with AV 138 adhesive.

Figure 6.15 illustrates the effect of overlap length and tube thickness on peak load under tension in joints with a brittle adhesive. Like the Betamate adhesive, there is an increase in peak load with increasing overlap length followed by a plateau at each tube thickness. Results indicate significant influence of tube thickness on peak load. Increase in tube thickness corresponds to a significant increase in peak load particularly for tubular section with 2.4 mm thick tubes which show the highest peak load with an overlap length of 25 mm. This could be due to a combination of higher shear stress in the bond with thicker tube along with higher shear strength of the adhesive resulting in greater bond strength. Also, the same factors result in higher peak load prior to bond failure at a particular overlap length with increasing tube thickness.

6.4.4 Effect of Loading Rate

The simulations in Sections 6.4.1 –6.4.3 were conducted with a top end nodal velocity of 1 mm/s which can be considered a quasi-static loading rate. Since mechanical properties of both 6061-T4 aluminum alloy and Betamate adhesive are strain rate sensitive, an increase in loading

rate will influence their response to stresses caused by tensile loading, and hence the performance of the joint. Strain-rate sensitivity of the aluminum alloy affects its yield strength and is modeled using Cowper-Symonds equation. In the case of the adhesive, both yield strength and fracture energy of the material are rate sensitive and are modeled using a log-linear model specified in LS-Dyna as described in Chapter 4. To study the effect of high loading rate, the top end nodal velocity is increased to 1 m/s and the joint performance is determined for different joint configurations considered under quasi-static loading rate of 1 mm/s. The adhesive thickness is maintained at 1.06 mm.

The results of the simulations at 1 m/s are plotted in Figure 6.16. Unlike the results at 1 mm/s shown in Figure 6.11 and 6.12, the peak load of the joint at 1 m/s increases with increasing tube thickness but is not affected by the overlap length. Adhesive failure is observed only in the case of 2.4 mm thick tubes with 10 mm overlap length. For the same overlap length, joints with 2.0 mm thick tubes showed more than 50% adhesive failure prior to tube failure. Other joint configurations showed tube failure with no significant adhesive failure. Hence, an increase in overlap length shows no significant increase in the peak load.

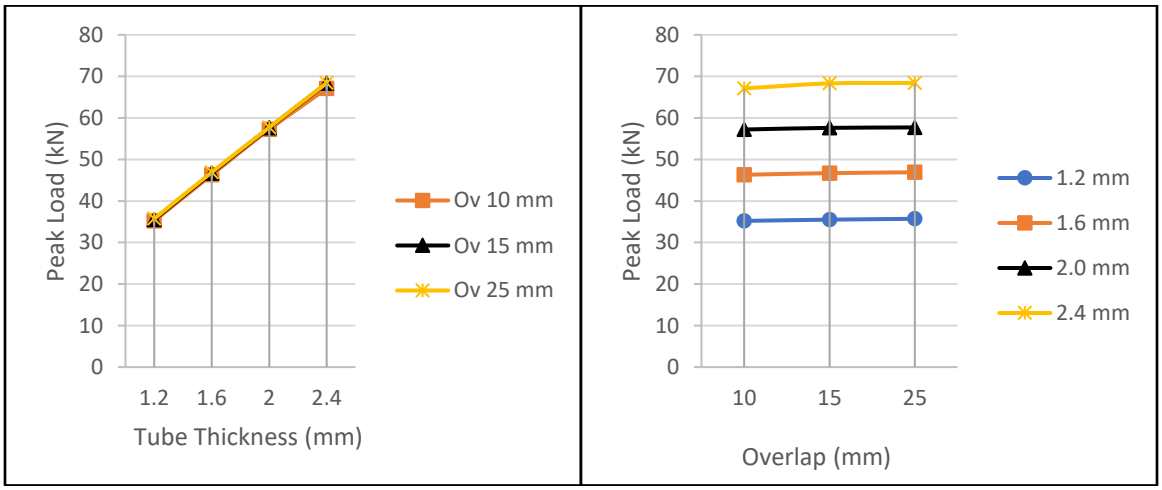

(a) (b)

Figure 6.16 Variation in peak load versus tube thickness (a) and overlap length (b) at 1 m/s loading rate.

Comparing the results at loading rates of 1 mm/s and 1 m/s, it is observed that occurrence of adhesive failure at 1m/s is limited to 10 mm overlap compared to quasi-static results where even with 20 mm overlap shows bond failure albeit at higher tube thickness. This is due to relatively low strain rate sensitivity of the aluminum alloy compared to the adhesive used in this study. Therefore, tubular adhesive lap joints show a better performance at higher loading rates compared to quasi-static applications. A simulation with hypothetically no strain rate sensitivity of the adhesive and aluminum modeled with rate sensitivity showed bond failure for all overlap lengths at 2.4 mm tube thickness.

6.4.5 Composite-Aluminum Tubular Joints

For composite-Al joints, the inner tube is the T700 carbon fiber/ epoxy composite with a layup of $[0/90]_{8s}$ and the outer tube is aluminum. Composite inner tube thickness is 2.16 mm for all joints and aluminum outer tube thickness is varied from 1.2 to 2.4 mm. Betamate 1496 is used as the adhesive and its thickness is 1.06 mm. The loading rate is 1 mm/s. Table 6.7 compares the peak loads of composite-Al and Al-Al tubular joints for different joint configurations. Results show that adhesive failure as the main failure mode for the composite-Al joints and the peak loads at which adhesive failure occurs in composite-Al joints are similar to the peak loads at which adhesive failure occurs in Al-Al joints. Outer Al tube failure occurs only for composite-Al joints with 1.2 mm thick Al outer tube and overlap lengths of 20 and 25 mm. In these two cases, the outer tube failure is by necking followed by fracture, similar to the inner tube failure in Al-Al joints. Hence, there is significantly high energy absorption for these joints.

Composite inner tube failed in the 25 mm overlap joint with 1.6 mm thick Al outer tube due to significant radial plastic deformation of Al tube. Figure 6.17 plots the force-displacement

curve for a joint with composite tube failure. The sequence of failure is as follows: (1) aluminum tube yielding followed by plastic deformation of Al tube and (2) composite tube failure. The von Mises stress in aluminum and composite tubes for an element close to the bonded region are plotted in Figures 6.18 and 6.19. Figure 6.20 shows the variation in adhesive stress. The composite tube is subjected to high axial stress in addition to radial stress due to Al plastic deformation. This results in a sharp increase in composite tube stress prior to failure as seen in Figure 6.19. The radial deformation of Al also results in a relatively high normal stress in the adhesive as seen in Figure 6.20. Similar process is observed in joint with 1.2 mm thick Al tube. However due to lower Al tube thickness, its strength is lower and Al tube fails prior to significant composite damage. For joints with higher thickness do not show sufficient Al radial deformation after yielding.

Table 6.7 Results comparing Al-Al and $[0/90]_{8s}$ composite-Al tubular joints under tensile loading (Adhesive: Betamate 1496, Adhesive thickness = 1.06 mm, Composite tube thickness = 2.16 mm).

Overlap (mm)	Al Tube Thickness (mm)	Al-Al Tubes			Composite-Al Tubes		
		Pmax (kN)	Failure Mode	E (J)	Pmax (kN)	Failure Mode	E (J)
10	1.2	19.9	A	23.1	19.9	A	16.6
	1.6	19.9	A	18.4	20.0	A	16.2
	2	20	A	16.2	20.0	A	15.7
	2.4	20	A	15.4	20.0	A	15.6
15	1.2	23.6	T	37.1	29.9	A	47.7
	1.6	29.1	T	54.1	30.0	A	26.3
	2	30	A	31.1	30.0	A	25.6
	2.4	29.5	A	24.8	30.0	A	25.1
20	1.2	24.2	T	46.3	32.2	OT	237.5
	1.6	28.7	T	52.9	40.1	A	64.6
	2	33.6	T	68.2	40.1	A	37.1
	2.4	39.5	A	67.9	40.1	A	35.9
25	1.2	23.5	T	37.3	32.2	OT	227.6
	1.6	29.6	T	51.0	42.6	T	129.6
	2	33.7	T	59.0	50.1	A	80.7
	2.4	39.5	T	71.9	50.1	A	48.0

A: Adhesive Failure, T: Inner Tube Failure, OT: Outer Tube Failure

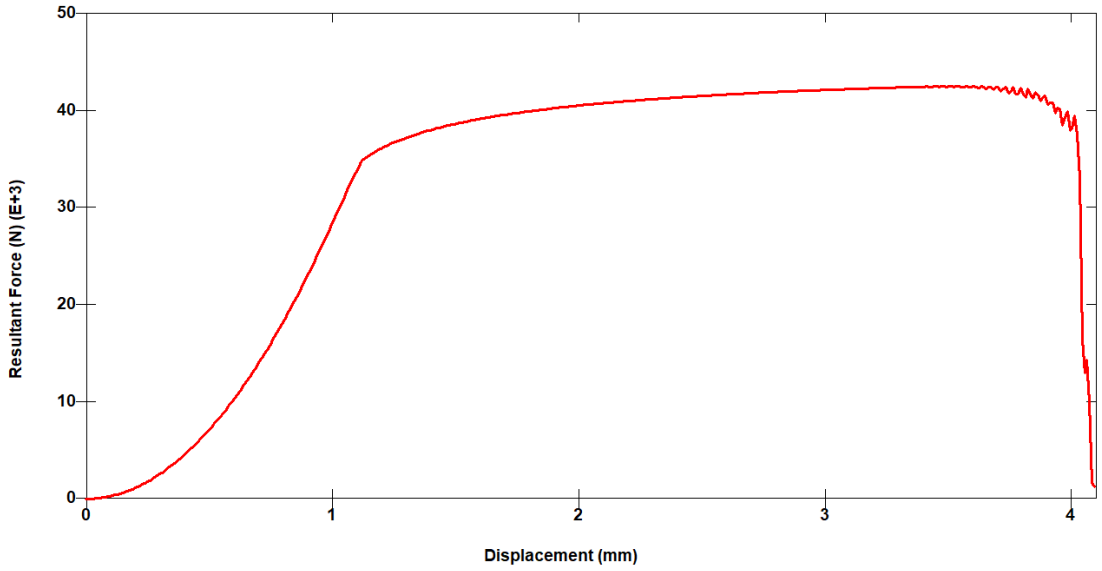

Figure 6.17 Force -displacement curve when adhesive fails under tensile load for composite-Al joint. Al tube thickness 1.6 mm, composite tube thickness 2.16 mm and overlap length 25 mm.

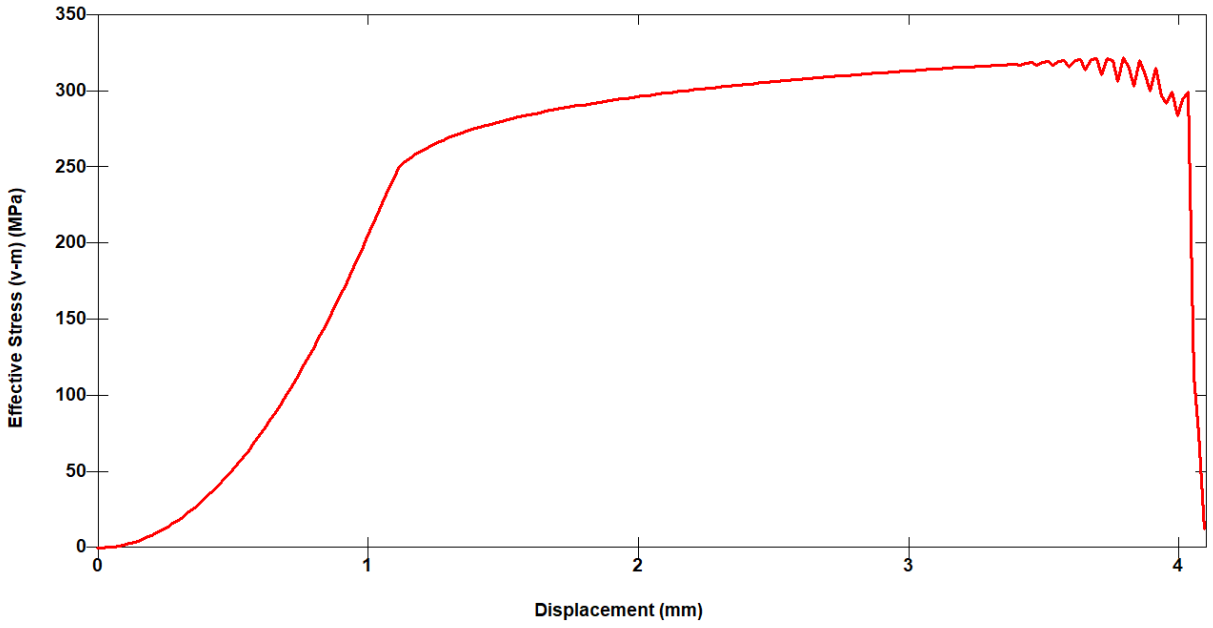

Figure 6.18 Variation of stresses in the aluminum tube for composite- Al joint. Al tube thickness 1.6 mm, composite tube thickness 2.16 mm and overlap length 25 mm.

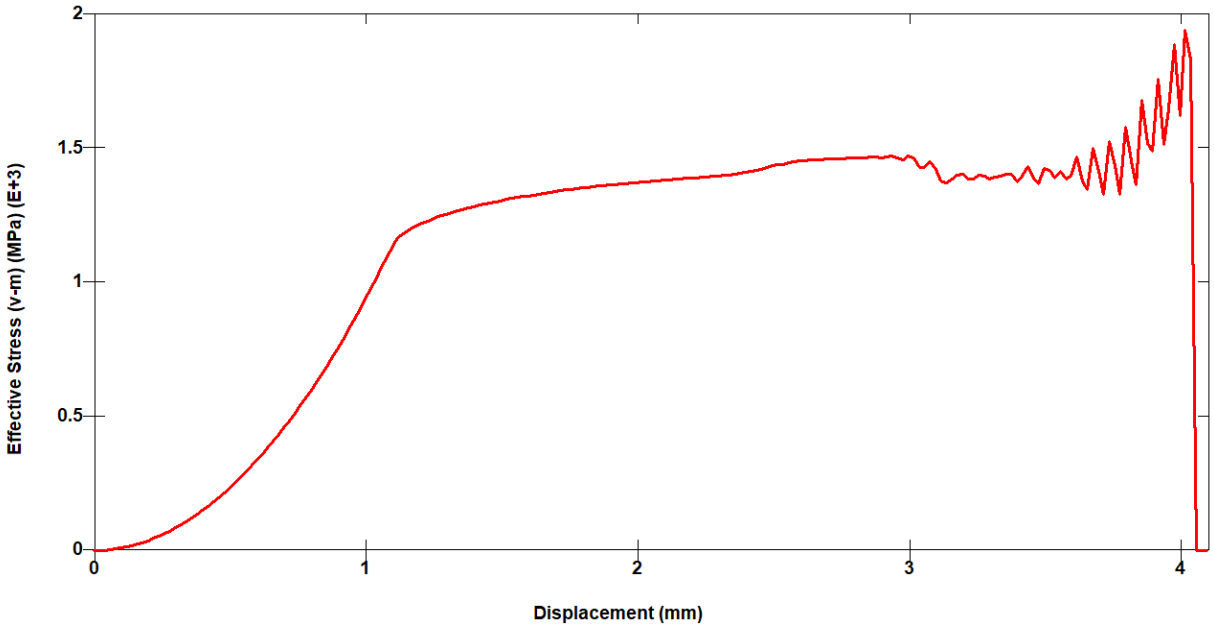

Figure 6.19 Variation of stresses in composite tube for composite- Al joint. Al tube thickness 1.6 mm, composite tube thickness 2.16 mm and overlap length 25 mm.

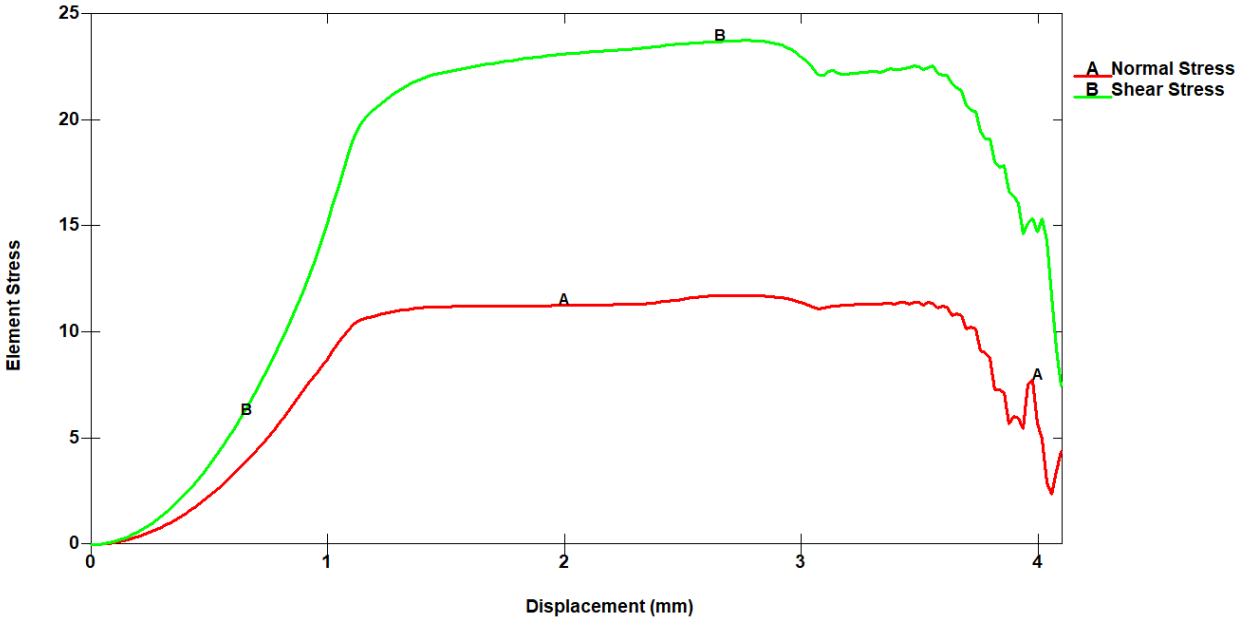

Figure 6.20 Variation of adhesive stresses in an element at leading edge of the bond versus displacement of loading end in the case of adhesive failure for composite-Al joint. Al tube thickness 1.6 mm, composite tube thickness 2.16 mm and overlap length 25 mm.

Figure 6.21 plots the force-displacement curve for a composite-Al joint under tension for the case of adhesive failure. It shows a steady increase in load up to a displacement of approximately 1 mm and then the load remaining constant until the adhesive layer fails. This behavior is similar to that observed in Al-Al joints that show adhesive failure. The adhesive stress-displacement plots shown in Figure 6.22 and tube stress-displacement plot in Figure 6.23 also have similar trends. The adhesive shear stress at the leading edge of the overlap increases up to a displacement of 1 mm which is then followed by a shear plateau and then failure at about the same displacement where the joint has failed. In composite-Al joints the magnitude of peel or normal stress is much lower compared to that in Al-Al joint with the same joint configurations.

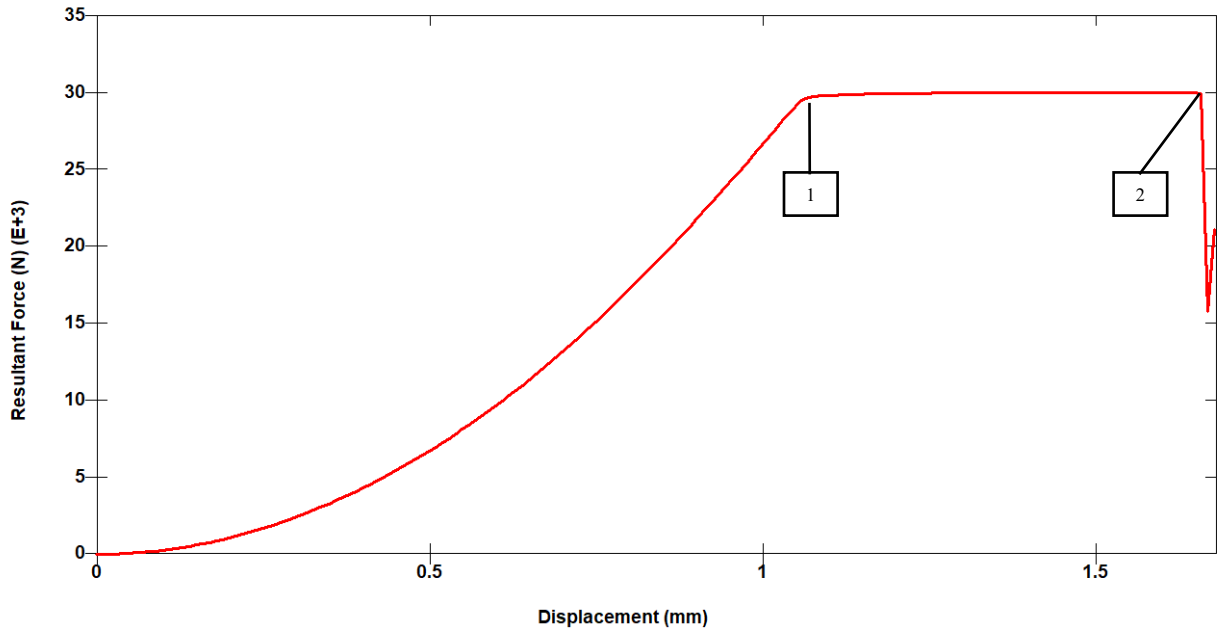

Figure 6.21 Force -displacement curve when adhesive fails under tensile load for composite-Al joint. Al tube thickness 1.6 mm, composite tube thickness 2.16 mm and overlap length 15 mm.

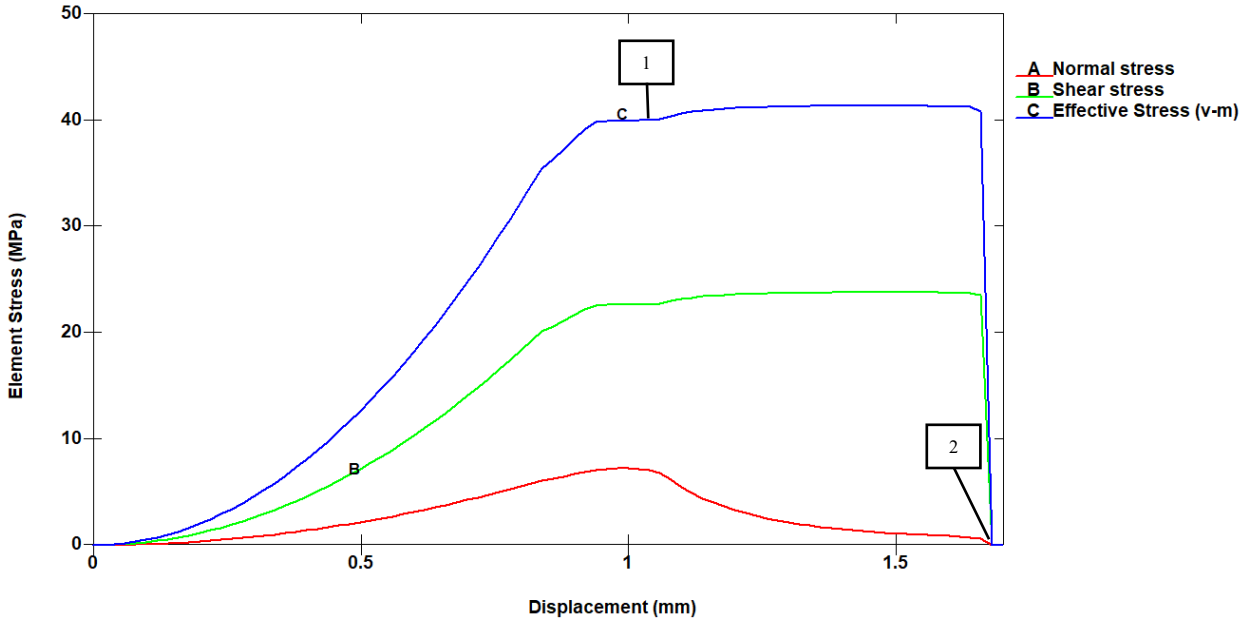

Figure 6.22 Variation of adhesive stresses in an element at leading edge of the bond versus displacement of loading end in the case of adhesive failure for composite-Al joint. Al tube thickness 1.6 mm, composite tube thickness 2.16 mm and overlap length 15 mm.

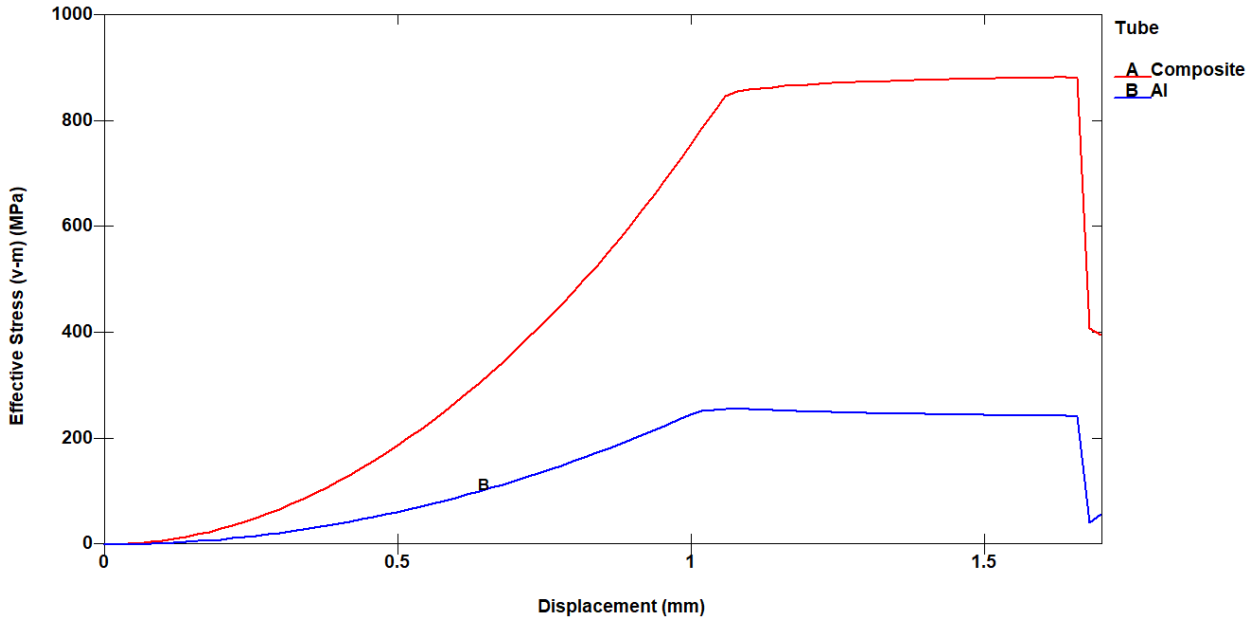

Figure 6.23 Variation of stresses in composite and aluminum tubes for composite-Al joint. Al tube thickness 1.6 mm, composite tube thickness 2.16 mm and overlap length 15 mm.

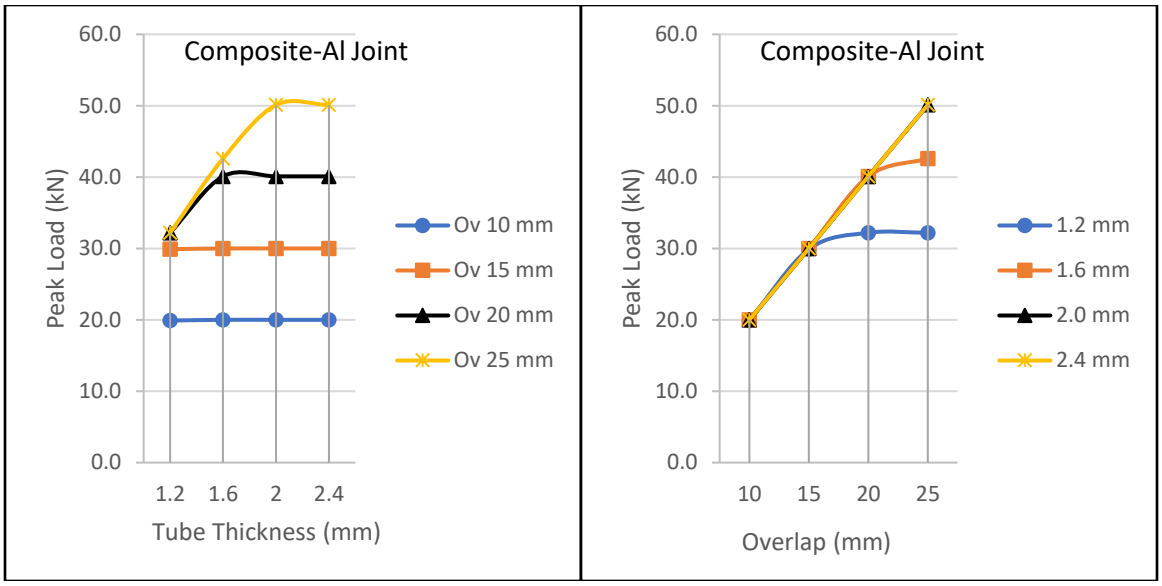

(a) (b)

Figure 6.24 Effect of (a) tube thickness and (b) overlap length for composite-Al joints.

Figures 6.24 (a) and (b) illustrate the influence of tube thickness and overlap length on peak load under tension for composite-Al joints. Tube thickness has no influence on peak load at low overlap length of 10 and 15 mm due to adhesive failure prior to yielding or tube failure. At higher overlap lengths, there is an increase in peak load followed by a plateau where the tensile stress in the composite tube reaches the strength of the composite and it fails.

6.5 Joint Design for Maximum Performance under Tensile Load

Tubular members used in structural applications are designed to withstand a variety of load conditions. This is true for tubular joints used in structural applications as well. Performance of the tubular adhesive lap joint under axial tension and compression is studied in this research. It is shown in Chapter 4 that for Al-Al tubular joints under compressive loading, tube thickness ratio and tube length ratio influence crush characteristics in addition to the parameters discussed so far in this chapter. Tube thickness is seen to play a significant role in tensile performance; hence it is possible for thickness ratio to also influence peak tensile load of the joint. To further

understand the influence of tube geometry, overlap and interaction between various geometric parameters in Al-Al joints under tensile loading, a DOE-based simulation plan is drawn up and carried out. The plan includes three variables: tube thickness ratio, t_i/t_o, at three levels (0.75, 1 and 1.33), tube length ratio, L_i/L_o, at three levels (0.75, 1 and 1.33), and overlap length at two levels (25 and 35 mm). These variables and their levels are the same as those investigated in the DOE-based study for optimum crush load performance in Chapter 4.

Figure 6.25 illustrates the peak tensile load results for different joint configurations. In all these simulations, the joint failure is due to inner Al tube failure. Overlap length and length ratio show no influence on peak load as expected. Results in section 6.4.2 have shown that tubes with 1.6- and 1.2-mm thick tubes do not fail by adhesive failure with overlap greater than 10 mm, hence the current set of overlap levels show no change in results. Changes in length ratio also has no impact on the joint strength under tensile load as there are no complex modes of deformation unlike crush. As load increases wither bond fails or tube fails, and tube failure is only governed by load and cross-sectional area. The length of tube plays no role in affecting failure load. Changes to thickness ratio do not change failure mode since cross-sectional area of the outer tubes remains higher in all cases, even with thicker inner tube. The strength of the joint however decreases when ratio is 0.75 since thickness of inner tube is limiting factor and is lower at 1.2 mm compared to other cases with 1.6 mm thickness.

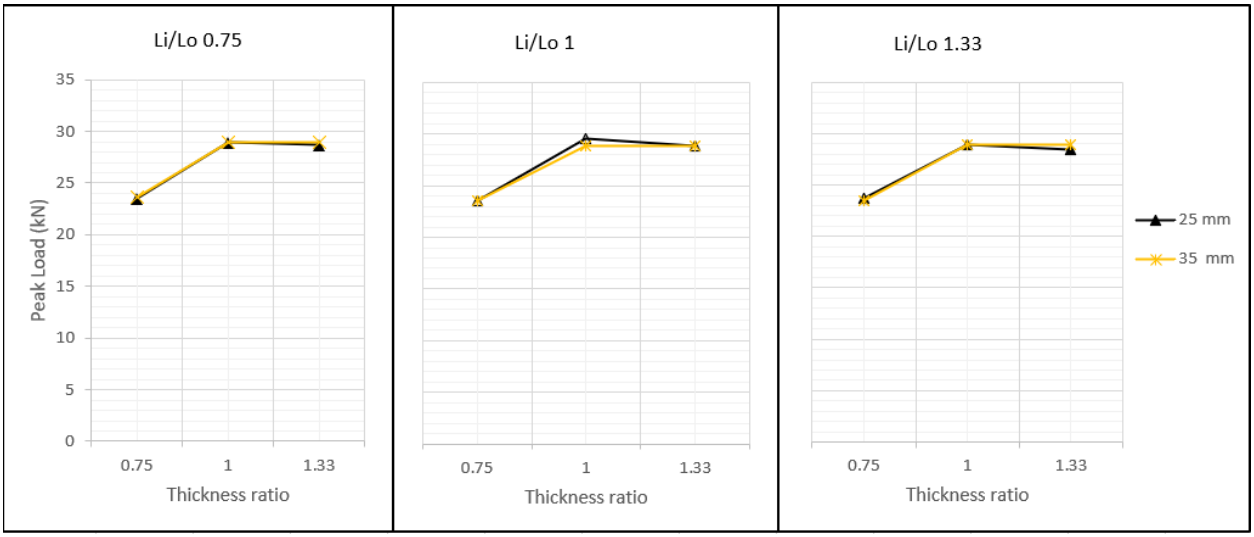

Figure 6.25 Variation in tensile strength with thickness ratio, length ratio and overlap length.

The critical parameters for design of joint subjected to both tension and crush are overlap length, tube thickness particularly inner tube and impact speed. For higher energy absorption a higher overlap length is preferred, and tube length and thickness ratios also have a positive influence on crush characteristics. Hence, comparing results of crush and tensile load on this set of joint configurations we can conclude that design for crush characteristics is more critical as it has a greater number of parameters influencing performance.

6.6 Conclusions

This chapter explored strength and failure characteristics of tubular adhesive lap joints under tensile load using finite element analysis. Depending on the tube diameter, tube thickness and overlap length, the Al-Al joints show two different failure modes under tensile loading: adhesive failure and inner tube failure. The key joint design parameters affecting the peak tensile load are overlap length and tube thickness. Increase in overlap length increases joint strength up to a certain limit and then plateaus. Similarly, with increase in thickness failure load increases and plateaus. In both cases, the limit is set by tube yield or failure load and adhesive

yield or failure load respectively. Change in adhesive thickness has little influence on peak load or failure characteristics.

Adhesive properties are seen to have a significant influence on failure load and characteristics. Tubular sections with brittle adhesive showed bond failure across all overlap lengths considered here. The tensile failure load is observed to increase with overlap length and tube thickness.

Increase in impact speed also increases joint strength and is also seen to improve bond performance as adhesive used in this study exhibits a much higher positive strain rate sensitivity compared to the aluminum tube.

Multi-material joints with composite inner tube and aluminum outer tube largely failed at the bond due to much higher strength of composite laminate. Such joints also showed increase in peak load with bond length.

If a tubular joint is expected to perform under tensile and compressive load, then design for optimal crush characteristics is more important unless there is a specific tensile strength requirement.

Chapter 7 Conclusions

7.1 Conclusions

The dissertation has presented the performance characteristics of crush- resistant tubular adhesive lap joints in aluminum and composite tubes under compressive and tensile loads. A commercial finite element software was used to simulate and analyze deformation and failure modes for of aluminum-aluminum, composite-composite and aluminum-composite tubular joints with different adhesive materials and geometric configurations. A cohesive zone model was used to model the adhesive failure behavior.

To start with, a linear elastic finite element analysis of the bonded region was conducted to gain insight into the stress distributions in the adhesive layer in tubular joints subjected to an axial compressive load. Adhesive overlap exhibits regions of shear stress concentrations at the overlap ends and relatively low shear stress across the bond length. Unlike tensile loading on the joint, compressive loading creates high compressive radial normal stresses at the leading overlap edge. Depending on adhesive thickness, the normal stress at the trailing edge is either compressive or tensile. Normal Stress values are higher at the leading edge compared to trailing edge. The study provides details on the influence of tube and overlap geometry, tube material modulus and adhesive modulus on the magnitude and nature of shear and radial normal stress distributions across the adhesive bond. Critical joint design parameters are found to be tube material modulus, tube thickness, adhesive thickness and overlap length.

A non-linear finite element model of the joint was developed to understand the crush characteristics and failure modes of aluminum-aluminum tubular joints under compressive load. A comparison of brittle and crush resistant adhesives illustrated the importance of adhesive ductility in the design of crush resistant joint. Overlap length, tube length and tube thickness are seen to play significant roles in determining whether or not the joint will fail by failure of the adhesive, folding of the aluminum tube or buckling of the aluminum tube. To understand the influence of different variables, a Design of Experiments approach was adopted. Variables considered for the study were inner-to-outer tube length ratio, inner-to-outer tube thickness ratio, adhesive overlap length, adhesive thickness and loading rate. The following conclusions were reached upon comparing results of different joint configurations: longer overlap improves crush characteristics as it promotes a more progressive crush behavior, longer and thinner inner tubes provide the highest energy absorption and peak load values, and a higher loading rate has a positive influence on the joint performance, particularly on the peak crush load. Best performance at higher speeds is observed for equal tube length and thickness with longer overlap length. Also, an increase in adhesive thickness has a negative influence on joint performance parameters.

The non-linear analysis was extended to analyze the crush characteristics of aluminum-composite and composite-composite tubular joints. Depending on the joint configuration, these tubular joints show three different failure modes: composite tube crush, aluminum tube folding and adhesive failure. In general, aluminum-composite joints in which aluminum tube folding occurs before the composite tube fail by crushing exhibit the highest energy absorption. In cases with progressive adhesive failure, plastic deformation of the aluminum tube continues in a stick-slip manner as it penetrates the composite tube. Overlap length and tube thickness show

significant influence on the joint performance Cross-plied and quasi-isotropic composite tube constructions were compared for their crush performance. Joints with cross-plied composite fail by crushing at a higher peak load while quasi-isotropic composite show a lower energy absorption.

In aluminum-aluminum tubular joints subjected to an axial tensile load, two different failure modes are observed, inner tube failure and adhesive failure. Critical parameters are overlap length and tube thickness. Increasing these two parameters produces an increase in joint strength until a plateau is reached as the joint failure mode changes from adhesive failure to inner tube failure. In composite-aluminum joints with composite inner and aluminum outer tubes, the principal failure mode is adhesive failure. An increase in joint strength also occurs as the outer aluminum tube thickness is increased relative to the inner composite tube thickness.

7.2 Intellectual Merit and Broader Impact

The existing literature on tubular adhesive lap joints is limited to studies on stress analysis in the adhesive or failure characteristics with brittle adhesives under tensile and torsional loads. Studies on structural or crash optimized adhesives are focused on the performance of simple lap joints which are largely used in panel or box sections. There is a lack of research on multi-material tubular adhesive lap joints in structural applications as explained in Chapters 1 and 2. This dissertation presents analysis of tubular adhesive lap joints with a crash-optimized ductile adhesive. Crush and tensile characteristics of tubular sections with adhesive lap joints are analyzed parametrically for different materials and geometries. Guidelines for tube and joint geometry selection are presented for improved crush performance.

The findings of this study can provide helpful insight for the design and performance of adhesively bonded lightweight tubular joints of aluminum and carbon fiber composites for

safety-related automotive structures, such as front rails and roof rails. The results of this study can also be applied in the structural design of other ground transportation vehicles such as trains, buses, and trucks where the use of lightweight materials, such as aluminum and composites are expected to grow. The adoption of multi-material designs with aluminum, composite and other lightweight materials in the transportation industry will lead to increase in fuel economy, load carrying capacity and reduction in greenhouse gas (GHG) emissions.

7.3 Scope for Future Work

Finite element models for crush resistant tubular adhesive lap joints between similar and dissimilar tubes was successfully developed in this dissertation and the critical parameters affecting their performance were determined. Future work will aim to experimentally verify the results presented in this dissertation. Quasi-static and impact testing of composite and aluminum tubular lap joints under crush and tensile loads will help to verify the results presented here. Different joint and tube geometries can also be considered for the experimental work.

Aluminum and composite tubes were considered in this dissertation for study of multi-material joints and results conclude that tube materials show considerable influence on the crush performance of tubular lap joints. Hence, further work can be done in this direction. Steel is also an important material and is widely used in vehicle structures. Future studies can include advanced high strength steel tubes in the study on tubular lap joints. In addition, composite tubes with different laminate configurations and different fiber-matrix combinations can be considered.

Further, several studies in literature show influence of adhesive spew and scarfed tubes on the stresses in the adhesive layer. It would be interesting to explore the influence of such joint alterations on crush and tensile failure characteristics.

A major challenge faced during finite element modeling of tubular adhesive lap joints was defining material parameters of the adhesive, particularly fracture properties. Most studies in the literature use double cantilever beam and single edge notch bending tests to determine adhesive fracture energy and traction-separation characteristics of adhesives. A drawback of this method is that properties obtained are dependent on bond thickness. There is also a lack of standards for the determination of adhesive fracture properties. Future goal is to develop an experimental method to determine fracture properties for bulk adhesive under different loading modes and verify application of these properties in FEA for different adhesive layer thicknesses

References

[1] M. W. Andure , S. C. Jirapure and L. P. Dhamande , "Advance Automobile Material for Light Weight Future – A Review," in *International Conference on Benchmarks in Engineering Science and Technology ICBEST 2012*, 2012.

[2] J. W. Van der Wiel, "Future of Automotive Design & Materials Trends and Developments in Design and Materials," Automotive Technology Centre, acemr.eu, 2012.

[3] S. Burns, "Revisiting the Car Wars: Steel is Still the Material Choice for Automotive Design," 05 April 2017. [Online]. Available: https://agmetalminer.com/2017/04/05/revisiting-the-car-wars-steel-is-still-the-material-of-choice-for-automotive-design/.

[4] S. Modi, M. Stevens and M. Chess, "Mixed Material Joining Advancements and Challenges," Center for Automotive Research, 2017.

[5] C. D. Horvath, "Future Material Opportunities and Direction for Lightweighting Automotive Body Structures," 09 February 2012. [Online]. Available: https://www.nist.gov/system/files/documents/mml/acmd/structural_materials/Future-Material-Opportunities-and-Direction-for-Lighweighting-Automotive-v-Final-v2.pdf.

[6] J. Sloan, "Composites' Future in Automotive," 17 November 2016. [Online]. Available: https://www.compositesworld.com/articles/composites-future-in-automotive.

[7] J. Huetter, "CAR whitepaper predicts future of body materials: Everything but mild steel," 21 June 2017. [Online]. Available: https://www.repairerdrivennews.com/2017/06/21/car-whitepaper-predicts-future-of-body-materials-everything-but-mild-steel/.

[8] *Joining & Bonding of Composite Parts - The Structural Adhesive Advantage.* St. Paul, Minnesota : 3M, 2016.

[9] M. A. Parvez, A. Y. Asiri, A. Badghaish, A. K. Al-Dossary and A. Al-Mehlisi, "Saudi Aramco details nonmetallic products deployment in oil, gas," *Oil and Gas Journal,* vol. 116, no. 1, pp. 51-60, 2018.

[10] T. Allan, "Experimental and Analytical Investigation of the Behavior of Cylindrical Tubes Subject to Axial Compressive Forces," *Journal of Mechanical Engineering and Science,*

vol. 10, no. 2, pp. 182-197, 1968.

[11] K. K. Dama, S. B. V, R. R N and I. J. Shaik, "State of the Art on Basic Methodologies for Crashworthy Design of Automotive Body Components Considering Axial Collapse Mode," in *International Conference on Recent Trends in Engineering and Material Science*, Jaipur, 2016.

[12] K. R. F. Andrews, G. L. England and E. Ghani , "Classification of the Axial Collapse of Cylindrical Tubes under Quasi-static Loading," *International Journal of Mechanical Sciences,* vol. 25, no. 9-10, pp. 687-696, 1983.

[13] J. M. Alexander, "An Approximate Analysis of The Collapse Of Thin Cylindrical Shells Under Axial Loading," *The Quarterly Journal of Mechanics and Applied Mathematics,* vol. 13, no. 1, pp. 10-15, 1960.

[14] G. S R, L. G and G. R H, "Quasi-static axial compression of thin-walled circular aluminium tubes," *International Journal of Mechanical Science,* vol. 43, no. 9, pp. 2103-2123, 2001.

[15] N. Jones, *Structural Impact*, Cambridge University Press, 2011.

[16] A. Pugsley, "The crumpling of tubular structures under impact conditions," in *Symposium on the use of aluminium in railway rolling stock. Institute of Locomotive Engineers. The Aluminium Development Association*, 1960.

[17] Z. Tang, S. Liu and Z. Zhang, "Analysis of Energy Absorption Characteristics of Cylindrical Multi-Cell Columns," *Thin-Walled Structures,* vol. 62, pp. 75-84, 2013.

[18] G. L. Farley and R. M. Jones, "Crushing Characteristics of Continuous Fiber-Reinforced Composite Tubes," *Journal of Composite Materials,* vol. 26, no. 1, pp. 37-50, 1992.

[19] C. Bisagni, "Experimental investigation of the collapse modes and energy absorption characteristics of composite tubes," *International Journal of Crashworthiness ,* vol. 14, no. 4, pp. 365-378, 2009.

[20] P. H. Thornton, "Energy Absorption in Composite Structures," *Journal of Composite Materials,* vol. 13, pp. 247-262, 1979.

[21] D. Hull, "A Unified Approach to Progressive Crushing of Fibre-Reinforced Composite Tubes," *Composites Science and Technology,* vol. 40, pp. 377-421, 1991.

[22] D. Ghosh, L. Pancholi and A. Sathaye, "Comparative Studies of Adhesive Joints in Automotive," in *SAE 2014 World Congress & Exhibition*, 2014.

[23] L. Goglio, L. Peroni, M. Peroni and M. Rossetto, "High strain-rate compression and tension behaviour of an epoxy bi-component adhesive," *International Journal of Adhesion and*

Adhesives, vol. 28, no. 7, pp. 329-339, 2008.

[24] H. Chai, "The Effect of Bond Thickness, Rate and Temperature on Deformation and Fracture of Structural Adhesives under Shear Loading," *International Journal of Fracture,* vol. 130, pp. 497-515, 2004.

[25] M. D. Banea, F. S. M. de Sousa, L. F. M. da Silva, R. D. S. G. Campilho and A. M. Bastos de Pereira, "Effects of Temperature and Loading Rate on the Mechanical Properties of a High Temperature Epoxy Adhesive," *Journal of Adhesion Science and Technology ,* vol. 25, no. 18, pp. 2461-2474, 2011.

[26] B. E. Read, G. D. Duncan and B. C. Duncan , "Strain Rate and Temperature Dependence of the Properties of Adhesives. Prediction of High-Rate Data," 1999.

[27] H. F. Brinson, M. P. Renieri and C. T. Herakovich, "Rate and time dependent failure of structural adhesives," *ASTM Special Technical Publication,* pp. 177-199, 1975.

[28] W. Chen and B. Zhou, "Constitutive Behavior of Epon 828/T-403 at Various Strain Rates," *Mechanics of Time-Dependent Materials,* vol. 2, pp. 103-111, 1998.

[29] D. J. Pohlit, D. A. Dillard, G. C. Jacob and J. M. Starbuck, "Evaluating the rate-dependent fracture toughness of an automotive adhesive," *The Journal of Adhesion,* vol. 84, no. 2, pp. 143-163, 2008.

[30] S. Lampman, *Characterization and Failure Analysis of Plastics*. ASM International, 2003.

[31] W. Lim and H. Mizumachi, "Fracture Toughness of Adhesive Joints. III. Temperature and Rate Dependencies of Mode II Fracture Toughness and Adhesive Shear Strength," *Journal of Applied Polymer Science,* vol. 63, no. 7, pp. 835-841, 1997.

[32] A. J. Kinloch, S. J. Shaw and D. L. Hunston, "Deformation and fracture behaviour of a rubber-toughened epoxy: 2. Failure criteria," *Polymer,* vol. 24, no. 10, pp. 1355-1363, 1983.

[33] T. Carlberger, A. Biel and U. Stigh, "Influence of temperature and strain rate on cohesive properties of a structural epoxy adhesive," *International Journal of Fracture,* vol. 155, no. 2, pp. 155-166, 2009.

[34] M. Angelidi, A. P. Vassilopoulos and T. Keller, "Ductility, recovery and strain rate dependency of an acrylic structural adhesive," *Construction and Building Materials,* vol. 140, no. 1, pp. 184-193, 2017.

[35] M. D. Banea and L. F. M. da Silva, "Adhesively Bonded Joints in Composite Materials: An Overview.," *Proceedings of the Institution of Mechanical Engineers, Part L: Journal of Materials: Design and Applications,* vol. 223, no. 1, pp. 1-18, 2009.

[36] L. J. Hart-Smith, "The Design of Repairable Advanced Composite Structures," in *Aerospace Technology Conference & Exhibition*, 1985.

[37] E. Ahmed and A. W. Tehami, "Evaluation of Strength of Adhesively Bonded Metallic Single Lap Joint with Different End Geometries," in *SAE WCX World Congress Experience.*, 2018.

[38] L. F. M. da Silva, T. N. S. S. Rodrigues, M. A. V. Figueiredo , M. F. S. F. de Moura and J. A. G. Chousal, "Effect of adhesive type and thickness on the lap shear strength," *The Journal of Adhesion,* vol. 82, no. 11, pp. 1091-1115, 2006.

[39] A. Baldan, "Adhesion phenomena in bonded joints," *International Journal of Adhesion and Adhesives,* vol. 38, pp. 95-116, 2012.

[40] A. J. Kinloch, *Adhesion and Adhesives: Science and Technology.* Springer, 1987.

[41] A. Deb, I. Malvade, P. Biswas and J. Schroeder, "An experimental and analytical study of the mechanical behaviour of adhesively bonded joints for variable extension rates and temperatures," *International Journal of Adhesion and Adhesives,* vol. 28, no. 1-2, pp. 1-15, 2008.

[42] F. Zhang, X. Yang, Y. Xia, Q. Zhou, H. Wang and T. Yu, "Experimental study of strain rate effects on the strength of adhesively bonded joints after hygrothermal exposure," *International Journal of Adhesion and Adhesives,* vol. 56, pp. 3-12, 2015.

[43] V. Srivastava, "Characterization of adhesive bonded lap joints of C/C–SiC composite and Ti–6Al–4V alloy under varying conditions," *International Journal of Adhesion and Adhesives,* vol. 23, pp. 59-67, 2003.

[44] A. Parashar and P. Mertiny, "Adhesively Bonded Tubular Joints: Review," *International Journal of Adhesion and Adhesives,* vol. 38, pp. 58-68, 2012.

[45] E. Dragoni and L. Goglio, "Adhesive stresses in axially-loaded tubular bonded joints - Part I: Critical review and finite element assessment of published models," *International Journal of Adhesion and Adhesives,* vol. 47, pp. 35-45, 2013.

[46] J. L. Lubkin and E. Reissner, "Stress distribution and design data for adhesive lap joints between circular tubes," *Transactions of ASME ,* vol. 78, pp. 1213-1221, 1956.

[47] R. D. Adams and N. A. Peppiatt, "Stress Analysis of Adhesive Bonded Tubular Lap Joints," *The Journal of Adhesion,* vol. 9, no. 1, pp. 1-18, 1977.

[48] Y. Nakano, M. Kawasaki and T. Sawa, "Stress analysis of adhesive lap joints of dissimilar hollow shafts subjected to an axial load," *Journal of Adhesion Science and Technology,* vol.

12, pp. 1-18, 1998.

[49] Y. P. Shi and S. Cheng, "Analysis of Adhesive-Bonded Cylindrical Lap Joints Subjected to Axial Load," *Journal of Engineering Mechanics,* vol. 119, no. 3, pp. 584-602, 1993.

[50] Y. G. Kim, S. J. Lee, D. G. Lee and K. S. Jeong, "Strength analysis of adhesively-bonded tubular single lap steel-steel joints under axial loads considering residual thermal stresses," *The Journal of Adhesion ,* vol. 60, no. 1-4, pp. 125-140, 1997.

[51] T. R. Guess and E. D. Reedy Jr., "Composite-to-metal tubular lap joints: strength and fatigue resistance," *International Journal of Fracture,* vol. 63, pp. 351-367, 1993.

[52] T. R. Guess, E. D. Reedy Jr. and A. M. Slavin , "Testing Composite-to-Metal Tubular Lap Joints," *Journal of Composites, Technology and Research,* vol. 17, no. 2, pp. 117-124, 1995.

[53] S. Braeik, R. Zitoune, A. B. Khalifa and M. Zidi, "Experimental and numerical study of adhesively bonded ±55° filament wound tubular specimens under uniaxial tensile loading," *Composite Structures,* vol. 172, pp. 297-310, 2017.

[54] S. Labbe and J. M. Drouet, "A multi-objective optimization procedure for bonded tubular-lap joints subjected to axial loading," *International journal of adhesion and adhesives,* vol. 33, pp. 26-35, 2012.

[55] D. R. Barbosa, R. D. S. G. Campilho, R. J. B. Rocha and L. R. F. and Ferreira, "Cohesive Zone Analysis of Tubular Adhesively-Bonded Joints," *Annals of "Dunarea de Jos" University of Galati. Fascicle XII, Welding Equipment and Technology,* vol. 29, pp. 11-18, 2018.

[56] D. R. Barbosa, R. D. S. G. Campilho, R. J. B. Rocha and L. R. F. Ferreira, "Experimental Experimental and numerical assessment of tensile loaded tubular adhesive joints," *Proceedings of the Institution of Mechanical Engineers, Part L: Journal of Materials: Design and Applications,* vol. 233, no. 3, pp. 452-464, 2019.

[57] A. N. Abood, A. H. Saleh and Z. W. Abdullah, " Effect of heat treatment on strain life of aluminum alloy AA 6061," *Journal of Materials Science Research,* vol. 2, no. 2, pp. 51-59, 2013.

[58] M. May, O. Hesebeck, S. Marzi, W. Böhme, J. Lienhard, S. Kilchert, M. Brede and S. Hiermaier, "Rate dependent behavior of crash-optimized adhesives–Experimental characterization, model development, and simulation," *Engineering Fracture Mechanics,* vol. 133, pp. 112-137, 2015.

[59] T. A. Fernandes, R. D. Campilho, M. D. Banea and L. F. da Silva, "Adhesive selection for single lap bonded joints: experimentation and advanced techniques for strength prediction,"

The Journal of Adhesion, vol. 91, no. 10-11, pp. 841-862, 2015.

[60] LS-DYNA Keyword User's Manual Volume II R9.0, Livermore Software Technology Corporation (LSTC), 2016.

[61] M. Feucht, A. Haufe and G. Pietsch, "Modeling of Adhesive Bonding in Crash Simulation," in *LS-DYNA Anwenderforum*, Frankenthal, 2007.

[62] T. Graf, A. Haufe and F. Andrade, *Adhesives modeling with LS-DYNA: Recent developments and future work,* Stuttgart : DYNAmore GmBH, 2014.

[63] D. Cox, N. Reid and N. Reid, *The Theory of the Design of Experiments*. CRC Press, 2000.

[64] J. Tomblin, J. Sherraden, W. Seneviratne and K. S. Raju, "A – Basis and B – Basis Design Allowables for Epoxy – Based Prepreg TORAY 7781 Finish 558/#2510 Fiberglass Fabric," AGATE-WP3.3-033051-133, September 2002.

[65] "T700SC 12K/ 2510 Plain Weave Fabric," in *Composite Materials Handbook (CMH-17)*, vol. 2, SAE International. 2017.

[66] F. Deleo and P. Feraboli, "Crashworthiness energy absorption of carbon fiber composites: Experiment and Simulation," in *11th-Annual Automotive Composites Conference and Exhibition, ACCE 2011*, Troy, 2011.

[67] A. Li, "Optimization of Composite Structures for Crashworthiness," M.S. Thesis, Delft University of Technology, 2019.

[68] P. Chatla, "LS-Dyna for Crashworthiness of Composite Structures," M.S. Thesis, University of Cincinnati, 2012.